Copyright Undertaking

NUMERICAL SIMULATION OF AEROSOL DYNAMICS AND COUPLING WITH CFD FOR SOOT MODELLING IN COMBUSTION FLOWS

WANG FEI

PhD

The Hong Kong Polytechnic University

2025

The Hong Kong Polytechnic University
Department of Mechanical Engineering

Numerical Simulation of Aerosol Dynamics and Coupling with CFD for Soot Modelling in Combustion Flows

Wang Fei

A thesis submitted in partial fulfillment of the requirements for the degree of Doctor of Philosophy

January 2025

CERTIFICATE OF ORIGINALITY

I hereby declare that this thesis is my own work and that, to the best of my knowledge and belief, it reproduces no material previously published or written, nor material that has been accepted for the award of any other degree or diploma, except where due acknowledgement has been made in the text.

____________________ (Signed)

WANG Fei (Name of student)

Abstract

The incomplete combustion of carbon-based fuels leads to the appearance of soot. It is required to predict and control soot emissions due to the detrimental effects on the environment and human health. Detailed soot models are based on aerosol dynamics, which is governed by the population balance equation (PBE). In the present study, solving the particle size distribution (PSD) of the PBE is conducted to deepen the understanding of aerosol dynamics and coupled with CFD to investigate soot formation and evolution in laminar and turbulent combustion flows.

A new sorting algorithm-based merging weighted fraction Monte Carlo (SAMWFMC) method is firstly proposed and developed to solve the PBE of coagulation based on sorting algorithm and a new merging scheme. Numerical results of the SAMWFMC method show excellent agreement with analytical solutions and very low stochastic errors in different order moments of PSD.

Instead of dealing with only one or several dynamic processes, a new sorting algorithm-based merging Monte Carlo method (SAMMC) capable of solving all aerosol dynamic processes is then proposed and developed based on a new neighbour merging method. Numerical results show that the SAMMC method has very high computational accuracy and can accurately deal with dynamic processes without introducing systematic errors.

Simultaneously, a new OpenFOAM solver incorporating a detailed transport model is developed for reacting flow simulations. Systematic validations are conducted to evaluate its computational performance. The successful development and implementation of the accurate numerical framework provide a new CFD tool for the combustion community.

A newly proposed dimer-based soot model involving various aerosol dynamics is then incorporated into the new numerical framework for investigating soot formation in laminar diffusion flames. Simulated soot volume fractions (SVFs) agree very well with experimental data under different oxygen mole fractions (X_O) and strain rates (K).

With X_O increasing or K decreasing, dimer production and surface growth are significantly enhanced, leading to an increase of SVF and skewness of SVF profile towards the fuel stream.

To gain a deeper understanding of turbulence modelling, a new one-equation turbulence model is developed in the numerical framework, which combines the best characteristics of standard k-ε and Wilcox's k-ω turbulence models. Numerical validation of benchmark flow configurations demonstrates that the new turbulence model has a great potential to predict flow separation and reattachment.

Finally, the numerical framework coupling an extended soot sectional method with a finite-rate chemistry model is used for soot modelling in turbulent bluff body flames. Results show that the numerical framework can accurately predict the flow and flame properties and well capture the soot formation and evolution processes. With bluff body radius increasing, soot PSD remains a bimodal shape and shifts towards the larger soot aggregate side at the centerline and within the recirculation zone. Coagulation predominantly occurs at small soot aggregates, while PAH condensation and HACA surface growth take significant effect at large soot aggregates.

In summary, numerical simulation of aerosol dynamics provides a better understanding of PSD evolution, and the newly developed CFD numerical framework demonstrates high capability in soot modelling.

Publications Arising from the Thesis

1. F. Wang, T.L. Chan* (2022). A new one-equation turbulence model based on the combined standard k-ε and k-ω turbulence models for benchmark flow configurations. In *Proceedings of the 7th World Congress on Momentum, Heat and Mass Transfer (MHMT'22)*, Lisbon, Portugal, 1-8. https://doi.org/10.11159/icmfht22.145.

2. F. Wang, T.L. Chan* (2023). A new sorting algorithm-based merging weighted fraction Monte Carlo method for solving the population balance equation for particle coagulation dynamics. *International Journal of Numerical Methods for Heat & Fluid Flow*, 33(2), 881-911. https://doi.org/10.1108/HFF-06-2022-0378.

3. F. Wang, L. An, T.L. Chan* (2023). Event-driven sorting algorithm-based Monte Carlo method with neighbour merging method for solving aerosol dynamics. *Applied Mathematical Modelling*, 120, 833-862. https://doi.org/10.1016/j.apm.2023.04.016.

4. F. Wang, L. An, T.L. Chan* (2025). An OpenFOAM solver incorporating detailed transport model for reacting flow simulations. *Computer Physics Communications*, 309, 109427. https://doi.org/10.1016/j.cpc.2024.109472.

5. F. Wang, L. An*, T.L. Chan* (2025). Numerical investigation on soot particle size distribution in turbulent non-premixed bluff body flames by using soot sectional method and detailed chemistry. *Combustion and Flame*. Submitted.

Acknowledgements

I would like to express my sincere thankfulness to my Former Chief Supervisor, Prof. CHAN Tat Leung for his inspiring guidance and support during my study at the Department of Mechanical Engineering of The Hong Kong Polytechnic University. I wish him a comfortable and joyful retirement. My thankfulness also goes to Dr. JIANG Xiao of Prof. CHAN's group for his kind guidance and selfless help.

I would like to extend my sincere appreciation and respect to my Chief Supervisor, Prof. AN Liang for his comprehensive guidance, understanding and patience during my study after the retirement of Prof. CHAN. I appreciate his strong encouragement and financial support throughout my research. My appreciation also goes to all members of Prof. AN's group for their kind friendship and help.

I would also like to express my gratefulness to Ms. TAM Lily, Ms. WONG Merlin and Ms. WONG Yan, who provided kind administrative support during my study. My gratefulness also goes to the financial support from the research studentship granted by The Hong Kong Polytechnic University for accomplishing this research work.

I would also like to express my thanks to Prof. LIN Cong, Dr. HU Liang, Mr. ZHU Yinggang and Ms. Ren Xiuyun as well as other friends in Hong Kong for their friendship, encouragement and help during my study at PolyU.

Finally, I would like to express my heartfelt gratitude to my beloved wife, Ms. YANG Lulu, and my lovely daughter, Miss WANG Yuqing, for their love, trust, support, understanding and encouragement. I am also grateful to my parents and other family members, who have always loved me unconditionally.

WANG Fei

Hong Kong

January 2025

Table of Contents

List of Figures

List of Tables

Nomenclature

a_p	Planck mean absorption coefficient
A_S	particle surface area per volume
C_0	total coagulation rate
C_{ij}	coagulation rate of numerical particles, *i* and *j*
C_p	specific heat capacity of the mixture at constant pressure
d_g	gyration diameter
d_m	mobility diameter
d_p	particle diameter
D_s	diffusion coefficient of soot
D_f	fractal dimension
D_{jk}	binary diffusion coefficient between species *k* and species *j*
$D_{k,\mathrm{mix}}$	diffusion coefficient of the *k*th species into the rest of the mixture
E_F	van der Walls enhancement factor
f_v	soot volume fraction
h	enthalpy
$h_{f,k}$	formation enthalpy of species *k*
h_k	specific enthalpy of species *k*
$h_{s,k}$	sensible enthalpy of species *k*
i	size of aerosols
$\mathbf{I}$	unit tensor
k	turbulent kinetic energy

k_B	Boltzmann constant
K	kinematic energy
L	turbulent length scale
Le	Lewis number
M	soot mass density
M_0	particle number concentration
M_k	*k*th order moment
Ma	Mach number
n	particle number density
N	soot number density
n_p	number of primary particles in an aggregate
N_0	initial total number concentration
N_A	Avogadro’s number
N_p	number of numerical particles
p	pressure
P_k	probability of a particle containing *k* primary particles
Q_r	radiative heat source
r	random number
Re	Reynolds number
R_u	universal gas constant
S_{ij}	strain rate tensor
t	time
T	temperature
$\mathbf{U}$	velocity

u_i	*i*th-component velocity
v_i	particle volume of the numerical particle
V	cell volume of the aerosol system in numerical simulation
$\mathbf{V}_C$	spatially varying correction velocity
$\mathbf{V}_T$	thermophoretic velocity
w_i	weight of the numerical particle
W	mean molecular weight of the mixture
W_k	molecular weight of the *k*th species
x_i	coordinates of *i*th-component
x_j	coordinates of *j*th-component
X_k	mole fraction of species *k*
Y	soot mass density
Y_k	mass fraction of species *k*
Z	mixture fraction
Z_{rot}	rotational relaxation collision number

Greek Symbols

α_{ij}	fraction function
β	coagulation kernel
Γ	diffusivities
γ_{ij}	sticking coefficient between PAH species i and j
δ	multiplicative constant
δ_{ij}	Kronecker delta
ε	turbulent dissipation
ζ	local mixture fraction
λ	thermal conductivity
λ_l	gas mean free path
μ	dynamic viscosity
ν	kinematic viscosity
ρ	density
σ	mean standard deviations
τ	waiting time
$\boldsymbol{\tau}$	viscous stress tensor
τ_c	characteristic coagulation time
τ_{ij}	viscous stresses components
Φ	coagulation rate
Ω	mean number of coagulation events
ω	turbulent specific dissipation rate

ω_k	reaction rate of species *k*
ω_T	heat production rate due to combustion

Abbreviations

AS	analytical solution
AVD	absolute volume difference
BC	boundary condition
CCK	constant coagulation kernel
CDF	counterflow diffusion flame
CFD	computational fluid dynamics
CFF	constant fraction function
CPU	central processing unit
DNS	direct numerical simulation
DSMC	direct simulation Monte Carlo
EFF	exponential fraction function
FVM	finite volume method
GDE	general dynamics equation
GPU	graphic processing unit
HACA	H-abstraction-C_2H_2-addition
HFF	hyperbolic fraction function
HPC	high performance cluster
ID	identification number
IED	initial exponential distribution
IMD	initial monodispersed distribution

JANAF	Joint Army Navy Air Force
LCK	linear coagulation kernel
LES	large eddy simulation
MC	Monte Carlo
MMC	multi-Monte Carlo
MOM	method of moments
NASA	National Aeronautics and Space Administration
OOP	object-oriented programming
OpenFOAM	open-source field operation and manipulation
PAH	polycyclic aromatic hydrocarbon
PBE	population balance equation
PISO	Pressure Implicit with Splitting of Operator
PNC	particle number concentration
PSD	particle size distribution
QCK	quadratic coagulation kernel
RANS	Reynolds-averaged Navier–Stokes
RVD	relative volume difference
SAMMC	sorting algorithm-based merging Monte Carlo
SAMWFMC	sorting algorithm-based merging weighted fraction Monte Carlo
SCFF	stepwise constant fraction function
SGS	sub-grid-scale
SIMPLE	Semi-Implicit Method for Pressure Linked Equations
SKE	standard k-ε

SM	sectional method
SST k-ω	shear stress transport k-ω
SVF	soot volume fraction
TMR	Turbulence Modeling Resource
WA	Wray-Agarwal turbulence model
WFMC	weighted fraction Monte Carlo
WKO	Wilcox’s k-ω

Chapter 1 Introduction

1.1 Research Background and Scope

At present, burning coal, oil and natural gas generates the most part of energy consumed by human activities. Except for energy conservation, improving energy efficiency is particularly important due to the finiteness of these natural resources. Ideally, the products of complete combustion of hydrocarbons are H_2O and CO_2, resulting in the maximum heat released and energy generation available [1,2]. However, the phenomenon of incomplete combustion of fuels is ubiquitous in nature and human activities [2-5] due to locally insufficient oxygen [1,2,6,7], unavoidably leading to the universal appearance of soot in the process of fuel combustion. Anthropogenic factors related to the consumption of hydrocarbon fuels, such as generating electricity by firing coal or natural gas, driving vehicles running on gasoline or diesel fuels and cooking on the gas stove on a daily basis, are primarily responsible for the considerable number of soot emissions from the exhaust of the different types of combustion devices. It should be noted that soot is black carbons generated by incomplete combustion of hydrocarbon fuels, while particulates describe a great variety of liquid and solid particles including soot.

Soot is a kind of small particles or aerosols produced by burning carbonaceous substances, and its size ranges from several nanometers (nm) to micrometers (μm) [3,4,7-9], which plays different roles in our daily life and industry. First of all, soot has an adverse impact on the environment as it is a main source of air pollution. The constantly high consumption and commonly incomplete combustion of carbon-based fuels have led to an increasing significant number of soot emissions. Although so far only restrictions on the total mass of soot are set out in most regulations, new regulations in the near future will call for control of soot number concentrations and particle size distributions (PSDs) due to the contributions of these two factors to the poor air quality. In addition, these small particles have posed a serious threat to human health because they may cause various particle-induced diseases including various respiratory diseases and even cancers due to the easy access of soot aerosols to the respiratory system and the lung. Safety issues such as traffic accidents may also happen due to limited visibility caused by suspended particles in the air. On the other hand, a controllable number of soot aerosols of flame synthesis with a specific size distribution and fractal structure can be a kind of technologically advanced and commercially valuable materials due to its wide application in various industries [10-12]. For example, it is reported that soot can enhance the heat transfer by radiation in industrial furnaces [13], and filling soot in tyres can markedly increase the strength and wear-resistance of rubber required in the auto sector; the toner and ink of printers are mainly composed of soot while a specific amount of soot can be used to prepare fabric dye. Consequently, it is demanded for decreasing its detrimental effects on the environment and human health, concurrently making full use of its advantages for better catering for practical applications. This can be achieved by accurately predicting and controlling the formation and evolution, and fractal structure of these nano to fine particles on a case-by-case basis. Under these circumstances, having a complete knowledge of soot formation and evolution processes in combustion flows leading from gas-phase molecules to soot aerosols can lay a sound foundation for flexible applications of corresponding technology into practice.

It is agreed that fuel-soot conversion occurs through a series of complex interactions, each of which involves a number of chemical and physical steps. Generally, soot formation and evolution are composed of inception, coagulation, agglomeration, surface growth and oxidation [4,8,12,14,15], which lead to the change of soot aerosol numbers or sizes. Non-linear and partial integrodifferential population balance equation (PBE) [5] governs these phenomena of number or size change, whose analytical solution only exists in a few special cases [9,10,16-20] due to its complex characteristics. These obtained analytical solutions are of great significance and can be used as a useful benchmark for validating other numerical methods [10], but it is normally based on some rigid assumptions [21]. In consequence, the selection of suitable numerical methods can be a sensible choice in approximating the solution of the PBE [18,22].

In order to solve the PBE for an aerosol system of interest, researchers have developed a number of methods aiming at different problems of aerosol dynamics, among which sectional method (SM), method of moments (MOM) and Monte Carlo (MC) methods are the most widely used. The SM is a discrete numerical approach to solve the PBE, which divides the particle size spectrum into several sections according to the particle sizes [22,23] and then disposes particle sizes by sections [18,22]. However, the solution accuracy of SM largely relies on the discretized section number. It implies the number of sections which are related to the particle sizes should increase if a higher computational accuracy is required. This may result in fairly complex algorithms, the increase of computational cost (i.e., computational time and computer memory), and even numerical diffusion. The MOM can be used to solve the PBE and simultaneously deal with the problem of high computational cost, which is typically encountered in the SM. But the MOM is a quite different approach from the SM. Unlike the SM that attempts to solve the particle size distribution (PSD) of the PBE, the MOM aims to compute the moments of the PBE [10,24-26]. As a result, a closure problem arises which may introduce approximation error into the moment solutions. Although the MOM has a big advantage in computational cost, it seems to be not highly flexible in dealing with complex aerosol dynamics due to its complexity [27,28]. The MC methods are conducted by adopting representative numerical particles towards the processes of the PBE, and these processes are randomly implemented based on probabilities. The discrete nature of the MC can perfectly match the stochastic properties of Brownian motion of particles, which means that it can be possible to closely simulate the behavior of particles. Moreover, the evolution of any number of particles can be tracked [27,28]. Despite these advantages, problems of stochastic property and computational cost remain in MC methods. In addition, due to the restriction of the computer memory and central processing unit speed, solely a limited number of numerical particles could be used, which inevitably influences the computational precision.

Except for straightforwardly adopting advanced computational techniques including high performance cluster (HPC) or graphic processing unit (GPU) to accelerate computations [29-31], a great variety of MC algorithms including direct simulation Monte Carlo (DSMC) method [17], multi-Monte Carlo (MMC) method [32] and weighted fraction Monte Carlo (WFMC) method [33] have been developed to reduce the stochastic errors and to increase the computational accuracy of MC methods, especially for coagulation which is regarded as the most demanding process for modelling among various aerosol dynamics [32,34]. Although the WFMC method reduces the stochastic errors in high-order moments of the PSD compared with the DSMC and MMC methods, the stochastic error in the total particle number concentration becomes considerable large. In addition, the WFMC method has a stringent restriction on the fraction functions, making few fraction functions applicable to the WFMC method except for several specifically selected adjustable fraction functions. To overcome these limitations, the sorting algorithm-based merging weighted fraction Monte Carlo (SAMWFMC) method [35] applicable to both adjustable and constant fraction functions is developed, which is aimed at solving the PBE in terms of coagulation with lower stochastic error.

Most MC methods are specifically aimed at only one dynamic process or several dynamic processes of interest instead of dealing with all aerosol dynamic processes, which greatly restricts the application of these MC methods to simulate all aerosol dynamic processes. Although the stepwise constant-volume method [36] and mass-based and number-based constant-number methods [37] could possibly deal with all dynamic aerosol processes, their performance in computational accuracy and efficiency still require further improvement and enhancement. In addition, the new numerical particle population may not completely preserve the information of old numerical particle population. Therefore, the sorting algorithm-based merging Monte Carlo (SAMMC) method [38] is proposed and developed in the present study to tackle these technical problems.

Besides aerosol dynamics, it is generally agreed that soot formation and evolution could be strongly influenced by the local reacting flow field involved, which requires coupling fluid dynamics with aerosol dynamics in soot modelling. Numerical simulations play an increasingly significant role in modelling soot aerosol dynamics in combustion flows due to the advancing computational methods and developing computational tools, and both macroscopic and microscopic information about soot formation and evolution may be possibly provided in detail besides experiment investigations. Normally, soot aerosols in the fluid flow can be treated as a continuous phase or a disperse phase in numerical simulations, which is called Eulerian and Lagrangian methods, respectively. In a Lagrangian method, each soot particle is tracked and their trajectories are obtained at an extremely high computational cost [39], leading to a limited number of applications of this method [39-50]. By comparison, it is very straightforward and computationally cheap to simulate soot aerosol dynamics in combustion flows by using Eulerian methods combined with computational fluid dynamics (CFD).

Open-source Field Operation and Manipulation (OpenFOAM) software is a leading free open-source CFD platform using C++ language, in which customized libraries and numerical solvers as well as pre- and post-processing utilities can be developed to solve continuum mechanics problems based on the finite volume method. However, the molecular transport model integrated into a reacting flow solver is highly simplified in the original OpenFOAM codes [51,52], which is only acceptable and valid in some specific combustion cases. In addition, this simplified model is not capable of resolving all physical scales for new insights into physical phenomena with direct or quasi-direct numerical simulations. To tackle this critical technical problem, a new library for calculating transport properties based on a detailed transport model is developed and coupled with a newly developed combustion solver called *standardReactingFoam* [53] for modelling reacting flows involving multi-species, in which a new utility for inputting molecular transport parameters required by the detailed transport model is also developed based on the numerical framework.

Apart from enhancing the understanding of solving fluid flow and gas-phase chemistry, an enhanced knowledge of soot aerosol dynamic mechanism for combustion flows is essentially required in both scientific research and engineering applications. Due to the least understood soot inception mechanism, accurate modelling of gas-phase species and soot transport processes is challenging especially in laminar flows due to the differential diffusion [10]. Specifically, as the diffusivity of soot aerosols in laminar flows is remarkably lower than gas-phase species counterparts, differential diffusion between them should be considered for accurately modelling their transport processes in CFD simulations. Therefore, a new dimer-based soot model is proposed and coupled with the newly developed numerical framework for simulating soot formation and evolution in laminar combustion flows, in which dimers are regarded as the link from polycyclic aromatic hydrocarbons (PAHs) to soot.

The presence of turbulence characterized by rapid and random fluctuations of the flow velocity normally leads to closure problems, which originate from the nonlinear convection terms involving unknown fluctuating variables. These problems can be tackled by establishing a set of equations and introducing a turbulence model for the unknow quantities. To gain a deeper understanding of turbulence modelling in CFD, a one-equation turbulence model [54] combining desirable features in two-equation turbulence models is newly proposed and implemented into the newly developed numerical framework of OpenFOAM.

As soot formation and evolution closely depend on the local gas-phase species and thermochemical conditions, successful soot prediction in a turbulent flow requires precise modelling of turbulence-chemistry and turbulence-soot interactions based on detailed chemistry. In finite-rate chemistry simulations, combustion described by detailed chemistry is solved in real-time to capture intricate chemical kinetics with high fidelity. Taking differential diffusion into account, soot could be fully coupled with the thermochemical state of the gas phase by simultaneously solving all governing equations together with considering turbulence-chemistry interactions. When a SM is adopted to simulate soot aerosol dynamics in combustion flows, detailed information on the local soot PSDs can be accessed directly [55]. Therefore, the newly developed OpenFOAM numerical framework coupling an extended soot sectional method with a finite-rate chemistry model based on detailed chemistry is developed for modelling soot aerosol dynamics in turbulent combustion.

1.2 Research Motivation and Objectives

Combustion of hydrocarbon fuels unavoidably leads to soot generation. The motivation of the present study is to develop a general numerical framework capable of studying soot formation and evolution in practical combustion devices with current and future fuels including ethylene, natural gas, liquefied petroleum gas and even hydrogen doping hydrocarbon fuels. Soot formation and evolution in combustion flows can be described by detailed soot models, which are normally composed of aerosol dynamics and chemical kinetics, therefore involving a series of complicated physicochemical processes involving nucleation, condensation, coagulation, aggregation, surface growth and oxidation. In the present study, a sorting algorithm-based merging weighted fraction Monte Carlo (SAMWFMC) method is proposed for specifically dealing with coagulation, and a new sorting algorithm-based merging Monte Carlo (SAMMC) method is then developed for simulating all aerosol dynamic processes, especially effective in those challenging aerosol dynamic processes generating additional numerical particles. Simultaneously, a detailed transport model based on the standard kinetic theory of gases is incorporated into computational fluid dynamics (CFD) solvers for accurate reacting flow simulations based on the OpenFOAM platform, and this numerical framework incorporates a newly proposed dimer-based soot model for investigating soot aerosol dynamics in laminar combustion flows. In addition, a one-equation turbulence model with high computational efficiency is developed based on this newly developed numerical framework to gain a deeper understanding of turbulence modelling. Finally, the developed numerical framework coupling an extended soot sectional method with a finite-rate chemistry model based on detailed chemistry is used for investigating soot PSDs evolution in turbulent flames.

Therefore, the objectives of this thesis are:

1. To deepen the understanding of numerical simulations in soot aerosol dynamics including coagulation, nucleation and surface growth in both laminar and turbulent combustion flows.

2. To propose a sorting algorithm-based merging weighted fraction Monte Carlo

(SAMWFMC) method dedicated to solving the most challenging coagulation with various conditions in aerosol dynamics.

3. To propose a sorting algorithm-based merging Monte Carlo (SAMMC) method applicable for the simulation of all aerosol dynamic processes (i.e., nucleation, coagulation, breakage, condensation/evaporation, deposition), especially effective in those challenging aerosol dynamic processes generating additional numerical particles.

4. To develop a numerical framework of incorporating a detailed transport model based on standard kinetic theory of gases into combustion solvers for accurate reacting flow simulations in OpenFOAM.

5. To develop a soot model including surface growth and oxidation, inception, condensation and coagulation to investigate soot formation in laminar combustion flows based on the newly developed numerical framework in OpenFOAM.

6. To derive a turbulence model incorporated into the new numerical framework of OpenFOAM to gain a deeper understanding of turbulence modelling as well as CFD.

7. To extend the new numerical framework coupling a soot sectional method with a finite-rate chemistry based on detailed chemistry for numerically investigating the evolution of soot PSDs in turbulent combustion flows.

1.3 Outline of the Thesis

The outline of this thesis is organized as:

Chapter 1 overviews the research background and scope of numerical simulations on aerosol dynamics especially soot aerosol dynamics in combustion flows, which indicates the motivations and objectives of the present study based on the research and knowledge gaps.

Chapter 2 presents the literature review of investigating soot aerosol dynamics for combustion flows, indicating the knowledge development and its limitations where the knowledge gap may lie.

Chapter 3 presents the mathematical models indicating the theoretical fundamentals of numerical simulations based on computational fluid dynamics (CFD) and aerosol dynamics.

Chapter 4 validates a newly proposed and developed sorting algorithm-based merging weighted fraction Monte Carlo (SAMWFMC) method aimed at various coagulation conditions in aerosol dynamics.

Chapter 5 describes the detailed development of sorting algorithm-based merging (SAMMC) method applicable for all aerosol dynamic processes with very high computational accuracy, with applications to those challenging aerosol dynamic processes generating additional numerical particles.

Chapter 6 introduces the detailed development of a numerical framework incorporating the mixture-averaged transport model based on the standard kinetic theory of gases into combustion solvers for reacting flow simulations in Open-source Field Operation and Manipulation (OpenFOAM).

Chapter 7 investigates soot formation and evolution in laminar combustion flows based on the new numerical framework by using a proposed dimer-based soot model involving surface growth and O_2 and OH oxidation, inception, condensation and coagulation, in which an ethylene laminar counterflow diffusion flame is used as a realization of the laminar flamelet for fundamental soot studies.

Chapter 8 provides the derivation of a newly proposed one-equation turbulence model combining the desirable features of the two-equation standard k-ε and Wilcox's k-ω turbulence models in the complete form without simplification in the diffusion terms based on the new numerical framework.

Chapter 9 investigates soot formation and evolution via the soot PSDs for turbulent combustion flames via the newly developed numerical framework coupling an extended soot sectional method with a finite-rate chemistry based on detailed chemistry.

Chapter 10 concludes the main research contributions and scientific findings with recommendations for future work.

Chapter 2 Literature Review

2.1 Introduction

Soot aerosol dynamics describe the continuous process transited from gas-phase hydrocarbon molecules to mature soot aerosols, which occur rapidly in high temperature zone of rich fuel combustion. Figures 2.1 and 2.2 present soot formation and evolution for coflow and counterflow flames, which includes fuel pyrolysis, polycyclic aromatic hydrocarbon (PAH) growth, soot nucleation, growth and oxidation [56]. Specifically, fuel decomposes to a broad range of small hydrocarbons before these degraded products form into small aromatic hydrocarbons [57]. After these small aromatic hydrocarbons grow larger by constantly adding hydrocarbon molecules as shown in Figure 2.3, these larger aromatic hydrocarbons containing more benzenoid rings become small soot aerosols. Once these soot aerosols are incepted, they experience the process of surface growth, aggregates, and later-oxidation. Surface growth (condensation) increases the size of soot aerosols but remains the number of particles unchanged, which is realised by condensing PAH species on the particles. It is also found that benzene can grow to inception particle via H-abstraction-C_2H_2-addition (HACA) mechanism [14,58-60], which demonstrates that precursors such as C_2H_2 and PAHs significantly influence the subsequent evolution of soot aerosols [4,61-63]. Aggregates refer to soot agglomerates taking the form of chain-like structures or particle collision. Because of inherent instability, small particles in the gas collide due to the Brownian motion and adhere through attractive forces to form larger particles or structures [9], in which the number of particles decreases while the size of each particle increases. However, surface oxidation by oxidizing agents (i.e., O_2 and OH) can destroy soot particles, therefore reducing the particle size and surface area [4,7,8,12,14,64].

Apart from relying on the local chemical composition including C_2H_2, PAHs, O_2 and OH, soot formation and evolution also strongly depend on the thermodynamics and surrounding air flows, which implies that it is required to couple soot models with fluid dynamics and transport properties in numerical simulations. The transport processes of gas-phase species and soot are rather important especially for laminar flows, which directly affect their local distributions, therefore necessitating considering differential diffusion when modelling. The presence of turbulence makes soot modelling even more challenging as all variables including velocity, temperature and concentrations of gas-phase species as well as soot properties fluctuate at random in turbulent combustion, which requires taking turbulence model as well as turbulence-chemistry and turbulence-soot interactions into account. These interactions generally lead to unclosed terms in transport equations, which should be appropriately modelled in numerical simulations.

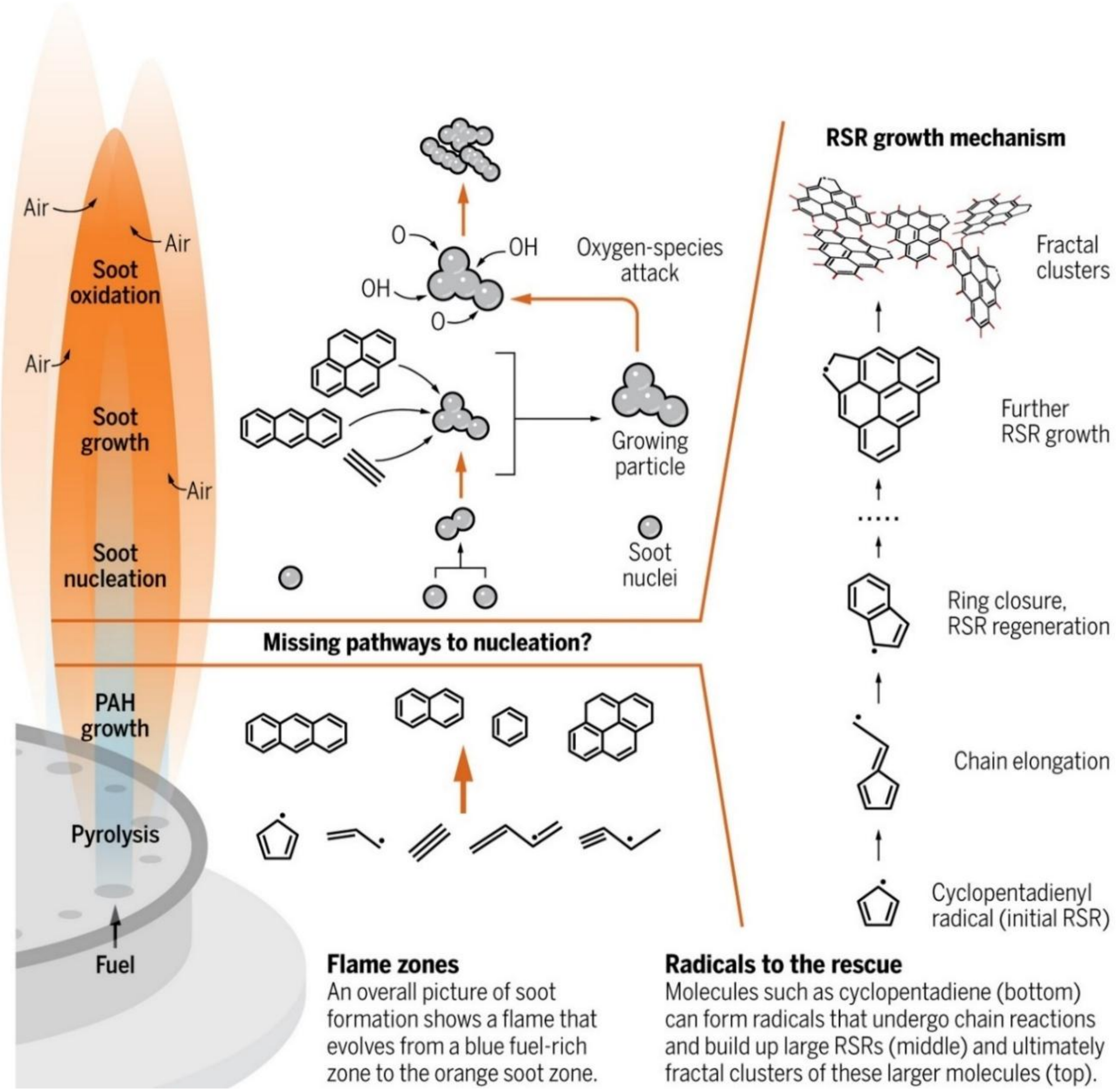

Figure 2.1 Soot formation and evolution from gas molecules to solid nanoparticles in coflow flames [56].

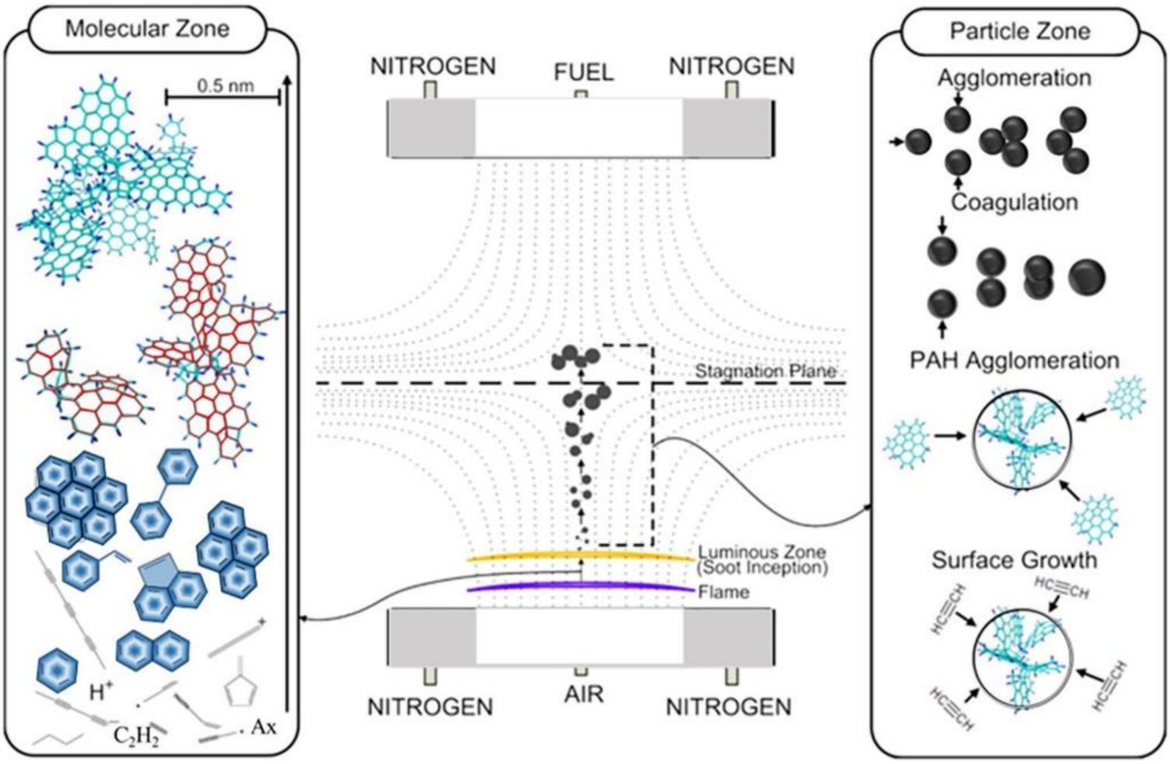

Figure 2.2 Soot formation and evolution from gas molecules to solid nanoparticles in counterflow flames [65].

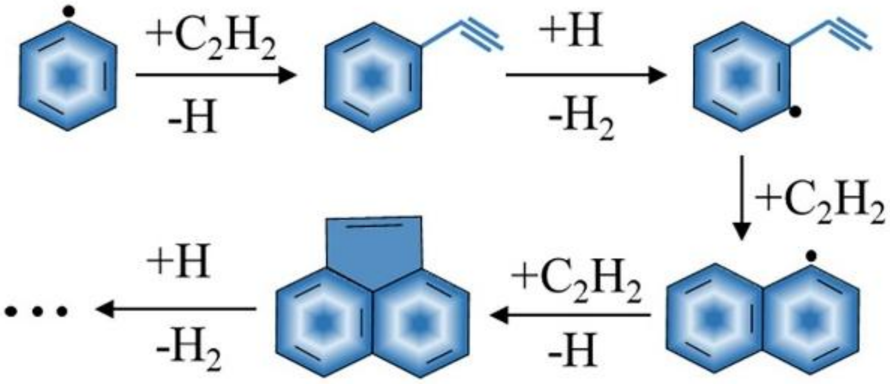

Figure 2.3 Polycyclic aromatic hydrocarbon formation via H-abstraction-C_2H_2-addition mechanism [65].

2.2 Transport Properties

Combustion normally leads to the production of a multi-species mixture, and the transport properties may change significantly with pressure and temperature as well as species composition, which should be fully considered in a numerical simulation. It is reported that transport properties of chemical species are as important as reaction rates in flame modelling [66], and flame shapes, velocities and emissions are all affected by transport properties [67], which implies that accurate combustion simulations should be based on precise transport properties and chemical kinetics. Physical properties of a substance depend directly on the nature of its molecule, and transport properties of a gas result from molecule collision interactions. Specifically, the thermodynamic state of a multi-species mixture in a reacting flow depends on molecular transport, as collisions between molecules can lead to mass, momentum or energy transfer. Accurately predicting the fundamental characteristics of a multi-species mixture in a combustion process requires taking into account the molecular transport of individual species. Therefore, specific attention in combustion simulations should be given to the mixture transport properties including multicomponent viscosities, thermal conductivities and diffusion coefficients, which are associated with the characterization of the molecular transport of species, momentum and energy in a multi-species mixture.

Many combustion codes involve transport properties of individual species, but most of them are not readily available [68]. Industrial and academic researchers tend to implement different computational methodologies for solving reacting flow problems within open-source applications. The open-source field operation and manipulation (OpenFOAM) software [51,52] is a leading free open-source computational fluid dynamics (CFD) platform using C++ language, in which customized libraries and numerical solvers as well as pre- and post-processing utilities can be developed to solve continuum mechanics problems based on the finite volume method (FVM) [54].

In the original OpenFOAM codes [52], the molecular transport model integrated into a reacting flow solver is highly simplified by assuming unity Schmidt number and Lewis number [68-71]. Under these assumptions, the thermal conductivity and mass diffusivity of a species are obtained from its viscosity, which is calculated from the Sutherland formula [71]. If the same Sutherland coefficients are used for each chemical species, the diffusion coefficients for all chemical species are the same, which may be not justified for most combustion cases. As a result, this model is only acceptable and valid in some specific cases, for example, strong turbulent reacting flows with negligible molecular mixing phenomena, where molecular viscosities and diffusivities can be negligible in comparison with eddy counterparts [68]. In addition, this simplified model is not capable of resolving all physical scales for new insights into physical phenomena with direct or quasi-direct numerical simulations [68]. It implies that effective measures should be taken to accurately simulate laminar or low turbulent flames.

Researchers in terms of combustion modelling has recognized the importance of transport models and have gradually paid attention to the appropriate treatment of molecular transport, the development of suitable methods and tools to study reacting flows for numerical combustion based on OpenFOAM evolves rapidly in the past few years. The simplest way to integrate a transport model into reacting flow simulations is to assume constant Lewis number either unity or non-unity, which can provide acceptable computational accuracy and reasonable computational cost [49,71,72]. However, detailed diffusion coefficients obtained from detailed transport models are essentially required to correctly capture flame structures in highly resolved combustion simulations. The multi-component transport model is considered as the most accurate but rather complex and computationally expensive model [73,74]. As a result, the mixture-averaged transport model has become the most widely used detailed transport model in combustion simulations.

Normally, there are two ways to incorporate detailed transport models into OpenFOAM for calculating transport properties in multi-species systems. One is to develop an interface between OpenFOAM and Cantera, as Cantera is freely developed and used for solving problems in terms of chemical kinetics, thermodynamics and transport processes [75]. Specifically, necessary parameters of a flow field computed by OpenFOAM are sent to Cantera for calculating transport properties, which are then sent back to OpenFOAM, therefore achieving the data exchange between OpenFOAM and Cantera [76]. The representative solvers adopting this method in the combustion community are diffusionFoam [77], EBIdnsFoam [78,79], reactingDNS [80], combustionFoam [81], CTreactingFoam [71], reactingFoam-SCI [69] and DeepFlame [82]. Essentially, these solvers can correctly deal with problems of reacting or non-reacting flows of a multi-species system due to the utilization of Cantera, which also demonstrates that all these solvers rely highly on this open-source software (i.e., Cantera). Specifically, the program structure of Cantera directly restricts the performance of these solvers [78] since the whole Cantera program should be performed to call a function. It is also required to reinstall Cantera every time on a target machine before running these solvers, which makes it very inconvenient and difficult for use and maintenance [78]. In addition, chemical reaction mechanisms in CHEMKIN [83] format should also be firstly converted into Cantera format and then used by these solvers. As chemical reaction mechanisms in Cantera format depend on the version of Cantera, these solvers become version-dependent. The frequent changes of Cantera version make these solvers difficult to use widely. An alternative way is to include a separate package for the evaluation of transport properties. Dasgupta et al. [68] developed an OpenFOAM-based code which is capable of calculating transport properties for flame modelling. As the code is written based on the OpenFOAM framework, it is viable to be coupled with OpenFOAM-based solvers. For example, this OpenFOAM-based code rather than Cantera [75] was used by reactingFoam-SCT [84-86] to calculate transport properties for reacting flows, while reactingFoam-SCT is an updated version of reactingFoam-SCI [69]. The detonationFoam [87] was also developed based on the transport property calculation codes provided by Dasgupta et al. [68] with dynamic load balancing algorithm [88]. It should be noted that since this code depends on several pre-compiled and pre-built utilities and libraries when using, the operation is relatively complicated. The same issue arose in the famous OpenSMOKE software [89-93]. Nguyen et al. [94] developed and implemented a set of transport models for real fluids at high pressure in OpenFOAM, which adopted parameter updating functions to avoid class interface problems. However, all the molecular transport parameters for each species should be pre-dealt with before serving as inputs for transport models, which means that this highly species-dependent method is not convenient to use for different cases with different species involved.

It should be noted that the reason why so many methods are developed for obtaining the transport properties in multi-species systems is attributed to the native algorithm of OpenFOAM, which is based on the use of Sutherland formula, and the assumption of unity Schmidt number and Lewis number [71]. As a result, only two parameters (i.e., Sutherland coefficient and Sutherland temperature) in the Sutherland's formula are required to be specified. By comparison, detailed transport models used in combustion simulations, which are developed based on Boltzmann's equation from the standard kinetic theory of gases [67], require completely different parameters to calculate transport properties. It should be noted that all these information are provided by a separate file of chemical reaction mechanisms in CHEMKIN format, but they are always ignored by OpenFOAM and do not work in solvers in terms of combustion modelling due to the use of Sutherland formula.

2.3 Turbulence Model

Apart from governing equations of fluid dynamics, creating a mathematical model to approximate the physical behaviour of turbulence flows is required as turbulence flows are a common and complicated phenomenon in fluid dynamics. Two-equation turbulence models normally use two transport equations for modelling two variables (i.e., length and time scales) in a turbulent flow region. A transport equation for the computation of turbulent kinetic energy, k and another transport equation for the turbulent dissipation, ε, the turbulent specific dissipation rate, ω or the turbulent length scale, L are most commonly used for two-equation turbulence models, which are known as the typical k-ε, k-ω or k-kL turbulence model, respectively. The eddy viscosity is then calculated through the turbulent length scale obtained by the two transport equations.

By comparison, one-equation turbulence models directly solve the transport equation of the eddy viscosity, rather than the algebraic length scales, which have the advantage of high computational efficiency [95-97]. Due to the obvious advantage in simplicity and accuracy, one-equation turbulence models have attracted increasingly attention [97-100]. Based on the wide scientific and engineering applications, many research studies have focused on the transformation of two-equation turbulence models to one-equation turbulence models [96,101]. Menter [96] proposed the transformation methodology of two-equation k-ε turbulence model to a one-equation turbulence model based on the assumption that there is a linear relationship between the turbulent shear stress and turbulent kinetic energy. It is worth noting that the coefficients in the diffusion terms are assumed to be equal in the process of the transformation, while they are not the same in the original formulations, therefore neglecting some specific terms in the derivational process. Following the assumption, Han et al. [101] proposed and improved the one-equation turbulence model derived from the two-equation k-ω turbulence model by including a cross diffusion term which made it possible to change the behaviour of the one-equation turbulence model between the two-equation k-ε and k-ω turbulence models. The results showed that the one-equation turbulence model has a good agreement with the experimental data. Note that all these one-equation turbulence models based on the two-equation k-ω turbulence models do not include the third-order velocity derivative-based length scale.

It is common practice to assume equal coefficients of the diffusion terms in the parent equations in many research studies due to simplicity [96,101]. However, a number of simplifying assumptions lead to neglecting several diffusion terms in the process of transformation of the parent two-equation turbulence model. The effect of these terms has not been fully examined and even for a very simple case, the performance of the resulting one-equation turbulence model may differ from the underlying parent two-equation turbulence model [96]. Based on the two-equation *k*-*ε* turbulence model, the one-equation turbulence model proposed by Elkhoury [95] does not assume equal coefficients of the diffusion terms leading to the emergence of the third-order velocity gradient term. The one-equation turbulence model is proved to be more accurate than other turbulence models due to the presence of the third-order velocity derivatives. Although the one-equation turbulence model retained the third-order velocity gradient term, a specific term related to the third-order velocity gradients is removed in the derivational process.

2.4 Turbulence-Chemistry Interaction

Combustion processes involve a great variety of species and elementary reactions, which necessitates solving detailed chemistry with numerous time and length scales in combustion modelling, especially for turbulent flows. Turbulence and chemistry interact in quite complex ways, which influence the temperature and composition distributions in the flow field. Accurate characterization of combustion processes requires the use of detailed chemistry to capture complex chemical kinetics with high fidelity, but direct resolution of the real-time complete chemistry in turbulent combustion flows is normally quite computationally expensive. By comparison, tabulated chemistry is a computational efficient strategy for the computation of gas-phase compositions [102], in which the assumption of high Damköhler number decouples chemistry evaluations from flow field evaluations [103]. Instead of real-time computing reaction mechanisms at every time step, tabulated chemistry looks up or interpolates pre-calculated chemical reaction data stored in a table to obtain real-time results, which significantly reduces the computational time. Tabulated chemistry has been widely used in flamelet approaches, which describe turbulent flames as a set of characteristic one-dimensional flames [103]. In flamelet-based models, thermochemical quantities of interest are represented by several control variables, and a pre-assumed probability density function would be employed for turbulence-chemistry interaction [104]. Transport equations of these variables are solved in CFD simulations, and thermophysical and thermochemical properties including temperature, dynamic viscosity and species mass fractions could be interpolated or looked up from the flamelet library [105]. The typical flamelet-based models successfully used for soot modelling in turbulent combustion flows include flamelet generated manifold model [106] and steady laminar flamelet model [107] as well as its extended flamelet/progress variable model [55,108].

Although tabulated chemistry can significantly reduce computational time, there are still several critical limitations. Mass exchange between gas-phase species and soot in flamelet-based models may not be accounted for, therefore neglecting the effect of the solid-phase soot on gas-phase compositions [102]. This cannot be avoided in a simpler manner due to the tabulated nature. It implies that the tabulated method may not be suitable for certain scenarios, where real-time feedback and dynamic adjustments are required, for example, unsteady combustion processes or systems that need dynamic adaptation. Additionally, it is reported that the impact of differential diffusion cannot always be neglected in turbulent diffusion flames [109] and may be significant in weak turbulent regions such as near the jet exit [55,110], and the assumed unity Lewis number may introduce large numerical errors [111]. It indicates that non-unity Lewis numbers may significantly affect the transport of species including pyrene (A4) [112,113]. Nevertheless, unity Lewis number is generally applied to evaluate the diffusion coefficients in flamelet equations [103,114,115], which may lead to quantitative underprediction of PAH and soot. This problem may be reduced by introducing a strain-sensitivity parameter to categorize each species and then applying non-unity Lewis number for PAHs, but unity Lewis number may be still assumed in other species [116]. It should be noted that retaining molecular diffusivity in the transport equations of PAHs may lead to an inconsistency when the flamelet table is generated based on unity Lewis number [55].

2.5 Soot Models

A soot model generally denotes the model of fundamental physicochemical soot kinetics, which mainly contains chemical kinetics and aerosol dynamics [10,15]. Chemical kinetics includes surface reactions kinetics of growth and oxidation as well as nucleation kinetics, while aerosol dynamics describe the particle size distribution (PSD) as well as soot population evolution due to the involved physicochemical processes including nucleation, coagulation, aggregation, surface growth and oxidation [10,15].

2.5.1 Chemical kinetics

As the complete pathway of soot aerosols with the smallest size formed from gas-phase species has not been fully understood, the successful modelling of soot yields requires accurately accounting chemical kinetics. Traditionally, soot is phenomenologically described by using empirical correlations to overall parameters, which are normally applied in practical engineering such as gas turbines and diesel engines [117]. Although these models could possibly present the effects of operating conditions including temperature, pressure, equivalence ratio, operation speed and load, on soot yields to some extent, their extensive application to different types of devices under different operating conditions is greatly restricted due to the correlation nature. In addition, the detailed insights of soot formation processes cannot be fully provided by these empirical models, which may assume that soot is monodisperse. With significant progress made in soot models, it is generally regarded that chemical kinetics rely heavily on the concentration of specific species, making it possible to offer detailed information on soot aerosol dynamics. According to the gas-phase chemistry in soot modelling, soot models could be categorised to classifications: detailed soot models as well as semi-empirical non-precursor and precursor models [10].

2.5.1.1 Semi-empirical non-precursor models

Soot could be considered only dependent on mixture fraction or temperature in the simplest models. Tesner et al. [118] proposed a two-equation model of soot and radical nuclei number densities, in which soot formation results from a branched-chain process and adsorption of radical nuclei on the soot surface. As soot formation is only linked with temperature in this model, the true mechanisms of soot formation cannot be reflected. In addition, soot surface growth has not been considered and important soot information such as soot volume fraction cannot be obtained. Kennedy et al. [119] linked mixture fraction with soot volume fraction (SVF) but neglected model variable for number density, making it not very realistic. By comparison, Moss et al. [120] proposed a more realistic soot model considering nucleation, surface growth and coagulation, and linked soot formation and growth rates with mixture fraction. Soot formation is described by soot number density, *n* and SVF, f_v, which could be formulated as [120]:

$$\frac{d(n/N_A)}{dt} = \underbrace{\alpha(\zeta)}_{\text{nucleation}} - \underbrace{\beta(\zeta)\left(\frac{n}{N_A}\right)^2}_{\text{coagulation}} \tag{2-1}$$

$$\rho_s \frac{d(f_v)}{dt} = \underbrace{\gamma(\zeta)n}_{\text{surface growth}} + \underbrace{C_\delta \alpha(\zeta)}_{\text{nucleation}} \tag{2-2}$$

where t is time; N_A and C_δ are Avogadro's number and a constant; ρ_s is the soot density and the local mixture fraction, ζ depends on fuel mole fraction, density and temperature. It is worth noting that surface growth is assumed irrespective of soot surface area here, making it unphysical. This critical problem was handled by Syed et al. [121] with modifications on soot surface growth, which is considered linear with surface area. Thus, the concept of two-equation soot models of SVF and soot number density has been introduced extensively.

2.5.1.2 Semi-empirical precursor models

Actual soot dynamic behaviours are normally represented by empirical kinetics in these models, in which complex soot phenomena are simplified via a global reaction and only essential soot formation and oxidation are considered. Thus, relatively detailed chemistry is required as soot is linked to specific species.

Fairweather et al. [122] proposed a two-equation soot model including nucleation, surface growth and coagulation, in which acetylene (C_2H_2) is treated as the precursor to represent all nucleation pathways and soot surface growth and oxidation occur via C_2H_2 and O_2 respectively, making it possible to use reduced chemical mechanisms. The general form of the soot model based on soot number density and soot mass concentration could be expressed by [123]:

$$\frac{dN_{\text{soot}}}{dt} = \left(\frac{dN}{dt}\right)_{\text{nucleation}} - \left(\frac{dN}{dt}\right)_{\text{coagulation}} \tag{2-3}$$

$$\frac{dM_{\text{soot}}}{dt} = \left(\frac{dM}{dt}\right)_{\text{nucleation}} + \left(\frac{dM}{dt}\right)_{\text{surface growth}} - \left(\frac{dM}{dt}\right)_{\text{oxidation}} \tag{2-4}$$

where nucleation (nuc) is related to the molar concentration of C_2H_2, which is expressed as [10]:

$$\mathrm{C_2H_2 \rightarrow 2C(s) + H_2} \tag{2-5}$$

$$R_{\text{nuc}} = k_{\text{nuc}}(T)[\mathrm{C_2H_2}] \tag{2-6}$$

where rate constant, k relies on temperature, T in an Arrhenius expression. Sometimes, two and three-ringed aromatics formed from C_6H_5 and C_6H_6 are also added as precursors in some extended soot models [124-127]. As the monodispersed soot PSDs are commonly assumed, the coagulation (coag) rate proportionally relies on the square of N by [10]:

$$R_{\mathrm{coag}} = k_{\mathrm{coag}}(T)N^2 \tag{2-7}$$

Investigations show that surface growth proportionally depends on surface area, S [128], and C_2H_2 is believed to contribute to soot surface growth [129]. The resulting expressions for surface growth (sg) is formulated as [10]:

$$\mathrm{C_2H_2} + n\mathrm{C(s)} \rightarrow (n+2)\mathrm{C(s)} + \mathrm{H_2} \tag{2-8}$$

$$R_{\mathrm{sg}} = k_{\mathrm{sg}}(T)S[\mathrm{C_2H_2}] \tag{2-9}$$

But Leung et al. [130] found that soot reactivity would reduce due to the effect of aging, so surface growth should be modified. Similar to surface growth, O_2 oxidation could be described based on temperature and soot surface area as [130]:

$$\mathrm{C(s)} + \frac{1}{2}\mathrm{O_2} \rightarrow \mathrm{CO} \tag{2-10}$$

$$R_{\mathrm{ox}} = k_{\mathrm{ox}}(T)S[\mathrm{O_2}] \tag{2-11}$$

Different expressions for soot oxidation have been developed due to different thermodynamic states and oxidant species. Lee et al. [131] takes the partial pressure of O_2 into account, and Nagle and Strickland-Constable [132] uses a nonlinear combination of Arrhenius-style rate constants. In addition, OH is also found to possibly contribute to soot oxidation [133-135].

Obviously, semi-empirical precursor soot models can provide some information about soot formation and some information about soot number density and diameters. Although not all fundamental mechanisms of soot phenomena such as soot morphology can be accurately captured by these models due to the use of rate constants in global reactions, they are popular in simulating combustion involving soot [91,92,136-138] due to the easy implementation and relatively low computational cost.

2.5.1.3 Detailed soot models

These models aiming at aerosol dynamics could provide complete information on soot particle size distribution (PSD) evolution. Especially, polycyclic aromatic hydrocarbon (PAH) chemistry is found only in these models, which contributes to soot inception and condensation, resulting in the requirement for detailed chemistry. Due to a much more expensive computational cost, most detailed soot models are normally applied to one- or two-dimensional laminar flows as well as ideal reactors [10].

Chemical kinetic mechanisms involving reaction and specie numbers have evolved rapidly for modelling soot formation in combustion simulations. The chemical kinetic mechanism of Appel et al. [59] could be used for soot modelling in combustion simulations, in which PAH growth has been considered and pyrene (A4) is the largest aromatic species. The detailed pathways of C_2H_2 and PAH formation are described by Slavinskaya et al. [139] in detail. The chemical reaction mechanism of Narayanaswamy et al. [140] could be employed for both gaseous and gasoline surrogate fuels for PAH formation. Wang et al. [141] developed a chemical kinetic mechanism containing PAH species up to coronene ($C_{24}H_{10}$), which leads to more accurate PAH results.

In general, the distribution of soot aerosols is assumed monodispersed in the free molecular regime in semi-empirical precursor models, while detailed models track the PSD of soot aerosols and are able to provide soot structure and morphology. A detailed model normally describes the whole processes from fuel pyrolysis to nucleation via PAH molecules as well as coagulation and surface growth and oxidation due to HACA [14,58,60]. In general, it is assumed that soot nuclei are generated by the PAH molecule dimerization, so the nucleation rate is calculated via the coagulation kernel based on the free molecular regime. Appel et al. [59] developed a commonly used dimerization model, which only takes the dimerization of A4 into account [142]. As it is considered that PAHs with different sizes may be involved in soot nucleation, the dimerization of PAHs with two and more aromatic rings is considered [143-148]. However, it is reported that the binding energy and lifetime of these dimers could be quite small, resulting in a small effective rate of dimer formation. Specifically, nucleated soot particles cannot be directly generated via effective interactions between PAHs due to the small sizes of PAHs [144]. As a result, Blanquart and Pitsch [147,148] introduced a sticking coefficient in a statistical soot model, which assumes that soot is formed via PAH dimer collision while a PAH dimer is generated by the free molecular coagulation of two PAH molecules [146]. However, it is argued that the direct nucleation of soot particles only occurs from the collisions of PAHs made up of 50 or more carbon atoms (i.e., 650 Da) [149] due to their stable Van der Waals forces [144], which implies that PAH species for dimer formation should be larger than phenanthrene ($C_{14}H_{10}$). It is worth noting that soot nucleation is assumed to be formed only via homogeneous collision of the same PAH species, which is not sufficiently realistic due to the random collision between PAH molecules [144]. By comparison, Wang et al. [150] proposed a homogeneous and heterogeneous dimerization model, which allows collisions between all combinations of two larger PAH molecules (A4 or higher) due to the higher inertia and sticking possibilities, leading to 36 nucleation reactions from 8 PAH molecules. Quadarella et al. [144] further proposed a physically consistent nucleation model including all PAHs from naphthalene (A2) to coronene (A7), which is only used to study the qualitative behaviour of stain rate sensitivity.

In most detailed models, the HACA mechanism [58,59] with rate expressions in the Arrhenius form is applied to describe the soot kinetics, in which elementary reactions are employed and soot surface growth and oxidation rates could be calculated from the steady state radical surface site number density. Furthermore, the pathway of soot surface growth also includes PAH condensation. It is also reported that methyl (CH_3), propargyl (C_3H_3) and ethynyl (C_2H) radicals are important in soot growth [150,151]. However, it is argued that the rate of PAH-soot collision is usually much smaller than that of PAH-PAH collision, so the dimer-soot collision mechanism for soot surface growth is developed [144,146-148].

More importantly, soot morphology in the form of fractal-like structures is normally considered in detailed models. It is reported that soot particles with diameters up to 50 nm are spherical while fractal aggregates would be formed via collision of larger soot particles. As a result, fractal aggregates are normally characterized by fractal dimension, D_f and primary particle diameter, d_p as [10]:

$$n_p = A\left(\frac{d_g}{d_p}\right)^{D_f} \tag{2-12}$$

where A is a constant, n_p and d_g are the primary particle number in an aggregate and gyration diameter, respectively. It should be noted that D_f is determined from MC simulations and experiments, which is 3.0 for spherical particles and 1.8 for soot aggregates.

2.5.2 Aerosol dynamics

Aerosol dynamics directly influence soot PSD and shape, therefore influencing soot formation and evolution in combustion flows. Modelling aerosol dynamics in terms of PSD necessities solving population balance equation (PBE). As it is impossible to directly solve the governing equation of aerosol dynamics (i.e., PBE) of interest due to its complexity, several methods have been developed to approximate its solution, among which Monte Carlo (MC) methods as stochastic methods are very flexible in simulating all aerosol dynamic processes, which can provide a deep insight into aerosol dynamic behaviours.

MC methods adopt representative particles to simulate the dynamic evolution of the dispersed system, so the behaviour of each representative particle can be closely simulated and the trajectory history of each particle can also be tracked. Specifically, each dynamic process in a MC simulation can be modelled by simply changing the particle number or volume, for example, adding a new particle for nucleation, removing an existing particle for deposition, increasing/decreasing the existing particle volume for condensation/evaporation, breaking one existing particle into several ones for breakage and colliding two existing particles into one for coagulation. All these straightforward operations make the MC simulation very robust [152].

However, stochastic property and computational cost are two shortcomings of stochastic methods due to the finite number of numerical particles, which is limited by the computer memory and central processing unit (CPU) speed, therefore would inevitably influence the computational precision. Although graphic processing unit or high performance cluster technique is efficient in accelerating computations [29-31], it is still of great importance to develop more accurate and efficient MC algorithms.

In practical engineering applications, particles are located in the computational domain, the volume of which is normally constant. Garcia et al. [153] developed a constant-volume method for coagulation, in which the number of numerical particles always decreases. But it may lead to only one numerical particle left in the computational domain and reduce the computational accuracy. In order to address these crucial issues, Liffman [154] presented a direct simulation Monte Carlo method for coagulation, in which the doubling operation is implemented to prevent statistical fatigue. Specifically, the number of numerical particles and volume of the computational domain are doubled to conserve the statistical properties when the number of numerical particles decreases by half. Maisels et al. [36] further extended the direct simulation Monte Carlo method aiming at more dynamic aerosol processes, which is called stepwise constant-volume method. Similarly, adding a copy of all existing numerical particles to the doubled computational domain is required when the number of numerical particles reduces by half. But the computational domain volume is halved when the numerical particle number exceeds twice of its initial value, in which a half of numerical particles are removed from the computational domain by a stochastic process while the other half of numerical particles remain in the computational domain. It should be noted that the doubling procedure can completely conserve the statistical properties but the halving operation may lead to mass non-conservation when the sizes of numerical particles are not equal. In fact, deposition or coagulation generally leads to a decrease in the computational accuracy due to the decreasing number of numerical particles, while nucleation and breakage significantly reduces the computational efficiency because of the increasing number of numerical particles. It implies that both computational accuracy and efficiency of these constant-volume-related methods depend highly on the number of numerical particles.

Therefore, Smith and Matsoukas [155] developed a constant-number method. The main idea of the constant-number method is to generate a copy of one numerical particle or to exclude one numerical particle by a stochastic process according to the decrease or increase in the number of numerical particles, respectively. Although indefinitely long numerical simulations are allowed in this constant-number method, the statistical properties possibly are not conserved during the numerical simulations. In order to tackle this technical problem, Lin et al. [37] improved the constant-number method to conserve the total particle mass/volume or number concentration through continuously changing the volume of the computational domain. Depending on whether the total particle number or mass/volume concentration is preserved, the number-based constant-number and mass-based constant-number methods were proposed. It should be noted that only when the volumes of all numerical particles are equal, the total particle mass/volume and number concentrations of mass- and number-based constant-number methods are conserved; otherwise, only total particle mass/volume or number concentration is conserved. The constant expansion or contraction for the volume of the computational domain and only conservation for the total particle number or mass/volume concentration greatly restrict the general applications of both mass-based and number-based constant-number methods.

By comparison, the volume of the computational domain is kept unchanged and the number of numerical particles always keeps constant in the multi-Monte Carlo (MMC) method in Zhao and Zheng [156], in which each numerical particle with different statistical weights represents some real particles in the computational domain. As real particles in the edge of the PSD are also represented, more detailed information of the PSD are presented and the statistical precision is then improved. In the MMC method, a probabilistic coagulation rule [32] is adopted to conserve the mass/volume between two numerical particles having different weights for coagulation. As for deposition, one numerical particle is not tracked after a deposition process, and a randomly selected existing numerical particle is divided into two numerical particles with the same volume but half weight. The treatment of a new numerical particle generated by nucleation and breakage processes is to merge it with an existing numerical particle with the most similar volume, where their weights are simply added together to only preserve the total particle number concentration, leading to the introduction of some systematic errors originated from mass non-conservation [157].

Eibeck and Wagner [158] developed an implicit stochastic weighted particle method to deal with coagulation, where the statistical weight of a numerical particle is related to the mass of real particles. Patterson et al. [159] proposed a new class of stochastic weighted particle methods based on the construction of weight transfer functions, in which the number of numerical particles remains constant during the simulation of coagulation. Boje et al. [160] developed a hybrid particle-number and particle model to deal with rapid formation and growth of particles with a finite ensemble size, where small particles are treated by the particle-number model while large particles and aggregates are resolved by the particle model, therefore improving the computational resolution of particles.

In order to conserve both the total particle number and mass/volume concentrations, Kotalczyk and Kruis [161] proposed a random removal method using the smart bookkeeping technique [17] and a new merging MC method, where all possible numerical particle pairs should be compared to obtain two numerical particles that are the most appropriate to be merged. But it is highly computationally expensive to conduct double MC loops from the beginning to the end by comparing to each numerical particle, so parallel computing technique and graphic processing units are used to accelerate computations, making the whole algorithm and programming much more complicated. Jiang and Chan [33] proposed a new weighted fraction Monte Carlo (WFMC) method for coagulation, in which one of the uncoagulated numerical particles is probabilistically removed. The WFMC method with introducing adjustable fraction functions can significantly improve the computational precision in second- and third- order moments of the PSD. It should be noted that both removal and merging operations can retain some or even all information (i.e., velocity, momentum, energy, electric charge, etc.) about old numerical particles while the resetting method [156] or reconstructing method [162] cannot fully transfer these information of old numerical particles to the new numerical particles, leading to some numerical errors.

In addition, there are some MC methods aimed at specific dynamic processes for an aerosol system of interest. For example, MC methods [156,162-165] are developed for breakage while the weighted flow algorithms [166] and fast MC methods [17,34] are focused on coagulation. Simultaneous coagulation and breakage is considered in [167-171] based on equal-weight scheme, which lead to limited computational accuracy, while Zhao et al. [172] proposed a different-weight-based MC method, but it may introduce systematic errors. Debry et al. [173] developed a mass flow algorithm for all aerosol dynamic processes except for breakage, and Celnik et al. [174] introduced an operator splitting approach to deal with simultaneous coagulation and surface growth, which requires special treatment due to their different characteristic times. Both the stochastically weighted operator splitting Monte Carlo method [91,175,176] and differentially weighted operator splitting Monte Carlo method [177-181] use the operator splitting technique combining deterministic and stochastic methods to deal with complex aerosol dynamic processes without considering breakage.

2.6 Summary

Fundamental investigation on soot aerosol dynamics in combustion flows is essentially required in terms of both scientific research and engineering applications, in which numerical simulations perform an increasingly significant role, leading to the requirement for developing advanced and efficient numerical methods.

Monte Carlo (MC) methods provide a stochastic approach to approximate the exact solution of soot aerosol dynamics, which makes it very flexible to simulate all aerosol dynamics processes of soot particles. As aerosol dynamic behaviours of soot particles are closely simulated, a deep insight into the aerosol dynamic processes of soot particles can be provided. But high stochastic errors and computational costs lead to the requirement of developing more accurate and efficient MC algorithms. Furthermore, soot formation and evolution in combustion processes could be rather complicated, which involve fluid dynamics, transport phenomena, chemical kinetic chemistry, aerosol dynamics and heat and mass transfer. Especially, the possible pathways from gas-phase species to condensed nanoparticles should be considered. In laminar flows, differential diffusion of gas-phase species with soot makes it difficult to accurately simulate their transport processes in CFD simulations. By comparison, it is required to account for the random fluctuations of variables in turbulent combustion, which should be properly modelled in numerical simulations.

The basic concepts, knowledge and methods in terms of numerical simulation on soot aerosol dynamics of combustion flows are described, in which the knowledge gap and recent important development are revealed. The literature review could be summarized as:

1. Accurately predicting and controlling soot formation and evolution as well as fractal structures are of great scientific and engineering importance, which requires having a complete knowledge of chemical kinetics and aerosol dynamics in combustion processes together with transport phenomena and turbulence-chemistry interaction.

2. Solving aerosol dynamics by MC method normally leads to the inevitable introduction of stochastic errors and a high computational cost. Many developed MC methods are mainly aimed at improving the computational accuracy, but their stochastic errors are still relatively large, especially for coagulation.

3. Many MC methods with high computational accuracy or efficiency are developed aimed at specific aerosol dynamic processes of interest. However, there does not exist a general MC method capable of dealing with all aerosol dynamic processes with high computational accuracy.

4. Accurate modelling of reacting flows requires coupling a detailed transport model as mass diffusivity of gas-phase species are normally different, especially in laminar flows. However, the use of simplified molecular transport model in Computational fluid dynamics (CFD) codes including OpenFOAM makes it impossible to resolve all physical scales for new insights into combustion phenomena.

5. It is accepted that soot formation depends on specific key species. Acetylene (C_2H_2) is normally treated as the soot precursor in semi-empirical precursor models, while the dimerization of polycyclic aromatic hydrocarbon (PAH) molecules is regarded to contributes to soot nucleation and surface growth via condensation in detailed soot models. Therefore, modelling soot aerosol dynamics in combustion flows should consider nucleation via the dimerization of PAH molecules and condensation by dimers as well as coagulation and surface growth and oxidation.

6. The presence of turbulence leads to non-linear unclosed terms, which should be modelled in CFD simulations. CFD is an important tool to solve problems in terms of fluid dynamics including combustion flows, in which turbulence modelling is a key ingredient. Turbulence flows are a common and complicated phenomenon in fluid dynamics, whose

physical behaviour can be approximated by creating a mathematical model in terms of length and time scales.

7. The turbulence-chemistry interaction in turbulent combustion directly influences temperature and composition distributions in the flow fields, which would influence soot formation and evolution. Accurate characterization of combustion processes requires the use of detailed chemistry to capture complex chemical kinetics with high fidelity. This can be achieved by finite-rate chemistry simulations, in which combustion described by detailed chemistry can be solved in real-time with taking the effect of differential diffusion into account. However, tabulated chemistry together with the unity Lewis number assumption is normally used for turbulent combustion simulations due to the cheap computational cost, which would possibly lead to some numerical errors in simulating soot formation and evolution in combustion flows.

Chapter 3 Theoretical Fundamentals of the Present Study

3.1 Introduction

The theoretical fundamentals of modelling soot aerosol dynamics in combustion flows by computational fluid dynamics (CFD) technique are introduced. Specifically, conservation equations of solving laminar and turbulent reacting flows would be formulated, and soot models involving aerosol dynamics governed by population balance equation (PBE) are presented. Furthermore, basic theories of coupling PBE with CFD as well as their approximation solutions based on the finite volume method (FVM) are described in detail.

3.2 Governing Equations

Mathematical model of physic phenomena generally includes boundary conditions as well as integro-differential or partial differential equations [182], and forms the basis of numerical methods. Transport equations of fluid flows in a conservative form could be expressed by introducing a general variable ϕ as [183]:

$$\frac{\partial(\rho\phi)}{\partial t} + \nabla \cdot (\rho\phi\mathbf{U}) = \nabla \cdot (\Gamma\nabla\phi) + S_{\phi} \tag{3-1}$$

where t and ρ are time and density, and $\mathbf{U}$ is velocity and Γ is diffusion coefficient. The first to fourth terms represent the rate of change, convection, diffusion and sources term, respectively.

Since analytical solutions of these differential equations possibly are not available, their solutions should be estimated by various algebraic equations describing the discrete temporal and spatial locations of a variable. The FVM integrals conservation equations to approximate all terms with physical meaning, which is very simple to understand and program, so it is popular with fluid engineers.

The volume integrals on the whole bounding surface (A) in a control volume (V) at a time interval (Δt) formulates the integration form of a transport equation as [183]:

$$\int_{\Delta t}\frac{\partial}{\partial t}\left(\int_V \rho\phi\, dV\right)dt + \int_{\Delta t}\int_A \mathbf{n}\cdot(\rho\phi\mathbf{U})dAdt$$
$$= \int_{\Delta t}\int_A \mathbf{n}\cdot(\Gamma\nabla\phi)dAdt + \int_{\Delta t}\int_V S_\phi dVdt \tag{3-2}$$

where **n** represents surface normal vector.

3.2.1 Continuity

By setting $\phi = 1$, the mass (continuity) conservation equation in fluid flows are derived as [182]:

$$\frac{\partial\rho}{\partial t} + \nabla\cdot(\rho\mathbf{U}) = 0 \tag{3-3}$$

3.2.2 Momentum equations

By setting $\phi = \mathbf{U}$, the momentum conservation equation in fluid flows are derived as [182]:

$$\frac{\partial(\rho\mathbf{U})}{\partial t} + \nabla\cdot(\rho\mathbf{U}\mathbf{U}) - \nabla\cdot\boldsymbol{\tau} = -\nabla p \tag{3-4}$$

where p represents pressure; viscous stress tensor, $\boldsymbol{\tau}$ could be formulated based on the Stokes hypothesis as:

$$\boldsymbol{\tau} = -\frac{2}{3}\mu(\nabla\cdot\mathbf{U})\mathbf{I} + \mu[\nabla\mathbf{U} + (\nabla\mathbf{U})^T] \tag{3-5}$$

where **I** and μ are unit tensor and dynamic viscosity, respectively.

3.2.3 Transport equations for species

Transport equations for mass conservation of *k*th species in reacting flows can be obtained by setting $\phi = Y_k$ as [183]:

$$\frac{\partial(\rho Y_k)}{\partial t} + \nabla\cdot(\rho Y_k\mathbf{U}) = \nabla\cdot(\rho D_k\nabla Y_k) + \omega_k \tag{3-6}$$

where ω_k and D_k are the reaction rate and diffusion coefficient of *k*th species, respectively.

3.2.4 Energy equation

Mixture composition and thermodynamic state determine temperature in combustion flows as heat could be released from chemical energy, which requires solving mixture enthalpy transport equation (i.e., $\phi = h$) as [183]:

$$\frac{\partial(\rho h)}{\partial t} + \nabla \cdot (\rho \mathbf{U} h) = \nabla \cdot \left(\frac{\lambda}{C_p} \nabla h - \sum_{k=1}^{N} \frac{\lambda}{C_p} h_k \nabla Y_k \right) + \nabla \cdot \left(\sum_{k=1}^{N} \rho h_k D_k \nabla Y_k \right) + \frac{\partial p}{\partial t} + Q_r \tag{3-7}$$

where C_p and λ are specific heat capacity at constant pressure and thermal conductivity of the mixture, respectively; Q_r and h_k represent radiative heat source and specific enthalpy of species k.

3.3 Turbulence Modelling

Fluid flows are observed to become unstable at a certain Reynolds number, which could be dictated by flow kinematic viscosity, length scale and characteristic velocity. Flows would be turbulent or laminar at high or low Reynolds number. Numerical methods for turbulence flows involve direct numerical simulation (DNS), large-eddy simulation (LES) and Reynolds-averaged Navier-Stokes (RANS) for obtaining mean and fluctuating equations.

With regard to the transport equations, there are closure issues associated with various variables of fluid dynamics. Theoretically, it is possible to solve the differential equations by numerical discretization techniques without closure and obtain detailed information about flows, but DNS is computationally expensive because time and length scales with a broad range exhibited in turbulent flows necessities many computational grids and time steps. In addition, DNS is believed to devote a great deal of effort to resolve insignificant scales concerning second-order quantities including the scalar flux and Reynolds stresses, therefore resulting in a waste of computational resources. LES, however, only resolves flow-dependent scales and spatially filters small scales. These small scales are considered to be flow-independent and can be modelled by sub-grid-scale (SGS) models. As a result, the closure problems still exist in SGS micro-mixing and chemical reactions due to the unresolved small scales and filtering of the chemical source term, and corresponding closure models still need to be proposed. Because of straightforward CFD applications and less expensive computational cost, RANS turbulence models are commonly used with various closure models proposed [184]. This strategy is considered as a compromise of computational accuracy and cost [184].

It is observed that turbulence results in a flow property (i.e., ϕ) randomly fluctuating around its steady mean value (i.e., $\bar{\phi}$), and the fluctuation component (i.e., ϕ') with zero mean value is time varying. This is called Reynolds decomposition. The resulting equation of a mean scalar quantity based on Equation (3-1) could be expressed by [182]:

$$\frac{\partial(\bar{\rho}\bar{\phi})}{\partial t}+\frac{\partial}{\partial x_j}\left(\bar{\rho}\bar{u}_j\bar{\phi}+\bar{\rho}\overline{u_j'\phi'}\right)=\frac{\partial}{\partial x_j}\left(\Gamma\frac{\partial\bar{\phi}}{\partial x_j}\right)+\overline{S_\phi} \tag{3-8}$$

Therefore, Reynolds-averaged Navier-Stokes (RANS) equations by averaging continuity and momentum equations for turbulent flow could be expressed by [183]:

$$\frac{\partial\bar{\rho}}{\partial t}+\frac{\partial}{\partial x_i}(\bar{\rho}\bar{u}_i)=0 \tag{3-9}$$

$$\frac{\partial(\bar{\rho}\bar{u}_i)}{\partial t}+\frac{\partial}{\partial x_j}\left(\bar{\rho}\bar{u}_i\bar{u}_j+\bar{\rho}\overline{u_i'u_j'}\right)=-\frac{\partial\bar{p}}{\partial x_i}+\frac{\partial\bar{\tau}_{ij}}{\partial x_j} \tag{3-10}$$

where $\bar{\tau}_{ij}$ is the mean viscous stress tensor given as [182]:

$$\bar{\tau}_{ij}=\mu\left(\frac{\partial\bar{u}_i}{\partial x_j}+\frac{\partial\bar{u}_j}{\partial x_i}\right) \tag{3-11}$$

The eddy viscosity and diffusion models should be introduced for the Reynolds stress and scalar quantity, which are expressed as [182]:

$$-\bar{\rho}\overline{u_i'u_j'}=\mu_t\left(\frac{\partial\bar{u}_i}{\partial x_j}+\frac{\partial\bar{u}_j}{\partial x_i}\right)-\frac{2}{3}\bar{\rho}\delta_{ij}k \tag{3-12}$$

$$-\bar{\rho}\overline{u_j'\phi'}=\Gamma_t\frac{\partial\bar{\phi}}{\partial x_j} \tag{3-13}$$

where δ_{ij} represents the Kronecker delta, and turbulent diffusivity, Γ_t could be calculated as [183]:

$$\Gamma_t=\frac{\mu_t}{\sigma_t} \tag{3-14}$$

where σ_t varies for different flows. Turbulent kinetic energy, k could be calculated by [182]:

$$k = \frac{1}{2}\overline{u_i' u_i'} \tag{3-15}$$

By using dimensional analysis, turbulent (or eddy) viscosity μ_t could be expressed by length and velocity scales (L and ϑ) as [183]:

$$\mu_t = \bar{\rho} C \vartheta L \tag{3-16}$$

where C is constant.

Therefore, turbulence description necessities velocity and length scale [182]. As the velocity scale is linked with turbulent kinetic energy, turbulence models could be developed to calculate turbulence length scale or equivalent as well as turbulent kinetic energy.

3.3.1 *k-ε* turbulence model

This model solves k and its dissipation rate, ε in the standard form by [185]:

$$\frac{\partial(\bar{\rho}k)}{\partial t} + \frac{\partial}{\partial x_j}\left(\bar{\rho}\bar{u}_j k\right) = \frac{\partial}{\partial x_j}\left[\left(\mu + \frac{\mu_t}{\sigma_k}\right)\frac{\partial k}{\partial x_j}\right] + P_k - \bar{\rho}\epsilon \tag{3-17}$$

$$\frac{\partial(\bar{\rho}\epsilon)}{\partial t} + \frac{\partial}{\partial x_j}\left(\bar{\rho}\bar{u}_j \epsilon\right) = \frac{\partial}{\partial x_j}\left[\left(\mu + \frac{\mu_t}{\sigma_\epsilon}\right)\frac{\partial \epsilon}{\partial x_j}\right] + C_{\epsilon 1} P_k \frac{\epsilon}{k} - \bar{\rho} C_{\epsilon 2}\frac{\epsilon^2}{k} \tag{3-18}$$

where P_k is the production rate of k, which is expressed as [185]:

$$P_k = \mu_t \left(\frac{\partial \bar{u}_i}{\partial x_j} + \frac{\partial \bar{u}_j}{\partial x_i}\right)\frac{\partial \bar{u}_i}{\partial x_j} \tag{3-19}$$

In this model, the length scale is determined as [185]:

$$L = \frac{k^{3/2}}{\epsilon} \tag{3-20}$$

Therefore, the eddy viscosity is expressed as [185]:

$$\mu_t = \bar{\rho} C_\mu \sqrt{k} L = \bar{\rho} C_\mu \frac{k^2}{\epsilon} \tag{3-21}$$

The model parameters commonly used in this model are [185]:

$$C_\mu = 0.09;\ C_{\epsilon 1} = 1.44;\ C_{\epsilon 2} = 1.92;\ \sigma_k = 1.0;\ \sigma_\epsilon = 1.3 \tag{3-22}$$

3.3.2 *k*-*ω* turbulence model

Another widely adopted turbulence model would be the k-ω turbulence model popularized by Wilcox [186], which uses an equation for k and an equation for an inverse time scale ω (i.e., specific dissipation rate) as [182]:

$$\frac{\partial(\bar{\rho}k)}{\partial t}+\frac{\partial}{\partial x_j}\left(\bar{\rho}\bar{u}_j k\right)=\frac{\partial}{\partial x_j}\left[\left(\mu+\frac{\mu_t}{\sigma_k^*}\right)\frac{\partial k}{\partial x_j}\right]+P_k-\bar{\rho}\beta^* k\omega \tag{3-23}$$

$$\frac{\partial(\bar{\rho}\omega)}{\partial t}+\frac{\partial}{\partial x_j}\left(\bar{\rho}\bar{u}_j \omega\right)=\frac{\partial}{\partial x_j}\left[\left(\mu+\frac{\mu_t}{\sigma_\omega^*}\right)\frac{\partial \omega}{\partial x_j}\right]+\alpha P_k\frac{\omega}{k}-\bar{\rho}\beta\omega^2 \tag{3-24}$$

The eddy viscosity for this model is calculated as [182]:

$$\mu_t=\bar{\rho}\frac{k}{\omega} \tag{3-25}$$

The model parameters commonly used in this model are [182]:

$$\alpha=\frac{5}{9};\ \beta=0.075;\ \beta^*=0.09;\ \sigma_k^*=\sigma_\omega^*=2;\ \epsilon=\beta^* k\omega \tag{3-26}$$

3.4 Combustion Modelling

CFD modelling of combustion is very complex as combustion itself involves a wide variety of processes, leading to a great number of models coupled for these physical and chemical processes. Governing equations of reacting flows would be provided in Equations (3-3) to (3-7). Specifically, combustion modelling may require solving transport equations of fluid flow, chemical species and heat, which involves chemical kinetics and thermodynamics.

3.4.1 Chemical kinetics

Chemical kinetics focus on studying reaction rates and reaction mechanisms, which ultimately determines the time for a chemically reacting flow system to an equilibrium state. In practical chemically reacting flow systems, there normally exists a large number of chemical species and reactions. Specifically, combustion of a fuel normally involves a few different steps, rather than occurs in a single overall reaction or a global reaction. Detailed reaction mechanisms involving many intermediate equations with appropriate rate constants are available in the literature. The famous GRI-Mech 3.0 [187] for methane combustion has been widely used, which takes NO formation into account. A detailed chemical reaction mechanism called ABF mechanism was reported by Appel et al. [59], in which the famous H-abstraction-C_2H_2-addition (HACA) mechanism describes surface growth and oxidation. The ABF mechanism [59] named from the initials of the author's last name has been successfully applied in soot modelling ofs various flames [49,143,188,189]. For a chemical kinetic model including N_S species, the N_R elementary reversible (or irreversible) reactions can be represented in the general form [83]:

$$\sum_{k=1}^{N_S}(\nu'_{kj}\chi_k) \Leftrightarrow \sum_{k=1}^{N_S}(\nu''_{kj}\chi_k) \tag{3-27}$$

where ν'_{kj} and ν''_{kj} represent stoichiometric coefficients of jth reaction and kth species; χ_k represents the chemical symbol of kth species and its production rate can be expressed as [83]:

$$\omega_k = W_k \sum_{j=1}^{N_R}(\nu''_{kj} - \nu'_{kj})\left(K_{fj}\prod_{k=1}^{N_S}[X_k]^{\nu'_{kj}} - K_{rj}\prod_{k=1}^{N_S}[X_k]^{\nu''_{kj}}\right) \tag{3-28}$$

The kth species molar concentration, $[X_k]$ is expressed as [83]:

$$[X_k] = \frac{\rho Y_k}{W_k} \tag{3-29}$$

The rate constants of forward or reverse reaction j, K_{fj} and K_{rj} could be given based on the Arrhenius law as [83]:

$$K_j = A_j T^{\beta_j} \exp\left(-\frac{E_j}{RT}\right) \tag{3-30}$$

where A_j is pre-exponential constant, β_j denotes temperature exponent and E_j represents activation energy. As most chemical kinetic models are developed by the widely used CHEMKIN [83] software package, these rate constants are normally provided by the literature in the CHEMKIN format, which are derived based on computational predictions and experimental measurements.

3.4.2 Thermodynamics

The thermodynamic properties in the standard state (293K) could be computed via National Aeronautics and Space Administration polynomial fits [83]. Specific heat at constant pressure of perfect gases in molar form can be calculated as [83]:

$$\frac{C_{p,k}^{o}}{R_u} = \sum_{n=1}^{N} a_{n,k} T^{n-1} \tag{3-31}$$

where superscript "*o*" represents 1 atmosphere of standard state. Standard-state enthalpy and entropy are calculated by specific heat integrals as [83]:

$$H_k^o = \int_0^T C_{p,k}^o dT = R_u T \sum_{n=1}^{N} \frac{a_{n,k} T^{(n-1)}}{n} + a_{N+1,k} R_u \tag{3-32}$$

$$S_k^o = \int_0^T \frac{C_{p,k}^o}{T} dT = a_{1,k} R_u \ln T + \sum_{n=2}^{N} \frac{a_{n,k} T^{n-1}}{n-1} + a_{N+2,k} R_u \tag{3-33}$$

where the constants of integration $a_{N+1,k}R_u$ and $a_{N+2,k}R_u$ are evaluated from the standard-state heat and entropy of formation at 298 K. Seven coefficients (i.e., $N = 5$) for each of two temperature ranges based on the Joint Army Navy Air Force (JANAF) table of thermodynamics are used in CHEMKIN software.

3.5 Soot Modelling

The dynamic behaviours of aerosols with size *i* at time *t* in terms of coagulation, surface growth and coagulation are normally described by PBE in a discrete form as [42]:

$$\begin{aligned}\frac{\partial}{\partial t} N(t,i) = &\frac{1}{2}\sum_{j=1}^{i-1} \beta(t,i-j,j) N(t,i-j) N(t,j) - \sum_{j=1}^{\infty} \beta(t,i,j) N(t,i) N(t,j) \\ &+ \sum_{l=1}^{4} \left[w^l\left(t,i-\delta_i^l\right) N\left(t,i-\delta_i^l\right) - w^l(t,i) N(t,i) \right] + R(t)\delta_{in}^{*}\end{aligned} \tag{3-34}$$

$$N(0,i) = N_0(i) \geq 0 \tag{3-35}$$

where $N(t,i)$ represents particle number density; $\beta(t,i,j)$ is coagulation kernel; $R(t)$ is particle inception rate, and δ_{in}^{*} is the smallest inception particle size; $w^l(t,i)$ represents rates of dynamic processes involving condensation, surface growth and oxidation, and δ_i^l is change in mass.

As soot formation and evolution closely relate to the local gas-phase species and thermodynamics conditions, investigation on soot aerosol dynamics should be based on precisely modelling of reacting flows, which requires coupling soot aerosol dynamics with combustion flows.

3.5.1 Soot nucleation

It is generally agreed that soot formation is closely associated with polycyclic aromatic hydrocarbons (PAHs), in which soot is modelled by coagulating two pyrene (A4) molecules [42,49,143,189]. Because the radii of A4 molecules could be quite smaller than mean molecular free path, particle inception can be modelled by the Smoluchowski's coagulation equation [190] based on the free molecular regime. On that account, the soot nucleation rate is written as [42]:

$$R_{\mathrm{nuc}} = \frac{1}{2}\beta_{\mathrm{A4,A4}} N_{\mathrm{A4}}^{2} \tag{3-36}$$

where N_{A4} is the number concentration of A4, and $\beta_{\mathrm{A4,A4}}$ represents A4 molecule coagulation kernel, which could be calculated as [60]:

$$\beta_{\mathrm{A4,A4}} = 4E_F \sqrt{\frac{\pi k_B T}{m_{\mathrm{A4}}}} d_{\mathrm{A4}}^{2} \tag{3-37}$$

where k_B and E_F are the Boltzmann constant and van del Waals enhancement factor equal to 2.2, respectively; T is temperature, and the diameter of A4, d_{A4} is expressed as [150]:

$$d_{\mathrm{A4}} = d_A \sqrt{\frac{2n_{C,\mathrm{A4}}}{3}} \tag{3-38}$$

where $n_{C,\mathrm{A4}}$ and d_A are carbon atomic number of a A4 molecule and an aromatic ring size, respectively. The mass of A4, m_{A4} is normally calculated as [191]:

$$m_{\mathrm{A4}} = C_{\mathrm{m}} n_{C,\mathrm{A4}} \tag{3-39}$$

where C_{m} is atomic mass of carbon.

3.5.2 Soot coagulation

Soot coagulation between two particles with masses m and μ can be expressed by Smoluchowski's equation as [9]:

$$R_{\mathrm{coag}}(m) = \frac{1}{2}\int_0^m \beta(\mu, m-\mu) n(\mu) n(m) d\mu - \int_0^\infty \beta(m,\mu) n(\mu) n(m) d\mu \tag{3-40}$$

where $n(m)$ represents particle size distribution; $\beta(m,\mu)$ is the collision frequency or coagulation kernel of two particles, which is calculated as [9]:

$$\beta(m,\mu) = E_F\left(\frac{\pi k_B T}{2}\right)^{1/2}\left(\frac{1}{m}+\frac{1}{\mu}\right)^{1/2}\left(\frac{6}{\pi\rho_s}\right)^{2/3}\left(m^{1/3}+\mu^{1/3}\right)^2 \tag{3-41}$$

where ρ_s is the soot density.

3.5.3 Soot surface growth and oxidation

These dynamic processes can be described via H-abstraction-C_2H_2-addition mechanism adopting Arrhenius rate expressions, in which OH oxidation could be modelled via the collision theory based on the free molecular regime, while soot surface growth via C_2H_2 and O_2 oxidation take place on the soot surface activated sites. In general, surface growth and oxidation rates can be expressed as [10,192]:

$$R_{\mathrm{sg},i} = \alpha k_{g,s}\chi_s C_g S_i N_i \tag{3-42}$$

where α and C_g are the fraction of available surface sites and gas species concentration, respectively; χ_s and $k_{g,s}$ are nominal surface site number density and per-site rate coefficient, respectively; N_i and S_i are the number density and surface area, respectively.

Apart from C_2H_2, it is reported that PAHs also significantly influence soot growth process in the PAH-based soot model [10]. Specifically, soot aerosols can grow by condensing PAHs on these particle surfaces, which would be modelled by the collision of PAH molecules with soot aerosols.

3.6 Modelling Soot Aerosol Dynamics in Combustion Flows

In CFD modelling of soot formation and evolution in reacting flows, soot population properties (soot mass and number densities) are solved in transport equations, in which soot aerosol dynamic processes are coupled as source terms. The most widely used transport equations for modelling soot aerosol dynamics in the general form is formulated as [92,125]:

$$\frac{\partial}{\partial t}(\rho N) + \nabla\cdot(\rho\mathbf{U}N) + \nabla\cdot(\rho\mathbf{V}_T N) - \nabla\cdot(\rho D_s\nabla N) = S^N \tag{3-43}$$

$$\frac{\partial}{\partial t}(\rho Y) + \nabla\cdot(\rho\mathbf{U}Y) + \nabla\cdot(\rho\mathbf{V}_T Y) - \nabla\cdot(\rho D_s\nabla Y) = S^Y \tag{3-44}$$

where N and Y are variables corresponding to soot number density and soot mass density; t and ρ are time and density; $\mathbf{U}$ and $\mathbf{V}_T$ are velocity and thermophoretic velocity; D_s is diffusion coefficient of soot; S^Y and S^N are source terms in terms of soot aerosol dynamic processes involved. It is worth noting that this model assumes that soot is monodisperse.

By comparison, soot aerosol dynamics normally described by detailed soot models compose a series of complicated physicochemical processes involving nucleation, condensation, coagulation, aggregation, surface growth and oxidation are governed by population balance equation (PBE) [25,33,35,38,176-178,193], which is normally approximated by Monte Carlo (MC) methods, method of moments (MOM) and sectional methods (SMs). In MC methods, an ensemble of particles is represented by several numerical particles with dynamic processes of particles handled probabilistically. Although the resulting solution is normally very accurate, the computational cost is rather high. In addition, coupling a MC method with the CFD framework for combustion simulations is not straightforward, which is only used as a postprocessing technique to study the soot dynamics [10,194], greatly limiting their application in soot modelling [43,49,50]. Instead of solving the PSD directly, MOM solves the moments of the PBE. This approach is computationally efficient but may encounter closure problems, so various MOM-based methods have been developed for soot modelling [92,146,195-200]. By comparison, the SMs are intuitive and easy to implement, in which the PSD is divided into several sections and then the aerosol dynamics described by the PBE in each section is solved [10]. The commonly used SM algorithm for soot modelling in turbulent flames is developed by Netzell et al. [114], which uses SVF to evaluate the soot number density in every section. Specifically, transport equations of SVF in every section, $Y_{s,i}$ are formulated with convection and diffusive terms, in which the soot dynamic processes are evaluated as source terms as [55,102,106,201]:

$$\frac{\partial}{\partial t}\left(\rho Y_{s,i}\right) + \nabla \cdot \left(\rho \mathbf{U} Y_{s,i}\right) + \nabla \cdot \left(\rho \mathbf{V}_T Y_{s,i}\right) - \nabla \cdot \left(\rho D_{s,i} \nabla Y_{s,i}\right) = S_{s,i} \tag{3-45}$$

where $S_{s,i}$ and $D_{s,i}$ are soot source terms and diffusion coefficient in ith section. However, this conventional SM algorithm is not capable of modelling fractal-like soot aggregate structure [202].

In order to fill this gap, an advanced SM of solving primary particle and soot aggregate size distributions in each section was developed [203,204], but this method was mainly used in laminar diffusion flames [202,205-207]. This is attributed to the high computational cost, and its application to computationally intricate turbulent flames is limited due to the involvement of several different dynamics processes occurring at the same time but different length scales. As soot dynamic processes in a turbulent combustion flow closely depend on the local fluctuated concentrations of related gas-phase species as well as thermochemical parameters, modelling of chemistry as well as turbulence-chemistry and turbulence-soot interactions is required to accurately predict soot in a turbulent combustion flow.

3.7 Summary

The basis of fundamental theories of the PBE for solving aerosol dynamics are described in detail, and transport equations of coupling soot aerosol dynamics with CFD in combustion flows are formulated in the present study.

Chapter 4 Development of Sorting Algorithm-based Merging Weighted Fraction Monte Carlo Method for Coagulation

4.1 Introduction

The objective of this chapter is to propose and develop a new Monte Carlo (MC) method for solving the population balance equation for the weighted fraction coagulation process in aerosol dynamics with high computational accuracy and efficiency. Although the introduction of adjustable fraction functions in the weighted fraction Monte Carlo (WFMC) method [33] are conducive to the computational accuracy of high-order moments of the particle size distribution (PSD), the stochastic error in the total particle number concentration significantly increases which is always much larger than the direct simulation Monte Carlo (DSMC) as well as multi-Monte Carlo (MMC) methods [33]. In addition, the WFMC method has a rigid limitation on the fraction functions, making few fraction functions applicable to the WFMC method except for those specifically selected adjustable fraction functions. For example, if the fraction function is a constant which is not equal to 1, a large statistical noise or even error will be shown. This significantly reduces the generality of fraction functions and limits the applicability of the WFMC method. To tackle these problems, a new sorting algorithm-based merging weighted fraction Monte Carlo (SAMWFMC) method is proposed and developed in the present study. Three adjustable fraction functions applicable to the WFMC method and constant fraction functions are also introduced to check the reliability of the SAMWFMC method. A new merging scheme is then proposed and developed to ensure a constant-number and constant-volume scheme. Six benchmark test cases with existing analytical solutions are used to validate the newly developed SAMWFMC method and the resulting stochastic errors are also compared with those of the DSMC, MMC and WFMC methods.

4.2 Methodology

The occurrence of aerosol dynamic processes normally leads to the change in the particle size distribution (PSD) with time and position, which are governed by the population balance equation (PBE) (i.e., general dynamic equation, GDE) [9]. Coagulation is one of the most important aerosol dynamic-processes, which refers to two particles colliding to form a large one and leads to the decrease of the particle number and the increase of the average particle size. As a coagulation event always occurs between two particles, it is regarded as the most demanding event for modelling among various aerosol dynamic events [32,34]. The dynamic evolution of PSD due to coagulation is described by the so-called Smoluchowski coagulation equation as [9]:

$$\begin{aligned}\frac{\partial n(v,t)}{\partial t} &= \frac{1}{2}\int_0^v \beta(u,v-u,t)n(u,t)n(v-u,t)du \\ &\quad - n(v,t)\int_0^\infty \beta(u,v,t)n(u,t)du\end{aligned} \tag{4-1}$$

where $n(v,t)$ is the PSD function at time t; $n(v,t)dv$ is the particle number concentration with size range between v and $v+dv$ at time t; $\beta(u,v,t)$ is the collision frequency or coagulation kernel of two particles with volume u and v at time t which is a description of the coagulation rate.

In Monte Carlo (MC) methods for particle coagulation, the construction of a jump Markov process depends on the coagulation rate between numerical particles with different particle weights, because the coagulation rate determines the time step between two successive coagulation events and the selection of a coagulation particle pair. The development of the new SAMWFMC method is presented.

4.2.1 Calculation of the coagulation rate

A numerical particle, i is a representative of a group of real particles with the number equals to w_i and the volume equals to v_i. The real particle number concentration of this group is w_i/V, where V is the volume of the computational domain. Similarly, w_j/V is the real particle number concentration of a group represented by the numerical particle, j. Therefore, the number of coagulation events among real particles per unit time and volume between ith-group and jth-group of numerical particles can be expressed by [32]:

$$\Phi_{ij}=\beta_{ij}\times\frac{w_i}{V}\times\frac{w_j}{V} \tag{4-2}$$

where Φ_{ij} is the coagulation rate between a random chosen real particle from the ith-group and a random chosen real particle from the jth-group, while β_{ij} is the coagulation kernel function of particles i and j. Thus, the number of coagulation events of the real particles between the ith-group and jth-group per unit time in the computational domain is $V\Phi_{ij}$.

In the present study, it is considered that coagulation events occur among a part of or all real particles between the *i*th-group and *j*th-group, which is characterized by a fraction function, α_{ij} [33,49]. The mean number of coagulation events within these real particles is given by [33]:

$$\Omega = \alpha_{ij} \min(w_i, w_j), \alpha_{ij} \in (0,1] \tag{4-3}$$

Therefore, the number of coagulation events of the real particles between the *i*th-group and *j*th-group per unit time in the computational domain can also be formulated by ΩC_{ij} [33]:

$$V\Phi_{ij} = \Omega C_{ij} \tag{4-4}$$

where C_{ij} is the coagulation rate between numerical particles, *i* and *j*, which can be written as [33]:

$$\begin{gathered} C_{ij} = \frac{\max(w_i, w_j)}{\alpha_{ij}} \frac{\beta_{ij}}{V} = \frac{\beta'_{ij}}{V} \\ \beta'_{ij} = \frac{\max(w_i, w_j)}{\alpha_{ij}} \beta_{ij} \end{gathered} \tag{4-5}$$

where β_{ij}' is the new coagulation kernel function which is used to construct the jump Markov process.

4.2.2 Determination of a time step

The waiting time between two events (i.e., coagulation) is an exponentially distributed random variable as [208]:

$$P(\tau) = C_0 \exp(-C_0 \tau) \tag{4-6}$$

where C_0 is the total coagulation rate which is written as [208]:

$$C_0 = \sum_{i=1}^{N-1} \sum_{j=i+1}^{N} C_{ij} \tag{4-7}$$

Therefore, the occurrence probability of a coagulation event of numerical particles, $P_{\text{coag}}(\Delta t)$ in the computational domain with a volume of V and within a time step of Δt is given by [33]:

$$P_{\text{coag}}(\Delta t) = 1 - \exp(-\Delta t C_0) \tag{4-8}$$

The time step is then determined as [153,208]:

$$\Delta t = \frac{\ln(1/r_1)}{C_0} \tag{4-9}$$

where r_1 is a random number from the uniform distribution between zero and one.

4.2.3 Selection of a coagulation particle pair

The acceptance-rejection method [153] and the cumulative probability method (i.e., the inverse method) [154] are two commonly used for selecting a coagulation pair at random basis. Since the inverse method needs to calculate the coagulation rates of all possible particle pairs which is time-consuming [17], the acceptance-rejection method is then adopted in the present study. At first, the numerical particles, i and j, are randomly selected, and then they would be accepted as a numerical particle pair to conduct a coagulation event if the following condition is satisfied as [153,208]:

$$r_2 \leq \frac{C_{ij}}{\max\limits_{\forall k, \forall m} C_{km}} \tag{4-10}$$

where r_2 is a random number from the uniform distribution in the unit interval. Otherwise, they are rejected, and then a new numerical particle pair is entirely selected at random basis to repeat the acceptance or rejection procedure until a satisfied numerical particle pair is obtained. It should be noted that the Markov process still can be exactly implemented even though the $\max\limits_{\forall k, \forall m} C_{km}$ in Equation (4-10) is overestimated [34,153].

4.2.4 Fraction functions

In the WFMC method, three types of adjustable fraction functions (i.e., hyperbolic fraction function (HFF), exponential fraction function (EFF) and stepwise constant fraction function (SCFF)) with a rigid assumption are specially selected [33] as presented in Equations (4-11) to (4-13). It should be noted that all these three types of adjustable fraction functions have a specific range from 0.5 to 1 closely related to the volumes of numerical particles i and j, which may lead to a totally different value of each numerical particle from others. In addition, all these fraction functions for numerical particles with large size discrepancy are strictly restricted to almost 1, which means that a numerical particle pair with small size difference undergoes a weighted fraction coagulation event while two numerical particles of large size discrepancy do not experience a weighted fraction coagulation. From this point of view, all these fraction functions are used to control the coagulation process of a numerical particle pair in terms of its volume ratio in the WFMC method. This is the prerequisite of adopting the WFMC method [33]. If this rule is not followed, the WFMC method can lead to a very large statistical noise or even error and cannot be used for simulating coagulation anymore. This is the reason why only a few fraction functions (i.e., HFF, EFF and SCFF) are applicable to the WFMC method. Actually, even though these three types of adjustable fraction functions are used in the WFMC method, the stochastic error in the total particle number concentration is still large [33].

In the present study, these three types of adjustable fraction functions (HFF, EFF and SCFF) are used in the newly proposed and developed SAMWFMC method to validate the computational accuracy and efficiency. Meanwhile, constant fraction functions (CFF) in Equation (4-14) are also introduced to extend the generality of the fraction functions and check the applicability of the new SAMWFMC method. It should be noted that *C* in Equation (4-14) can be an arbitrary number between zero and unity, which is consistent with the expression in Equation (4-3).

$$\alpha_{ij} = \frac{1}{1 + \min(v_i, v_j) \,/\, \max(v_i, v_j)} \tag{4-11}$$

$$\alpha_{ij} = 1 - 2^{-\max(v_i,v_j)/\min(v_i,v_j)} \tag{4-12}$$

$$\alpha_{ij} = \begin{cases} 0.5, & \max(v_i,v_j)/\min(v_i,v_j) \le 2 \\ 1, & \max(v_i,v_j)/\min(v_i,v_j) > 2 \end{cases} \tag{4-13}$$

$$\alpha_{ij} = C \tag{4-14}$$

4.2.5 A new merging scheme

Every time when a numerical particle pair undergoes a weighted fraction coagulation event, there is an additional new numerical particle generated in the computational domain, leading to the continuous increasing in the number of numerical particles when more coagulation events occur. As a result, the computational efficiency will drop. It should be noted that the additional numerical particle with the lowest weight after a coagulation event is represented by “New *x*” as shown in Figure 4.1. In order to keep the number of numerical particles constant in the constant computational domain, Jiang and Chan (2021) have recently proposed a probabilistic removal scheme by randomly removing one of the coagulated numerical particles ("New *i*" or "New *j*" as shown in Figure 4.1) out of the computational domain and then adjusting the weight of the other coagulated numerical particle after the coagulation event. However, this probabilistic removal scheme may result in the fluctuation of the total particle number concentration.

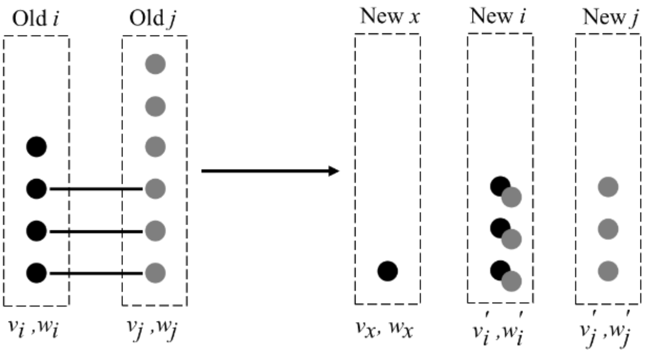

Figure 4.1 Schematic diagram of numerical particles undergoing a weighted fraction coagulation [35].

In the present study, a new merging scheme is proposed and developed to ensure a constant-number and constant-volume scheme. If the fraction function is equal to 1 and the weights of two coagulated numerical particles are equal, it is straightforward to distribute the equal volume and weight to the two new numerical particles as shown in Figure 4.2. Otherwise, the schematic diagrams of the merging scheme in terms of different volumes and weights of a coagulated numerical particle pair are shown in Figures 4.3 and 4.4. Instead of removing one coagulated numerical particle out of the computational domain in the WFMC method [33], the idea of the merging scheme in the present study is to add the "New *x*" in Figure 4.1 to an existing numerical particle in the computational domain.

If the volumes of two coagulated numerical particles are equal, only these two coagulated numerical particles are required to be involved in the merging scheme. If the weight of the "Old *i*" is not larger than that of the "Old *j*" as shown in Figure 4.3(a), the "Old *i*" will be replaced by the "New *i*" with the volume equal to ($v_i + v_j$), and the "New *x*" will be added to the "Old *j*" and the "New *j*" will then be formed. If the weight of the "Old *i*" is larger than that of the "Old *j*" as shown in Figure 4.3(b), the "Old *j*" will be replaced by the "New *j*" with the volume equals to ($v_i + v_j$), and the "New *x*" will be added to the "Old *i*" and the "New *i*" will then be formed.

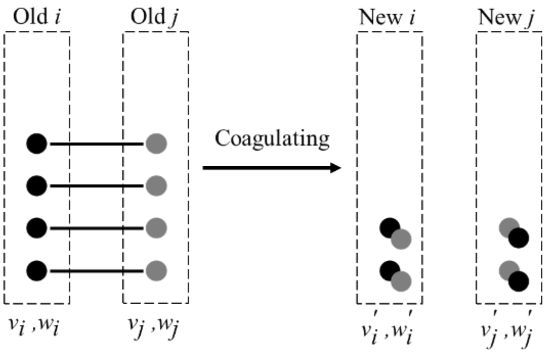

Figure 4.2 Schematic diagram of merging weighted fraction when $\alpha_{ij} = 1$ and $w_i = w_j$ [35].

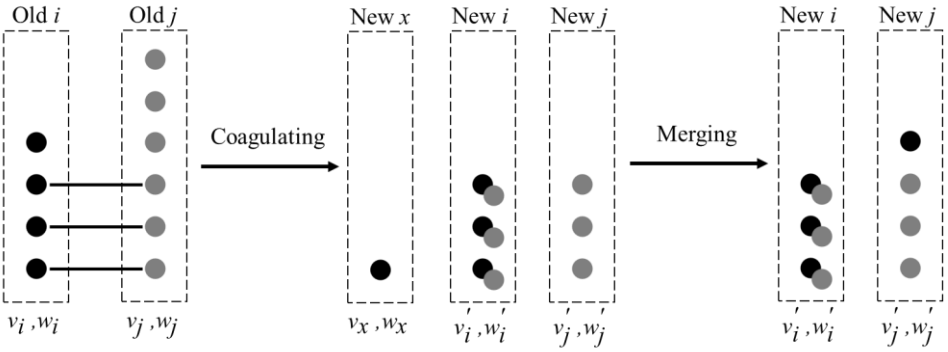

(a) $w_i \leq w_j$

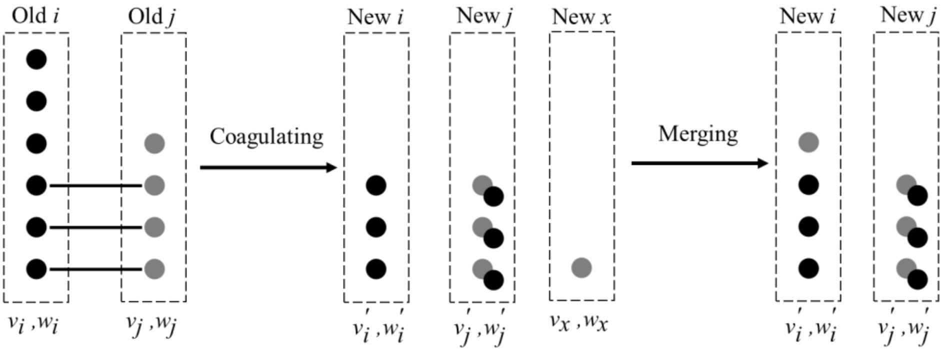

(b) $w_i > w_j$

Figure 4.3 Schematic diagram of merging weighted fraction when $v_i = v_j$ [35].

By comparison, the handling of the “New *x*” is completely different when the volumes of these two numerical particles, v_i and v_j, are not equal. Under this circumstance, a totally new numerical particle, “Old *k*”, neither “Old *i*” nor “Old *j*”, in the computational domain is introduced to implement the merging scheme as shown in Figure 4.4. If the weight of the “Old *i*” is not larger than that of the “Old *j*” as shown in Figure 4.4(a), the “Old *i*” will be replaced by the “New *i*” with the volume equal to ($v_i + v_j$), the “Old *j*” will be replaced by the “New *j*” with the same volume v_j, and the “New *x*” will be added to the “Old *k*” and the “New *k*” will then be formed. But if the weight of the “Old *i*” is larger than that of the “Old *j*” as shown in Figure 4.4(b), the “Old *j*” will be replaced by the “New *j*” with the volume equals to ($v_i + v_j$), and the “Old *i*” will be replaced by the “New *i*” with the same volume v_i and the “New *x*” will be added to the “Old *k*” and the “New *k*” will then be formed.

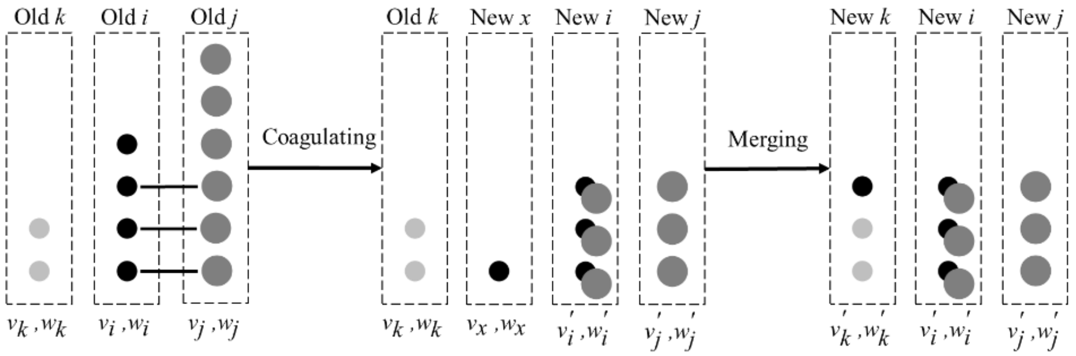

(a) $w_i \leq w_j$

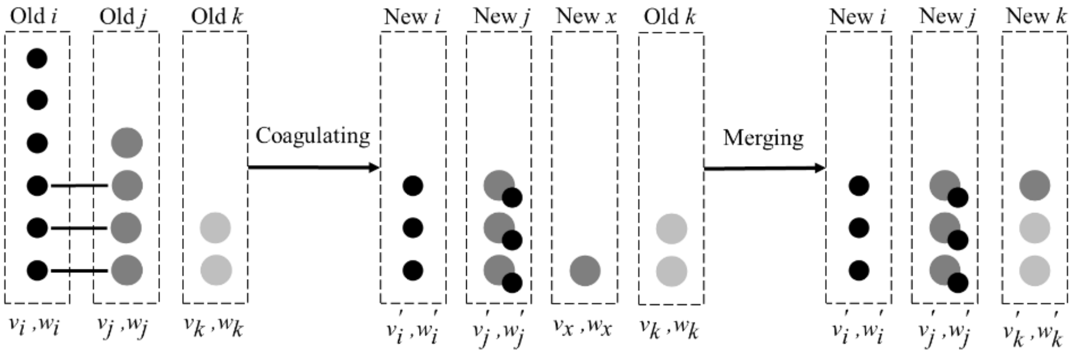

(b) $w_i > w_j$

Figure 4.4 Schematic diagram of merging weighted fraction when $v_i \neq v_j$ [35].

Therefore, the choice of the numerical particle, “Old *k*” becomes of great importance in the merging scheme because a randomly chosen “Old *k*” in the computational domain undoubtedly leads to the introduction of large statistical noise. However, if the volume of the “Old *k*” is close or equal to that of the “New *x*”, the statistical noise of the new merging scheme can significantly reduce. Clearly, the most appropriate “Old *k*” has the same properties as the

"New *x*" or has the nearest properties to the "New *x*", so the property (i.e., volume) difference between the "New *x*" and "Old *k*" is defined as:

$$S_x = |v_k - v_x| \tag{4-15}$$

when S_x is the minimal where the corresponding k is the most appropriate numerical particle for "New *x*" to be merged.

It should be noted that the volume of the "New *k*" is treated as the same as the "Old *k*" after merging, while the weight of the "New *k*" would be adjusted according to the volume/mass conservation rule, which will be presented later in Section 4.2.7. Therefore, the newly proposed merging scheme in the present study is completely different from those used in Kotalczyk and Kruis [161] and Zhao et al. [172]. In order to deal with an additional numerical particle generated by a breakage event, Zhao et al. [172] adopted a merging measure where the number of numerical particles is kept to be constant by directly adding the weights of the additional numerical particle and a randomly selected one with the similar volume together. Although the total particle number concentration is conserved exactly, the stochastic error in the total particle volume/mass concentration may occur. By comparison, Kotalczyk and Kruis [161] introduced a technique of merging a generated numerical particle due to nucleation, breakage or transport to conserve both the total particle number and volume/mass densities, but the purpose of each merging treatment is to reduce one numerical particle and vacate a position in the computational domain by selecting two existing numerical particles to form a new one. But these two existing numerical particles should be specially selected; otherwise a very large stochastic noise or even error would be introduced. A low weight merging scheme is then introduced to minimize the stochastic error, in which the most appropriate merging numerical particle pair should be determined by comparing all possible numerical particle pairs. If the number of numerical particles used is N, the number of comparisons in numerical particle pairs is then $N(N\text{-}1)$, which is very computationally expensive. Although the time complexity of this merging scheme is reduced to $O(\log N)$ which can be achieved to accelerate computations by using both parallel computing and graphic processing units (GPUs), the whole algorithm and programming are fairly complex.

Obviously, it is not sensible to compare the properties of all the numerical particles one-by-one with that of "New *x*" because it is highly time-consuming, especially when the number of numerical particles is large. But if the properties (i.e., volume and weight) of numerical particles are sorted and stored in the computer memory, it is more convenient to find the target "Old *k*" by adopting the 1-nearest neighbour (1-NN) algorithm. In Figure 4.4(a), if the "Old *k*" is one of the nearest neighbours of the "Old *i*", it is obvious that the "Old *k*" has a similar volume with the "New *x*". Therefore, the "Old *k*" can be determined by:

$$k=\begin{cases} i\text{-}1, & S_{i\text{-}1}<S_{i+1} \\ i+1, & S_{i\text{-}1}\geq S_{i+1} \end{cases} \tag{4-16}$$

Similarly, the "Old *k*" in Figure 4.4(b) is determined as:

$$k=\begin{cases} j\text{-}1, & S_{j\text{-}1}<S_{j+1} \\ j+1, & S_{j\text{-}1}\geq S_{j+1} \end{cases} \tag{4-17}$$

Therefore, the sorting algorithm-based merging weighted fraction scheme is newly proposed and developed for easily and rapidly determining the target "Old *k*" with the nearest property to the "New *x*" by using 1-NN algorithm.

4.2.6 Selection of a sorting algorithm

As sorting numerical particles is vital to the computational accuracy in the newly developed SAMWFMC method, the selection of the most efficient sorting algorithm is essentially required for reducing the computational cost.

As discussed in the Section 4.2.5, the number of numerical particles remains constant during the numerical simulation by introducing the new merging scheme, so there is no need to implement the operation of adding or removing numerical particles anymore. This feature matches well with the data structure of array in the computer programming. More importantly, array supports random access, which implies that every numerical particle can be directly accessed by its index, which can significantly improve computational efficiency especially when the number of numerical particles is large. An object-oriented programming (OOP) language, C++ has classes and objects. A class is a type of data which includes properties and functions while an object is an instance of a class. In the present study, a class of the numerical particle including properties (e.g., identification number [ID], volume and weight) is defined. Then each object is created as an instance of the numerical particle class. Finally, an array is used to store a collection of objects of the numerical particle class.

As the prerequisite of implementing the merging scheme is that the numerical particle array should be sorted, it is necessary to sort the numerical particle array before the next coagulation event. Note that it is unnecessary to sort the initial numerical particle array if the initial PSD is monodispersed; otherwise, sorting the initial numerical particle array is required when the initial numerical particle system is generated. In the present study, the numerical particles are sorted by their properties (i.e., volume and weight), so all numerical particles are in order in terms of their properties. When two numerical particles, "Old *i*" and "Old *j*" with the same volume coagulate as shown in Figures 4.2 and 4.3, they are replaced in place by the "New *i*" and "New *j*"; otherwise, the "Old *i*", "Old *j*" and "Old *k*" are replaced in place by the "New *i*", "New *j*" and "New *k*" after coagulation as shown in Figure 4.4. Other numerical particles in the array remain constant, which demonstrate that there are only two or three numerical particles required to be sorted, so only an efficient sorting algorithm for the nearly sorted numerical particle array is needed.

There are a great variety of sorting algorithms such as bubble sort, selection sort, insertion sort, merge sort, heapsort and quicksort, and their variations [209] as there is no one sorting method that can deal with every situation [210]. The performance of a sorting algorithm is evaluated by the complexities of time and space in the notation of the standard big $O(n)$, where n is the size of the input data [211]. The average time complexities of the bubble, selection and insertion sorts are $O(n^2)$ while the average time complexities of the merge sort, heapsort and quicksort are $O(n\log n)$. But, if the array is nearly or completely sorted, the time complexities of the selection sort, merge sort, heapsort and quicksort remain unchanged, while the time complexities of the bubble and insertion sorts become $O(n)$, which implies that bubble and insertion sorts have high efficiency for nearly or completely sorted arrays [212]. It is worth noting that both bubble and insertion sorts aim at small numbers of elements in the array. It is better to choose a suitable sorting algorithm with the time complexity of $O(n\log n)$ when the number of elements needed to be sorted is large. In addition, the bubble sort adopts the exchanging method when sorting, which is not as efficient as the insertion method by the insertion sort. Therefore, in the newly proposed and developed SAMWFMC method, the insertion sort is used to sort the numerical particle array after a coagulation event is taken place as the numerical particle array is already in order except for only two or three numerical particles. Furthermore, if the initial PSD is not monodispersed, the quicksort is adopted to sort the initial numerical particle array after the numerical particle system is generated.

4.2.7 Treating a coagulation event

If two numerical particles undergo a coagulation event, the real particles represented by these two numerical particles also experience coagulation, which leads to the change in the properties (i.e., volume and weight) of these two numerical particles. If the fraction function, α_{ij} in Equation (4-3) is equal to 1 and the weights of "Old *i*" and "Old *j*" are the same as shown in Figure 4.2, all real particles would be coagulated. The consequence of this coagulation event is denoted as [32]:

$$\text{if } w_i = w_j,\ \begin{cases} v_i' = v_i + v_j,\ w_i' = w_i/2 \\ v_j' = v_i + v_j,\ w_j' = w_j/2 \end{cases} \tag{4-18}$$

Otherwise, two or three numerical particles are involved as shown in Figures 4.3 and 4.4. The volume/mass of the "New *x*" is $(w_i\text{-}\alpha_{ij}w_i)v_i$ in Figures 4.3(a) and 4.4(a), and $(w_j\text{-}\alpha_{ij}w_j)v_j$ in Figures 4.33(b) and 4.4(b), respectively, which is merged with a selected numerical particle based on mass conservation, so the consequence of a coagulation event in terms of merging scheme is formulated as:

if $v_i = v_j$ and $w_i \leq w_j$,

$$\begin{cases} v_i' = v_i + v_j,\ w_i' = \alpha_{ij} w_i \\ v_j' = v_j, w_j' = w_j - \alpha_{ij} w_i + (w_i - \alpha_{ij} w_i)\dfrac{v_i}{v_j} = w_i + w_j - 2\alpha_{ij} w_i \end{cases} \tag{4-19}$$

if $v_i = v_j$ and $w_i > w_j$,

$$\begin{cases} v_i' = v_i, w_i' = w_i - \alpha_{ij} w_j + (w_j - \alpha_{ij} w_j)\dfrac{v_j}{v_i} = w_i + w_j - 2\alpha_{ij} w_j \\ v_j' = v_i + v_j,\ w_j' = \alpha_{ij} w_j \end{cases} \tag{4-20}$$

if $v_i \neq v_j$ and $w_i \leq w_j$,

$$\begin{cases} v_i' = v_i + v_j,\ w_i' = \alpha_{ij} w_i \\ v_j' = v_j, w_j' = w_j - \alpha_{ij} w_i \\ v_k' = v_k, w_k' = w_k + (w_i - \alpha_{ij} w_i)\dfrac{v_i}{v_k} \end{cases} \tag{4-21}$$

if $v_i \neq v_j$ and $w_i > w_j$,

$$\begin{cases} v_i' = v_i, w_i' = w_i - \alpha_{ij} w_j \\ v_j' = v_i + v_j,\ w_j' = \alpha_{ij} w_j \\ v_k' = v_k, w_k' = w_k + \left(w_j - \alpha_{ij} w_j\right) \dfrac{v_j}{v_k} \end{cases} \tag{4-22}$$

It should be noted that if the fraction function, α_{ij} is always equal to 1, the Equations (4-18) to (4-22) are completely consistent with those of the MMC method [32], which demonstrate that the MMC method is only a special case of the newly proposed SAMWFMC method when $\alpha_{ij} = 1$.

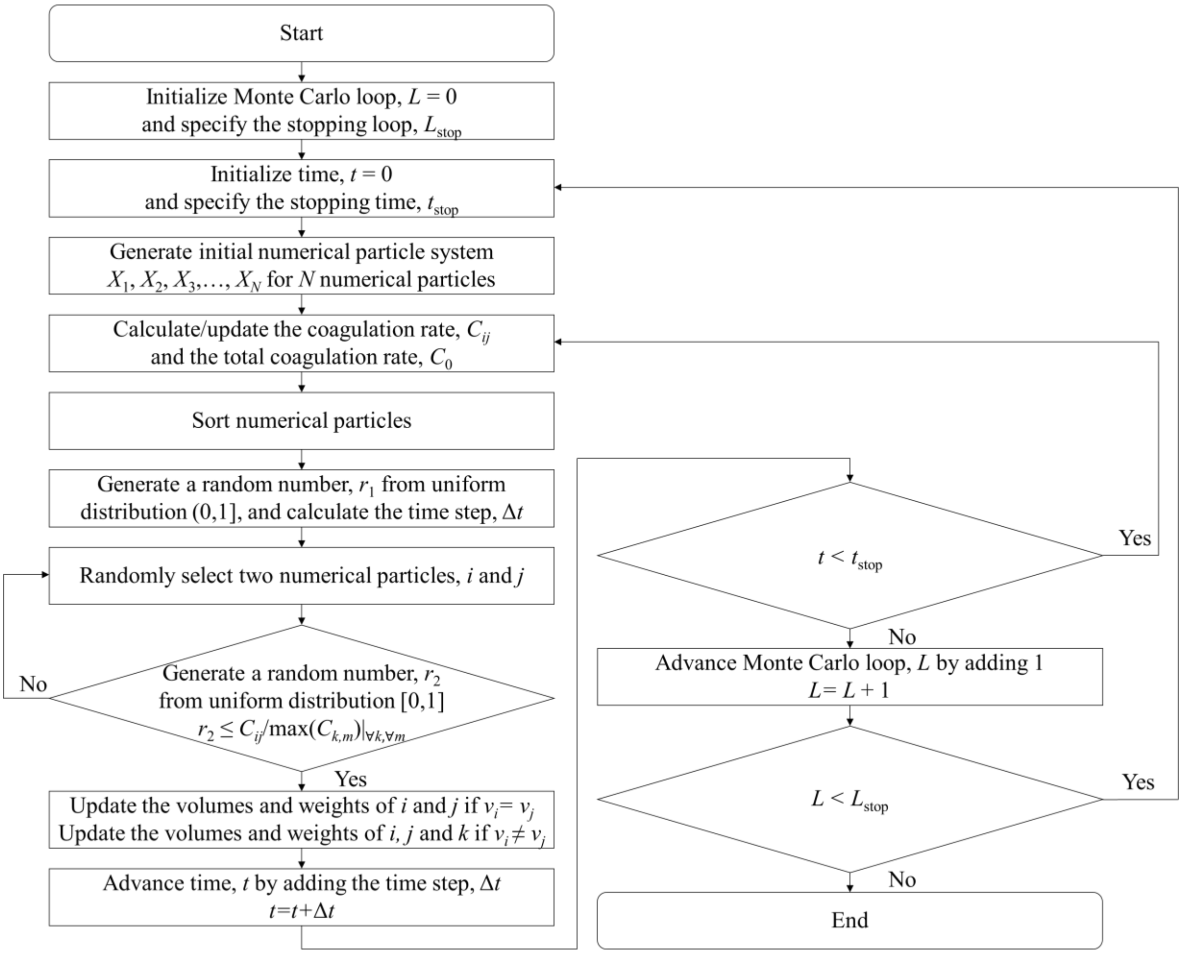

Figure 4.5 Flowchart of the newly proposed and developed SAMWFMC algorithm [35].

Every time when a coagulation event takes place, the coagulation rate C_{ij} in Equation (4-5), the total coagulation rate, C_0 in Equation (4-7) and $\max\limits_{\forall k,\forall m} C_{km}$ in Equation (4-10) should be recalculated since there are two or three numerical particles in the array whose volumes and weights are changed in the SAMWFMC method. In the present study, the smart bookkeeping technique [17] is used to calculate C_0 in Equation (4-7) and $\max\limits_{\forall k,\forall m} C_{km}$ in Equation (4-10), which can avoid spending a large amount of time for recalculating the coagulation rates, C_{ij} of those uncoagulated numerical particles. More specifically, double traversing and counting on each numerical particle from the beginning to the end only takes place in the initial calculation of the total coagulation rate, C_0 and there is no further double traversing and counting anymore during the numerical simulation.

4.2.8 Description of the SAMWFMC algorithm

Figure 4.5 shows the flowchart of the newly proposed and developed SAMWFMC algorithm for particle coagulation, in which the full algorithm is described.

4.3 Results and Discussion

In the present study, two initial particle size distributions (i.e., initial monodispersed distribution [IMD] and initial exponential distribution [IED]), three coagulation kernels (i.e., constant coagulation kernel [CCK], linear coagulation kernel [LCK] and quadratic coagulation kernel [QCK]) and four fraction functions (i.e., hyperbolic fraction function [HFF], exponential fraction function [EFF], stepwise constant fraction function [SCFF] and constant fraction function [CFF]) are completely used. The newly proposed SAMWFMC method is fully validated by comparing the numerical results of the PSD and corresponding different orders of moments with the existing analytical solutions [154,213] to assess the computational accuracy. In addition, a comparison of stochastic errors as well as computational efficiency with the DSMC [17], MMC [32] and WFMC [33] methods is performed. The general moment of the PSD function can be defined by the expression [9]:

$$M_k = \int_0^\infty v^k n(v)\,\mathrm{d}v \tag{4-23}$$

where k is the order of the moment. Different order moments normally have their specific physical meanings. For example, the zeroth moment, M_0 and the first moment, M_1 are the total particle number and mass (volume) densities, respectively. The mean standard deviations of the M_k are denoted as σ_{M_k} [32,34,214].

$$\sigma_{M_k}(t) = \frac{1}{Q}\sum_{i=1}^{Q}\sqrt{\frac{1}{t}\int_0^t \left[\frac{M_k^{MC(i)}(t) - M_k^{AS}(t)}{M_k^{AS}(t)}\right]^2 dt} \tag{4-24}$$

where Q is the number of MC repetitions. The analytical solution is represented by "AS" while MC(i) is the numerical results of the i-th MC simulation. In the present study, the number of MC repetitions used for all studied cases is 200 for achieving good enough stable mean standard deviations. The initial number of numerical particles used in the present study is 2000 [17,32,152,156,161,176,177,214] for all MC methods, which can achieve highly accurate numerical results. It has been proved that the choosing of the initial number of numerical particles to be 2000 can achieve high computational accuracy with a reasonable computational time.

4.3.1 Initial monodispersed distribution and constant coagulation kernel

Aerosols composed of particles with all the same size are called monodisperse aerosols. A typical case with the initial monodispersed distribution (IMD) and constant coagulation kernel (CCK) function is a benchmark for algorithm validation, as the analytical solution of the Smoluchowski equation exists [154]. In this case, the initial total particle number concentration, $N_0 = 10^6$ particles/cm^3 [17] and the coagulation kernel β_{ij} is equal to a constant A where $A = 10^{-6}$ cm^3/s [17]. The characteristic coagulation time is defined as $\tau_c = 1/(AN_0)$.

Figure 4.6 shows the time evolutions of zeroth-order to third-order moments (i.e., M_0, M_1, M_2 and M_3) obtained from DSMC, MMC, WFMC and SAMWFMC methods and their corresponding mean standard deviations (i.e., σ_{M_0}, σ_{M_1}, σ_{M_2} and σ_{M_3}) for different fraction functions (i.e., HFF, EFF, SCFF and CFF) with the IMD and CCK when compared with analytical solutions [154]. In Figure 4.6(a), the total particle number concentrations, M_0 for all studied MC methods decrease over time and show excellent agreement with the analytical solution due to the reduction in the number of real particles in each coagulation process. But the mean standard deviations, σ_{M_0} vary for different MC methods. It can be found that the σ_{M_0} obtained from the new SAMWFMC method are always lower than the counterparts of WFMC method [33], which demonstrates that the SAMWFMC method always has higher computational accuracy in predicting M_0 than the WFMC method. Especially, the σ_{M_0} for the

WFMC method with the HFF is the largest, even larger than that of the DSMC method, and keeps increasing with time, which are also found in Jiang and Chan [33]. It implies that the stochastic error in M_0 for the WFMC method with the HFF is very large and this method cannot allow for indefinitely long numerical simulations of the particle coagulation. It is because more coagulation events will occur with time advancing, the stochastic error will be even larger and the computational accuracy will be further reduced. By comparison, the σ_{M_0} for the SAMWFMC method with the HFF still remains at a very low stochastic error level and nearly unchanged with time, which demonstrates that the new merging scheme implemented in the proposed SAMWFMC method can effectively reduce the stochastic error in M_0. More importantly, as the WFMC method is not applicable to a CFF due to the limitation of the particle size discrepancy while the applicability of the SAMWFMC method is fully assessed for different CFFs (i.e., C = 0.5, 0.6, 0.7, 0.8 and 0.9) in the present study. It is found that different constants of the CFF have little effect on the σ_{M_0}, as all the σ_{M_0} obtained from the SAMWFMC method with $C = 0.5$ to 0.9 are very close and lower than that of the MMC method [32]. As the coagulation process does not change the total volume/mass of numerical particles due to volume/mass conservation, the total volume concentrations, M_1 for all MC methods remain constant during the numerical simulation, therefore leading to no stochastic error in M_1 as shown in Figure 4.6(b).

In Figures 4.6(c) and 4.6(d), the time evolutions of higher-order moments (i.e., M_2 and M_3) obtained from different MC methods are also in very good agreement with the analytical solutions. The DSMC method has the largest σ_{M_2} and σ_{M_3} than other MC methods, while the σ_{M_2} and σ_{M_3} obtained from the both WFMC and SAMWFMC methods are lower than those of the MMC method, which demonstrates that the introduction of the fraction function in the both WFMC and SAMWFMC methods has a significant reduction of stochastic errors in the higher-order moments. When the fraction function (i.e., HFF, EFF or SCFF) used in both WFMC and SAMWFMC methods is the same, the σ_{M_2} and σ_{M_3} for the SAMWFMC method are only slightly larger than those of the WMFC method, respectively, which implies that the new SAMWFMC method can achieve almost the same computational accuracy as the WFMC method. Furthermore, the effect of different CFFs for the SAMWFMC method on the σ_{M_2} and σ_{M_3} is also studied. Results show that with the CFF, the σ_{M_2} and σ_{M_3} obtained from the SAMWFMC method with $C = 0.5$ are the lowest, and the σ_{M_2} and σ_{M_3} gradually increase with increasing C from 0.5 to 0.9. When C = 0.9, the σ_{M_2} and σ_{M_3} for the SAMWFMC method are almost equal to those of the MMC method.

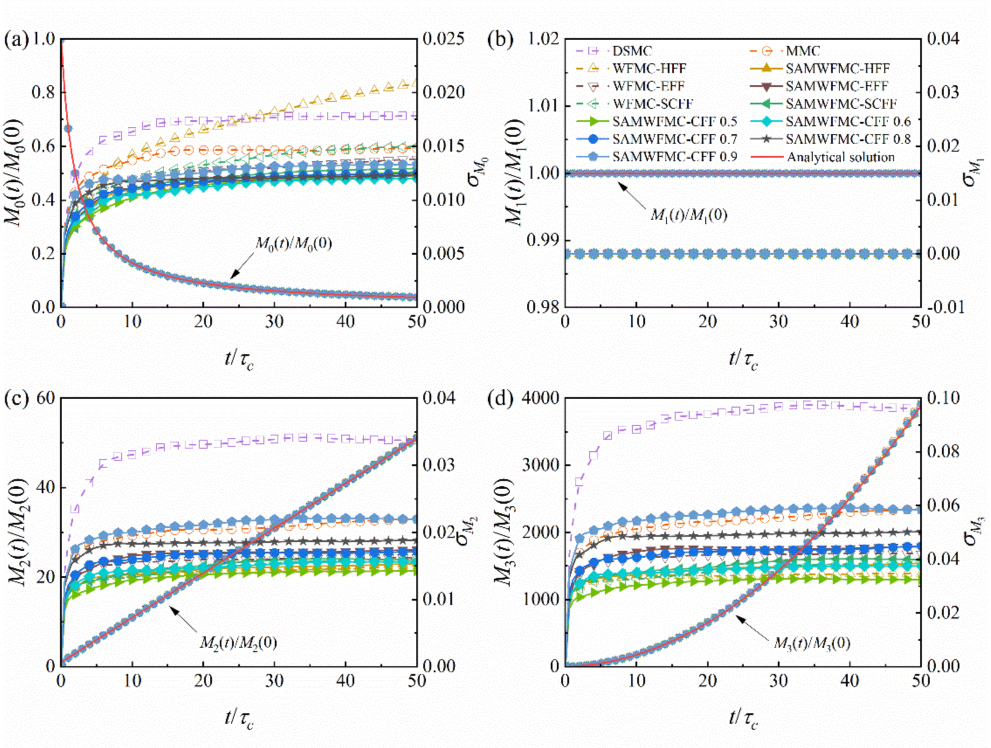

Figure 4.6 Time evolutions of zeroth-order to third-order moments and mean standard deviations obtained from DSMC, MMC, WFMC and SAMWFMC methods for different fraction functions with the IMD and CCK when compared with analytical solutions [35].

Figure 4.7 shows the probabilities of obtaining a cluster containing k primary particles, P_k obtained from DSMC, MMC, WFMC and SAMWFMC methods for different fraction functions (i.e., HFF, EFF, SCFF and CFF) at t/τ_c = 50 when compared with the analytical solution [154], where P_k represents the PSD at $k = v/v_0$. Results show that all MC methods follow the analytical solution and track the PSD well, but there are varying degrees of fluctuations in the PSD for different MC methods. The DSMC method is found to have the narrowest PSD and the MMC method is slightly wider, the fluctuation in the PSD for the latter is smaller than the former when the particle size is the same at the high-end of the PSD. It can be also found that larger size particles can be obtained in both WFMC and SAMWFMC methods than those in the DSMC and MMC methods, so both WFMC and SAMWFMC methods with different fraction functions have wider PSDs than the MMC method, which implies that the introduction of the fraction function can significantly extend the prediction range of the PSD. When the fraction function used in the WFMC and SAMWFMC methods is the same (i.e., HFF, EFF or SCFF), the SAMWFMC method has almost the same wide PSDs as the WFMC method, while the PSD obtained from the SAMWFMC method with the CFF becomes wider when decreasing C from 0.9 to 0.5.

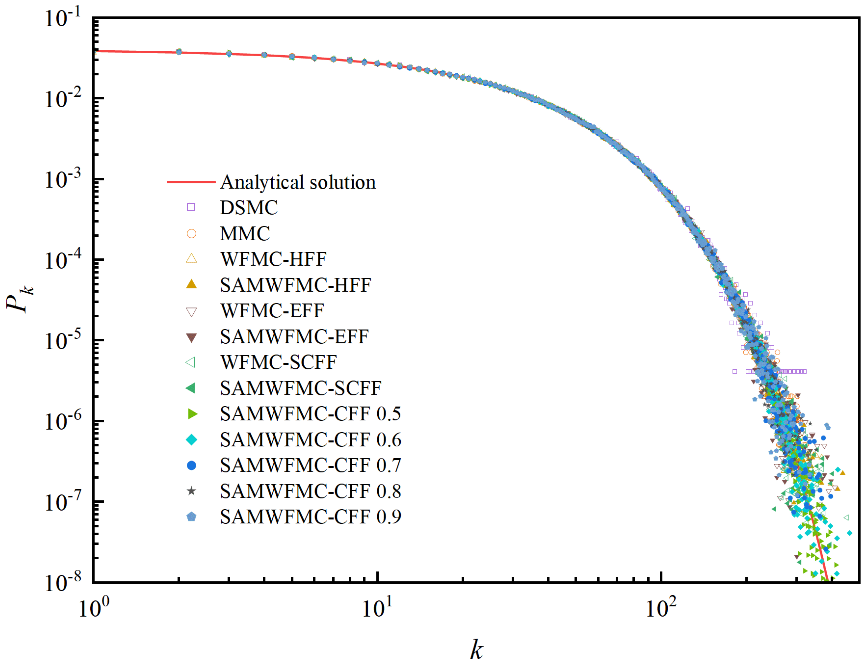

Figure 4.7 Probabilities of obtaining a cluster containing k primary particles, P_k obtained from DSMC, MMC, WFMC and SAMWFMC methods for different fraction functions with the IMD and CCK at $t/\tau_c = 50$ when compared with analytical solution [35].

Figure 4.8 shows the number of numerical particles, N_{NP} at different particle volumes, v/v_0 obtained from DSMC, MMC, WFMC and SAMWFMC methods for different fraction functions (i.e., HFF, EFF, SCFF and CFF) at $t/\tau_c = 50$. The DSMC method has the most numerical particles at $v/v_0 = 1$, but the number of numerical particles significantly reduces with the increase of the particle size. Finally, DSMC method has the least numerical particles at the high-end of the PSD, which implies that there are few or no numerical particles to represent the large real particles. This leads to the narrowest PSD among all MC methods, which is also shown in Figure 4.7, and the largest fluctuations in the high-order moments of the PSD (i.e., M_2 and M_3) are shown in Figures 4.6(c) and 4.6(d). By comparison, the MMC method distributes more numerical particles to represent the large real particles and extends the prediction of the PSD at the high-end, which reduces the fluctuations of M_2 and M_3 as shown in Figures 4.6(c) and 4.6(d). The number of numerical particles for the WFMC method for different fraction functions (i.e., HFF, EFF and SCFF) increases at first and then decreases with the increasing particle sizes, especially for the HFF, which is totally inconsistent with the DSMC and MMC methods. This implies that the WFMC method changes the number distribution of the numerical particles, in which more numerical particles are used to represent larger real particles, but few numerical particles to represent smaller real particles. As a result, the WFMC method reduces the fluctuations in the high-order moments of the PSD (i.e. M_2 and M_3) as shown in Figures 4.6(c) and 4.6(d), but results in large fluctuation in the total number concentration, M_0 as shown in Figure 4.6(a), which is also found in the original work of Jiang and Chan [33]. The reason is that the statistic precision of stochastic approaches is inversely proportional to the square root of the numerical particle numbers. The SAMWFMC method for different fraction functions (i.e., HFF, EFF and SCFF) has the same trend as the MMC method in the number distribution of numerical particles, which decreases with the increase of the particle sizes. Compared with the WFMC method, more numerical particles at the low-end of the PSD but slightly less numerical particles at larger particle size areas are observed in the SAMWFMC method, therefore reducing the fluctuation in M_0 with less change in M_2 and M_3. In addition, it is found that the number distribution of numerical particles for the SAMWFMC method with the CFF gradually moves to the high-end of the PSD with the decrease of the constant, C from 0.9 to 0.5 as shown by the arrow in the Figure 4.8. It implies that the number of numerical particles with small sizes gradually decreases while the number of numerical particles with larger sizes increases, therefore resulting in the gradual reduction of the fluctuation in the high-order moments (i.e., M_2 and M_3) of the PSD as shown in Figures 4.6(c) and 4.6(d). It should be noted that the SAMWFMC method for the CFF ($C = 0.5$) has wider PSD and more numerical particles at $v/v_0 > 60$ than the WFMC method for the HFF, so smaller σ_{M_2} and σ_{M_3} for the former are shown in Figures 4.6(c) and 4.6(d). Although the PSD obtained from the SAMWFMC method for the CFF ($C = 0.7$) is almost as the same wide as the WFMC method for the HFF, the number of numerical particles for the former is less than that of the latter at $v/v_0 > 25$, leading to larger σ_{M_2} and σ_{M_3} for the former as shown in Figures 4.6(c) and 4.6(d).

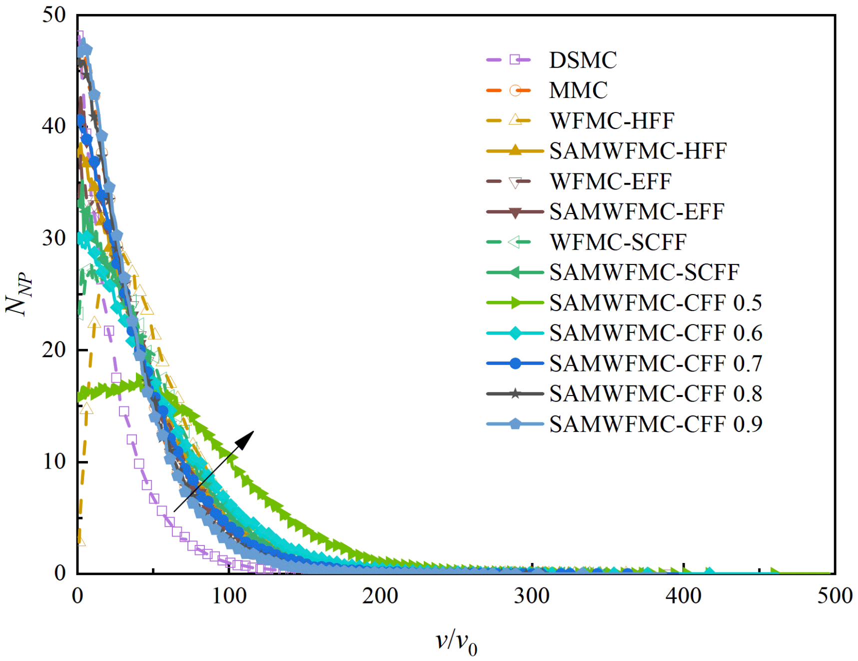

Figure 4.8 Number of numerical particles, N_{NP} at different particle volumes, v/v_0 obtained from DSMC, MMC, WFMC and SAMWFMC methods for different fraction functions with the IMD and CCK at $t/\tau_c = 50$ [35].

4.3.2 Initial monodispersed distribution and linear coagulation kernel

The analytical solution of the Smoluchowski equation with the initial monodispersed distribution (IMD) and linear coagulation kernel (LCK) function is well known [154], which is also used to validate the newly proposed SAMWFMC method. The initial total particle number concentration, $N_0 = 10^6$ particles/cm^3 [17] and the coagulation kernel $\beta_{ij} = A(v_i+v_j)$ where $A = 10^{-6}$ cm^3/s [17], v_i and v_j are the dimensionless volumes of the two coagulation particles, i and j, respectively. The characteristic coagulation time is defined as $\tau_c = 1/(AN_0)$. For simplicity, only the HFF for both WFMC and SAMWFMC methods and the CFF with C= 0.7 for the SAMWFMC method are used.

Figure 4.9 shows a very good agreement for zeroth-order to third-order moments (M_0, M_1, M_2 and M_3) between the analytical solutions [154] and DSMC, MMC, WFMC and SAMWFMC methods for different fraction functions (i.e., HFF and CFF) with the IMD and LCK, and their corresponding mean standard deviations are also presented. All MC methods show an excellent mass/volume conservation, as the total volume/mass concentrations, M_1 for all MC methods remain constant during the numerical simulation, therefore leading to no stochastic error in M_1 as shown in Figure 4.9(b). The mean standard deviations of zeroth-order to third-order moments (i.e., M_0, M_2 and M_3) obtained from different MC methods have a similar trend with time. The DSMC method has the largest σ_{M_0}, σ_{M_2} and σ_{M_3} among all MC methods. Although the σ_{M_2} and σ_{M_3} for the WFMC method are almost smaller than those of other MC methods, the WFMC method has larger σ_{M_0} than the MMC method but has just slightly smaller than the DSMC method. By comparison, the SAMWFMC method has the smallest σ_{M_0} among all MC methods and can achieve as low σ_{M_2} and σ_{M_3} as the WFMC method, which shows the advantage of the SAMWFMC method in reduction of the stochastic errors for M_0, M_2 and M_3, respectively. In addition, the SAMWFMC method for the CFF with $C = 0.7$ also has smaller σ_{M_0}, σ_{M_2} and σ_{M_3} than those of the DSMC and MMC methods, which demonstrates the newly proposed SAMWFMC method can deal with different fraction functions at very small stochastic error.

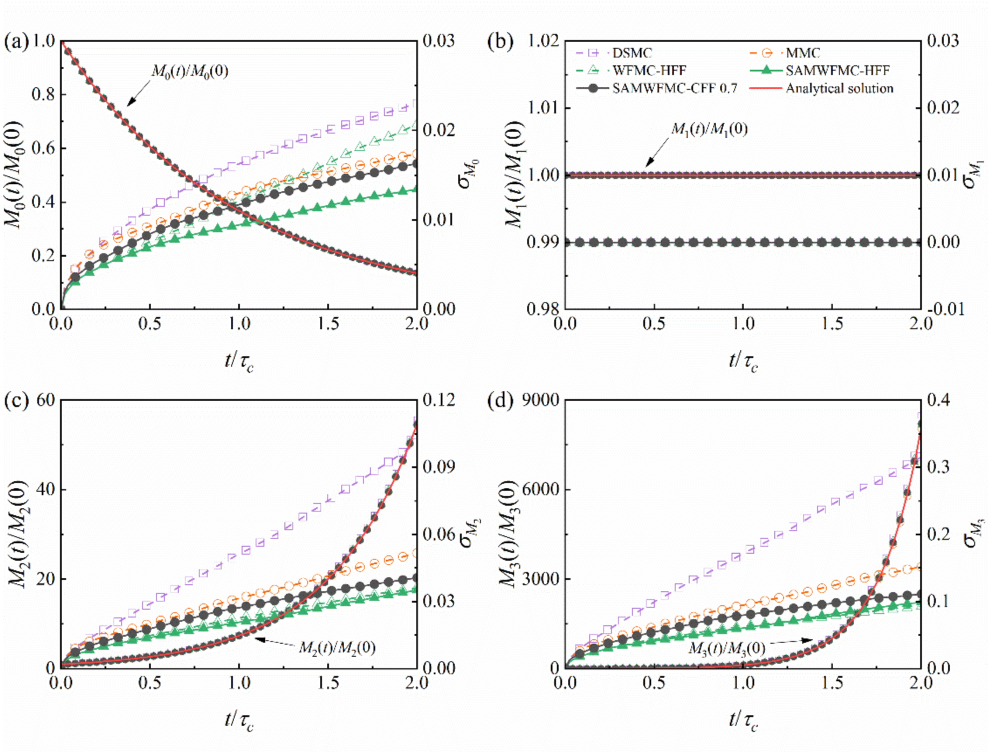

Figure 4.9 Time evolutions of zeroth-order to third-order moments (M_0, M_1, M_2 and M_3) and mean standard deviations obtained from DSMC, MMC, WFMC and SAMWFMC methods for different fraction functions with the IMD and LCK when compared with analytical solutions [35].

Figure 4.10 shows that the DSMC method has the narrowest particle size range and a slight wider particle size range with smaller fluctuation at the high-end is observed in the MMC method, which results in the differences of the σ_{M_2} and σ_{M_3} as shown in Figures 4.9(c) and 4.9(d), respectively. Compared with the MMC method, the fraction functions introduced in the WFMC and SAMWFMC methods can effectively extend the prediction of the particle size range and then obtain wider particle size ranges, which finally reduce the σ_{M_2} and σ_{M_3}. Small differences of σ_{M_2} and σ_{M_3} between the WFMC and SAMWFMC methods are found due to the almost identical width of particle size ranges.

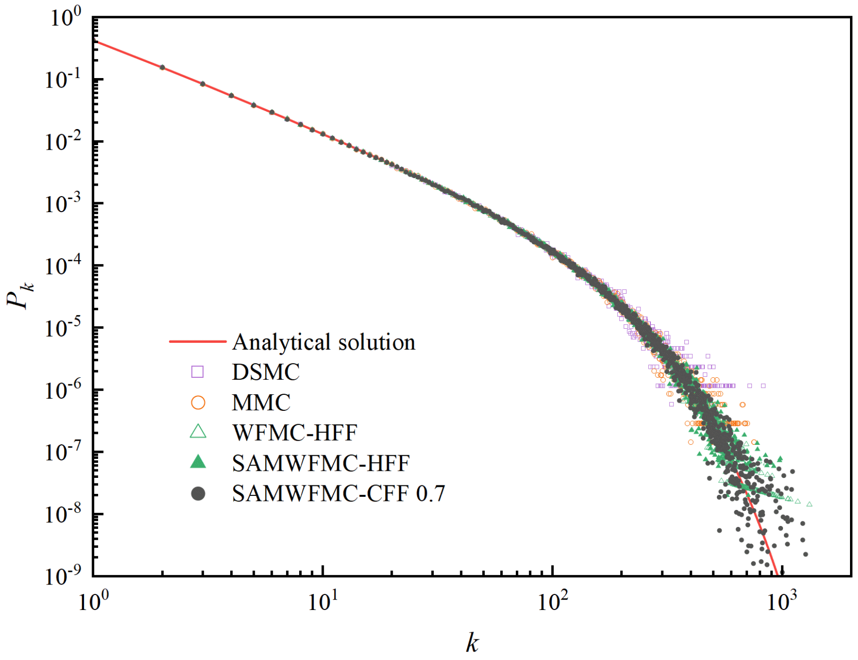

Figure 4.10 Probabilities of obtaining a cluster containing k primary particles, P_k obtained from DSMC, MMC, WFMC and SAMWFMC methods for different fraction functions with the IMD and LCK at $t/\tau_c = 2$ when compared with analytical solution [35].

4.3.3 Initial monodispersed distribution and quadratic coagulation kernel

Another benchmark test case with initial monodispersed distribution (IMD) and quadratic coagulation kernel (QCK) function is also validated in the present study, the analytical solution of this case exists in [154]. The initial total particle number concentration, $N_0 = 10^6$ particles/cm^3 [17] and the coagulation kernel, $\beta_{ij} = A(v_i \times v_j)$, where $A = 10^{-6}$ cm^3/s [17], v_i and v_j are the dimensionless volumes of a coagulation particle pair, i and j, respectively. The characteristic coagulation time is defined as $\tau_c = 1/(AN_0)$. It should be noted that if the time is greater than τ_c, the analytical solution of the Smoluchowski equation does not exist [17] in this case due to the formation of the supercluster when $t = \tau_c$ [154].

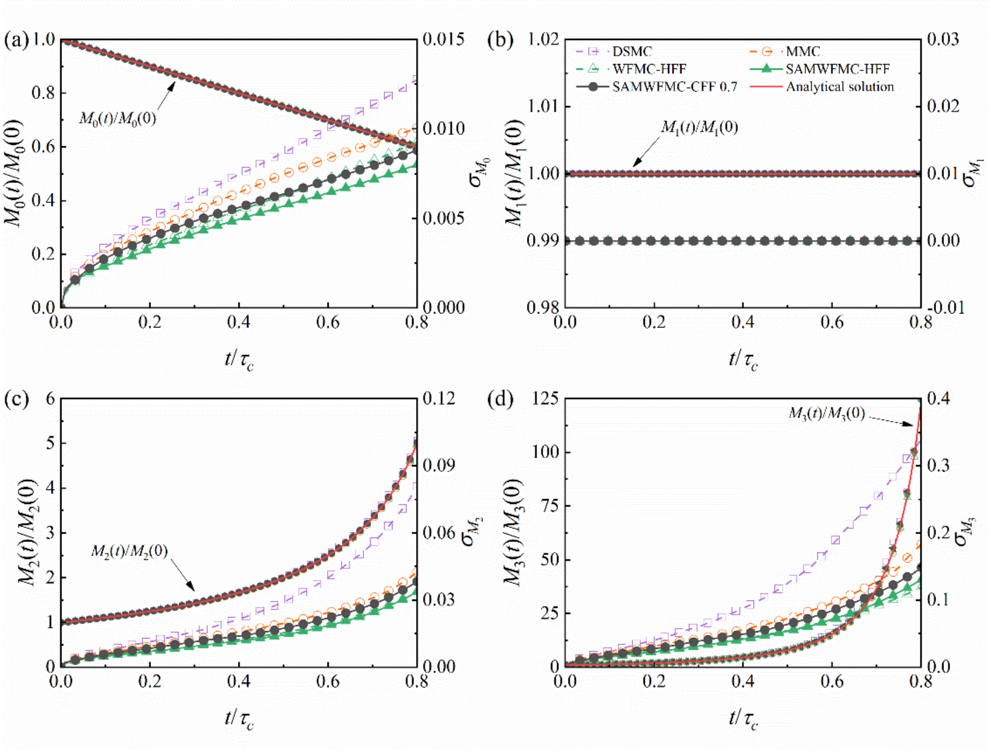

Figure 4.11 Time evolutions of zeroth-order to third-order moments and mean standard deviations for DSMC, MMC, WFMC and SAMWFMC methods for different fraction functions with the IMD and QCK when compared with analytical solutions [35].

Figures 4.11 and 4.12 are the time evolutions of zeroth-order to third-order moments and corresponding mean standard deviations and PSDs for different MC methods when compared with analytical solutions [154], respectively. An excellent agreement of the first four moments for different MC methods and the analytical solutions with the IMD and QCK is observed in Figure 4.11. As the total volume/mass concentrations, M_1 for all MC methods remain constant, the resulting σ_{M_1} is always zero during the numerical simulation as shown in Figure 4.11(b). The SAMWFMC method has the lowest σ_{M_0} than other MC methods, while the σ_{M_2} and σ_{M_3} obtained from the SAMWFMC method are very close to those of the WFMC method because of the almost identical width of the PSDs as shown in Figure 4.12, which are lower than those of the DSMC and MMC methods. This further demonstrates the contribution of the fraction functions to the PSD.

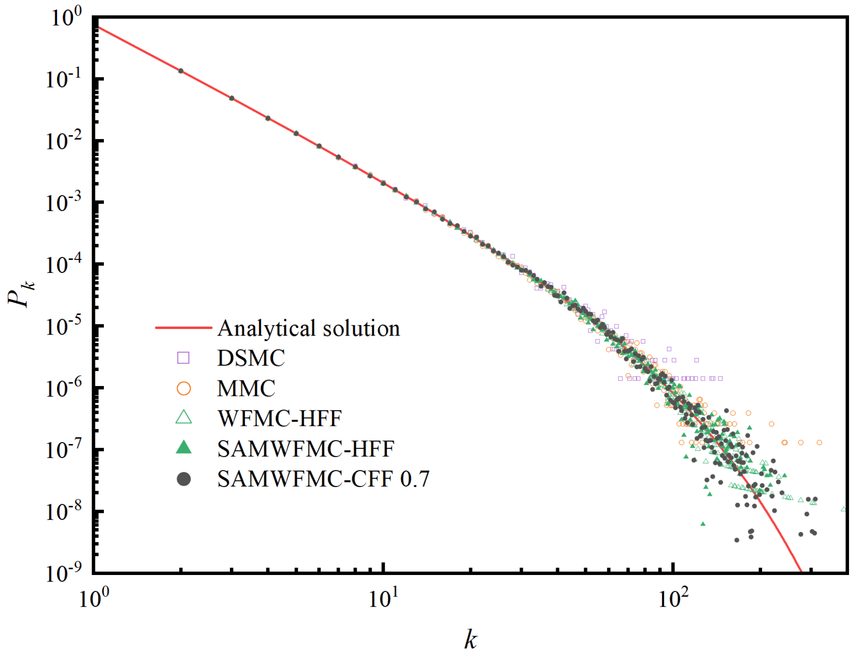

Figure 4.12 Probabilities of obtaining a cluster containing k primary particles, P_k obtained from DSMC, MMC, WFMC and SAMWFMC methods for different fraction functions with the IMD and QCK at $t/\tau_c = 0.8$ when compared with analytical solution [35].

4.3.4 Initial exponential distribution and constant coagulation kernel

As particles with different sizes are more common than those with the same size in most practical cases involved in combustion emission sources and atmospheric aerosols [9], the newly proposed SAMWFMC method must be validated the computational accuracy with the initial polydisperse PSD. In the present study, an exponential function is chosen as the initial polydisperse PSD, which is given by [213]:

$$n_p(v,0) = N_0/v_0[\exp(-v/v_0)] \tag{4-25}$$

where N_0 is the initial total particle number concentration of real particles with the initial mean particle volume of v_0. The analytical solution of the Smoluchowski equation with the initial exponential distribution (IED) and constant coagulation kernel (CCK) function is provided in [213]. In the present study, $N_0 = 10^6$ particles/cm^3 [213] and $v_0 = 1$ (dimensionless) are used. The coagulation kernel, $\beta_{ij} = A$, where $A = 10^{-6}$ cm^3/s. The characteristic coagulation time is defined as $\tau_c = 1/(AN_0)$.

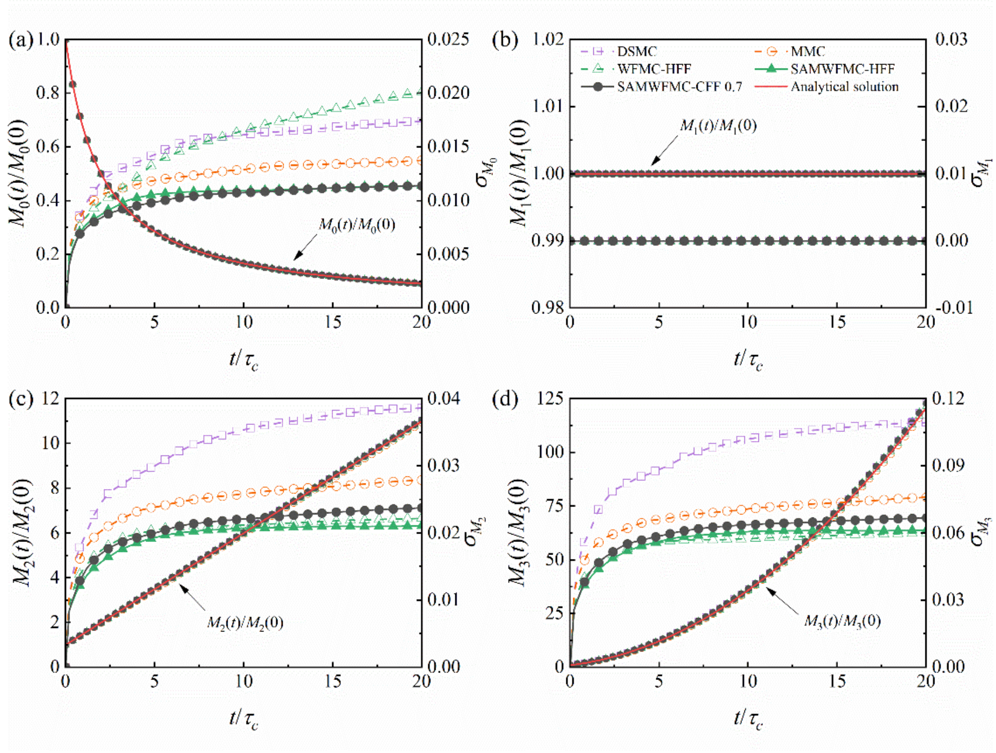

Figure 4.13 Time evolutions of zeroth-order to third-order moments and mean standard deviations obtained from DSMC, MMC, WFMC and SAMWFMC methods for different fraction functions with the IED and CCK when compared with analytical solutions [35].

A very good agreement between the analytical solutions [213] and the first four moments (M_0, M_1, M_2 and M_3) obtained from different MC methods (i.e., DSMC, MMC, WFMC and SAMWFMC) for different fraction functions (i.e., HFF and CFF) with the IED and CCK is shown in Figure 4.13. The results of M_1 obtained from the four MC methods remain constant and there are no changes in σ_{M_1} for all MC methods during the numerical simulation as shown in Figure 4.13(b). The SAMWFMC method with the HFF and CFF has the lowest σ_{M_0}, while the WFMC method has the largest σ_{M_0} among all MC methods, which is even larger than that of the DSMC method and keeps increasing with time. With the HFF, the σ_{M_2} and σ_{M_3} for the SAMWFMC and WFMC methods are very close to each other and have the lowest stochastic errors. It demonstrates that the SAMWFMC method can achieve lower stochastic error in M_0 and nearly the equally lowest stochastic errors in M_2 and M_3, respectively when compared with the WFMC method. It also implies that the SAMWFMC method surpass the WFMC method in obtaining accurate numerical results. In addition, the SAMWFMC method with CFF has lower σ_{M_0}, σ_{M_2} and σ_{M_3} than the MMC and DSMC methods, which also demonstrates the significant improvement in computational accuracy by the SAMWFMC method.

Figure 4.14 shows the dimensionless particle number concentration (PNC) functions at different particle volumes, v/v_0 obtained from DSMC, MMC, WFMC and SAMWFMC methods for different fraction functions (i.e., HFF and CFF) with the IED and CCK at t/τ_c= 0, 1, 5 and 20 when compared with analytical solutions [213]. In here, t/τ_c= 0 is the initial particle number concentration function. A very good agreement between the analytical solutions and the numerical results obtained from different MC methods is observed at different times, t/τ_c. As coagulation events take place, particle sizes become larger with time and the PNC functions gradually moves to the right side, but the PNC functions still remain the “self-preserving” form [9]. As the PNC functions expand and the number of large particles increases, the maximum value of the PNC gradually decreases. It is still shown that the WFMC and SAMWFMC methods can obtain particles with larger volumes than the DSMC and MMC methods, and also extend the prediction of the particle volumes at the high-end. It also implies that the introduction of the fraction functions can significantly reduce the σ_{M_2} and σ_{M_3} in the MC simulations with initial polydispersed distribution. The particle size range obtained from the MMC method are slightly wider than that of the DSMC method, which leads to the differences in the stochastic errors of the high-order moments in Figures 4.13(c) and 4.13(d). The large particle size regime for the WFMC and SAMWFMC methods are almost identical at t/τ_c = 1, but the difference becomes larger with time. The WFMC method can obtain larger particles at the high-end than the SAMWFMC method when t/τ_c = 20, and the volume of particles at the low-end for the WFMC method is also larger than those of all the MC methods. It further demonstrates that the WFMC method is developed to obtain more particles with large volumes, in which smaller real particles are poorly or even not represented. As a result, the WFMC method achieves very low σ_{M_3} as shown in Figures 4.13(d) by the contribution of those large volume particles but deteriorates the statistical precision at the low-end. By comparison, although the volume of particles obtained from the SAMWFMC method at the high-end is smaller, the small particles at the low-end is still represented, which lead to slightly larger σ_{M_3} and even lower σ_{M_2}, but significantly lower σ_{M_0} as shown in Figures 4.13(c), 4.13(d) and 4.13(a), respectively. As the volume/mass is always conserved during numerical simulation, the σ_{M_1} for both WFMC and SAMWFMC methods are equal to zero as shown in Figure 4.13(b).

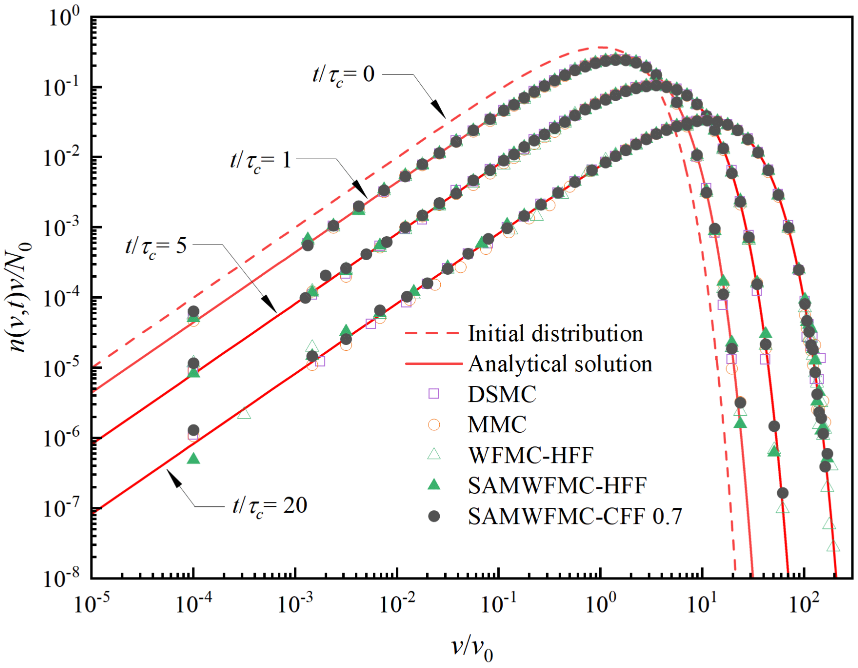

Figure 4.14 Dimensionless particle number concentration functions at different particle volumes, v/v_0 obtained from DSMC, MMC, WFMC and SAMWFMC methods for different fraction functions with the IED and CCK at t/τ_c = 0, 1, 5 and 20 when compared with analytical solutions [35].

4.3.5 Initial exponential distribution and linear coagulation kernel

There also exists the analytical solution of the Smoluchowski equation with the initial exponential distribution (IED) and linear coagulation kernel (LCK) function in [213]. In the present study, $N_0 = 10^6$ particles/cm^3 [213] and $v_0 = 1$ (dimensionless) are used. The coagulation kernel, $\beta_{ij} = A(v_i+v_j)$, where $A = 10^{-6}$ cm^3/s, v_i and v_j are the dimensionless volumes of the two coagulation particles, i and j, respectively. The characteristic coagulation time is defined as $\tau_c = 1/(AN_0v_0)$.

Figure 4.15 shows the time evolutions of first four moments (i.e., M_0, M_1, M_2 and M_3) obtained from different MC methods and corresponding mean standard deviations (i.e., σ_{M_0}, σ_{M_1}, σ_{M_2} and σ_{M_3}) for different fraction functions (i.e., HFF and CFF) with the IED and LCK when compared with analytical solutions [213]. The first four moments for all MC methods have a very good agreement with the analytical solutions. The SAMWFMC method with the

CFF has the lowest σ_{M_0}, while the σ_{M_0} for the DSMC method is the largest. The stochastic error in M_0 introduced by the WFMC method is still larger than that of the MMC method, but the SAMWFMC method with HFF has lower σ_{M_0} than the MMC method. The σ_{M_2} and σ_{M_3} for the SAMWFMC and WFMC methods with different fraction functions (i.e., HFF and CFF) are very close to each other but are smaller than those of the DSMC and MMC methods. There are no changes in σ_{M_1} for all MC methods as shown in Figure 4.15(b) since the volume/mass is always conserved during the numerical simulation.

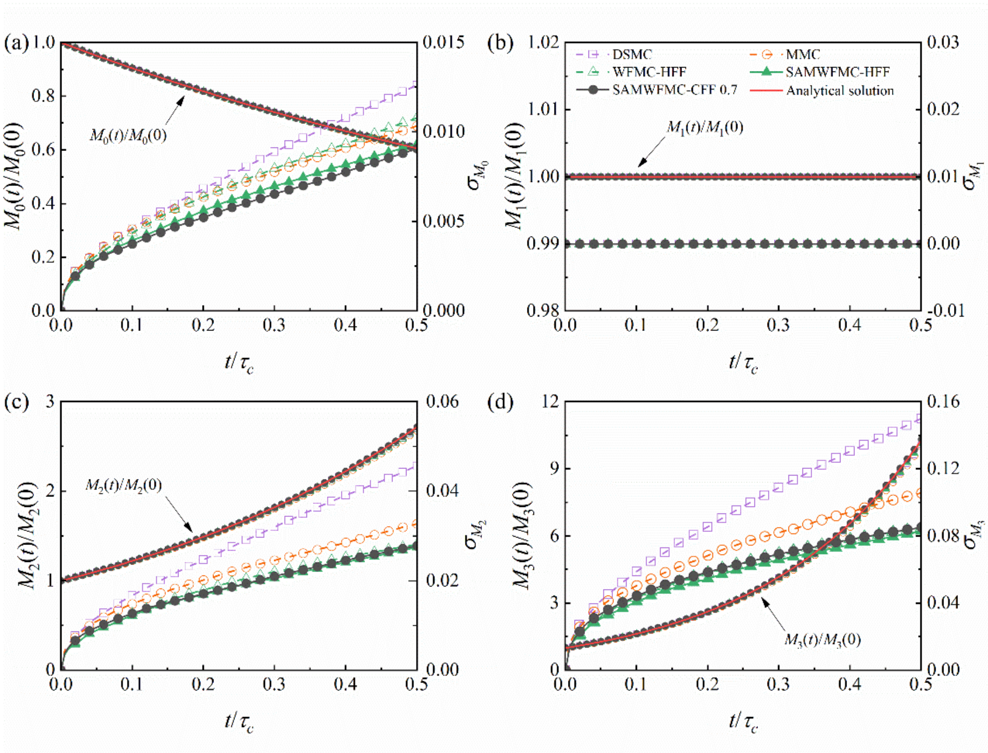

Figure 4.15 Time evolutions of zeroth-order to third-order moments and mean standard deviations obtained from DSMC, MMC, WFMC and SAMWFMC methods for different fraction functions with the IED and LCK when compared with analytical solutions [35].

Figure 4.16 shows the dimensionless PNC functions at different particle volumes, v/v_0 for different MC methods for different fraction functions with the IED and LCK at $t/\tau_c = 0$ and 0.5 when compared with the analytical solution [213]. In here, $t/\tau_c = 0$ is the initial particle number concentration function. The numerical results obtained from DSMC, MMC, WFMC and SAMWFMC methods have an excellent agreement with the analytical solution. The DSMC method has narrower particle size range than other MC methods while the particle size range for the MMC method is obviously wider due to the introduction of the weight numerical particles. Compared with the DSMC and MMC methods, the WFMC and SAMWFMC methods have wider particle size ranges due to the occurrence of the larger size particles at the high-end, which have been proved to have contribution to the high-order moments.

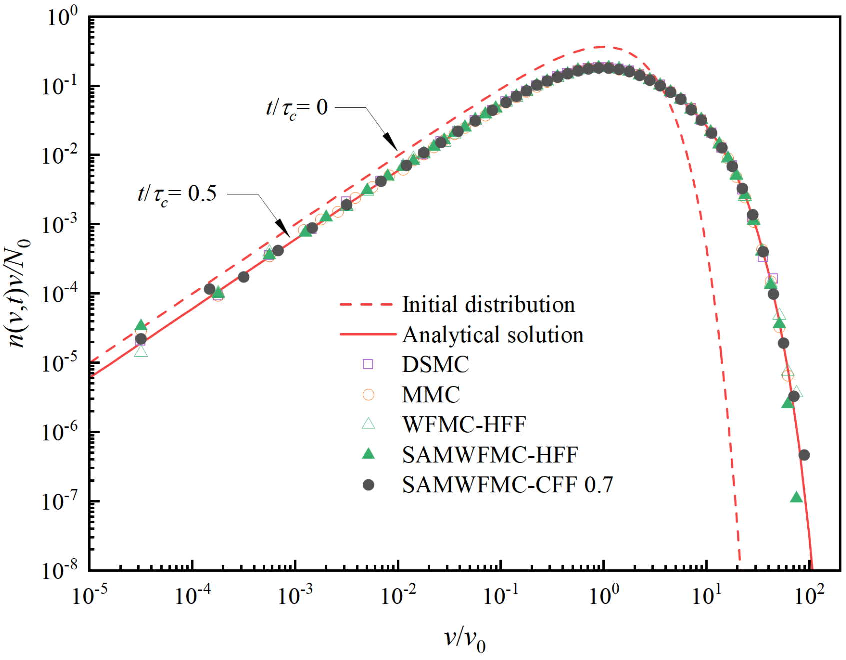

Figure 4.16 Dimensionless particle number concentration functions at different particle volumes, v/v_0 obtained from DSMC, MMC, WFMC and SAMWFMC methods for different fraction functions with the IED and LCK at $t/\tau_c = 0.5$ when compared with analytical solution [35].

4.3.6 Initial exponential distribution and quadratic coagulation kernel

The initial exponential distribution (IED) and quadratic coagulation kernel (QCK) function are also used to validate the computational accuracy of the SAMWFMC method when compared with the analytical solution [213]. In this case, $N_0 = 10^6$ particles/cm^3 [213] and $v_0 = 1$ (dimensionless) are used. The coagulation kernel, $\beta_{ij} = A(v_i \times v_j)$, where $A = 10^{-6}$ cm^3/s, v_i and v_j are the dimensionless volumes of the two coagulation particles, i and j, respectively. The characteristic coagulation time is defined as $\tau_c = 1/(AN_0v_0^2)$. It is reported that the critical phenomena of gelation may be caused by the quadratic coagulation kernel in this case, but the existing analytical solution is still useful for the algorithm validation [213].

Figure 4.17 shows that the time evolutions of first four moments (i.e., M_0, M_1, M_2 and M_3) obtained from different MC methods (i.e., DSMC, MMC, WFMC and SAMWFMC) have a very good agreement with analytical solutions [213]. The results of M_1 and σ_{M_1} obtained from all MC methods remain constant during the numerical simulation as shown in Figure 4.17(b). The SAMWFMC method has smaller σ_{M_0}, σ_{M_2} and σ_{M_3} than other MC methods. A very good agreement of the PNC functions at different particle volumes, v/v_0 between the analytical solution and numerical results for all MC methods is also found at $t/\tau_c = 0.3$ in Figure 4.18, but the differences among these MC methods are also clear. The particle size ranges obtained from the WFMC and SAMWFMC methods are still found to be wider than those of the DSMC and MMC methods, which leads to lower stochastic errors in the high-order moments. This further demonstrates the significant effect of the fraction functions on the computational accuracy in the high-order moments.

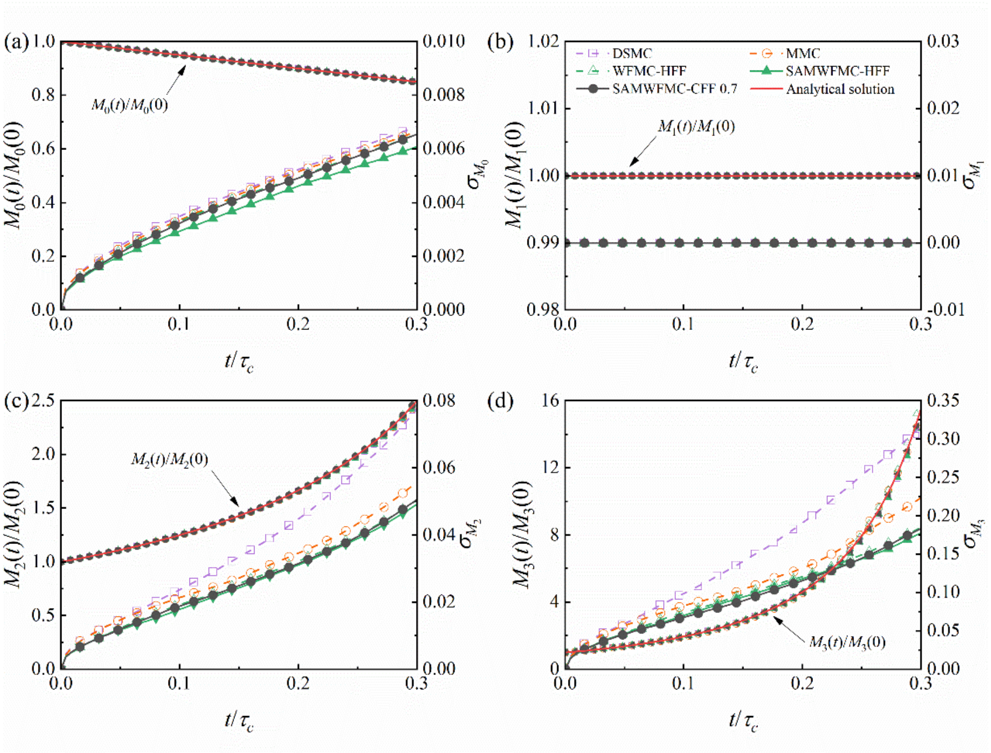

Figure 4.17 Time evolutions of zeroth-order to third-order moments and mean standard deviations obtained from DSMC, MMC, WFMC and SAMWFMC methods for different fraction functions with the IED and QCK when compared with analytical solutions [35].

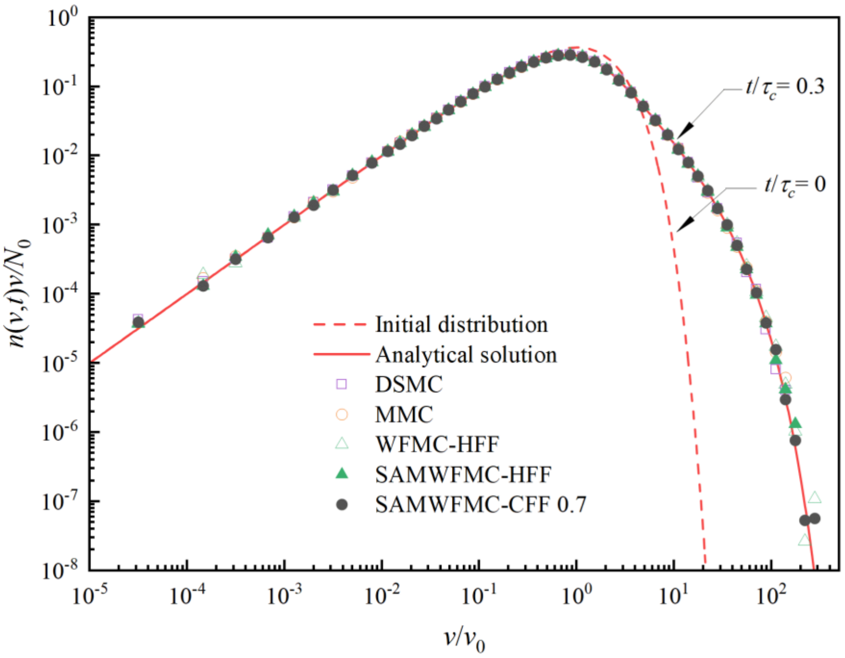

Figure 4.18 Dimensionless particle number concentration functions at different particle volumes, v/v_0 obtained from DSMC, MMC, WFMC and SAMWFMC methods for different fraction functions with the IED and QCK at t/τ_c = 0.3 when compared with analytical solution [35].

4.3.7 Computational efficiency

The computational efficiency of the new SAMWFMC method is evaluated by comparing with other studied MC methods. The computational time required for the WFMC method with the HFF in each case is regarded as the reference time because the WFMC method with the HFF has been fully tested for different cases in Jiang and Chan [33] and also used for studying soot aerosol dynamics in Jiang and Chan [49]. Hence, the corresponding normalized computational times of different cases required for all MC methods are listed in Table 4.1.

Results show that the computational times required for the DSMC method are the lowest among all MC methods, the reason is that when the DSMC method is used, the number of numerical particles gradually reduces with time due to the occurrence of coagulation events, which lowers the computational cost. However, the decrease in the number of numerical particles has a significant adverse effect on the computational accuracy. The MMC, WFMC and SAMWFMC methods remain the number of numerical particles unchanged during the numerical simulation which can improve the computational accuracy but it definitely leads to larger consumption of computational times. As the introduction of fraction functions to the WFMC and SAMWFMC methods leads to larger C_{ij} in Equation (4-5) and C_0 in Equation (4-7) but has smaller time step, Δt in Equation (4-9) than those of the MMC method, therefore requiring more computational times. When the fraction function (i.e., HFF, EFF or SCFF) is the same, the computational times for the SAMWFMC method are slightly longer than those of the WFMC method in each case. The reason is that when compared with the WFMC method, the central processing units (CPUs) require more computational cost to deal with the operations of sorting and merging numerical particles in the SAMWFMC method. The computational cost required by Case 1 with and without insertion sort is also evaluated. It is worth noting that if the sorting algorithm (i.e., insertion sort) is not used, then a very large statistical noise is obtained and the computational accuracy is largely reduced. Hence, only the computational efficiency is discussed here. Numerical results show that the computational cost for sorting numerical particles is 1.05 times of that without having insertion sort. It implies that the insertion sort is highly computational efficient when dealing with nearly sorted arrays. Hence, the finding and merging numerical particles require a slightly more computational cost in the SAMWFMC method when compared with the removing operation in the WFMC method. However, considering the high computational accuracy in high-order moments and significant reduction in the stochastic error in the particle number concentration, the computational cost of the SAMWFMC method is highly acceptable. In addition, the computational time for the SAMWFMC method with the CFF significantly reduces when the constant C increases from 0.5 to 0.9, the reason is that the C_{ij} in Equation (4-5) and C_0 in Equation (4-7) become smaller while the time step, Δt in Equation (4-9) becomes larger. As the stochastic errors in different moments (i.e., M_0, M_2 and M_3) are very low and the stochastic errors in M_1 are always zero due to volume/mass conservation for the SAMWFMC method for the CFF with $C = 0.5$ to 0.9, the choice of the constant, C is mainly dependent on the computational cost.

Table 4.1 Normalized computational times of different cases for all studied MC methods [35].

Case	DSMC	MMC	WFMC		SAMWFMC		SAMWFMC	
1	0.21	0.65					CFF 0.5	2.82
			HFF	1	HFF	1.40	CFF 0.6	2.14
			EFF	1.00	EFF	1.44	CFF 0.7	1.83
			SCFF	1.72	SCFF	2.51	CFF 0.8	1.50
							CFF 0.9	1.39
2	0.07	0.45	HFF	1	HFF	1.01	CFF 0.7	1.49
3	0.17	0.55	HFF	1	HFF	1.19	CFF 0.7	1.32
4	0.22	0.63	HFF	1	HFF	1.39	CFF 0.7	1.83
5	0.25	0.62	HFF	1	HFF	1.25	CFF 0.7	1.69
6	0.30	0.64	HFF	1	HFF	1.22	CFF 0.7	1.47

4.4 Summary

A new Monte Carlo method based on sorting algorithm is proposed and developed for solving the weighted fraction coagulation process in aerosol dynamics. In the new sorting algorithm-based merging weighted fraction Monte Carlo (SAMWFMC) method, three types of fraction functions (HFF, EFF and SCFF) are used to validate the computational accuracy and efficiency. Constant fraction functions are not applicable to the WFMC method but are also introduced to extend the generality of the fraction functions and used to evaluate the reliability of the newly developed SAMWFMC method. A new merging weighted fraction scheme is also proposed to ensure that the number of numerical particles and the volume of computational domain are constant. Six benchmark test cases are used to fully validate the SAMWFMC method by comparing with the existing analytical solutions as well as the numerical results of the direct simulation Monte Carlo (DSMC), multi-Monte Carlo (MMC) and weighted fraction Monte Carlo (WFMC) methods. The main conclusions are drawn as follows:

1. The particle number concentration (PNC) function and the zeroth-order to third-order moments (i.e., M_0, M_1, M_2 and M_3) obtained from the SAMWFMC method show excellent agreement with analytical solutions. As M_1 for all MC methods remain constant, their corresponding stochastic errors are always zero during the numerical simulation.

2. The SAMWFMC method has lower stochastic errors in M_0, M_2 and M_3 than the DSMC and MMC methods. Compared with the WFMC method, the SAMWFMC method does not increase the stochastic errors in high-order moments (i.e., M_2 and M_3) but significantly reduces the stochastic error in the total particle number concentration, M_0, even though the computational cost of the new SAMWFMC method is slightly higher than that of the WFMC method. Furthermore, the numerical results obtained from the SAMWFMC method with constant fraction functions show excellent agreement with analytical solutions with very low stochastic errors in M_0, M_2 and M_3 and no stochastic error in M_1.

3. The new SAMWFMC method shows a significant advantage in dealing with weighted fraction coagulation process in aerosol dynamics. It also demonstrates that the SAMWFMC method provides excellent potential to deal with various fraction functions with high computational accuracy and efficiency.

Chapter 5 Development of Sorting Algorithm-based Merging Monte Carlo Method for Aerosol Dynamics

5.1 Introduction

In this chapter, a new event-driven sorting algorithm-based merging Monte Carlo (SAMMC) method is proposed and developed for solving the general dynamic equation in aerosol dynamics. A neighbour merging method is proposed to maintain a constant-volume and constant-number scheme with minimal interference to the numerical particle population, where absolute volume difference (AVD) and relative volume difference (RVD) are used as the crucial merging criteria. The SAMMC method can be used for simulating all aerosol dynamic processes with very high computational accuracy, especially effective in those aerosol dynamic processes generating additional numerical particles. Very comprehensive computational conditions are used to study their impacts on computational accuracy and efficiency by comparing the SAMMC method to previous Monte Carlo (MC) methods and analytical solutions.

5.2 Methodology

The occurrence of a dynamic aerosol process may alter the number or volume of particles in the dispersed system, leading to the change of the particle size distribution (PSD) with time as well as position. The dynamic evolution of PSD due to aerosol dynamic processes involving coagulation, breakage, nucleation, condensation/evaporation and deposition is mathematically described by the general dynamic equation (i.e., population balance equation, PBE) [157]:

$$\begin{aligned}\frac{\partial n(v,t)}{\partial t} =& \left\{\frac{1}{2}\int_0^v \beta(u,v\text{-}u,t)n(u,t)n(v\text{-}u,t)\mathrm{d}u - n(v,t)\int_0^\infty \beta(u,v,t)n(u,t)\mathrm{d}u\right\}_{\text{coagulation}} \\ &+ \left\{\int_v^\infty \gamma(u,v,t)b(u,t)B(u,t)n(u,t)\mathrm{d}u - B(v,t)n(v,t)\right\}_{\text{breakage}} + \{J(v,t)\delta(v,v_{\min})\}_{\text{nucleation}} \qquad (5\text{-}1) \\ &+\{C_sK_s(v-v_s,t)n(v-v_s,t) - C_sK_s(v,t)n(v,t)\}_{\text{condensation/evaporation}} \\ &- \{D(v,t)n(v,t)\}_{\text{deposition}}\end{aligned}$$

where v is the particle volume; $n(v,t)$ is the PSD function at time t; $n(v,t)\mathrm{d}v$ is the particle number concentration with volumes ranging from v to $v+\mathrm{d}v$ at time t; $\beta(u,v,t)$ is the coagulation kernel for the particles of volumes u and v at time t; $B(v,t)$ is the breakage rate for the particle with volume v at time t; $\gamma(u,v,t)$ is the probability of generating a daughter particle with volume v from a parent particle with volume u, while $b(u,t)$ is the number of child particles resulting from the breakage of a parent particle with volume u, so $\gamma(u,v,t)b(u,t)$ represents the size distribution of the fragment with volume v forming from a parent particle with volume u; $J(v,t)$ is the nucleation kernel for the particle with volume v at time t, and v_{min} is the volume of nucleus; v_s and C_s are the volume and number concentration of condensing monomers, respectively, while $K_s(v,t)$ is the proportional coefficient of the condensation/evaporation rate for the particle with volume v at time t; $D(v,t)$ is the deposition kernel of the particle with volume v at time t.

In event-driven MC methods for dynamic processes in the dispersed system, the development of the jump Markov process is based on the rates of all aerosol dynamic processes involved. The new sorting algorithm-based merging Monte Carlo (SAMMC) method for all aerosol dynamic processes (i.e., deposition, condensation/evaporation, breakage, nucleation, and coagulation) is developed as below.

5.2.1 Flowchart of the SAMMC algorithm

Figure 5.1 shows the detailed flowchart of the event-driven sorting algorithm-based merging Monte Carlo (SAMMC) algorithm for all dynamic processes (i.e., deposition, condensation/evaporation, breakage, nucleation, and coagulation) in the dispersed system. Overall, the initial numerical particles are generated at the time of initialization, and the total dynamic process rates are calculated before sorting numerical particles. The inter-event time of quiescence (i.e., time step), the dynamic process and the selected numerical particle(s) are determined by the jump Markov process, which is constructed based on the rates of all aerosol dynamic processes involved. If the merging is required to deal with a new numerical particle generated in a dynamic process, an existing neighbour numerical particle pair should be found to merge for accommodating the new numerical particle. Before advancing the time step, the total dynamic process rates are updated for the next dynamic process according to the change in volumes or weights of numerical particles involved in the current dynamic process. The details of each step are described as follows.

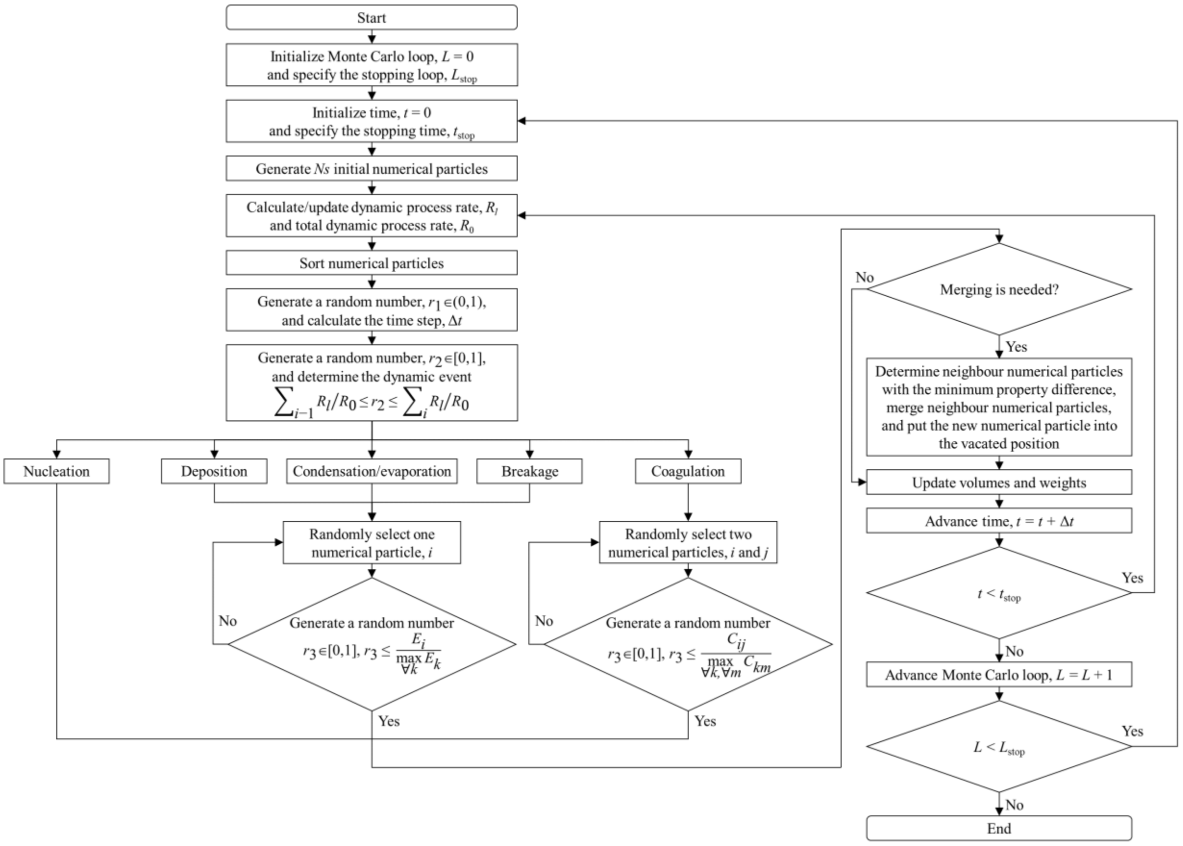

Figure 5.1 Flowchart of the event-driven SAMMC method [38].

5.2.2 Calculation of the dynamic event rates

Table 5.1 lists the rates of all dynamic processes taking place in the dispersed system in terms of equal- and different-weight schemes. As deposition, condensation/evaporation and breakage processes involve only one existing numerical particle, the formulations of the corresponding rates are the same in both equal- and different-weight schemes. However, the rates of nucleation and coagulation are different in these two types of weight schemes. Nucleation is associated with a newly generated numerical particle, irrespective of any existing numerical particles. The nucleation rates of a real particle in both equal- and different-weight schemes are the same, but the nucleation rates of a numerical particle which would be added to the computational domain are slightly different in these two types of weight schemes. In the equal-weight scheme, the weights of all numerical particles are always the same, which requires the weight of the newly nucleated numerical particle to be equal to the weights of other existing numerical particles. Specifically, the weights of all numerical particles are guaranteed to be the same after a nucleation process in the equal-weight scheme, where the weight refers to the number of real particles. It can be achieved by dividing the nucleation rate of a numerical particle by "w" where "w" is the weight of other numerical particles in the computational domain before each nucleation process. But it is not required that all the weights of numerical particles are equal in the different-weight scheme. Therefore, each nucleation process of one real particle is tracked and each nucleated real particle is represented by a numerical particle with a certain weight. By comparison, the calculation of coagulation rate is totally different from those of other dynamic processes due to its always involvement of two existing numerical particles.

Table 5.1 The rates of different dynamic processes for equal- and different-weight schemes [38].

Dynamic process	R_l (s^{-1})	Equal-weight scheme	Different-weight scheme
Deposition	D_0	$\sum_{i=1}^{N_s} D_i$	$\sum_{i=1}^{N_s} D_i$
Condensation/evaporation	K_0	$C_s \sum_{i=1}^{N_s} K_{s,i}$	$C_s \sum_{i=1}^{N_s} K_{s,i}$
Breakage	B_0	$\sum_{i=1}^{N_s} B_i$	$\sum_{i=1}^{N_s} B_i$
Nucleation	J_0	$\frac{V_s^2 J(v)\delta(v_{\min}, v)}{w}$	$V_s^2 J(v)\delta(v_{\min}, v)$
Coagulation	C_0	$\sum_{i=1}^{N_s-1}\sum_{j=i+1}^{N_s} \frac{\beta_{ij}}{V_s} w$	$\sum_{i=1}^{N_s-1}\sum_{j=i+1}^{N_s} \frac{\max(w_i, w_j)}{\alpha_{ij}} \frac{\beta_{ij}}{V_s}$

In the present study, the coagulation rate is derived based on the different-weight scheme. For a different-weight-based MC method, each numerical particle is considered to represent a group of real particles, so the weight of numerical particles is defined as $w = N_R/N_S$, where N_R and N_S are the numbers of real and numerical particles, respectively [178]. The weights of all numerical particles are set to the same value at the time of initialization.

A numerical particle, *i* is used to represent a group of real particles with number w_i and volume v_i, and a numerical particle, *j* is used to represent a group of real particles with number w_j and volume v_j. Thus, the real particle number concentrations of these groups are w_i/V_S and w_j/V_S, respectively, where V_S is the volume of the computational domain. The number of coagulation processes among real particles of these two numerical particles groups per unit time and volume is then expressed by:

$$\Phi_{ij} = \beta_{ij} \times \frac{w_i}{V_S} \times \frac{w_j}{V_S} \tag{5-2}$$

where Φ_{ij} is the coagulation rate of two real particles from *i*th and *j*th groups at both randomly chosen basis, respectively, and β_{ij} is the coagulation kernel of particles *i* and *j*.

If the probabilistic coagulation rule [32] is adopted, it means that not all real particles from the *i*th and *j*th groups would participate in a coagulation process [32]. Jiang and Chan [33] introduced a fraction function, $\alpha_{ij} \in (0,1]$ to characterize coagulation that occurs among all or partial real particles between the *i*th and *j*th groups. Thus, the mean coagulation number between real particles from the *i*th and *j*th groups is expressed by:

$$\Omega = \alpha_{ij} \min\left(w_i, w_j\right) \tag{5-3}$$

When the fraction function, $\alpha_{ij} = 1$, all real particles from the *i*th or *j*th group would participate in a coagulation process, which is called homogeneous coagulation in the present study; otherwise, the partial real particles from the *i*th group and partial real particles from the *j*th group would coagulate, and this is called non-homogeneous coagulation in the present study. One of the most widely used fraction functions is the hyperbolic fraction function [33,35,49] which is defined as:

$$\alpha_{ij} = \frac{1}{1 + \min\left(w_i, w_j\right) / \max\left(w_i, w_j\right)} \tag{5-4}$$

The coagulation rate, C_{ij} of numerical particle, *i* and numerical particle, *j*, is then calculated by:

$$C_{ij} = \frac{V_S \Phi_{ij}}{\Omega} = \frac{\max\left(w_i, w_j\right)}{\alpha_{ij}} \frac{\beta_{ij}}{V_S} \tag{5-5}$$

Therefore, the total coagulation rate, C_0 is expressed as:

$$C_0=\sum_{i=1}^{N_s-1}\sum_{j=i+1}^{N_s}\frac{\max\left(w_i,w_j\right)}{\alpha_{ij}}\frac{\beta_{ij}}{V_s} \tag{5-6}$$

It should be noted that when the weights of all numerical particles are equal (i.e., $w_i = w_j = w$) for homogeneous coagulation (i.e., $\alpha_{ij} = 1$), the Equation (5-6) is completely consistent with that in the equal-weight scheme. It demonstrates that the equal-weight scheme is only a special case of the different-weight scheme.

5.2.3 Determination of the time step

As the occurrence of a dynamic process in the dispersed system is regarded as a standard Markov process, the quiescent time interval between two successive dynamic processes is an exponentially distributed random variable [215]. The time step is calculated [167] as:

$$\Delta t=\frac{\ln(1/r_1)}{\sum_i R_i} \tag{5-7}$$

where $\sum_i R_i$ is the sum of the rates of all related dynamic processes that take place in the computational domain, and r_1 is a uniformly distributed random number from zero and one.

5.2.4 Determination of the dynamic process

For a dispersed system with only one single dynamic process, l, the dynamic process always happens after every waiting time. But if more dynamic processes take place in the dispersed system, the probability of a related dynamic process, l is obtained [37,156,167] by:

$$P_l=\frac{R_l}{\sum_i R_i} \tag{5-8}$$

where l represents a dynamic process (i.e., deposition, condensation/evaporation, breakage, nucleation or coagulation). The probabilities of all these dynamic processes in the dispersed system are P_D, P_K, P_B, P_J and P_C, respectively, which are used to determine the dynamic process by using a stochastic process as shown in Figure 5.2. A random number, r_2 is generated from the uniform distribution between zero and one. If $0 \le r_2 \le P_D$, the dynamic process is determined as deposition; if $P_D < r_2 \le P_D+P_K$, the dynamic process is condensation/evaporation; if $P_D+P_K < r_2 \le P_D+P_K+P_B$, breakage is chosen; if $P_D+P_K+P_B < r_2 \le P_D+P_K+P_B+P_J$, nucleation is selected as the dynamic process; if $P_D+P_K+P_B+P_J < r_2 \le P_D+P_K+P_B+P_J+P_C = 1$, coagulation occurs.

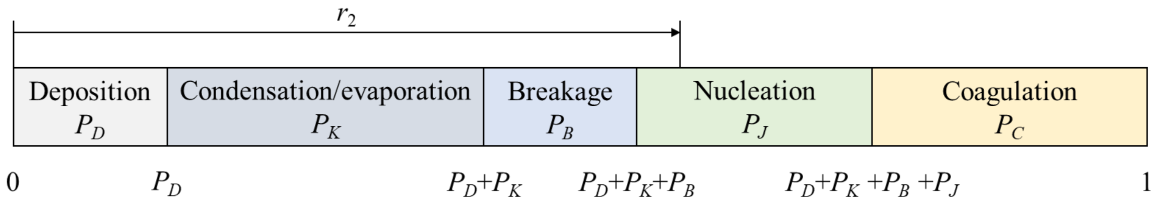

Figure 5.2 Determination of the dynamic process by a stochastic process [38].

5.2.5 Determination of the selected numerical particle(s)

If nucleation is determined as the dynamic process, there is no need to select the existing numerical particle because a nucleation process itself is independent of any existing numerical particles. Otherwise, the numerical particle(s) existing in the array for this process should be selected once the dynamic process is determined. Two commonly used methods for determining the numerical particle(s) existing in the computational domain are the acceptance-rejection method [153] and the inverse method (i.e., cumulative probability method) [154]. It should be noted that it is very computational time-consuming to calculate the rates of all dynamic events in the cumulative probability method, especially when the numerical particle array is large [17]. Hence, the acceptance-rejection method is employed in the present study.

For a dynamic process associated with only one single numerical particle (i.e., deposition, condensation/evaporation or breakage), a numerical particle, *i* is randomly selected and then accepted if the following inequality is satisfied [168]:

$$r_3 \leq \frac{E_i}{\max\limits_{\forall k} E_k} \tag{5-9}$$

where r_3 is a random number from the uniform distribution in the unit interval and E_i is the rate of a dynamic process (i.e., deposition, condensation/evaporation or breakage) accordingly. Otherwise, *i* is rejected and the acceptance-rejection procedure is repeated until a new, randomly selected numerical particle is accepted. By comparison, two randomly selected numerical particles, *i* and *j* are accepted as a coagulation pair if the following condition is satisfied [35,153,208] as:

$$r_3 \leq \frac{C_{ij}}{\max\limits_{\forall k,\forall m} C_{km}} \tag{5-10}$$

If the numerical particle pair is rejected, another two numerical particles are randomly chosen until the Equation (5-10) is satisfied according to the acceptance-rejection method. It should be noted that the Markov process can still be implemented exactly in the acceptance-rejection method, even though the maximum rate of the dynamic event in Equations (5-9) and (5-10) is overestimated [34,35,153,156].

5.2.6 Neighbour merging method

For a MC method for dynamic processes in the dispersed system, it is vital to keep both the volume of the computational domain and number of numerical particles constant. Increasing the number of numerical particles leads to a reduction in the computational efficiency, while decreasing the number of numerical particles deteriorates the statistical precision [156]. In addition, any change (i.e., expansion or contraction) in the volume of the computational domain results in a poor applicability of the MC methods. Therefore, additional numerical particles generated by nucleation, breakage or non-homogeneous coagulation should be properly treated to ensure that the volume of the computational domain and number of numerical particles are kept constant.

For dynamic aerosol processes in which an additional numerical particle is generated, the main idea is to merge two existing numerical particles into one and then put the additional numerical particle into the vacated position of the numerical particle array, so that the total number of numerical particles is kept unchanged.

It should be noted that these two numerical particles should be properly selected to avoid introducing a large statistical noise. Hence, it means that the sizes of these two selected numerical particles should be close or equal to each other, so the statistical noise can significantly be reduced. Specifically, finding two existing numerical particles with the same or similar volume in the numerical particle array can minimize the stochastic error of the merging method. But it is very computational time-consuming and is unwise to compare the volumes of a large number of numerical particles one-by-one. But when the sequence of numerical particles is already sorted in the array based on their volumes and weights, any two neighbour numerical particles always have similar or even the same properties. When the property difference between two neighbour numerical particles is found to be the minimal, the stochastic error introduced by merging these two neighbour numerical particles would also be the minimal. It should be noted that this method is called the neighbour merging method in the present study. Thus, the minimal property difference of two neighbour numerical particles should be determined before the merging operation is implemented. In the present study, the absolute volume difference (AVD) and relative volume difference (RVD) are defined as:

$$\varepsilon_i = v_{i+1} - v_i \tag{5-11}$$

$$\varepsilon_i = \frac{v_{i+1} - v_i}{v_i} \tag{5-12}$$

where i is the index of a numerical particle in the array, $i \in [1, N_S - 1]$. It should be noted that only one numerical particle, i needs to be determined in the proposed neighbour merging method, because the other numerical particle is the neighbour of i and is selected automatically (i.e., i+1) due to the introduction of sorting algorithm. Thus, finding two numerical particles is then transformed to search the only one numerical particle, i, which is called the target numerical particle in the present study. Therefore, a numerical particle pair for merging operation is determined as i and i+1, if the volume difference, ε_i in Equation (5-11) or (5-12) is the minimal in the array of numerical particle. From this point of view, sorting algorithm introduced in the MC method not only helps to improve the computational efficiency of finding a numerical particle pair but also to minimize the numerical error originating from the merging operation and increase the computational precision.

The most straightforward method for determining the target numerical particle is the traversing method, where the neighbour numerical particles with the minimal volume difference is obtained by comparing the volume differences of all neighbour numerical particle pairs from the beginning to the end. The number of comparisons in the neighbour numerical particles is equal to $N_S - 1$. When there are several numerical particle pairs whose volume differences are the same, the numerical particle with the lowest weight would be selected as the target numerical particle, which can minimize the alteration of the PSD. It implies that not only the volume differences in the array of numerical particles but also the weights of the numerical particles should also be compared. After comparing the volume differences, re-comparing the weights of those potential target numerical particles is not desirable, as it is very computational time-consuming. Therefore, a comparison class including properties (i.e., volume difference and weight) is defined, and then an object as an instance of this comparison class is created based on each numerical particle. Specifically, if the volume differences of two objects are not the same, the object with lower volume difference is selected; otherwise, the object with lower weight would be chosen. This is described by the property difference in terms of volume difference and weight in the present study. Therefore, only one traversing is needed to obtain the target numerical particle and the time complexity is still O(N_S). It should be noted that this traversing method has very high computational efficiency when one numerical particle pair should be merged for only one newly generated additional numerical particle.

However, the traversing method might not be appropriate anymore when more additional numerical particles are generated by a dynamic process. For example, if the target numerical particles with number k (i.e., $k > 1$) are needed to add into the computational domain, k pairs of neighbour numerical particles in the array should be merged to vacate k positions. This leads to k times of searching the numerical particle array if the traversing method is used, which is very computational time-consuming especially when k and N_S are large. Thus, two methods based on the complete binary tree data structure [216,217] are introduced to determine k target numerical particle pairs with their property differences lower than those of other numerical particles in the array. One is to create a max heap with k nodes, where the value of the root node is greater than or equal to either of its child nodes. Each node stores the property difference (i.e., volume difference and particle weight) of a neighbour numerical particle pair. If the property difference of the root node is larger than that of the numerical particle in the array, the root node is removed and the numerical particle is inserted to recreate a max heap; otherwise, the next numerical particle in the array is traversed. Finally, the k target numerical particle pairs with the minimal property differences are stored at the k nodes of the max heap. This is called the max-heap method. It should be noted that this max-heap method is highly efficient when the number of numerical particles is very large and the time complexity of this method is O($N_S\log k$). The other one is called min-heap method, in which a min heap with N_S-1 nodes is firstly created and the value of each node is equal to or greater than that of its parent node. The k target numerical particles with the minimal property differences are obtained by removing the root node to store, and creating a min heap for k times, leading to a time complexity of only O($k\log N_S$).

Figure 5.3 shows the neighbour merging method based on the sorted numerical particle array. If only one additional numerical particle (i.e., $k = 1$) is generated by a dynamic process which needs to be added to the computational domain, the first step is to determine the target numerical particle, i with the minimal property difference by using the traversing method, and then the target numerical particle, i is merged with numerical particle, i+1. The merging of i and i+1 follows volume/mass conservation, so the merged numerical particle with weight

(w_i+w_{i+1}) and volume $(v_iw_i+v_{i+1}w_{i+1})/(w_i+w_{i+1})$ replaces in place the original $i+1$. Finally, the position vacated by i is filled by the newly generated additional numerical particle with weight w_{new} and volume v_{new}. But if $k \neq 1$, k target numerical particles with the minimal property differences can be obtained by the min-heap method. As the numbers of numerical particles and target numerical particle pairs are small in the present study, the min-heap method is more computationally efficient than the max-heap method. k repetition times are needed to merge each numerical particle pair and to place the merged and additional numerical particles. It should be noted that all chosen k target numerical particles are not neighbour particles in the sorted numerical particle array.

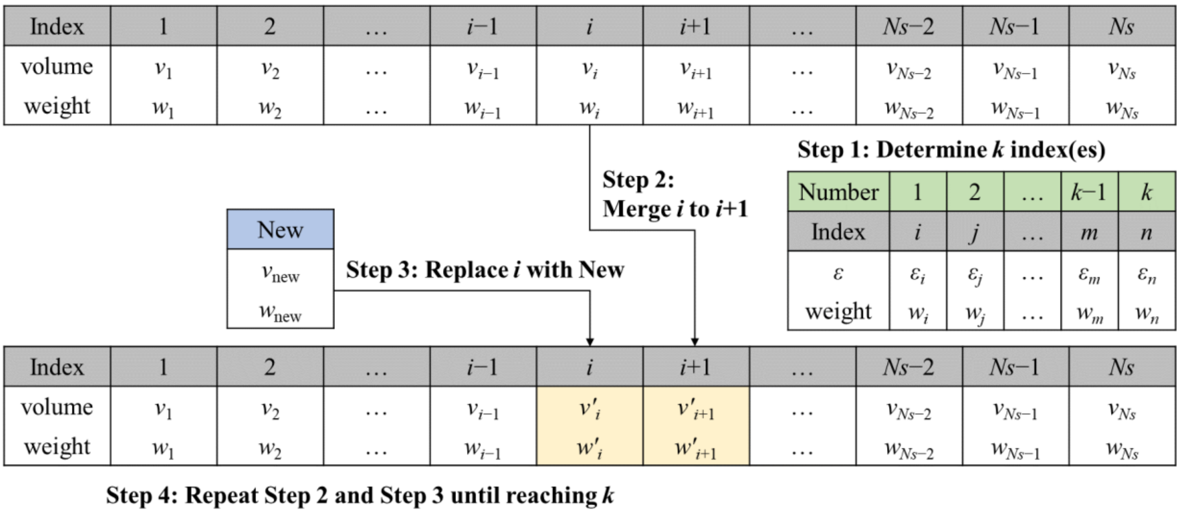

Figure 5.3 Neighbour merging method based on sorted numerical particle array [38].

5.2.7 Selecting the sorting algorithm

A sorted array of numerical particles can significantly improve the computational precision and efficiency of the newly proposed SAMMC method because merging two neighbour numerical particles in an already sorted numerical particle array can greatly reduce the stochastic error and a numerical particle pair can be easily and rapidly determined by only finding one target numerical particle. Thus, it is of great importance to select the most efficient sorting algorithm.

Numerical particles are sorted according to their volumes and weights in the present study, where volumes and weights are the properties of numerical particles. As quicksort is a highly efficient sorting algorithm for dealing with a completely unsorted array [209], it is used to sort the array of numerical particles which are initially generated with polydisperse PSD. But if the numerical particle array is generated with an initial monodispersed PSD, there is no need to sort the numerical particles. After a dynamic process takes place in the computational domain of a dispersed system, the volumes or weights of the related numerical particles possibly may be changed. Actually, a few numerical particles are only involved in the dynamic process in each time step, making the properties of most numerical particles unchanged. It demonstrates that the array of numerical particles is nearly sorted and only a few numerical particles need to be sorted after a dynamic process. Under this circumstance, the insertion sort has the highest computational efficiency for a completely or nearly sorted array among all sorting algorithms [209] which is then adopted to sort the array of numerical particles.

5.2.8 Treating the dynamic process

As the volumes or weights of several numerical particles are changed after a dynamic process occurring in a dispersed system, properly treating the volumes and weights of all related numerical particles is required to maintain constant for the volume of the computational domain and the number of numerical particles. It should be noted that not all dynamic processes lead to a change in the number of numerical particles.

Deposition refers to the removal of numerical particles out of the computational domain, resulting in the constant decrease of the number of numerical particles. Numerical particle, i is not tracked anymore if being selected to conduct deposition, resulting in the reduction in the number of numerical particles. As the position vacated by i should be filled and the number of numerical particles should be maintained unchanged, a numerical particle, j with volume v_j and the highest weight w_j among all other numerical particles is selected and grouped into two equal parts. One part with volume v_j and weight $w_j/2$ replaces in place the original j, and the other one with volume v_j and weight $w_j/2$ is put into the vacancy of the original i, therefore always keeping a constant-volume and constant-number scheme.

Condensation/evaporation does not change the number of numerical particles but increases/decreases the volume/mass of numerical particles accordingly. If a numerical particle, i with volume v_i and weight w_i experiences a condensation process, the weight of i remains w_i and the volume of i becomes (v_i+v_s) after the process, where v_s is the volume of the condensing monomer.

A breakage process of a parent numerical particle, *i* with volume v_i and weight w_i leads to generating child numerical particles with number $b(v_i,t)$, and the volumes of child numerical particles are determined by the probability of obtaining a child numerical particle with volume v, $\gamma(v_i,v,t)$. It implies that there are child numerical particles with number $b(v_i,t)-1$ required to be added to the numerical particle array, as the parent numerical particle, *i* can be replaced by one of the child numerical particles. If a breakage process leads to the generation of two child numerical particles (i.e., $b(v_i,t) = 2$), one child numerical particle directly replaces the parent numerical particle and the other one is placed on the position vacated by the merging operation of two neighbour numerical particles with the minimal property difference, which is found and determined by the traversing method. But if more child numerical particles are generated by a breakage process, $(b(v_i,t)-1)$ pairs of numerical particles are found by the min-heap method and merged to vacate the positions for the child numerical particles to be filled in. It should be noted that the weights of all child numerical particles are equal to that of the parent numerical particle (i.e., w_i).

There is a new numerical particle, *i* with volume v_i and weight w_i generated in the computational domain when a nucleation process takes place, which results in the increase in the number of numerical particles. The traversing method is used to determine two neighbour numerical particles with the minimal property difference, and the vacancy obtained by the neighbour merging method is filled by the newly nucleated numerical particle, *i* with volume v_i and weight w_i, where v_i is equal to the volume of a nucleus or precursor, $v_{\min}$.

Both homogeneous and non-homogeneous coagulation are considered in the present study. If a coagulation process occurs between two numerical particles, the volumes and weights of this numerical particle pair possibly change, which demonstrates the coagulation of real particles. For a homogeneous coagulation process as shown in Figure 5.4, the fraction function in Equation (5-3) $\alpha_{ij} = 1$, and the consequence of this coagulation process is formulated [32] as:

$$\text{if } w_i = w_j, \begin{cases} w_i' = w_i/2, v_i' = v_i + v_j \\ w_j' = w_j/2, v_j' = v_i + v_j \end{cases} \tag{5-13}$$

$$\text{if } w_i \neq w_j, \begin{cases} w_i' = \max(w_i, w_j) - \min(w_i, w_j), v_i' = v_m|_{w_m=\max(w_i,w_j)} \\ w_j' = \min(w_i, w_j), v_j' = v_i + v_j \end{cases} \tag{5-14}$$

where v_i and w_i are the volume and weight of numerical particle, *i*, and v_j and w_j are the volume and weight of numerical particle, *j*, respectively. But when numerical particles, *i* and *j* undergo non-homogeneous coagulation (i.e., $\alpha_{ij} \neq 1$), it leads to the generation of an additional numerical particle and then a completely different consequence after a coagulation process is taken place as shown in Figure 5.5. Only these two coagulated numerical particles are needed when their volumes are equal to each other, as shown in Figure 5.5(a). The consequence is then treated [35] as:

$$\text{if } v_i = v_j, \begin{cases} w_i' = w_i + w_j - 2\alpha_{ij}\min\left(w_i, w_j\right), \; v_i' = v_m\big|_{w_m = \max\left(w_i, w_j\right)} \\ w_j' = \alpha_{ij}\min\left(w_i, w_j\right), \; v_j' = v_i + v_j \end{cases} \tag{5-15}$$

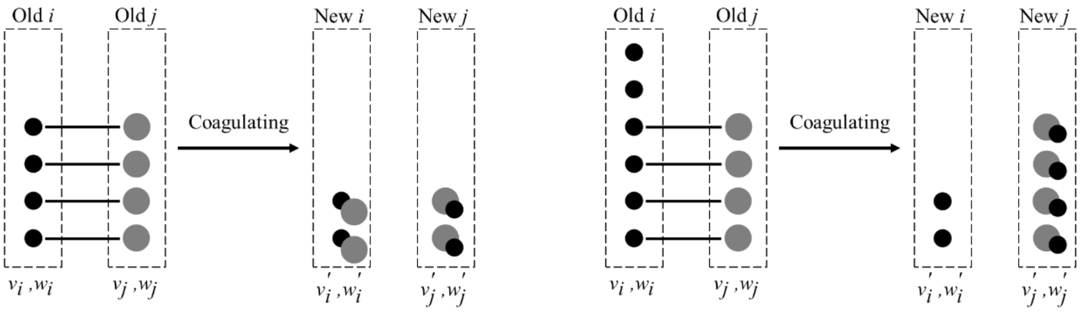

(a) $w_i = w_j$ (b) $w_i \neq w_j$

Figure 5.4 Homogeneous coagulation between two weighted numerical particles [38].

However, when the volumes of both numerical particles are not the same in a non-homogeneous coagulation process, two neighbour numerical particles, k and k+1 with the minimum property difference are determined by the traversing method and are then merged to one numerical particle based on volume/mass conservation, which would be placed on the position of k+1. Finally, the additional numerical particle replaces k in the numerical particle array as shown in Figure 5.5(b). Thus, the consequence of a non-homogeneous coagulation is denoted as:

$$\text{if } v_i \neq v_j, \begin{cases} w_i' = w_i - \alpha_{ij}\min\left(w_i, w_j\right), \; v_i' = v_i \\ w_j' = w_j - \alpha_{ij}\min\left(w_i, w_j\right), \; v_j' = v_j \\ w_k' = \alpha_{ij}\min\left(w_i, w_j\right), \; v_k' = v_i + v_j \\ w_{k+1}' = w_k + w_{k+1}, \; v_{k+1}' = \left(v_k w_k + v_{k+1} w_{k+1}\right) / \left(w_k + w_{k+1}\right) \end{cases} \tag{5-16}$$

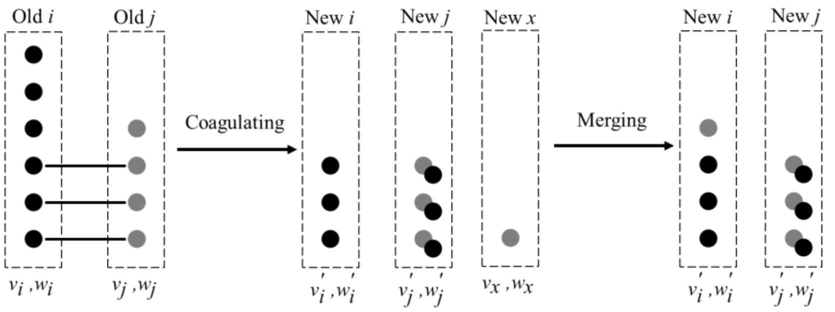

(a) $v_i = v_j$

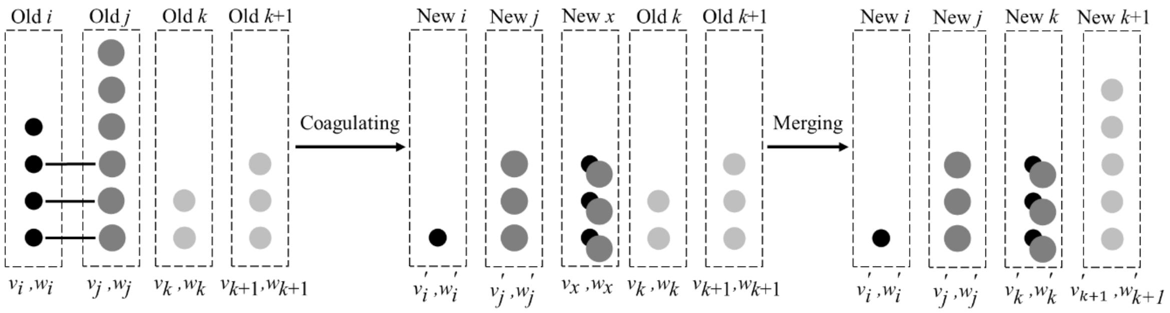

(b) $v_i \neq v_j$

Figure 5.5 Non-homogeneous coagulation between two weighted numerical particles and merging [38].

It should be noted that Wang and Chan [35] have innovatively introduced the sorting algorithm into the MC method and have recently developed a new sorting algorithm-based merging weighted fraction Monte Carlo (SAMWFMC) method for coagulation. As a result, very low stochastic errors in each moment of the PSD with arbitrary fraction functions are shown, which is mostly attributed to the merging method. As one of the neighbour numerical particles is merged with the uncoagulated numerical particle with the lowest weight, the merging error introduced is the minimal after a coagulation process. As the main idea in the present study is to merge two existing numerical particles, the newly proposed neighbour merging method is totally different from that in the SAMWFMC method [35], where only one existing numerical particle are used to conduct merging with the additional generated numerical particle. Therefore, the treatment of a dynamic process in the SAMMC and SAMWFMC methods are completely different.

After a dynamic process, the rates of different dynamic events listed in Table 5.1 should be recalculated as the volumes or weights of relevant numerical particles may be changed. As the number of numerical particles involved in a dynamic process is only a few and those without undergoing a dynamic process do not need to change the rates of dynamic processes, the smart bookkeeping technique [17] is highly efficient to update the rates of dynamic processes and to obtain their maximum rates. Especially for coagulation which always involves two numerical particles, the calculation of the total coagulation rate by double loops only takes place once at the beginning of the numerical simulation, but it is not required to double traverse and count on every numerical particle anymore.

When the volumes and weights of a numerical particle pair (i.e., i and j) after coagulation are calculated by Equations (5-13) to (5-15), the total coagulation rate, C_0 is updated by Equation (5-17). If two neighbour numerical particles (i.e., k and k+1) are needed to merge for the coagulation of i and j, the volumes and weights of i, j, k and k+1 after coagulation are obtained by Equation (5-16), while Equation (5-18) is used to update the total coagulation rate. Thus, only one single loop is needed to update the total coagulation rate, and there is no further double counting during the numerical simulation. It should be noted that even though the coagulation kernel (i.e., β_{ij}) or fraction function (i.e., α_{ij}) is a function of the volumes or weights of the numerical particle pair in a physical case, which results in a varying coagulation rate, Equation (5-17) or (5-18) can still be used to calculate the total coagulation rate because those uncoagulated numerical particles remain unchanged.

$$\begin{aligned} C_0^{\text{new}} = C_0^{\text{old}} &- \left(\sum_{m=1,\, m\neq i,\, m\neq j}^{N_s} C_{im}^{\text{old}} + \sum_{m=1,\, m\neq i,\, m\neq j}^{N_s} C_{jm}^{\text{old}} + C_{ij}^{\text{old}} \right) \\ &+ \left(\sum_{m=1,\, m\neq i,\, m\neq j}^{N_s} C_{im}^{\text{new}} + \sum_{m=1,\, m\neq i,\, m\neq j}^{N_s} C_{jm}^{\text{new}} + C_{ij}^{\text{new}} \right) \end{aligned} \tag{5-17}$$

$$\begin{aligned} C_0^{\text{new}} = C_0^{\text{old}} &- \left(\sum_{m=1,\, m\neq i,\, m\neq j,\, m\neq k,\, m\neq k+1}^{N_s} C_{im}^{\text{old}} + \sum_{m=1,\, m\neq i,\, m\neq j,\, m\neq k,\, m\neq k+1}^{N_s} C_{jm}^{\text{old}} \right) \\ &+ \left(\sum_{m=1,\, m\neq i,\, m\neq j,\, m\neq k,\, m\neq k+1}^{N_s} C_{im}^{\text{new}} + \sum_{m=1,\, m\neq i,\, m\neq j,\, m\neq k,\, m\neq k+1}^{N_s} C_{jm}^{\text{new}} \right) \\ &- \left(C_{ij}^{\text{old}} + C_{ik}^{\text{old}} + C_{i(k+1)}^{\text{old}} + C_{jk}^{\text{old}} + C_{j(k+1)}^{\text{old}} + C_{k(k+1)}^{\text{old}} \right) \\ &+ \left(C_{ij}^{\text{new}} + C_{ik}^{\text{new}} + C_{i(k+1)}^{\text{new}} + C_{jk}^{\text{new}} + C_{j(k+1)}^{\text{new}} + C_{k(k+1)}^{\text{new}} \right) \end{aligned} \tag{5-18}$$

5.2.9 Choice of efficient implementation

As each numerical particle has properties including identification number (ID), weight and volume, it well matches the object-oriented programming (OOP) language, where each numerical particle is regarded as an instance object of a class. An OOP language (i.e., C++) is used to define a particle class including properties (i.e., ID, weight and volume) and to create each numerical particle object. It should be noted that the data structure of an array rather than a linked list is used in the present study. Numerical particles are then placed in contiguous computer memory locations by using the data structure of an array, which supports random access by using its index. Even though the array of numerical particles is large, it is still highly accurate and computationally efficient to access each numerical particle when compared with a linked list. In addition, an array shows greater advantage of computational efficiency than a linked list if there is no adding or removing operation of numerical particles and the number of numerical particles in the array always remains unchanged. Thus, all numerical particles in the array are readily available for access.

5.3 Results and Discussion

Aerosols with equal sizes, called monodisperse aerosols, can be carefully produced by taking special measures in the laboratory setting [9]. By comparison, particles of different sizes are more common in the atmosphere due to several different mechanisms. Those with a wide range of particle sizes form the polydisperse aerosols. An example of initial polydisperse PSD is the exponential distribution function [172], which is defined as:

$$n(v,0) = \frac{N_0}{v_0}\exp\left(-\frac{v}{v_0}\right) \tag{5-19}$$

where N_0 and v_0 are the initial total particle number concentration and mean particle volume, respectively. The kth-order moment of the PSD function is defined [9] as:

$$M_k = \int_0^\infty v^k n(v)\mathrm{d}v \tag{5-20}$$

Different order moments represent different physical interpretations. The first two moments, M_0 and M_1 are the total particle number concentration and the total particle volume (mass) concentration, respectively. MC methods normally show stochastic errors related to the random sampling process and statistics, but the stochastic errors can be determined by randomly repeating enough numerical simulations. The mean standard deviation of M_k is used to quantify the corresponding stochastic error [32,34,35,214] as:

$$\sigma_{M_k}(t) = \frac{1}{Q}\sum_{i=1}^{Q}\sqrt{\frac{1}{t}\int_0^t \left[\frac{M_k^{MC(i)}(t) - M_k^{AS}(t)}{M_k^{AS}(t)}\right]^2 dt} \tag{5-21}$$

where superscripts “AS” and “MC(i)” represent the analytical solution and numerical results of the i-th MC simulation, respectively. Q is the repetitions of the MC simulation.

The MC repetitions in the present study are 200 which is enough to obtain stable mean standard deviations. The volume of the computational domain $V_S = 1$ m^3. The initial number of numerical particles $N_S = 2000$, which has proved to be able to provide high accuracy numerical results [17,32,33,35,152,156,161,176,177]. The initial particle volume for initial monodispersed PSD and the initial mean particle volume for initial exponential PSD are unity (dimensionless) (i.e., $v_0 = 1$). The computational accuracy and efficiency of the newly developed SAMMC method are assessed by comparing with the stepwise constant-volume method [36], mass- and number-based constant-number methods [37] and multi-Monte Carlo (MMC) method [156] as well as the corresponding analytical solutions. The computational environment used is dual Intel Xeon processor E5-2630 v3 16 cores 2.4GHz CPU and 64GB RAM. As absolute volume difference (AVD) and relative volume difference (RVD) are used as the crucial merging criteria, the effects of AVD and RVD on the computational accuracy and efficiency are also fully assessed. It should be noted that the volumes of the computational domain remain unchanged in three equal-weight-based MC methods (i.e., the stepwise constant-volume method and mass- and number-based constant-number methods) in the present study, but the weights of numerical particles are doubled/halved in the stepwise constant-volume method while the weights of numerical particles in both mass- and number-based constant-number methods are adjusted at each time step according to the conserved property. In addition, as SAMMC method can be used to deal with non-homogeneous coagulation, the resulting computational accuracy and efficiency are compared with the numerical results of the weighted fraction Monte Carlo (WFMC) method [33], sorting algorithm-based merging weighted fraction Monte Carlo (SAMWFMC) method [35] and the corresponding analytical solutions, because WFMC and SAMWFMC methods are specifically developed for non-homogeneous coagulation. It should be noted that the mass- and number-based constant-number methods are referred to simply as “constant-number (mass)” and “constant-number (number)” respectively, and the SAMMC method with different merging criteria (i.e., AVD and RVD) are denoted as “AVD-based SAMMC” method and “RVD-based SAMMC” method, respectively in the present study.

5.3.1 Pure nucleation

For nucleation, new particles are considered to be formed by a first-order irreversible chemical reaction [218], irrespective of any other particle growth mechanism. Specifically, nucleation refers to the transformation of precursors into nuclei via chemical reactions, and the conversion rate (i.e., chemical reaction rate) is proportional to the precursor number concentration, which is expressed [218] by:

$$V_S J(t)\delta(v_{\mathrm{min}},v) = -\frac{\mathrm{d}C_{\mathrm{pre}}(t)}{\mathrm{d}t} = K_N C_{\mathrm{pre}}(t) \tag{5-22}$$

where V_S is the volume of the computational domain, K_N is the chemical reaction rate constant and $C_{\mathrm{pre}}(t)$ is the precursor number concentration at time t. The analytical solution of nucleation by first order chemical reaction is provided in [157]. In Case 1, $K_N = 5.0\times10^{-6}$ s^{-1}, $C_{\mathrm{pre}}(0) = 10^5$ m^{-3}. The initial nuclei number concentration, N_0 = 3000 m^{-3} with initial precursor and nuclei volumes, $v_{\mathrm{pre}} = v_0 = 1$ (dimensionless) [157]. The characteristic nucleation time is defined as $\tau_N = 1/K_N$. When the PSD remains monodispersed, the difference between the particle number concentration and particle volume/mass concentration is a multiplicative constant. As the volumes of the precursor and nuclei are assumed to be 1, the values of the particle number and particle volume/mass concentrations along with time are always the same. Therefore, only numerical results in terms of the particle number concentration are shown.

Figure 5.6 shows the time evolutions of total particle number concentrations, M_0 and mean standard deviations, σ_{M_0} obtained from six MC methods for nucleation when compared with the corresponding analytical solution. Numerical results of M_0 obtained from all MC methods grow over time because of the continuous increase in the number of new real particles in every nucleation process, but the growth rate of M_0 gradually reduces along with time because of the gradual reduction in the precursor number concentration. As M_0 for all MC methods agree excellently with the analytical solution, all these MC methods can be used to deal with nucleation process in aerosol dynamics.

But the differences of σ_{M_0} among these MC methods indicate different levels of computational accuracy. As the volumes of all numerical particles are always 1 during the numerical simulation, the mass-based constant-number method functions as the same as the number-based constant-number method, which leads to almost the same stochastic error in M_0. The stepwise constant-volume method has lower stochastic error in M_0 than both mass- and number-based constant-number methods, which is attributed to two reasons. On one hand, the number of numerical particles in mass- and number-based constant-number methods is always N_S, while the numerical particle number is between N_S and $2N_S$ during the numerical simulation in the stepwise constant-volume method. As the number of numerical particles used in the mass- and number-based constant-number methods is always fewer than that used in the stepwise constant-volume method, the computational accuracy of the former methods is accordingly lower than that of the latter method. The main reason is that the computational accuracy is inversely proportional to the square root of the number of numerical particles [154], which implies that the greater number of numerical particles in the stepwise constant-volume method would lead to higher computational accuracy and lower stochastic error. On the other hand, the frequency of the sample restoration has a negative effect on the computational accuracy. More specifically, less sample restoration means less disturbance to the statistical ensemble [156], therefore achieving higher statistical precision. The number of numerical particles in the array would only be adjusted when reaching $2N_S$ in the stepwise constant-volume method where a half of numerical particles are randomly chosen and are removed out of the computational domain. By comparison, both mass- and number-based constant-number methods restore the number of numerical particles in every time step by removing a randomly chosen numerical particle from the array and accordingly adjusting the weights of each numerical particle. Obviously, the stepwise constant-volume method has a far smaller number of sample restorations than both mass- and number-based constant-number methods, therefore having lower stochastic error in M_0 than both mass- and number-based constant-number methods.

It can be also found that different-weight-based MC methods (i.e., MMC, AVD- and RVD-based SAMMC methods) have far lower stochastic errors than equal-weight-based methods (i.e., stepwise constant-volume, mass- and number-based constant-number methods). The σ_{M_0} of all the different-weight-based MC methods are less than 0.013%, much lower than those of three respective equal-weight-based MC methods (i.e., 1.17%, 1.42% and 1.43%) as shown in Figure 5.6. It implies that different-weight-based MC methods have much higher computational accuracy than equal-weight-based MC methods. The reason is that each real particle generated by a nucleation process for the different-weight-based MC methods is represented while the equal-weight-based MC methods track a nucleation process with several real particles generated in the computational domain, leading to more accurate statistical properties of the different-weight-based MC methods than those of the equal-weight-based MC methods. As a result, the time steps of the different-weight-based MC methods are always smaller than those of the equal-weight-based MC methods.

The difference of the time step between equal-weight-based and different-weight-based MC methods also leads to the different levels of computational time-consumption. Smaller time step normally requires longer computational time, so the different-weight-based MC methods have higher computational cost than their counterparts as shown in Table 5.2 for Case 1. The essential reason is the larger nucleation rate of the different-weight-based MC methods as shown in Table 5.1. It implies that it is possible to reduce the computational time of different-weight-based MC methods by decreasing the nucleation rate to increase the time step, which can be achieved by tracking each nucleation process with more generated real particles (instead of only one real particle). Accordingly, the weight of each generated numerical particle becomes larger, but this may increase the stochastic error in the statistical properties. Therefore, a trade-off between the computational accuracy and efficiency may be required in the different-weight-based MC methods. In addition, AVD- and RVD-based SAMMC methods have higher computational cost than the MMC method, which is attributed to the sorting algorithm. Specifically, the finding and sorting operations of numerical particles in the array in AVD- and RVD-based SAMMC methods are more computational time-consuming than only finding an existing numerical particle of the similar volume with the nucleated one in the MMC method. As the difference between AVD- and RVD-based SAMMC methods is the expression of the volume difference, the computational costs of AVD- and RVD-based SAMMC methods are almost the same. Furthermore, as the number of numerical particles changes between N_S and $2N_S$ in the stepwise constant-volume method while the numerical particle numbers in both constant-number methods remain N_S, the computational time consumed by the stepwise constant-volume method is higher than those of both mass- and number-based constant-number methods. The reason is that the number of numerical particles negatively affects the computational efficiency.

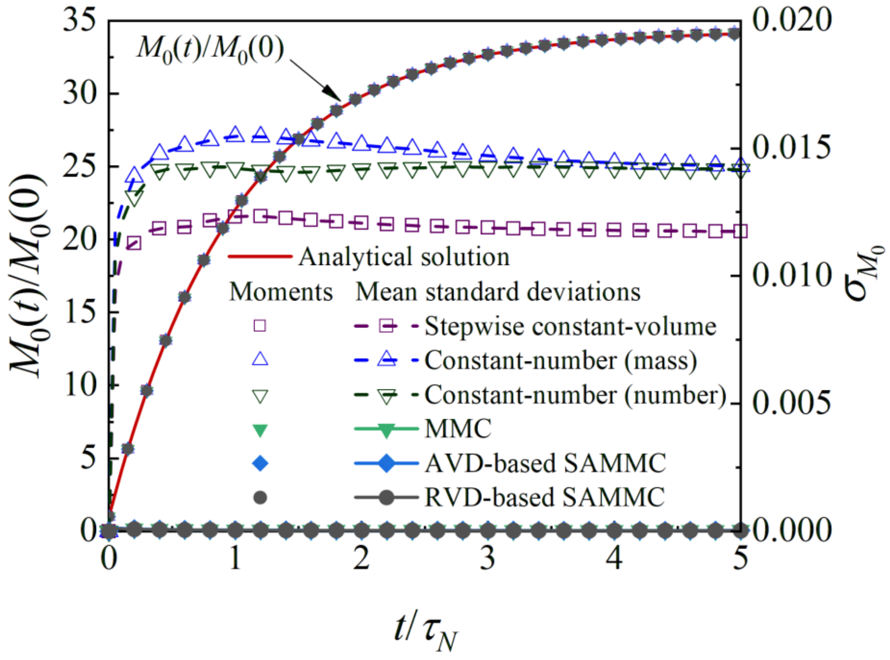

Figure 5.6 Time evolutions of total particle number concentrations, M_0 and their corresponding mean standard deviations for nucleation in Case 1 [38].

5.3.2 Pure coagulation

Binary coagulation between particles is considered in the present study, which describes the collision of two particles and then the formation of a large one, therefore leading to an increase of the average particle size and a reduction in the particle number. It is considered that modelling a coagulation process involving two particles is always more demanding than other aerosol dynamic processes [34]. Both homogeneous and non-homogeneous coagulations as well as initial monodispersed and exponential PSDs are considered to validate newly proposed AVD- and RVD-based SAMMC methods. Homogeneous coagulation is considered in both Cases 2 and 3, but the difference is that the initial PSD of Case 2 is monodispersed while in Case 3 it is an exponential distribution. As a non-homogeneous coagulation process leads to the generation of an additional numerical particle, it can be used to validate the computational accuracy and efficiency of the newly proposed and developed AVD- and RVD-based SAMMC methods. In Case 4, the coagulation is non-homogeneous with initial monodispersed PSD. The initial total particle number concentration, N_0 = 10^6 cm^{-3}, and the coagulation kernel β_{ij} is a constant A, where $A = 10^{-6}$ cm^3/s [17,35]. The characteristic coagulation time, $\tau_C = 1/(AN_0)$.

5.3.2.1 Homogeneous coagulation with initial monodispersed distribution

Figure 5.7 shows the time evolutions of M_0, M_1 and M_2 as well as corresponding σ_{M_0}, σ_{M_1} and σ_{M_2} and the resulting PSDs at $t/\tau_C = 50$ obtained from different MC methods for homogeneous coagulation with initial monodispersed distribution when compared with the corresponding analytical solutions [17].

Numerical results show that M_0 obtained from all these MC methods decrease constantly over time because of the continuous occurrence of coagulation processes and have excellent agreements with the analytical solution, while their corresponding σ_{M_0} vary for different MC methods as shown in Figure 5.7(a). Although M_0 during the numerical simulation in the stepwise constant-volume method is always conserved, the constant change in the number of numerical particles adversely affects the computational accuracy, leading the mean standard deviation to 1.79%. The most significant feature between the stepwise constant-volume method and the mass-based constant-number method is that the number of numerical particles for the former method is always between $0.5N_S$ and N_S while the latter method restores the sample at every time step. But the latter method has larger σ_{M_0} than the former method, which implies that the frequency of sample restoration has a more obvious effect on the computational accuracy than the number of numerical particles. By comparison, AVD- and RVD-based SAMMC methods treat a homogeneous coagulation process as the same as the MMC method, so the stochastic errors in M_0 among these three different-weight-based MC methods are almost the same. In addition, the number-based constant-number method has almost the same σ_{M_0} as three different-weight-based MC methods, where M_0 for all these four methods (i.e., number-based constant-number method, MMC method, and AVD- and RVD-based SAMMC methods) are always conserved, leading to lower stochastic errors than other two methods (i.e., stepwise constant-volume method and the mass-based constant-number method). But the σ_{M_1} obtained from the number-based constant-number method is the largest at 2.38% because of mass/volume non-conservation, while M_1 of other MC methods are always conserved and their corresponding σ_{M_1} are always zero as shown in Figure 5.7(b). All these MC methods can precisely predict the evolution of the high-order moment, M_2 as shown in Figure 5.7(c), but σ_{M_2} obtained from the number-based constant-number method is the largest, while the other two equal-weight-based MC methods have significantly lower σ_{M_2}. The resulting σ_{M_2} obtained from mass-based constant-number method is slightly lower than that of the stepwise constant-volume method, which demonstrates that the computational accuracy of M_2 of the number-based constant-number is the lowest, and the mass-based constant-number method has higher computational accuracy of M_2 than the stepwise constant-volume method. By comparison, the corresponding σ_{M_2} of all different-weight-based MC methods are the lowest and almost the same, which implies that different-weight-based MC methods have higher computational accuracy than the equal-weight-based MC methods, and AVD- and RVD-based SAMMC methods show the same computational precision as the MMC method.

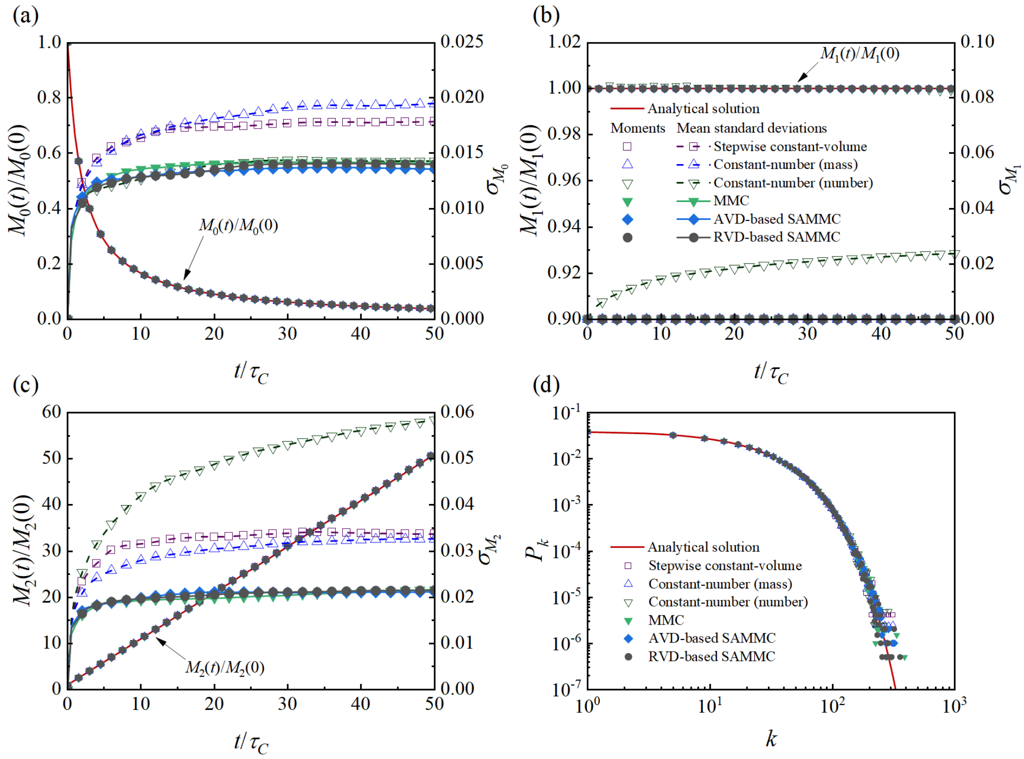

Figure 5.7 Time evolutions of zeroth- to second-order moments and their corresponding mean standard deviations, and PSDs for homogeneous coagulation with initial monodispersed distribution in Case 2 [38].

Figure 5.7(d) shows the PSD at $t/\tau_C = 50$, where P_k is the probability of obtaining a cluster containing k primary particles and $k = v/v_0$. Numerical results of these six MC methods agree and track well with the corresponding analytical solution, but different resolutions of large size particles are shown for different MC methods. The different-weight-based MC methods have wider PSD than the equal-weight-based MC methods because the different-weight-based MC methods are better suited for resolving larger size particles. As a result, the fluctuation in M_2

of different-weight-based MC methods is reduced, leading to lower statistical noise in M_2 and higher computational accuracy than equal-weight-based MC methods in Figure 5.7(c). It is also found that the different-weight-based MC methods have smaller fluctuations in the PSD at the high end than the equal-weight-based MC methods, which further implies that the different-weight-based MC methods have higher computational accuracy than the equal-weight-based MC methods. Since AVD- and RVD-based SAMMC methods work in the similar way as the MMC method in the homogeneous coagulation process, the PSDs obtained from AVD- and RVD-based SAMMC methods are almost the same width as the MMC method, therefore leading to almost the same σ_{M_2} as shown in Figure 5.7(c). In addition, the stepwise constant-volume method has a narrower PSD than all the other MC methods. Hence, the real particles at the high end are poorly represented by the numerical particles, which results in a large stochastic error in M_2. The mass-based constant-number method has slightly wider PSD, and the resulting σ_{M_2} is slightly lower. Although the PSD obtained from the number-based constant-number method is almost as wide as that of the mass-based constant-number method, the total particle mass/volume concentration is not conserved, which results in the largest σ_{M_2} of the number-based constant-number method.

5.3.2.2 Homogeneous coagulation with initial exponential distribution

Figure 5.8 shows the time evolutions of M_0, M_1 and M_2 and their corresponding σ_{M_0}, σ_{M_1} and σ_{M_2} and the resulting PSDs at $t/\tau_C = 0, 1, 5$ and 20 obtained from different MC methods for homogeneous coagulation with initial exponential distribution when compared with the corresponding analytical solutions [213]. M_0 obtained from all these MC methods show excellent agreement with the analytical solution as shown in Figure 5.8(a), but the mass-based constant-number method has the largest stochastic error in M_0, which is not preserved. Another equal-weight-based MC method (i.e., the stepwise constant-volume method) has the second largest σ_{M_0} due to the constant alteration of numerical particle numbers. The resulting σ_{M_0} obtained from the number-based constant-number method and three different-weight-based MC methods are the lowest and almost the same, which is attributed to the preservation of the total particle number concentration during the numerical simulation. As the total particle mass/volume concentration is not conserved, the number-based constant-number method has the largest stochastic error in M_1. The M_1 of other MC methods remain constant as shown in Figure 5.8(b) because of the conserving mass/volume, therefore resulting in no stochastic error in M_1. The high-order moment, M_2 obtained from all these MC methods are in excellent agreement with the analytical solution with the variations of σ_{M_2} in different MC methods in Figure 5.8(c). It is found that the number-based constant-number method and the stepwise constant-volume method have the largest σ_{M_2}, while the resulting σ_{M_2} of the mass-based constant-number method is slightly lower. The lowest and almost the same σ_{M_2} are observed in three different-weight-based MC methods, which demonstrates that these three methods have the highest and almost the same level of computational accuracy in terms of M_2. Figure 5.8(d) shows the particle number concentrations (PNCs) at different v/v_0 at $t/\tau_C = 0$, 1, 5 and 20, which also represents the PSD. The PNCs obtained from different MC methods have excellent agreement with the analytical solutions at different times t/τ_C. With coagulation taking place over time, particle volumes become larger and the PNC moves to the large volume regime on the right side, but it still remains the “self-preserving” form.

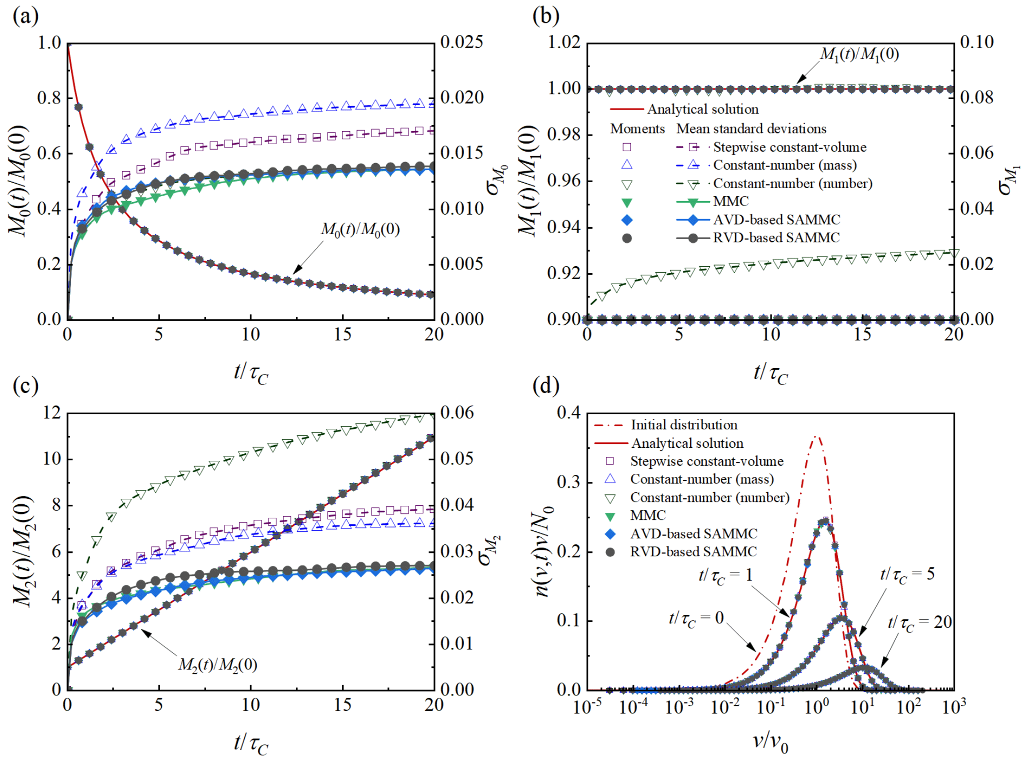

Figure 5.8 Time evolutions of zeroth- to second-order moments and their corresponding mean standard deviations and PSDs for homogeneous coagulation with initial exponential distribution in Case 3 [38].

5.3.2.3 Non-homogeneous coagulation with initial monodispersed distribution

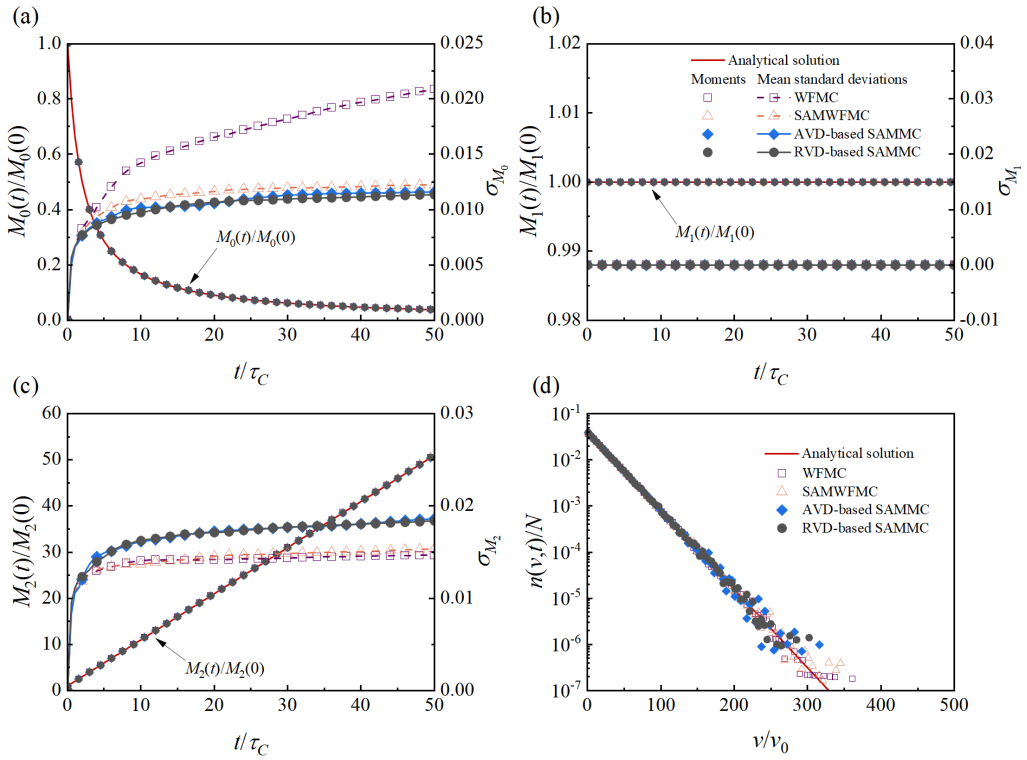

Figure 5.9 Time evolutions of zeroth- to second-order moments and their corresponding mean standard deviations, and PSDs for non-homogeneous coagulation with initial monodispersed distribution in Case 4 [38].

A non-homogeneous coagulation process leads to the generation of an additional numerical particle, which is necessary for validating the computational accuracy and efficiency of the newly developed AVD- and RVD-based SAMMC methods. Evolutions of M_0 to M_2 and corresponding σ_{M_0} to σ_{M_2} over time, and the resulting PSDs at $t/\tau_C = 50$ obtained from different MC methods for non-homogeneous coagulation with initial monodispersed distribution when compared with the corresponding analytical solutions [154] are shown in Figure 5.9. Excellent agreements with analytical solutions are presented in the numerical results obtained from all different MC methods. Figure 5.9(b) shows that the total volume/mass concentrations, M_1 and the resulting σ_{M_1} are always constant because of mass conservation. Both AVD- and RVD-based SAMMC methods show lower σ_{M_0} than the SAMWFMC method [35] as shown in Figure

5.9(a), which implies that AVD- and RVD-based SAMMC methods have higher computational accuracy of M_0 than the SAMWFMC method. The resulting σ_{M_0} obtained from the WFMC method [33] is the largest and remains increasing over time, which implies that it does not allow indefinitely long numerical simulation of non-homogeneous coagulation. But both WFMC and SAMWFMC methods have lower σ_{M_2} than AVD- and RVD-based SAMMC methods as shown in Figure 5.9(c), which is attributed to wider particle size ranges of the former methods as shown in Figure 5.9(d). This implies that WFMC and SAMWFMC methods are developed to obtain larger size particles and to further predict the PSD, therefore reducing the stochastic error in the high-order moment. In addition, the AVD- and RVD-based SAMMC methods have lower σ_{M_0} to σ_{M_2} in non-homogeneous coagulation than those in homogeneous coagulation of Case 2 in Section 5.3.2.1.

5.3.2.4 Computational time for pure coagulation

Table 5.2 Comparison of computational times for Cases 1 to 4 [38].

t (s)	Case 1	Case 2	Case 3	Case 4
Stepwise constant-volume	3.35	24.84	19.03	_
Constant-number (mass)	2.44	85.51	61.61	_
Constant-number (number)	2.58	89.65	63.81	_
MMC	16.59	73.20	53.74	–
SAMMC (absolute)	17.43	76.50	55.65	154.94
SAMMC (relative)	18.23	75.50	55.27	154.89
WFMC	–	–	–	92.92
SAMWFMC	–	–	–	130.21

Remarks: The WFMC and SAMWFMC methods are specifically developed for non-homogeneous coagulation in Case 4 and are not aimed at nucleation and homogeneous coagulation for Cases 1 to 3, so their corresponding computational times for Cases 1 to 3 are not shown here. Similarly, stepwise constant-volume method, mass-and number-based constant-number methods and MMC method are not applicable to non-homogeneous coagulation in Case 4, their corresponding computational times for Case 4 are not shown here.

The computational costs of all MC methods for pure coagulation are presented in Table 5.2 from Cases 2 to 4. For homogeneous coagulation (i.e., Cases 2 and 3), the computational times consumed by the stepwise constant-volume method are the lowest, which is owing to the decreasing number of numerical particles. Mass- and number-based constant-number methods require higher computational cost than other three different-weight-based MC methods. It is because both mass- and number-based constant-number methods restore the sample at every time step, leading to a large amount of time consumption. The computational time required by the MMC method is only slightly smaller than those of the AVD- and RVD-based SAMMC methods, which implies that AVD- and RVD-based SAMMC methods have almost the same level of computational efficiency as the MMC method. By comparison, AVD- and RVD-based SAMMC methods have larger computational time consumption than the WFMC and SAMWFMC methods for non-homogeneous coagulation (i.e., Case 4), since sorting and finding neighbour numerical particles with the minimal property difference in the array in AVD- and RVD-based SAMMC methods require more computational cost than only removing operation in the WFMC method and only finding and merging operations in the SAMWFMC method.

5.3.3 Pure breakage

Breakage is classified into two types according to the number of daughter particles. They are binary breakage and multi-breakage. Binary breakage refers to a particle fragmented into two smaller numerical particles while a multi-breakage process normally leads to more fragments generated. If the sizes of child fragments are the same, it is equal daughter PSD. If a uniform daughter PSD is used, the volumes of child fragments are determined by the stochastic process. For example, a parent particle, i with volume v_i undergoes a binary breakage, the volumes of both child fragments (i.e., j and k) for the equal daughter PSD are $v_j = v_k = 0.5v_i$, but for the uniform daughter PSD, the volume of one fragment is $v_j = r_4v_i$ while the other one is $v_k = (1-r_4)v_i$, where r_4 is a uniformly distributed random number between zero and one. Different breakage cases with different computational conditions as listed in Table 5.3 are selected for validation purpose of the new AVD- and RVD-based SAMMC methods. Cases 5 and 6 are binary breakage cases with the initial monodispersed distribution and linear breakage rate in the particle volume. The difference is that the daughter PSD in Case 5 is equal, while Case 6 is uniform. An initial exponential distribution with quadratic breakage rate in the particle volume is considered in Case 7. Case 8 is a very complicated breakage case, in which twelve daughter fragments with equal volume are fragmented by a parent particle with the power law breakage rate. The number of numerical particles considerably increases with the occurrence of breakage processes. The initial total particle number concentration, N_0 = 3000 m^{-3}, and the characteristic breakage time, $\tau_B = 1/B(v_0)$.

Table 5.3 The computational conditions for Cases 5 to 8 [38].

Case	Breakage type	Initial PSD	Daughter PSD	$\gamma(v,u)$	$b(v)$	$B(v)$
5	binary breakage	monodispersed	equal	$\delta(v,u/2)$	2	v
6	binary breakage	monodispersed	uniform	$1/u$	2	v
7	binary breakage	exponential	uniform	$1/u$	2	v^2
8	multi-breakage	monodispersed	equal	$\delta(v,u/12)$	12	$v^{1.8}$

5.3.3.1 Binary breakage of linear breakage rate with initial monodispersed distribution and equal daughter PSD

Figure 5.10 shows the time evolutions of M_0 to M_2 and corresponding σ_{M_0} to σ_{M_2}, and the resulting PSDs at t/τ_B = 25 and 50 obtained from different MC methods for binary breakage of linear breakage rate with initial monodispersed distribution and equal daughter PSD when compared with the corresponding analytical solutions [219]. With binary breakage processes taking place, the total particle number concentration, M_0, increases constantly but the total particle mass/volume concentration, M_1, remains unchanged. M_1 obtained from the stepwise constant-volume method, number-based constant-number method and MMC method significantly deviate from the analytical solution as shown in Figure 5.10(b), leading to large σ_{M_1} during the numerical simulation. In addition, σ_{M_0} and σ_{M_2} for these three MC methods are also the largest as shown in Figures 5.10(a) and 5.10(c), although the corresponding M_0 and M_2 are in good agreements with analytical solutions. By comparison, mass-based constant-number method and AVD- and RVD-based SAMMC methods have excellent agreements of M_0, M_1

and M_2 with analytical solutions. Because of mass conservation, the σ_{M_1} for these three MC methods are zero and remain constant. But AVD- and RVD-based SAMMC methods have lower σ_{M_0} and σ_{M_2} than other MC methods including the mass-based constant-number method, which implies that AVD- and RVD-based SAMMC methods have the highest computational accuracy among all MC methods. It is also found that the stochastic errors of AVD- and RVD-based SAMMC methods are almost the same, which implies that it has no effect using AVD or RVD method as the crucial merging criteria on the computational accuracy. Figure 5.10(d) shows the PNCs for different particle volumes at t/τ_B = 25 and 50, which also describes the results of PSD. As all fragments are of equal volume, the volumes of particles are powers of 0.5 and the resulting PSD is sparse. With time advancing, the particle volumes gradually decrease and the PNC moves to the smaller volume regime on the left side, while the "self-preserving" form still remains. The PNCs of all MC methods agree excellently with the analytical solutions at different t/τ_B.

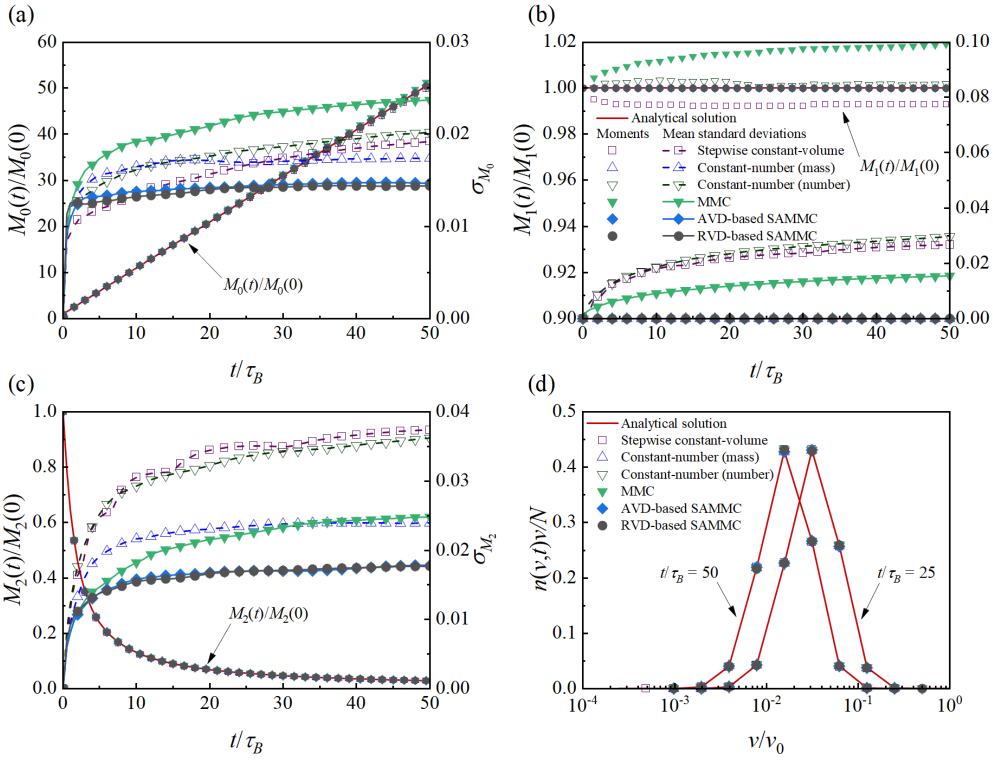

Figure 5.10 Time evolutions of zeroth- to second-order moments and their corresponding mean standard deviations, and PSDs for binary breakage of linear breakage rate with initial monodispersed distribution and equal daughter PSD in Case 5 [38].

5.3.3.2 Binary breakage of linear breakage rate with initial monodispersed distribution and uniform daughter PSD

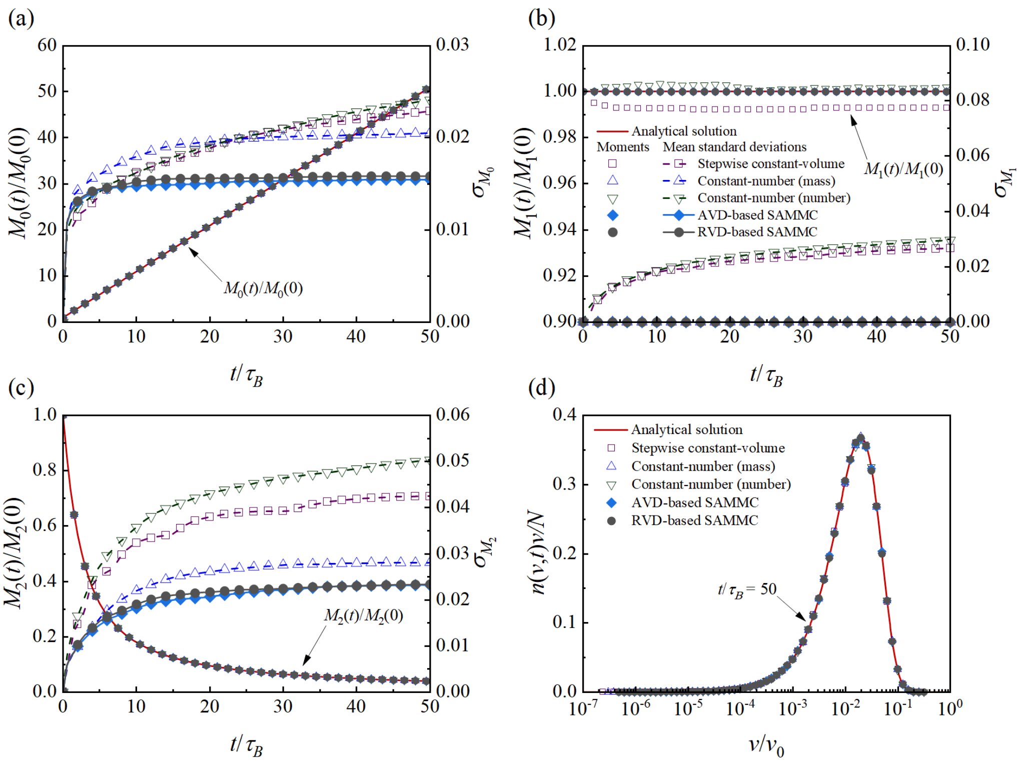

Figure 5.11 Time evolutions of zeroth- to second-order moments and their corresponding mean standard deviations, and PSDs for binary breakage of linear breakage rate with initial monodispersed distribution and uniform daughter PSD in Case 6 [38].

Compared with Case 5, the daughter PSD in Case 6 is uniform. The numerical results of Case 6 with the corresponding analytical solutions [220] are shown in Figure 5.11. As the treatment after a breakage process is only adding the weights of a fragment and a numerical particle with the similar volume directly in the MMC method, the systematic errors are unavoidably introduced which are originated from mass non-conservation [156,157]. These large systematic errors demonstrate that the MMC method cannot be used to precisely simulate a breakage process. Hence, the numerical results of MMC method are not shown. Similarly, the systematic errors are also shown in the stepwise constant-volume method, while M_1 of the number-based constant-number method fluctuates around 1, which are also attributed to the non-conserving mass as shown in Figure 5.11(b). The resulting σ_{M_1} of these two MC methods (i.e., stepwise constant-volume method and number-based constant-number method) are the largest while σ_{M_1} of other methods (i.e., mass-based constant-number method, MMC method, and AVD- and RVD-based SAMMC methods) are always zero. Actually the resulting σ_{M_0} and σ_{M_2} of these two MC methods are also the largest, and the mass-based constant-number method has lower σ_{M_0} and σ_{M_2}. AVD- and RVD-based SAMMC methods has the lowest σ_{M_0} and σ_{M_2} as shown in Figures 5.11(a) and 5.11(c), which demonstrates the highest computational accuracy of AVD- and RVD-based SAMMC methods. It is also found that the PNCs obtained from all MC methods agree excellently with the analytical solution at $t/\tau_B = 50$ in Figure 5.11(d).

5.3.3.3 Binary breakage of quadratic breakage rate with initial exponential distribution and uniform daughter PSD

A quadratic breakage rate and an initial exponential distribution for binary breakage are also simulated in the present study with analytical solutions in [221]. The MMC method still shows large systematic errors due to mass non-conservation, so the corresponding numerical results are not shown. Two MC methods (i.e., stepwise constant-volume method and number-based constant-number method) with non-conserving mass (i.e., M_0) still have the largest σ_{M_0}, σ_{M_1} and σ_{M_2}, although M_0 and M_2 agree well with analytical solutions as shown in Figures 5.12(a), 5.12(b) and 5.12(c), respectively. By comparison, zeroth- to second-order moments obtained from all three mass conservation methods (i.e., mass-based constant-number method, and AVD- and RVD-based SAMMC methods) exhibit excellent agreement with analytical solutions, and the resulting σ_{M_1} always remain zero. The mass-based constant-number method has slightly higher σ_{M_0} and almost the same σ_{M_2} when compared with AVD- and RVD-based SAMMC methods. It demonstrates that AVD- and RVD-based SAMMC methods still have higher computational accuracy in handling binary breakage of quadratic breakage rate with initial exponential distribution than the mass-based constant-number method. As the volumes of particles decrease with the occurrence of breakage, time evolution of the PNC moves to the smaller size regime but still remains the exponential distribution. The PNCs obtained from all these MC methods follow the “self-preserving” curve well as shown in Figure 5.12(d).

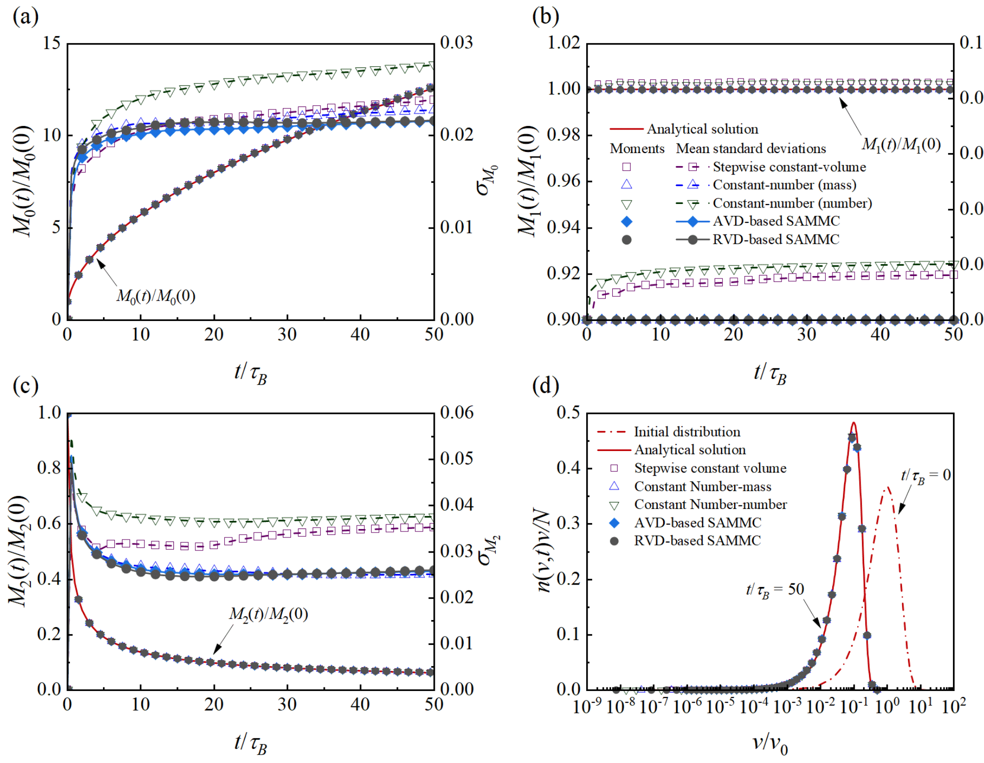

Figure 5.12 Time evolutions of zeroth- to second-order moments and their corresponding mean standard deviations, and PSDs for binary breakage of quadratic breakage rate with initial exponential distribution and uniform daughter PSD in Case 7 [38].

5.3.3.4 Multi-breakage of power law breakage rate with initial monodispersed distribution and equal daughter PSD

In Case 8, one parent particle breaks into twelve child particles with equal volumes, leading to a dramatic increase in the number of numerical particles. The analytical solutions for multi-breakage can be obtained from [219]. In the stepwise constant-volume method, when the number of numerical particles exceeds twice of its initial value (i.e., $2N_S$), several numerical particles are randomly chosen and discarded and finally only N_S numerical particles are left in the computational domain, which leads to non-conserving mass. The total particle number concentration instead of the total particle mass/volume concentration is only conserved in the number-based constant-number method. By comparison, when a new numerical particle is generated, the treatment in the MMC method is to merge it with an existing numerical particle having the most similar volume, where their weights are simply added together to only preserve the total particle number concentration, resulting in mass non-conservation. Compared with

Case 5, Case 8 is more challenging for the stepwise constant-volume method and MMC method, as larger systematic errors are introduced in both methods because of non-conserving mass. Therefore, the numerical results of both stepwise constant-volume method and MMC method are not shown here. Another non-conserving mass method (i.e., the number-based constant-number method) shows a deviation of M_1 from the analytical solution, leading to the largest σ_{M_0}, σ_{M_1} and σ_{M_2} in Figure 5.13. As other three MC methods (i.e., mass-based constant-number method and AVD- and RVD-based SAMMC methods) are mass-conserved, the M_1 and σ_{M_1} remain constant in Figure 5.13(b). Only mass is conserved in the mass-based constant-number method, while the statistical properties are entirely conserved in AVD- and RVD-based SAMMC methods, leading to lower stochastic errors in M_0 and M_2 of the latter methods than those of the former method as shown in Figures 5.13(a) and 5.13(c). It is worth noting that the σ_{M_0} and σ_{M_2} obtained from the RVD-based SAMMC method are lower than those of the AVD-based SAMMC method. The reason is that the volume differences for RVD are constants while the volume differences are possibly linear with the particle volume for AVD. As a result, the particle weight would be compared in the RVD-based SAMMC method but not in the AVD-based SAMMC method, thus leading to lower stochastic error of the RVD-based SAMMC method than the AVD-based SAMMC method. It implies that the former method has higher computational precision than the latter method in Case 8. Twelve equally sized child particles are generated by one parent particle, so the child particle volumes are 1/12 of the parent particle volume. The numerical results in a sparsely discretized PSD are shown in Figure 5.13(d). The number-based PSDs obtained from all MC methods agree excellent with analytical solutions and remain “self-preserving” form when moving towards the smaller size regime over time.

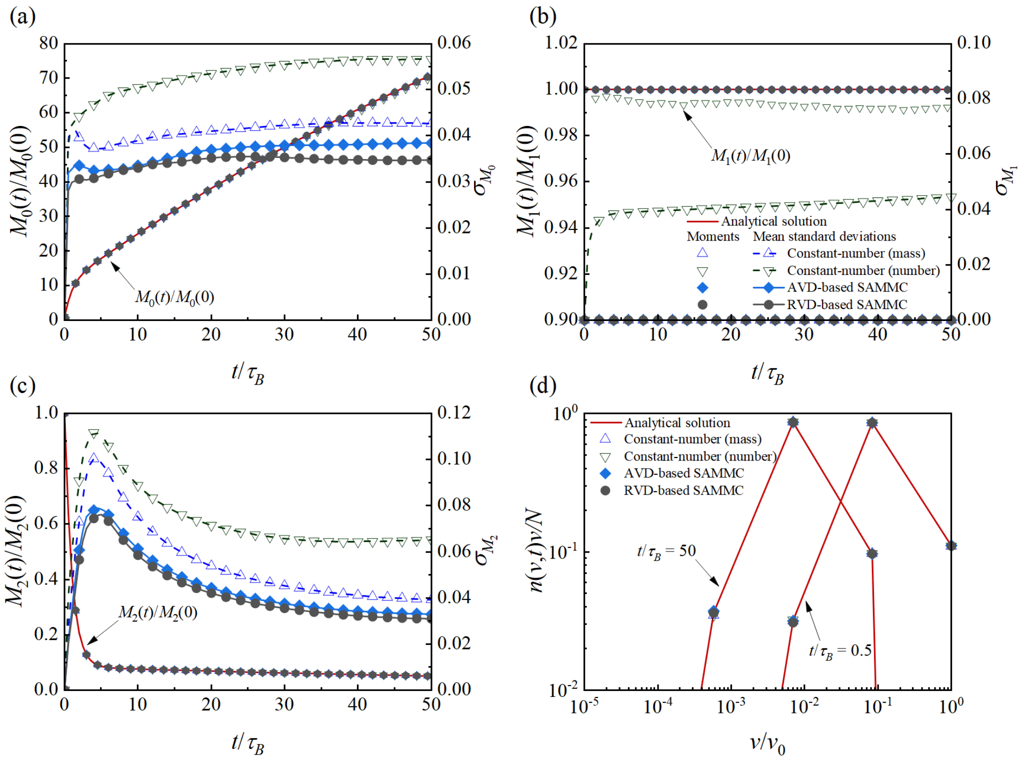

Figure 5.13 Time evolutions of zeroth- to second-order moments and their corresponding mean standard deviations, and PSDs for multi-breakage of power law breakage rate with initial monodispersed distribution and equal daughter PSD in Case 8 [38].

5.3.3.5 Computational time for pure breakage

Table 5.4 shows the computational times required by different MC methods for pure breakage from Cases 5 to 8. Different-weight-based MC methods normally have larger computational time than the equal-weight-based MC methods. The reason is that randomly removing method used in equal-weight-based MC methods requires less computational time than the merging method in the counterparts. In addition, the daughter PSD has little effect on the computational time when comparing Case 5 with Case 6. The computational time of mass- and number-based constant-number methods are the lowest while the stepwise constant-volume method requires slightly higher computational times in Cases 5 and 6. The reason is that the numbers of numerical particles for the former methods always remain N_S while that of the latter method changes between N_S and $2N_S$ with breakage taking place. However, mass- and number-based constant-number methods have a significant larger computational time than the stepwise constant-volume method in Case 7. It demonstrates that the computational time of both constant-number methods are closely related to the initial exponential distribution. In the stepwise constant-volume method, every time when the number of numerical particles reaches or exceeds twice of its initial value (i.e, $2N_S$) due to breakage, several numerical particles are randomly selected and discarded and finally only N_S numerical particles are left in the computational domain [36]. It leads to a great reduction in the total breakage rate and then a dramatic increase in the time step. Therefore, the computational time for stepwise constant-volume method is significantly reduced. By comparison, mass- and number-based constant-number methods randomly remove only one numerical particle from the computational domain at every breakage process, therefore resulting in very small change in the total breakage rate and time step. The small change of the time step is also observed in AVD- and RVD-based SAMMC methods, in which the merging operation of numerical particles is implemented. Therefore, the computational time of AVD- and RVD-based SAMMC methods are slightly higher than those of constant-number methods due to the introduction of sorting algorithm. It is also found that the computational time of AVD- and RVD-based SAMMC methods are higher than that of the MMC method in Case 5 due to the sorting operation of numerical particles. Considering the large systematic errors unavoidably introduced in the MMC method, AVD- and RVD-based SAMMC methods are only the different-weight-based MC methods with high computational accuracy developed for breakage. Actually, both AVD- and RVD-based SAMMC methods have the highest computational accuracy among all these MC methods with highly acceptable computational time.

Table 5.4 Comparison of the computational times for Cases 5 to 9 [38].

t (s)	Case 5	Case 6	Case 7	Case 8	Case 9
Stepwise constant-volume	3.41	4.11	6.73	––	142.78
Constant-number (mass)	3.16	3.26	36.04	1.85	157.22
Constant-number (number)	3.39	3.31	34.61	1.87	156.20
MMC	8.19	––	––	––	––
SAMMC (absolute)	12.36	11.58	40.74	6.31	291.25
SAMMC (relative)	12.51	11.50	42.12	6.32	297.93

Remarks: Very large systematic errors are found in MMC method for Cases 6 to 9 and stepwise constant-volume method for Case 8, so the corresponding computational times as well as numerical results are not shown here.

5.3.4 Simultaneous coagulation and nucleation

Simultaneous coagulation and nucleation in the dispersed system is used to validate the computational accuracy and efficiency of the newly developed SAMMC method, as a nucleation-related process involves the generation of a new numerical particle, which is very suitable for testing the neighbour merging method. Analytical solutions for the total particle number and mass/volume concentrations could be obtained through integration of the corresponding general dynamic equation in [36]. It should be noted that if each nucleation process occurring is tracked and each real particle generated in the computational domain is represented by a numerical particle in the different-weight-based methods, the time step would be very small, leading to great computational time. One effective way to improve the computational efficiency is to track each nucleation process with more real particles as discussed in Section 5.3.1 (i.e., Case 1). Thus, the number of real particles represented by a numerical particle in the different-weight-based methods in the present study is set equal to the initial weights of numerical particles. The initial total precursor and particle number concentrations are constants (i.e., $C_{\mathrm{pre}}(0) = 5.0\times10^{4}$ cm^{-3} and $N_0 = 10^5$ cm^{-3}). The nucleation rate constant, $K_N = 20$ s^{-1}, and the homogeneous coagulation is chosen with a constant coagulation kernel, $\beta_{ij} = A = 10^{-5}$ cm^3/s. The characteristic nucleation and coagulation times are defined as $\tau_N = 1/K_N$ and $\tau_C = 1/(AN_0)$.

The resulting total particle number concentration, M_0, grows rapidly due to the domination of nucleation at first, but the growth rate decreases over time with the occurrence of coagulation. The stationary state of M_0 between nucleation and coagulation is finally reached. By comparison, the total particle mass/volume concentration, M_1 linearly increases with time. As the systematic errors in the MMC method are unavoidable due to the non-conserving mass, the numerical results are not shown here. Numerical results of M_0 and M_1 obtained from different MC methods agree fairly well with analytical solutions as shown in Figure 5.14, but the resulting σ_{M_0} and σ_{M_1} are different. The mass-based constant-number method has the largest σ_{M_0}, while the σ_{M_1} of the number-based constant-number method is the largest. The σ_{M_0} and

σ_{M_1} obtained from the stepwise constant-volume method are lower than those of both mass- and number-based constant-number methods. It further demonstrates that frequently changing the number of numerical particles leads to higher stochastic errors and lower computational accuracy. Stochastic errors obtained from AVD- and RVD-based SAMMC methods are the lowest, leading to the highest computational accuracy. The computational time of AVD- and RVD-based SAMMC methods are higher than those of equal-weight-based MC methods as shown in Table 5.4 for Case 9 due to the finding and sorting operations of numerical particles.

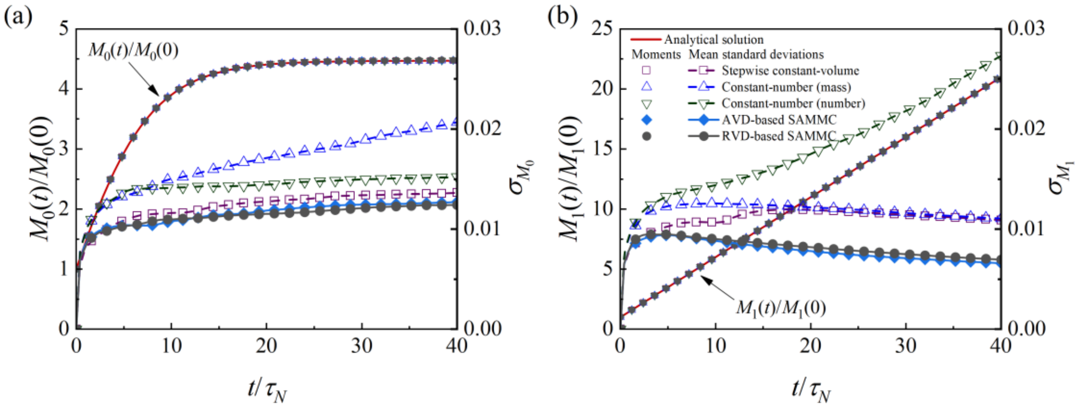

Figure 5.14 Time evolutions of total particle number and mass/volume concentrations and their corresponding mean standard deviations for simultaneous coagulation and nucleation with the initial monodispersed distribution in Case 9 [38].

5.3.5 Simultaneous coagulation and breakage

A coagulation process leads to the reduction in the total number of real particles while breakage increases the total number of real particles. For simultaneous coagulation and breakage, the total particle number concentration is therefore determined by the competition between coagulation and breakage in the dispersed system. It implies that the resulting steady state of total particle number concentration depends on the relative strength of coagulation and breakage. It is necessary to adopt different computational conditions to study the computational accuracy and efficiency of the newly developed SAMMC method as well as other MC methods for different competing mechanisms. The MMC method introduces large systematic errors due to mass non-conservation when dealing with breakage-related processes as discussed in Section 5.3.3, so the corresponding numerical results regarding simultaneous coagulation and breakage are not shown here. The initial total particle number concentration, $N_0 = 10^7$ cm^{-3} and the homogeneous coagulation is chosen with a constant coagulation kernel, $\beta_{ij} = A = 10^{-7}$ cm^3/s [172]. The characteristic coagulation and breakage times are defined as $\tau_C = 1/(AN_0)$ and $\tau_B = 1/B(v_0)$, respectively.

Table 5.5 lists six cases with different computational conditions for simultaneous coagulation and breakage. The initial PSDs for Cases 10 to 13 are monodispersed distribution while the other two Cases 14 and 15 are exponential distribution. Both Cases 10 and 12 are in the equilibrium state between coagulation and breakage, but the difference is that the daughter PSD of Case 10 is equal while Case 12 is uniform. The dominating dynamic processes at the beginning of the numerical simulation in Cases 11 and 13 are coagulation and breakage, respectively. The breakage rate in Case 15 is linearly dependent on the particle volume, i.e., $B(v) = 0.5v$.

Table 5.5 List of computational conditions for Cases 10 to 15 [38].

Case	Initial PSD	β_{ij}	Daughter PSD	$\gamma(v,u)$	$B(v)$
10	monodispersed	A	equal	$\delta(v,u/2)$	0.5
11	monodispersed	A	uniform	$1/u$	0.25
12	monodispersed	A	uniform	$1/u$	0.5
13	monodispersed	A	uniform	$1/u$	10
14	exponential	A	uniform	$1/u$	0.5
15	exponential	A	uniform	$1/u$	$0.5v$

5.3.5.1 Simultaneous coagulation and breakage of constant breakage rate (i.e., 0.5) with initial monodispersed distribution and equal daughter PSD

Figures 5.15 shows the time evolutions of M_0 and M_1 and their corresponding σ_{M_0} and σ_{M_1} obtained from different MC methods for simultaneous coagulation and breakage with initial monodispersed distribution and equal daughter PSD when compared with analytical solutions [37], where the breakage rate is a constant and is independent of particle volumes. It should be noted that the competition between coagulation and breakage is of the same intensity when $B(v)$

= 0.5, so the M_0 is always constant during the numerical simulation. Numerical results show that M_0 obtained from all MC methods agree excellently with the analytical solution. The mass-based constant-number method has the largest σ_{M_0}, while σ_{M_0} of other MC methods are lower and are almost the same. By comparison, non-conserving mass of the number-based constant-number method leads to the largest σ_{M_1}, but M_1 and σ_{M_1} remain constant in all other MC methods. It is found that the computational accuracy of the stepwise constant-volume method is almost the same as AVD- and RVD-based SAMMC methods in Case 10.

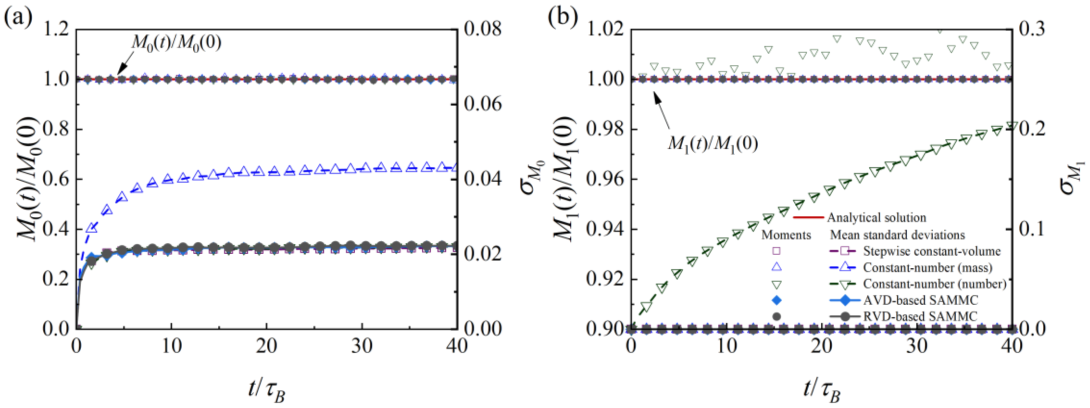

Figure 5.15 Time evolutions of total particle number and mass/volume concentrations and their corresponding mean standard deviations for simultaneous coagulation and breakage of constant breakage rate (i.e. 0.5) with initial monodispersed distribution and equal daughter PSD in Case 10 [38].

5.3.5.2 Simultaneous coagulation and breakage of constant breakage rate (i.e., 0.25, 0.5 and 10) with initial monodispersed distribution and uniform daughter PSD

Figures 5.16 to 5.18 show the effect of the breakage rate on M_0 and M_1 obtained from all MC methods. Coagulation is dominated when the breakage rate is equal to 0.25, leading to the decrease in the total particle number concentration until a steady state between coagulation and breakage is reached. If the breakage rate is increased to 0.5, coagulation and breakage are in the equilibrium state. Further increasing the breakage rate to 10, the total particle number concentration sharply increases at the beginning and it finally remains unchanged with time. This trend is well followed by all MC methods. Analytical solutions of Cases 11 to 13 are provided by Lin et al. [37]. It should be noted that simultaneous coagulation and breakage does not change the total particle mass/volume concentration, so M_1 always remains constant. As the mass is not conserved in the number-based constant-number method, σ_{M_1} is the largest among all MC methods. The mass is no longer conserved in the stepwise constant-volume method when the breakage rate is increased to 10. Although M_1 of the mass-based constant-number method remains unchanged, the resulting stochastic error in M_0 is the largest for Cases 11 to 13. By comparison, AVD- and RVD-based SAMMC methods have very low stochastic error in M_0 and they do not have any stochastic error in M_1, which demonstrates the high computational accuracy of both methods. Compared Case 12 with Case 10, the daughter distribution is independent of the computational accuracy of M_0 and M_1 in AVD- and RVD-based SAMMC methods, which have almost the same computational accuracy.

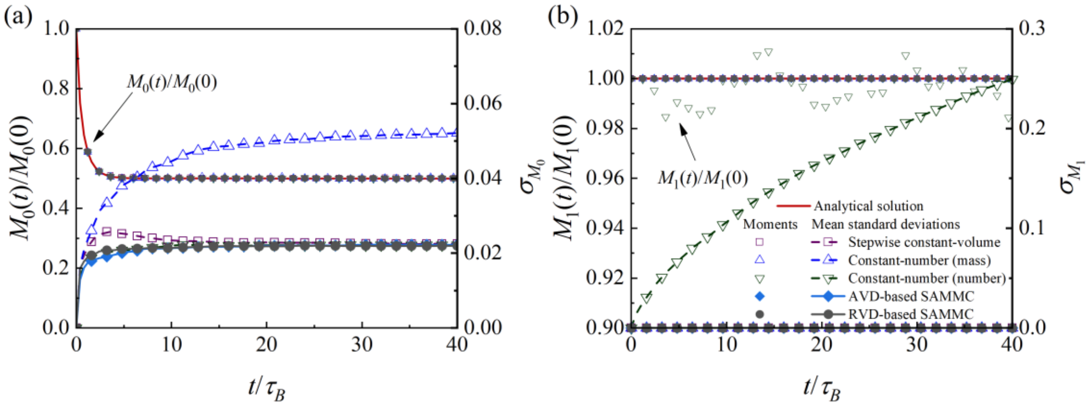

Figure 5.16 Time evolutions of total particle number and mass/volume concentrations and their corresponding mean standard deviations for simultaneous coagulation and breakage of constant breakage rate (i.e. 0.25) with initial monodispersed distribution and uniform daughter PSD in Case 11 [38].

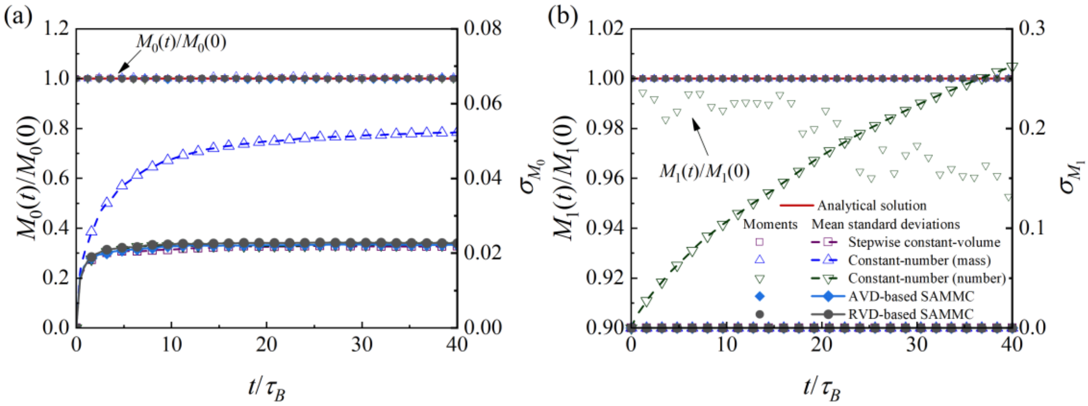

Figure 5.17 Time evolutions of total particle number and mass/volume concentrations and their corresponding mean standard deviations for simultaneous coagulation and breakage of constant breakage rate (i.e. 0.5) with initial monodispersed distribution and uniform daughter PSD in Case 12 [38].

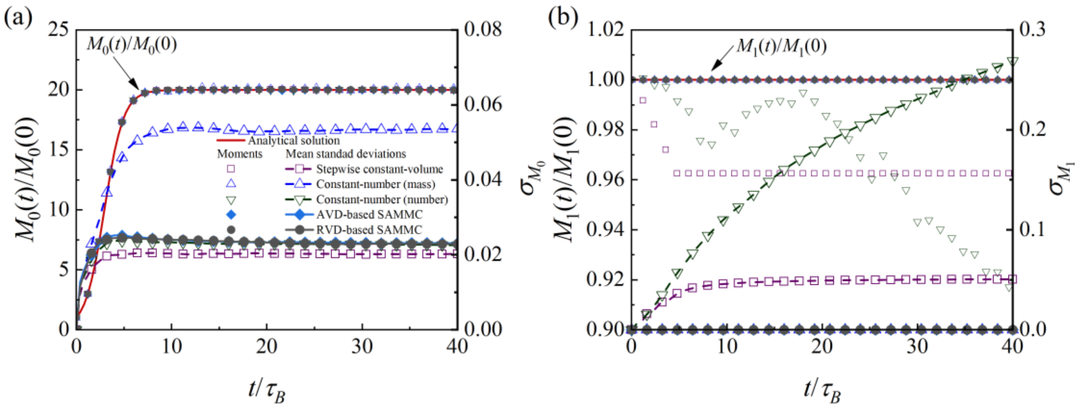

Figure 5.18 Time evolutions of total particle number and mass/volume concentrations and their corresponding mean standard deviations for simultaneous coagulation and breakage of constant breakage rate (i.e. 10) with initial monodispersed distribution and uniform daughter PSD in Case 13 [38].

5.3.5.3 Simultaneous coagulation and breakage of constant breakage rate (i.e., 0.5) with initial exponential distribution and uniform daughter PSD

Unlike Case 12, the initial PSD of Case 14 is exponential distribution, which is used to study the effect of initial PSD on the computational accuracy of M_0 and M_1 in the newly developed SAMMC methods by comparing with analytical solutions [37]. Numerical results show that σ_{M_0} and σ_{M_1} obtained from AVD- and RVD-based SAMMC methods for initial exponential distribution are at the same level of those for initial monodispersed distribution, which demonstrates that the initial PSD has no effect on the computational accuracy of AVD- and RVD-based SAMMC methods. Mass- and number-based constant-number methods only conserve either total particle number concentration or total particle mass/volume concentration, which lead to large σ_{M_0} or σ_{M_1}, respectively. The stepwise constant-volume method and AVD- and RVD-based SAMMC methods agree excellent with the analytical solutions, which have the lowest stochastic error in M_0 and do not have any stochastic error of M_1 in Figure 5.19.

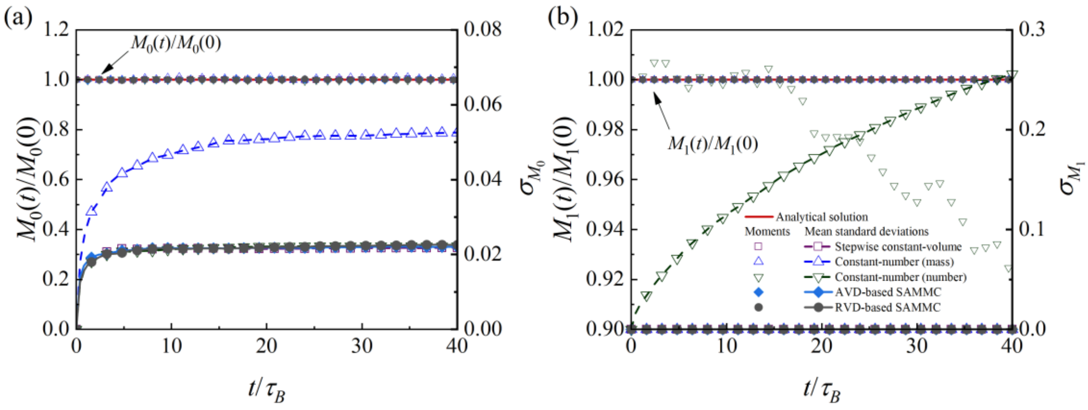

Figure 5.19 Time evolutions of total particle number and mass/volume concentrations and their corresponding mean standard deviations for simultaneous coagulation and breakage of constant breakage rate (i.e. 0.5) with initial exponential distribution and uniform daughter PSD in Case 14 [38].

5.3.5.4 Simultaneous coagulation and breakage of linear breakage rate (i.e., 0.5*v*) with initial exponential distribution and uniform daughter PSD

This Case 15 is very special for simultaneous coagulation and breakage, because the initial exponential PSD is also its steady state solution, which implies that the PSD at any time remains constant, leading to M_1, M_2 and M_3 remaining unchanged with time. The analytical solutions are presented by Patil and Andrews [222], Figure 5.20 shows the time evolutions of M_0, M_1 and M_2 and their corresponding mean standard deviations (i.e., σ_{M_0}, σ_{M_1} and σ_{M_2}) and the resulting number-based PSDs at t/τ_B = 0, 0.5, 1, 1.5 and 2.5 obtained from different MC methods. The number-based constant-number method shows obvious mass non-conservation, and the largest stochastic error in M_1 is still observed in the mass-based constant-number method. AVD- and RVD-based SAMMC methods and the stepwise constant-volume method show excellent agreement of M_1, M_2 and M_3 with analytical solutions and have almost the same stochastic errors. The PSDs with the exponential distribution obtained from all MC methods agree well with the analytical solutions and are always preserved at different times, t/τ_B.

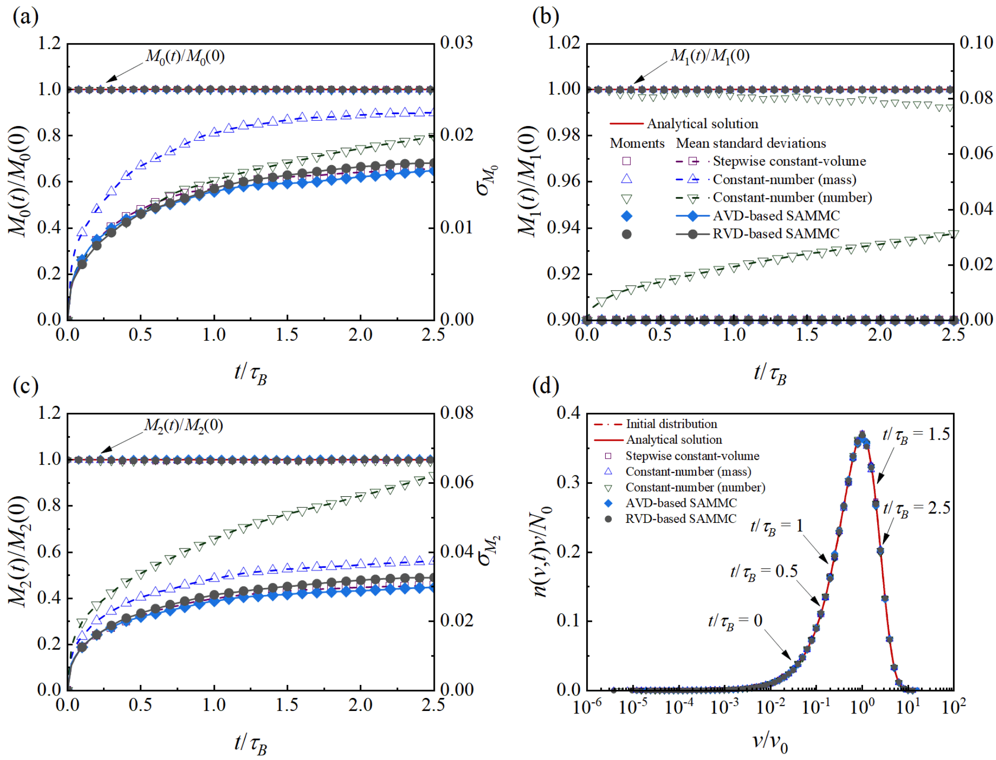

Figure 5.20 Time evolutions of total particle number and mass/volume concentrations and their corresponding mean standard deviations for simultaneous coagulation and breakage of linear breakage rate (i.e. 0.5*v*) with initial exponential distribution and uniform daughter PSD in Case 15 [38].

5.3.5.5 Computational time for simultaneous coagulation and breakage

The computational time of all MC methods for simultaneous coagulation and breakage are compared and listed in Table 5.6. As the MMC method introduces large systematic errors in Cases 10 to 15, the computational time is not shown here. Generally, the stepwise constant-volume method has the highest computational efficiency, because the number of numerical particles survived in the array is normally smaller than other MC methods. But the exception is the Case 13 which is dominated by breakage as the number of numerical particles always changes between N_S and $2N_S$, leading to less computational efficiency. The reason is that when the number of numerical particles is larger than N_S, more computational time would be required than using N_S numerical particles. By comparison, other MC methods spend almost the same time for different cases (i.e., Cases 11, 12, 14 and 15), and AVD- and RVD-based SAMMC methods have only slightly higher computational time than mass- and number-based constant-number methods. It demonstrates that AVD- and RVD-based SAMMC methods are highly computationally efficient in dealing with simultaneous coagulation and breakage for different computational conditions.

Table 5.6 Comparison of computational times for Cases 10 to 15 [38].

t (s)	Case 10	Case 11	Case 12	Case 13	Case 14	Case 15
Stepwise constant-volume	1128.78	1126.82	1127.62	1812.92	1105.38	52.71
Constant-number (mass)	1802.14	1807.00	1816.43	1796.78	1809.26	79.46
Constant-number (number)	1935.85	1908.52	1917.84	1814.61	1810.76	78.71
MMC	—	—	—	—	—	—
SAMMC (absolute)	1910.70	1920.14	1935.05	1863.68	1916.05	85.06
SAMMC (relative)	1965.08	2049.78	1964.26	1943.42	1932.55	85.18

Remarks: There exist large systematic errors in MMC method for simultaneous coagulation and breakage, so the corresponding computational times as well as numerical results for Cases 10 to 15 are not shown here.

5.3.6 Deposition

Deposition refers to the removal of numerical particles out of the computational domain, resulting in the constant decrease of the number of numerical particles. Numerical particle, i is not tracked anymore if being selected to conduct deposition, resulting in the reduction of the number of numerical particles. The initial total particle number concentration for pure deposition, $N_0 = 10^{10}$ m^{-3} [157] is used with monodispersed PSD, and constant deposition rate, $D(v) = D_0 = 10^{-5}$ s^{-1} [157] is used. The corresponding analytical solution is calculated and obtained from the derived equation in Zhao et al. [157]. The numerical particle number, N_S used is 2000, and $\tau_D = 1/D_0$ represents the characteristic deposition time. In Case 16, the PSD is always monodispersed with volume $v = 1$ (dimensionless), the evolutions of the particle number and particle volume/mass concentrations over time are always the same. Thus, only the particle number concentration (i.e., M_0) over time is shown here. Figure 5.21 shows that the total particle number concentration (i.e., M_0) has an excellent agreement with analytical solution.

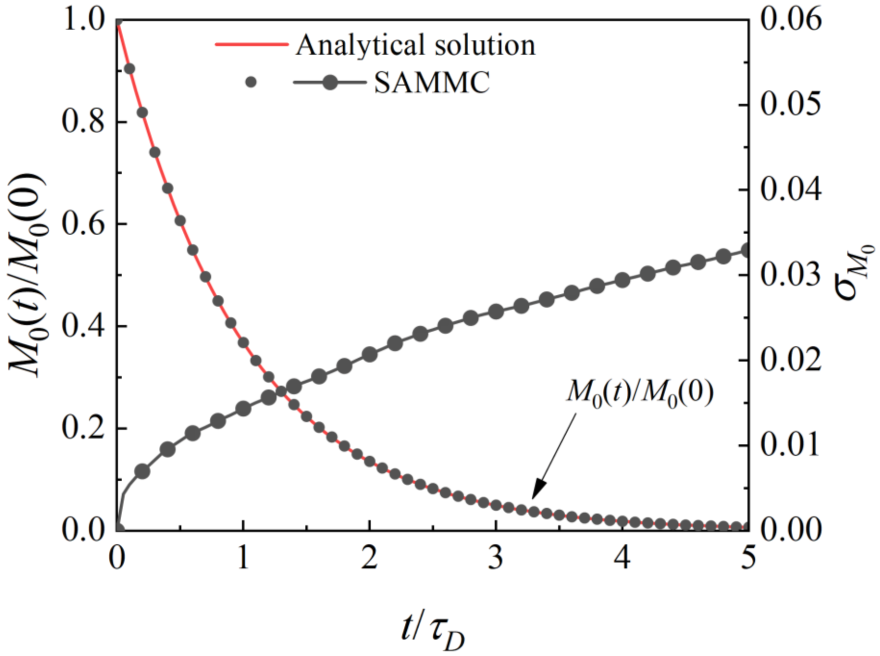

Figure 5.21 Time evolutions of total particle number concentrations and the corresponding mean standard deviations for deposition with initial monodispersed distribution in Case 16 [38].

5.3.7 Condensation/evaporation

Condensation/evaporation leads to the change in the particle volumes but would not change the particle number. The PBE for condensation/evaporation in the continuous form is used, and the condensation rate is linear with particle volumes, $I(v) = \sigma_1 v$ [16]. It should be noted that condensation occurs if $\sigma_1 > 0$, while it is an evaporation process when $\sigma_1 < 0$. Only the condensation process is considered in Case 17 for simplicity as evaporation can be similarly considered. The initial total particle number concentration for condensation, $N_0 = 10^6$ m^{-3} is used with initial exponential PSD and the rate constant, $\sigma_1 = 1$ s^{-1} is used [176]. The corresponding analytical solution is calculated and obtained from the derived equations in Ramabhadran et al. [16]. The numerical particle number, N_S used is 2000, and $\tau_K = 1/\sigma_1$ represents the characteristic condensation time. Figure 5.22 shows the numerical results (i.e., M_0, M_1, M_2 and PSD) for condensation. As condensation would not change the total particle number, M_0 remains unchanged with time, therefore the mean standard deviation, σ_{M_0}, always equal to 0. M_1 and M_2 are in excellent accord with analytical solutions with very small mean standard deviations. The resulting PSD shows a “self-preserving” form with time, which agrees excellently with analytical solutions.

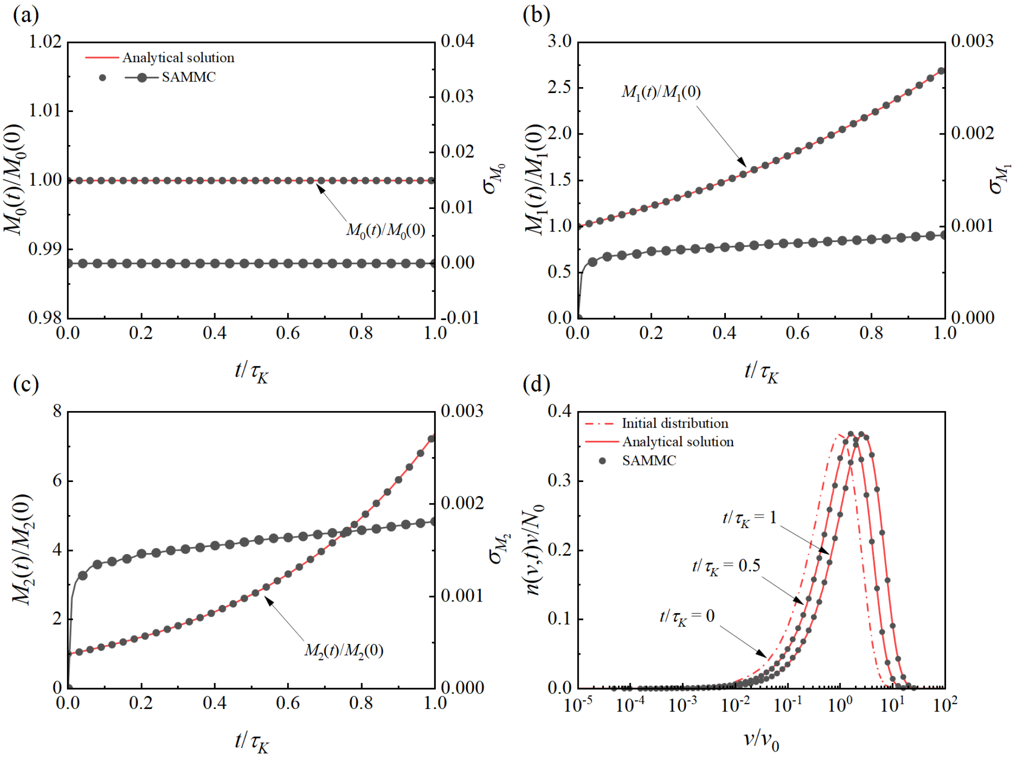

Figure 5.22 Time evolutions of zeroth- to second-order moments and their corresponding mean standard deviations, and PSDs for condensation with initial exponential distribution in Case 17 [38].

5.4 Summary

A new sorting algorithm-based merging Monte Carlo (SAMMC) method is developed to solve the general dynamic equation for aerosol dynamics. A neighbour merging method is newly proposed to maintain constant for the volume of the computational domain and the number of numerical particles with the information of numerical particle population preserved, where absolute volume difference (AVD) and relative volume difference (RVD) are used as the crucial merging criteria, respectively. Compared to previous MC methods, AVD- and RVD-based SAMMC methods proposed in the present study can be used for modelling all aerosol processes without introducing any systematic errors and the event-driven scheme is adopted to avoid introducing uncoupling errors during the numerical simulation. Hence, high-precision numerical results can be obtained.

The newly developed SAMMC method is applied to simulate aerosol dynamic processes involving nucleation, coagulation and breakage. The resulting statistical properties are compared with those obtained from the stepwise constant-volume method, mass- and number-based constant-number methods, multi-Monte Carlo (MMC) method, weighted fraction Monte Carlo (WFMC) method and sorting algorithm-based merging weighted fraction Monte Carlo (SAMWFMC) method. The computational accuracy is assessed by the mean standard deviations in the zeroth- to second-order moments of the PSDs in comparison with corresponding analytical solutions, while the computational efficiency is evaluated by the computational time consumed by the central processing unit.

Numerical results of AVD- and RVD-based SAMMC methods agree excellently with analytical solutions, which proves that these two methods have very high computational accuracy. For pure nucleation, AVD- and RVD-based SAMMC methods have lower stochastic errors and higher computational accuracy than equal-weight-based MC methods (i.e., stepwise constant-volume method and mass- and number-based constant-number methods), and they have the same computational efficiency and accuracy as the MMC method. The similar numerical results are also found in pure homogeneous coagulation. Although the stochastic errors in the high-order moment for AVD- and RVD-based SAMMC methods are higher than those of WFMC and SAMWFMC methods in non-homogeneous coagulation, more accurate total particle number concentrations are found in AVD- and RVD-based SAMMC methods but have slightly higher computational times. In addition, large systematic errors for breakage-related processes and simultaneous coagulation and nucleation are introduced in the MMC method, leading numerical results to a large deviation from analytical solutions. By comparison, the newly proposed AVD- and RVD-based SAMMC methods can completely deal with breakage-related processes and simultaneous coagulation and nucleation process with very high computational accuracy at only slightly higher computational cost. It is also found that the computational accuracy of AVD- and RVD-based SAMMC methods are generally almost the same except for multi-breakage, where RVD-based SAMMC methods has higher computational accuracy than the AVD-based SAMMC methods. Furthermore, the computational efficiencies of AVD- and RVD-based SAMMC methods for all aerosol dynamic processes are also almost the same.

Chapter 6 Development of Reacting Flow Solver Incorporating Detailed Transport Model for Combustion Simulations

6.1 Introduction

OpenFOAM (Open-source Field Operation and Manipulation) has become an important scientific tool for solving computational fluid dynamics due to its free and open-source nature, but its application in reacting flows may be restricted due to either the use of a simplified transport model or the requirement for pre-specified species (binary) mass diffusion coefficients as well as the use of Sutherland's formula. Since two empirical parameters (i.e., Sutherland coefficient and Sutherland temperature) are used in the Sutherland's formula, it is not accurate enough to calculate the transport properties of a number of species. To fill this gap, a detailed transport model using a mixture-averaged formulation based on the standard kinetic theory of gases is newly incorporated into combustion solvers for dealing with reacting flow simulations in OpenFOAM. This is achieved by developing a new utility to input molecular transport parameters and a new library to calculate transport properties. All the codes are completely written under the code framework of OpenFOAM, making them very easy to read, use, maintain, enhance and extend. The developed utility and library are then coupled with a new reacting flow solver developed for the governing equations in terms of mass, momentum, species and energy by configurating an interface. In the present study, the function of the new utility is firstly examined and then a new solver (i.e., *standardReactingFoam*) is developed for solving reacting flows. A systematical validation and assessment in different flame configurations with detailed chemical kinetics is studied to evaluate the computational performance of these new solvers.

6.2 Mathematical Models

6.2.1 Governing equations

The present study aims at computational fluid dynamics (CFD) calculations of reacting flows, where the mixture-averaged transport model is used as the detailed transport model for differential diffusion of species. The governing equations in terms of mass, momentum, species and energy without considering Soret and Dufour effects [80,81] are formulated as [223,224]:

$$\frac{\partial \rho}{\partial t} + \nabla \cdot (\rho \mathbf{U}) = 0 \tag{6-1}$$

$$\frac{\partial (\rho \mathbf{U})}{\partial t} + \nabla \cdot (\rho \mathbf{U}\mathbf{U}) - \nabla \cdot \boldsymbol{\tau} = -\nabla p \tag{6-2}$$

$$\frac{\partial (\rho Y_k)}{\partial t} + \nabla \cdot (\rho Y_k \mathbf{U}) + \nabla \cdot (\rho Y_k \mathbf{V}_{\boldsymbol{k}}) = \omega_k \tag{6-3}$$

$$\begin{aligned} \frac{\partial (\rho h_s)}{\partial t} + \nabla \cdot (\rho \mathbf{U} h_s) + \frac{\partial (\rho K)}{\partial t} + \nabla \cdot (\rho \mathbf{U} K) - \frac{\partial p}{\partial t} \\ = -\nabla \cdot \mathbf{q} + Q_r + \omega_T + \nabla \cdot (\boldsymbol{\tau} \cdot \mathbf{U}) \end{aligned} \tag{6-4}$$

where t is time and **U** is velocity; ρ and p are density and pressure, respectively; Y_k and ω_k are the mass fraction and reaction rate of species k, respectively; h_s is mixture sensible enthalpy and K is kinematic energy; $\boldsymbol{\tau}$ is viscous stress tensor, which is formulated based on the Stokes hypothesis [80,81] as [224]:

$$\boldsymbol{\tau} = -\frac{2}{3}\mu(\nabla \cdot \mathbf{U})\mathbf{I} + \mu[\nabla \mathbf{U} + (\nabla \mathbf{U})^T] \tag{6-5}$$

where μ is dynamic viscosity and **I** is the unit tensor. The mass-average diffusion velocity of species k, $\mathbf{V}_k$ is computed in terms of the mole fraction gradient as [223,224]:

$$\mathbf{V}_k = -\frac{D_{k,\mathrm{mix}}}{X_k} \nabla X_k \tag{6-6}$$

where $D_{k,\mathrm{mix}}$ is the diffusion coefficient of the kth species into the rest of the mixture. It should be noted that it is required to correct the diffusion velocity for maintaining the global mass conservation [224], which is expressed as:

$$\mathbf{V}_k^C = \mathbf{V}_k + \mathbf{V}_C \tag{6-7}$$

where $\mathbf{V}_C$ is a spatially varying correction velocity but the same for all species at each time step [224], which is calculated as:

$$\mathbf{V}_C = -\sum_{k=1}^{N} Y_k \mathbf{V}_k \tag{6-8}$$

where N is the number of species. It is common in the combustion community to solve the transport equations of all species except for the inert species firstly, and then to obtain the mass fraction of the inert species by explicitly subtracting the solved mass fractions of the rest of species from one. As a result, all inconsistencies introduced by the system can be absorbed by the inert species. It should be noted that this method is still effective when the correction velocity is introduced and used. Similarly, the diffusion flux of the inert species is explicitly computed to satisfy the condition of zero net species diffusion flux [224] as:

$$\sum_{k=1}^{N} \rho Y_k \mathbf{V}_k = 0 \tag{6-9}$$

In Equation (6-4), the heat flux including heat conductivity and mass diffusion of species is computed as [81,224]:

$$\mathbf{q} = -\lambda \nabla T + \sum_{k=1}^{N} \rho h_{s,k} Y_k \mathbf{V}_k = -\left(\frac{\lambda}{C_p} \nabla h_s - \sum_{k=1}^{N} \frac{\lambda}{C_p} h_{s,k} \nabla Y_k \right) + \sum_{k=1}^{N} \rho h_{s,k} Y_k \mathbf{V}_k \tag{6-10}$$

where T is temperature and $h_{s,k}$ is the sensible enthalpy of species k; λ and C_p are thermal conductivity and specific heat capacity of the mixture at constant pressure, respectively. The heat production rate due to combustion, ω_T is given as [224]:

$$\omega_T = -\sum_{k=1}^{N} h_{f,k} \omega_k \tag{6-11}$$

where $h_{f,k}$ is the formation enthalpy of species k. Q_r is the radiative heat source, while the heat source originating from viscous stress can be neglected in low Mach number flows [223].

The ratio of thermal diffusivity to mass diffusivity of a species is defined by a dimensionless number, Le_k, which is expressed as [72]:

$$Le_k = \frac{\lambda}{\rho C_p D_{k,\mathrm{mix}}} \tag{6-12}$$

When Lewis numbers of all species are assumed to be unity (i.e., unity Lewis number transport model), the contribution from mass diffusion of species in Equation (6-10) to energy transport is neglected [81], leading to a simplified energy transport equation. By comparison, the constant non-unity Lewis number approximation can lead to acceptable numerical results, but the Lewis number is highly species-dependent [72].

The governing equations are closed by the perfect gas assumption [81], where the equation of state of a mixture is expressed as [223,224]:

$$p = \rho \frac{R_u}{W} T \tag{6-13}$$

where R_u is the universal gas constant and W is the mean molecular weight of the mixture. For a mixture composed of N perfect gases, the total pressure of the mixture is the sum of the partial pressures of each gas [223,224].

$$p = \sum_{k=1}^{N} p_k = \sum_{k=1}^{N} \rho_k \frac{R_u}{W_k} T \tag{6-14}$$

where ρ_k and W_k are the density and molecular weight of the kth species, respectively.

6.2.2 Thermodynamic properties

The thermodynamic properties of a perfect gas only vary with temperature, which are obtained from the National Aeronautics and Space Administration (NASA) polynomials based on the Joint Army Navy Air Force (JANAF) table of thermodynamics [225]. Therefore, the molar specific heat capacity (i.e., $C_{p,k}$) at constant pressure, enthalpy (i.e., H_k) and entropy (i.e., S_k) of kth species at standard state are calculated as [83,90]:

$$\frac{C_{p,k}}{R_u} = \sum_{n=1}^{5} a_{n,k} T^{n-1} \tag{6-15}$$

$$\frac{H_k}{R_u T} = \sum_{n=1}^{5} \frac{a_{n,k} T^{n-1}}{n} + \frac{a_{6,k}}{T} \tag{6-16}$$

$$\frac{S_k}{R_u} = a_{1,k} \ln T + \sum_{n=2}^{5} \frac{a_{n,k} T^{n-1}}{n-1} + \frac{a_{7,k}}{T} \tag{6-17}$$

where $a_{n,k}$ are the least-squares coefficients [90] which are different for each species. The thermodynamic properties of a multi-species mixture on a per mass basis are then calculated by summing up the contributions of each species in terms of mass fraction.

6.2.3 Transport properties

The mixture-averaged approach based on the pure species properties is used to efficiently approximate the transport properties of the mixture. The mixture viscosity is calculated as [223,226]:

$$\mu = \sum_{k=1}^{N} \frac{X_k \mu_k}{\sum_{j=1}^{N} X_j \Phi_{kj}} \tag{6-18}$$

where

$$\Phi_{kj} = \frac{1}{\sqrt{8}} \left(1 + \frac{W_k}{W_j}\right)^{-\frac{1}{2}} \left[1 + \left(\frac{\mu_k}{\mu_j}\right)^{\frac{1}{2}} \left(\frac{W_j}{W_k}\right)^{\frac{1}{4}}\right]^2 \tag{6-19}$$

where μ_k and μ_j are the viscosity of pure species, *k* and *j*, respectively.

A combination averaging formula is used to calculate the mixture-averaged thermal conductivity, which is given as [223,226]:

$$\lambda = \frac{1}{2} \left(\sum_{k=1}^{N} X_k \lambda_k + \frac{1}{\sum_{k=1}^{N} X_k / \lambda_k} \right) \tag{6-20}$$

where X_k represents the mole fraction of *k*th species, and λ_k is the thermal conductivity of pure species *k*.

The mixture-averaged diffusion coefficient of species *k* in the rest of the mixture, $D_{k,\mathrm{mix}}$, is approximated as [223,226]:

$$D_{k,\mathrm{mix}} = \frac{1 - Y_k}{\sum_{j=1, j \neq k}^{N} X_j / D_{jk}} \tag{6-21}$$

where D_{jk} is the binary diffusion coefficient between species *k* and species *j*.

6.2.3.1 Pure species properties

For a pure species *k*, its viscosity μ_k is calculated by the standard kinetic theory expression as [223,226]:

$$\mu_k = \frac{5}{16} \frac{\sqrt{\pi m_k k_B T}}{\pi \sigma_k^2 \Omega_{kk}^{(2,2)*}} \tag{6-22}$$

where k_B is the Boltzmann constant, m_k is the molecular mass, σ_k is the Lennard-Jones collision diameter, and $\Omega_{kk}^{(2,2)*}$ is the reduced collision integral.

The thermal conductivity (i.e., λ_k) of pure species *k* comprising translational, rotational and vibrational contributions is obtained from its viscosity (i.e., μ_k) as [223,226]:

$$\lambda_k = \frac{\mu_k}{W_k}\left(f_{\text{trans}}C_{v,\text{trans}} + f_{\text{rot}}C_{v,\text{rot}} + f_{\text{vib}}C_{v,\text{vib}}\right) \tag{6-23}$$

where

$$f_{\text{trans}} = \frac{5}{2}\left(1 - \frac{2}{\pi}\frac{C_{v,\text{rot}}}{C_{v,\text{trans}}}\frac{A}{B}\right) \tag{6-24}$$

$$f_{\text{rot}} = \frac{\rho D_{kk}}{\mu_k}\left(1 + \frac{2}{\pi}\frac{A}{B}\right) \tag{6-25}$$

$$f_{\text{vib}} = \frac{\rho D_{kk}}{\mu_k} \tag{6-26}$$

$$A = \frac{5}{2} - \frac{\rho D_{kk}}{\mu_k} \tag{6-27}$$

$$B = Z_{\text{rot}} + \frac{2}{\pi}\left(\frac{5}{3}\frac{C_{v,\text{rot}}}{R_u} + \frac{\rho D_{kk}}{\mu_k}\right) \tag{6-28}$$

where D_{kk} is the self-diffusion coefficient of molecule k, and the rotational relaxation collision number, Z_{rot} is dependent on temperature expressed by [223,226]:

$$Z_{\text{rot}}(T) = Z_{\text{rot}}(298)\frac{F(298)}{F(T)} \tag{6-29}$$

where

$$F(T) = 1 + \frac{\pi^{3/2}}{2}\left(\frac{\epsilon_k/k_B}{T}\right)^{1/2} + \left(\frac{\pi^2}{4} + 2\right)\left(\frac{\epsilon_k/k_B}{T}\right) + \pi^{3/2}\left(\frac{\epsilon_k/k_B}{T}\right)^{3/2} \tag{6-30}$$

where ϵ_k is Lennard-Jones potential well depth of molecule k.

The total molar specific heat capacity at constant volume is denoted by C_v, and the contributions to C_v from translation, vibration and rotation are denoted as $C_{v,\text{trans}}$, $C_{v,\text{vib}}$ and $C_{v,\text{rot}}$, respectively. The molar heat capacities depend on the geometry of the molecule (i.e., single atom, linear or non-linear), which are given as [223,226]:

$$C_{v,\text{trans}} = \frac{3}{2}R_u \tag{6-31}$$

$$C_{v,\text{rot}} = \begin{cases} 0, \text{single atom} \\ R_u, \text{linear molecule} \\ \frac{3}{2}R_u, \text{nonlinear, polyatomic molecule} \end{cases} \tag{6-32}$$

$$C_{v,\text{vib}} = C_v - C_{v,\text{trans}} - C_{v,\text{rot}} \tag{6-33}$$

6.2.3.2 Binary diffusion coefficient

The binary diffusion coefficient is associated with temperature and pressure, which is defined as [223,226]:

$$D_{jk} = \frac{3}{16}\frac{\sqrt{2\pi k_B^3 T^3/m_{jk}}}{p\pi\sigma_{jk}^2\Omega_{jk}^{(1,1)*}} \tag{6-34}$$

where the reduced mass, m_{jk} is defined as [223,226]:

$$m_{jk} = \frac{m_j m_k}{m_j + m_k} \tag{6-35}$$

The collision integrals $\Omega_{jk}^{(1,1)*}$ and $\Omega_{jk}^{(2,2)*}$ are calculated by [223]:

$$\Omega_{jk}^{(1,1)*} = [a_1(T^*)^{-a_2} + (T^* + a_3)^{-a_4}]\left[1 + \frac{\left(e^{a_5/T^*} - e^{-a_6/T^*}\right)\left(\delta_{jk}^*\right)^2}{2 + 2.5\delta_{jk}^*}\right] \tag{6-36}$$

$$\Omega_{jk}^{(2,2)*} = [b_1(T^*)^{-b_2} + (T^* + b_3)^{-b_4}]\left[1 + \frac{\left(e^{b_5/T^*} - e^{-b_6/T^*}\right)\left(\delta_{jk}^*\right)^2}{2 + 2.5\delta_{jk}^*}\right] \tag{6-37}$$

where coefficients, a_m and b_m, are provided in Table 6.1.

Table 6.1 Coefficients [223] of Equations (6-36) and (6-37) [53].

Coefficient	$m = 1$	$m = 2$	$m = 3$	$m = 4$	$m = 5$	$m = 6$
a_m	1.0548	0.15504	0.55909	2.1705	0.093193	1.5
b_m	1.0413	0.11930	0.43628	1.6041	0.095661	2.0

T^* and δ_{jk}^* are the reduced temperature and dipole moment, respectively, which are defined as [223,226]:

$$T^* = \frac{Tk_B}{\epsilon_{jk}} \tag{6-38}$$

$$\delta_{jk}^* = \frac{1}{2}\frac{\bar{\mu}_j\bar{\mu}_k}{\epsilon_{jk}\sigma_{jk}^3} \tag{6-39}$$

where $\bar{\mu}_k$ is the dipole moment of the *k*th species, and σ_{jk} and ϵ_{jk} are the effective collision diameter and Lennard-Jones potential well depth of species *j* and *k*, respectively, which are associated with their polarizabilities α_j and α_k. For two polar molecules or two nonpolar molecules *j* and *k*, the reduced quantities are calculated as [223,226]:

$$\epsilon_{jk} = \sqrt{\epsilon_j\epsilon_k} \tag{6-40}$$

$$\sigma_{jk} = \frac{1}{2}\left(\sigma_j + \sigma_k\right) \tag{6-41}$$

But when a polar molecule interacts with a nonpolar molecule, the reduced quantities are corrected as [223,226]:

$$\epsilon_{jk} = \xi^2\sqrt{\epsilon_j\epsilon_k} \tag{6-42}$$

$$\sigma_{jk} = \frac{1}{2}\left(\sigma_j + \sigma_k\right)\xi^{-1/6} \tag{6-43}$$

where

$$\xi = 1 + \frac{1}{4}\alpha_n^*\bar{\mu}_p^*\sqrt{\frac{\epsilon_p}{\epsilon_n}} \tag{6-44}$$

The subscripts "*n*" and "*p*" denote the "nonpolar" and "polar", respectively. $\bar{\mu}_p^*$ and α_n^* are the reduced dipole moment of the polar molecule and polarizability of the nonpolar molecule, which are defined as [223,226]:

$$\alpha_n^* = \frac{\alpha_n}{\sigma_n^3} \tag{6-45}$$

$$\bar{\mu}_p^* = \frac{\bar{\mu}_p}{\sqrt{\epsilon_p\sigma_p^3}} \tag{6-46}$$

It should be noted that when substituting the subscript "*j*" with "*k*" in the Equation (6-34), the self-diffusion coefficient, D_{kk} used in Equations (6-25) to (6-28) is obtained. Similarly, the $\Omega_{kk}^{(2,2)*}$ in Equation (6-22) is calculated by changing "*j*" to "*k*" in Equation (6-37).

6.3 Implementation

In this section, the critical incorporation of a detailed transport model into a new combustion solver for reacting flow simulations in OpenFOAM is presented in detail, which is achieved by a newly developed utility named *standardChemkinToFoam* and a newly developed library named *thermophysicalModels*. The new *thermophysicalModels* library includes several sub-libraries, which are generated by *ThermoType*, *ChemistryReader*, *MixtureType* and *BasicType* code blocks. All the newly developed codes with a user guide are provided, which involves three versions of OpenFOAM (i.e., OpenFOAM 6, OepenFOAM 11 and OpenFOAM v2306). Developing the libraries, utility and solvers of different OpenFOAM versions can meet the requirements of users using different OpenFOAM versions. In the present study, the authors use OpenFOAM 6 as an example to explain the development of all the libraries, utility and solvers. The code structures of OpenFOAM v2306 related to the developed libraries, utility and solvers are nearly the same as OpenFOAM 6. It should be noted that due to the significant change in the code structure of OpenFOAM 11 (a recent version of OpenFOAM by The OpenFOAM Foundation), some modifications should be made to the development procedures in the user manual of OpenFOAM 6 when implementing in OpenFOAM 11. Specifically, the development of libraries and utility in OpenFOAM 11 is similar with those in OpenFOAM 6 and OpenFOAM v2306, but the development of solvers in OpenFOAM 11 is totally different. For example, the *reactingFoam* solver was provided in all versions of OpenFOAM by ESI OpenCFD as well as OpenFOAM 10 and earlier versions by The OpenFOAM Foundation. By comparison, OpenFOAM 11 uses a modular library named *multicomponentFluid* to replace the *reactingFoam* solver in other versions with significant changes in the code structure. In order to follow these new features in OpenFOAM 11, the *standardReactingFoam* solver incorporating the detailed transport model in the present study is correspondingly modified to a library named *standardMulticomponentFluid*, which is developed based on the *multicomponentFluid* library. All these newly developed libraries, utility and solvers of these OpenFOAM versions are provided in the source codes to facilitate users. In addition, the computational performance (i.e., performance implications, simulation time and memory usage) of the solvers in different versions of OpenFOAM (i.e., OpenFOAM 6, OpenFOAM v2306 and OpenFOAM 11) are evaluated, which would facilitate users in choosing the solvers of different versions of OpenFOAM. It should also be noted that the resulting library and sub-libraries are applicable for any multi-species system involving molecular transport.

Based on the standard kinetic theory of gases, the calculation of transport properties in combustion modeling according to the derivation in Section 6.2 is accomplished by using the value of collision integrals developed from the Stochmayer potential [223], which is based on the Lennard-Jones potential [223] with polar interaction. The potential depends on six molecular transport parameters for each species that should be specified for eventually evaluating transport properties [67]. They are the indicator of molecule geometrical configuration in Equation (6-32), Lennard-Jones potential well depth (i.e., ϵ) in Equation (6-40), Lennard-Jones collision diameter (i.e., σ) in Equation (6-41), dipole moment (i.e., $\bar{\mu}$) in Equation (6-39), polarizability (i.e., α) in Equation (6-45) and rotational relaxation collision number (i.e., Z_{rot}) at 298K in Equation (6-29). Actually, all information in terms of these molecular transport properties are included in chemical reaction mechanisms in CHMEKIN format. Therefore, measures should be taken to handle these molecular transport parameters of a species.

Figure 6.1 shows the class diagram of a *ThermoType* Block in terms of a species. Following the object-oriented programming language (i.e., C++), each box denotes a class which consists of members and member functions, where "–" and "+" represent private and public, respectively. A solid line with a hollow arrow describes an inheritance relationship from a derived class to a base class.

The physical properties of a species are directly or indirectly calculated and stored in individual classes. For example, the *specie* class is developed to input and store data including name, mass fraction and mole weight of a species, and then species density is determined by pressure and temperature according to the selected equation of state (i.e., perfect gas). The thermodynamic properties of this perfect-gas species including specific heat capacity and absolute enthalpy are calculated based on the Joint Army Navy Air Force (JANAF) tables [52] of thermodynamics. In the original code of OpenFOAM [52], the *sutherlandTransport* class derived from the *thermo* class is developed to accommodate transport properties of a species, which should be replaced in the present study. Thus, a new class in terms of transport properties should be developed to read and store molecular transport parameters of a species. As detailed transport models are based on the standard kinetic theory of gases, this newly developed class is referred to as "*standardKineticTransport*" in the present study, which is presented by a red box in Figure 6.1.

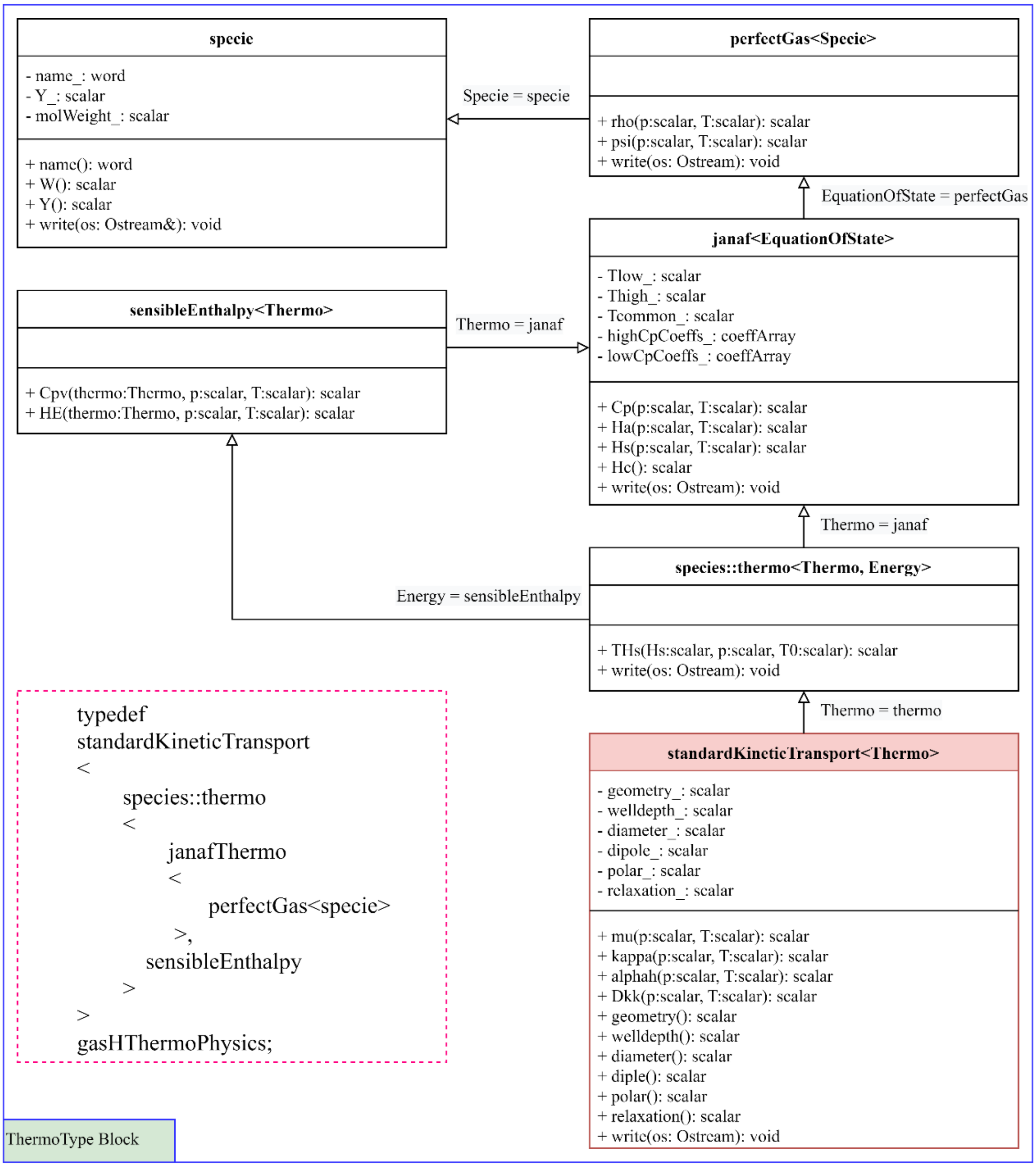

```
typedef
standardKineticTransport
<
    species::thermo
    <
        janafThermo
        <
            perfectGas<specie>
        >,
      sensibleEnthalpy
    >
>
gasHThermoPhysics;
```

Figure 6.1 Class diagram of *ThermoType* Block based on standard kinetic theory [53].

The six critical molecular transport parameters of a species required by a detailed transport model are performed as private members of the *standardKineticTransport* class with self-explanatory names, which can be accessed by individual public member functions. The transport properties of a species including dynamic viscosity, thermal conductivity, thermal diffusivity of enthalpy and self-diffusion coefficient are evaluated by individual member functions of the *standardKineticTransport* class, which are dependent on pressure and temperature. Consequently, all parameters of a species involved in a detailed transport model are available by the member functions of the *standardKineticTransport* class. It should be noted that the *standardKineticTransport* class is derived from many base classes, leading to a rather long name as shown in Figure 6.1, so an alias of "*gasHThermoPhysics*" is provided for later convenient use.

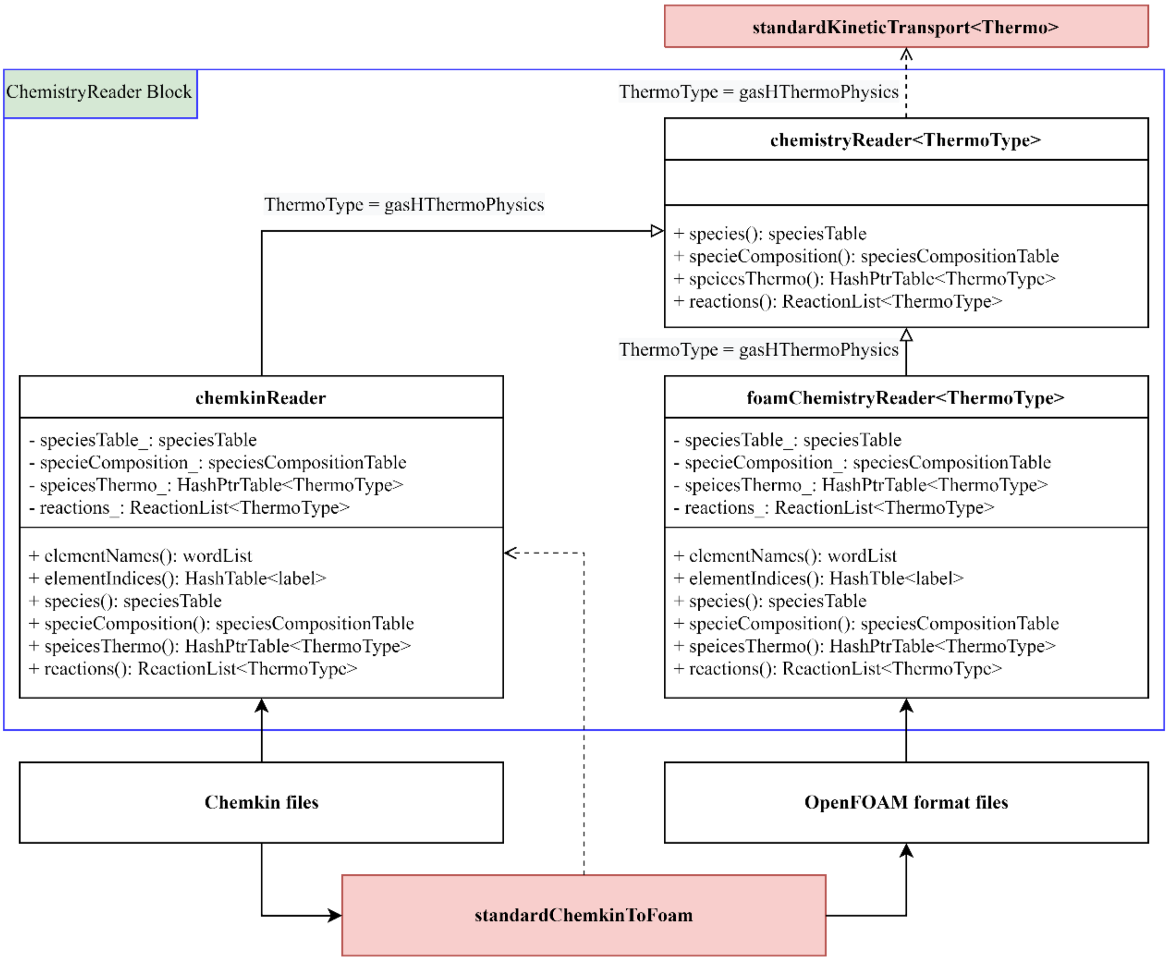

Figure 6.2 Class diagram of *ChemistryReader* Block interfacing with *standardChemkinToFoam* utility based on standard kinetic theory [53].

Before storing the six molecular transport parameters of a species with respect to a detailed transport model, all these information should be inputted first, which is accomplished by the *chemistryReader* class. Figure 6.2 shows the class diagram of the *ChemistryReader*

Block interfacing with a newly developed *standardChemkinToFoam* utility to achieve the input of all parameters required by chemically reacting flow simulations. A dashed line with an arrow denotes the dependency of one class on another, which means that the *chemistryReader* class uses the newly developed *standardKineticTransport* class. Specifically, the *chemkinReader* or *foamChemistryReader* class derived from the *chemistryReader* class is used to achieve reading chemical kinetic, thermodynamic and transport quantities, where all transport properties of all species are then stored due to the use of the *standardKineticTransport* class. As a result, a chemical reaction mechanism transformed by the *standardChemkinToFoam* utility is inputted by either *chemkinReader* or *foamChemistryReader*, which is based on the *standardKineticTransport* class in the present study, leading to the dependence of any case of reacting flows on the *standardKineticTransport* class.

It should be noted that the format of a file comprising molecular transport parameters should be readable by OpenFOAM, so a new utility named *standardChemkinToFoam* with a highlighted red box is developed as shown in Figure 6.2, which is based on the existing *chemkinToFoam* utility in original OpenFOAM. The solid line with a solid arrow shows the procedure of file processing. The *standardChemkinToFoam* utility uses the *chemkinReader* class to read chemical reaction mechanism files in CHEMKIN format and transforms them to OpenFOAM format. After executing the new utility, both chemistry readers (i.e., *chemkinReader* and *foamChemistryReader*) can correctly read and store all the information provided by the chemical reaction mechanism file, especially those neglected by the original OpenFOAM. It is of great significance to note that the use of the *standardChemkinToFoam* utility is completely the same as that of the original *chemkinToFoam* utility so that the operation is very friendly and easy.

Figure 6.3 presents the critical class diagram of the *MixtureType* block where multi-species mixture properties are handled according to a detailed transport model. Protected members and member functions are marked by “#” in a C++ box. The class boxes requiring modification to be compatible with the detailed transport model are highlighted in light blue in Figure 6.3. Modifications of the *multiComponentMixture* class should be carried out to compute binary diffusion coefficient of two species as well as the dynamic viscosity and thermal diffusivity of enthalpy in a cell, patch and face. These variables are evaluated by adding corresponding member functions to the *multiComponentMixture* class, which are dependent on pressure and temperature. It should be noted that a member function also requires to be specified in this class when the unity Lewis or constant non-unity Lewis number transport model is considered for a multi-species system, where the interface between a running case and the selection of a transport model is configurated in the *thermophysicalProperties* file at the *constant* directory of the running case. In addition, a member function used to obtain the boundary and internal fields of diffusion coefficients of each species in the rest of the mixture should be added to the *reactingMixture* class, in which each cell, patch and face in the whole computational domain are looped. The diffusion coefficient of a species in the rest of the mixture is a function of pressure, temperature and mass fraction of each species. Therefore, all mixture properties of a multi-species system in the computational domain can be obtained by accessing corresponding member functions of the *reactingMixture* class, which is the base class of the *SpeciesMixture* class.

Figure 6.4 shows the class diagram of the *BasicType* block interfacing with a combustion solver for combustion modelling. It should be noted that the *BasicType* block can be psi-based or rho-based. As the implementation logics of psi-based and rho-based *BasicType* blocks are the same, an example of psi-based *BasicType* block is selected here to specify the algorithm. The *heThermo* class is derived from the *SpeciesMixture* class, which means that all mixture properties of the muti-species system can be also accessed by the *heThermo* class as well as its derived *hePsiThermo* class. This is also the same for the derived *heRhoThermo* class. It should be noted that dynamic viscosities and thermal diffusivities of enthalpy in each cell, patch and face are updated by the member function of the *hePsiThermo* class, which depends on the *psiThermo* class. Therefore, the thermophysical properties involving energy, heat and physical properties are computed by using the specified thermophysical models as shown in Figure 6.4. For reacting flow simulations, a combustion model depends on the *psiReactionThermo* class derived from the *psiThermo* class to return the thermophysical properties of the computational domain, which would be finally used by a combustion solver. Simultaneously, the dependency of the code blocks of chemistry models and turbulence models as well as radiation models on the *BasicType* code block should be updated accordingly. It demonstrates that the corresponding interface should be configured in a reacting flow solver, therefore leading to the requirement of developing a new combustion solver for governing equations in terms of mass, momentum, species and energy. It should be noted that the combustion solver relies on the *reactingMixture* class to provide diffusion coefficients of each species, which are finally used in the species and energy equations. Consequently, a new combustion solver incorporating a detailed transport model is developed with the combination of different chemistry models, turbulence models and radiation models, which is aimed at reacting flows of a multi-species system.

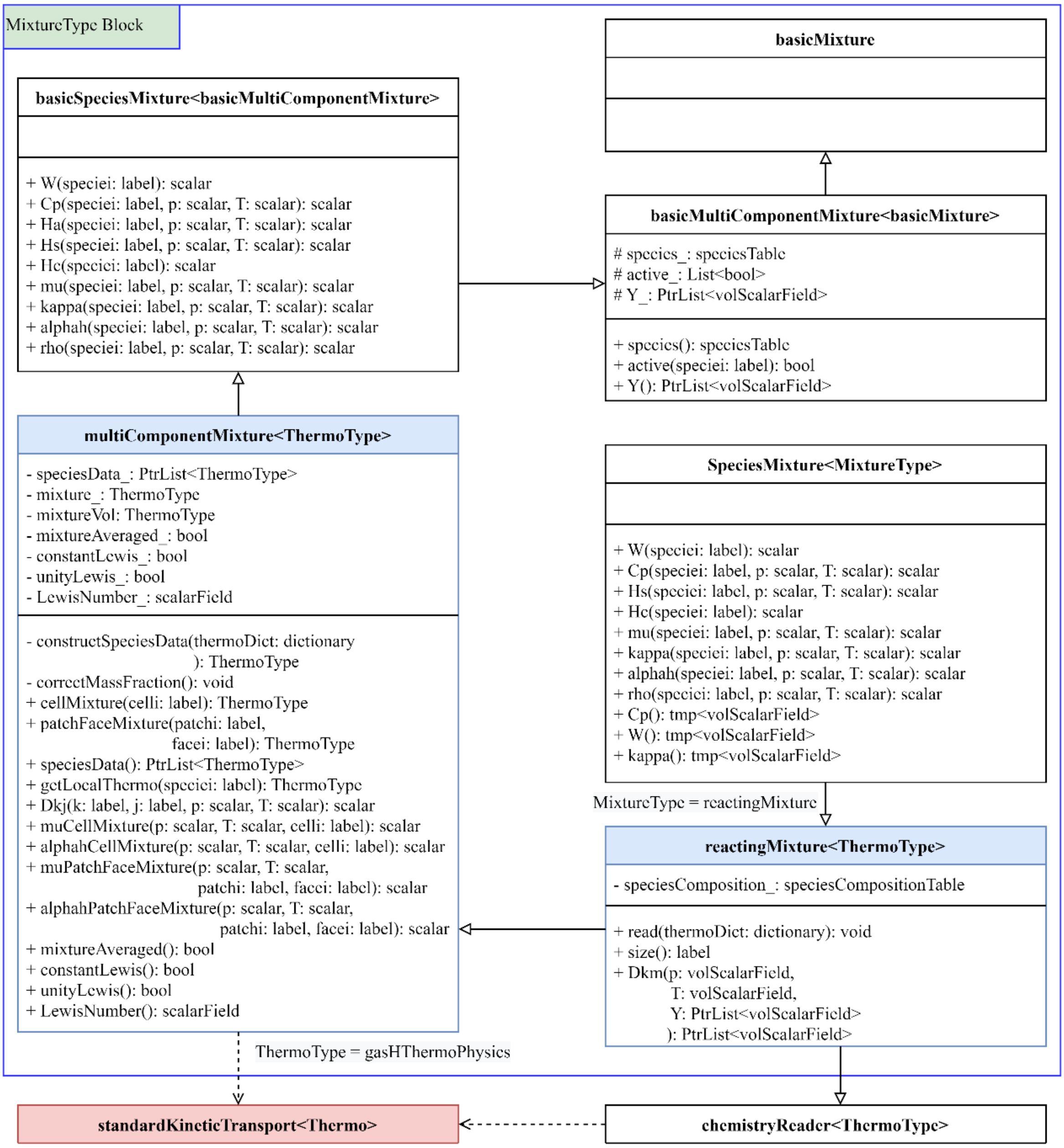

Figure 6.3 Class diagram of *MixtureType* Block based on standard kinetic theory [53].

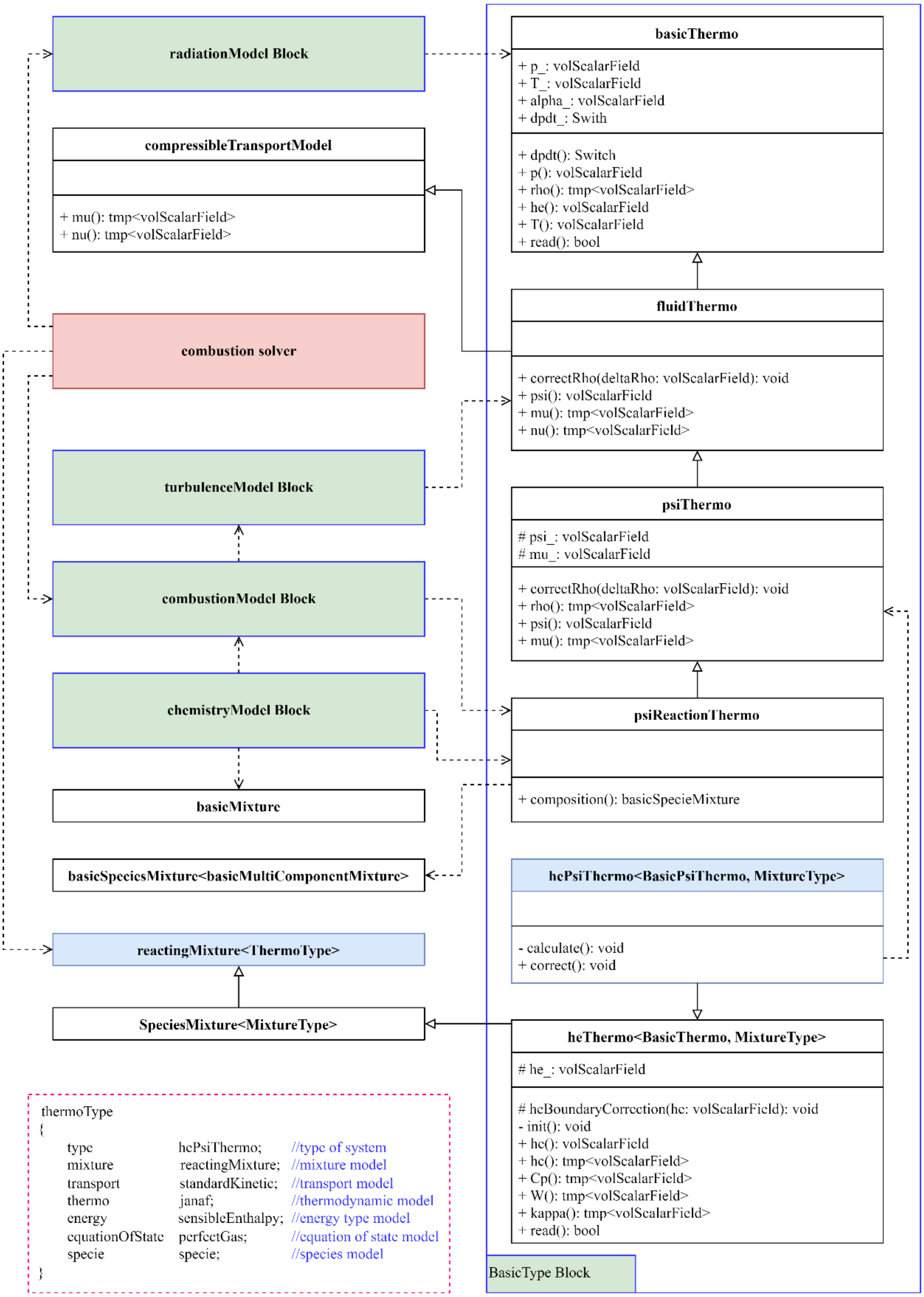

Figure 6.4 Class diagram of *BasicType* interfacing with combustion solver based on standard kinetic theory [53].

6.4 Results

Following the basic structure of OpenFOAM, governing equations including unsteady, convection, diffusion and source terms are approximated based on the finite volume method. The pressure implicit with splitting of operator (PISO) algorithm [227] is adopted to achieve the pressure-velocity coupling. Different numerical schemes for different physically meaningful terms are readily available in OpenFOAM [52]. In the present study, unsteady terms are discretized by a first-order time-stepping while a second-order central differencing scheme is adopted to discretize the convection and diffusion terms. The chemical reaction mechanism used is the well-known GRI-Mech 3.0 [187] involving 325 reactions and 53 species, which does not involve a pressure-dependent reaction type (i.e., pressure logarithmic interpolation, PLOG). It should be noted that this specific PLOG reaction type is used in some newly developed reaction mechanisms, which is not defined by the original OpenFOAM due to the lack of necessary functions to handle this reaction type [70,71]. As a result, PLOG cannot be supported by the libraries, utility and solvers developed in the present study. An Euler implicit solver is used for chemistry. Specifically, the Euler implicit integration based on the Jacobian matrix of reaction rates is used for solving the composition while the Euler explicit integration is used for solving temperature. The separation of temperature integration from composition integration significantly enhances stability for exothermic reaction systems. It should be noted that a well-balanced second-order accurate Strang splitting scheme may be required to handle flame extinction and re-ignition predictions since the splitting scheme used in the original OpenFOAM is the first-order accurate, which is not well-balanced [70,71]. The maximum Courant number is set to be 0.2 for constraining the time step of integration. Transport properties are calculated by the mixture-averaged transport model, and it is newly implemented and coupled with combustion solvers (i.e., *standardChemFoam* and *standardReactingFoam*) for a multi-species system, where the *standardChemFoam* solver is used for examining the function of the newly developed *standardChemkinToFoam* utility and then the *standardReactingFoam* solver is also newly developed for solving reacting flows.

In the present study, the newly developed solvers for chemically reacting flows are systematically validated in different flame configurations. Specifically, a zero-dimensional auto ignition is used to verify the chemical source term in governing equations by the newly developed *standardChemFoam* solver while verification of convection and diffusion terms in governing equations are then conducted by the new *standardReactingFoam* solver using a one-dimensional premixed flame. A counterflow configuration is also simulated to examine the *standardReactingFoam* solver for a two-dimensional axisymmetric non-premixed laminar flame. Numerical simulation results of these flames are validated against Cantera [75] and CHEMKIN [83] simulations with the same chemical and physical conditions. In addition, the *standardReactingFoam* solver is applied for a realistic combustion simulation of a two-dimensional partially premixed coflow flame. The detailed experimental datasets were available in literature [228], which are used as a reference benchmark to assess the performance of the *standardReactingFoam* solver.

6.4.1 Zero-dimensional auto ignition

The zero-dimensional (0D) auto ignition is a canonical case [79] for assessing the temporal numerical integration accuracy of chemical source terms, because convection and diffusion do not take effect in the 0D simulation. Therefore, this configuration is very appropriate for evaluating the calculation of chemical reaction rates. As any case involving reacting flows requires inputting a readable chemical reaction mechanism, the *standardChemkinToFoam* utility is newly developed to transform a chemical reaction mechanism from the *chemkin* format. The resulting chemical reaction mechanism is then inputted by the *chemkinReader* or *foamChemistryReader* as shown in Figure 6.2 for any combustion solver. Due to the dependence of any combustion case on the newly developed *standardKineticTransport* class as discussed in Section 7.3, it is required to examine the correct reading of all the information in the chemical reaction mechanism. Thus, the purpose of using this case in the present study is mainly to check the function of the newly developed *standardChemkinToFoam* utility. Derived from the original rho-based *chemFoam* solver in the OpenFOAM, a new combustion solver named *standardChemFoam* is developed for a muti-species system, which is coupled with the newly implemented detailed transport model involving molecular transport parameters based on the standard kinetic theory of gases. The flame setup is a homogeneous and constant-volume batch reactor filling an unburned methane-air mixture with unity equivalence ratio, where one cell of computational mesh is generated in OpenFOAM with a time step of 1×10^{-5} s. The initial pressure of the gas mixture is 13.5 bar with temperature of 1000 K. As initial temperature is larger than the temperature of auto-ignition, unburned methane-air mixture starts to ignite when the numerical simulation begins and gradually becomes a burned state. The same initial conditions are set up in Cantera and CHEMKIN, whose results are taken as benchmarks.

Figure 6.5 presents the time evolution of temperature profiles of ignition process by the developed *standardChemFoam*, which is in excellent agreement with those obtained from Cantera and CHEMKIN platforms. The time evolution of mass fraction profiles of main species obtained from the *standardChemFoam* solver, Cantera and CHEMKIN are presented in Figures 6.6 and 6.7. Numerical simulation results of the newly developed solver are consistent with both benchmarks [75,83], which validate the correctly implemented algorithm for chemistry problems.

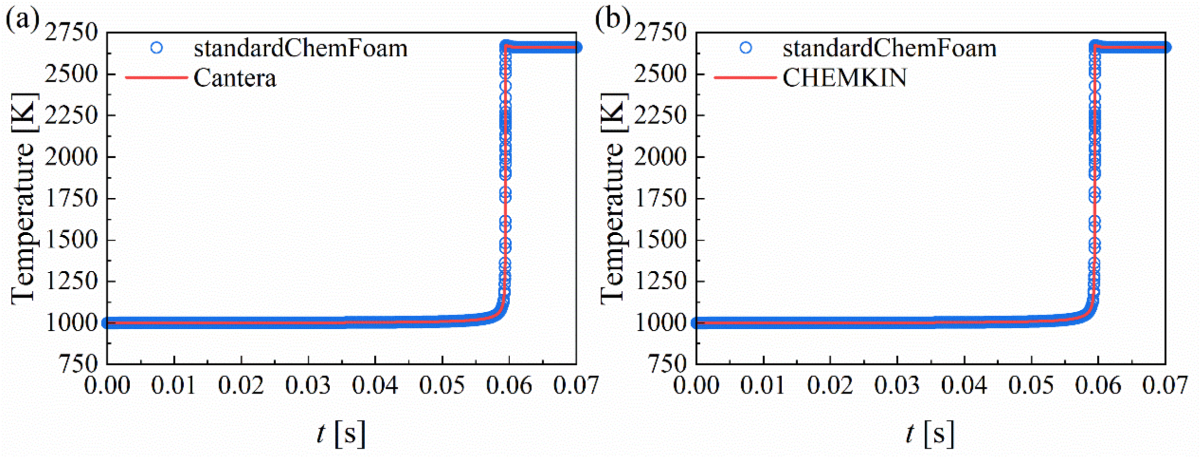

Figure 6.5 Time evolution of temperature profiles of *standardChemFoam* in comparison with Cantera and CHEMKIN of 0D auto-ignition [53].

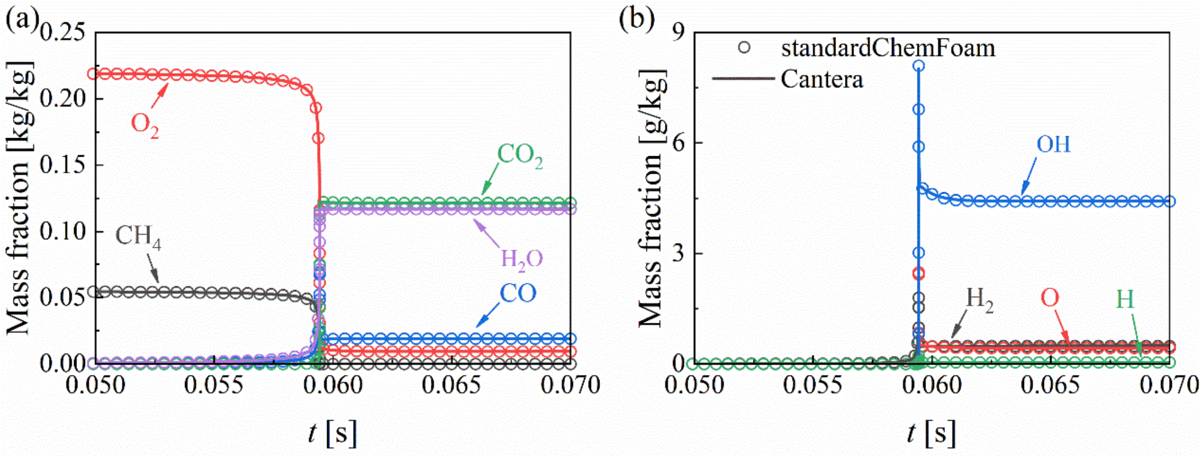

Figure 6.6 Time evolution of species mass fraction profiles of *standardChemFoam* in comparison with Cantera of 0D auto-ignition [53].

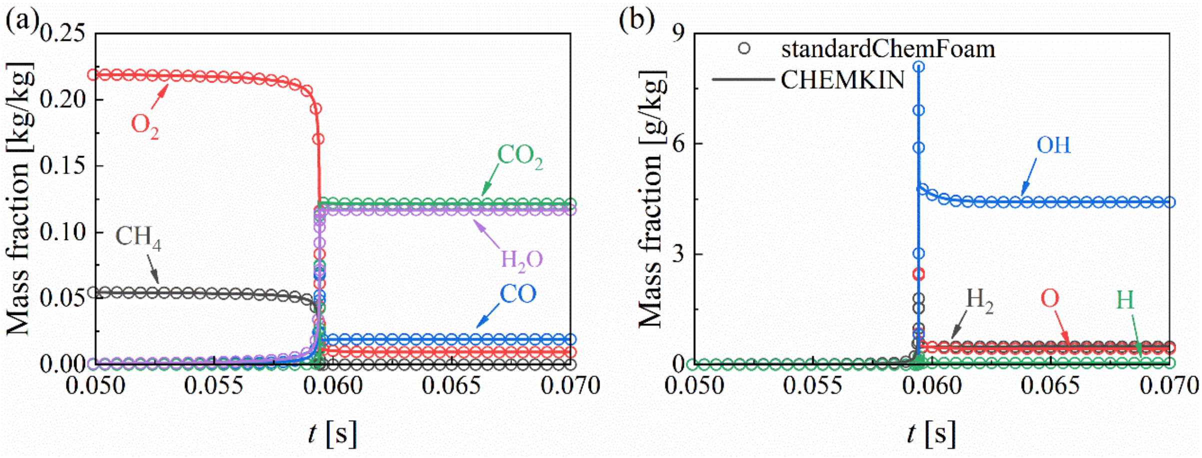

Figure 6.7 Time evolution of species mass fraction profiles of *standardChemFoam* in comparison with CHEMKIN of 0D auto-ignition [53].

6.4.2 One-dimensional premixed flame

In the present study, a case of a one-dimensional (1D) freely propagating premixed planar laminar flame [79] is investigated to evaluate the implementation of the detailed transport model involving molecular transport parameters based on the standard kinetic theory of gases, which takes the effects of convection and diffusion into account. Correspondingly, a new combustion solver named *standardReactingFoam* derived from the original psi-based *reactingFoam* solver in the OpenFOAM is developed for chemically reacting flows with mixture-averaged transport properties. The computational domain consists of an inlet of a fresh gas mixture with unity equivalence ratio of methane and air, where the mixture is consumed and the flame propagates against the fresh mixture due to combustion. When the inlet velocity is equal to the burning velocity, a steady state is reached and the flame front in the computational domain remains unchanged. The inlet velocity is set the same as the laminar flame speed (i.e., 38 cm/s) in the present study. The inlet temperature is set to be 300 K and the pressure of the computational domain is set to be 1 bar while the outlet boundary conditions are set to be zero-gradient. The length of the computational domain is 100 cm, and the grid independence is verified by using a uniform grid resolution of 200 μm, 100 μm, 50 μm and 25 μm. Numerical simulation results show that converged solutions have achieved at a grid size of 25 μm.

Numerical simulation results obtained from the *standardReactingFoam* solver, Cantera and CHEMKIN are shown in Figures 6.8 to 6.10, where the axial location of the resulting maximum heat release rate is set to zero. Results show that the calculated temperature profile and mass fraction profiles of main species obtained from the *standardReactingFoam* solver are in excellent agreement with the Cantera and CHEMKIN solutions. The minor deviations between the numerical results obtained from the *standardReactingFoam* solver and Cantera as well as CHEMKIN platform are mainly attributed to the different computational grids used in these platforms [78]. In the present study, different adaptive grid refinement strategies are used at the flame front by the Cantera and CHEMKIN platforms while a static grid is used by the *standardReactingFoam* solver in OpenFOAM. It should be noted that it is impossible to achieve the agreement by the original *reactingFoam* solver in the OpenFOAM due to the lack of a detailed transport model [229]. It also validates the newly developed *standardReactingFoam* solver incorporating a detailed transport model involving molecular transport properties for a multi-species system in chemically reacting flows, which can be further used for more complicated two- and three-dimensional combustion simulations.

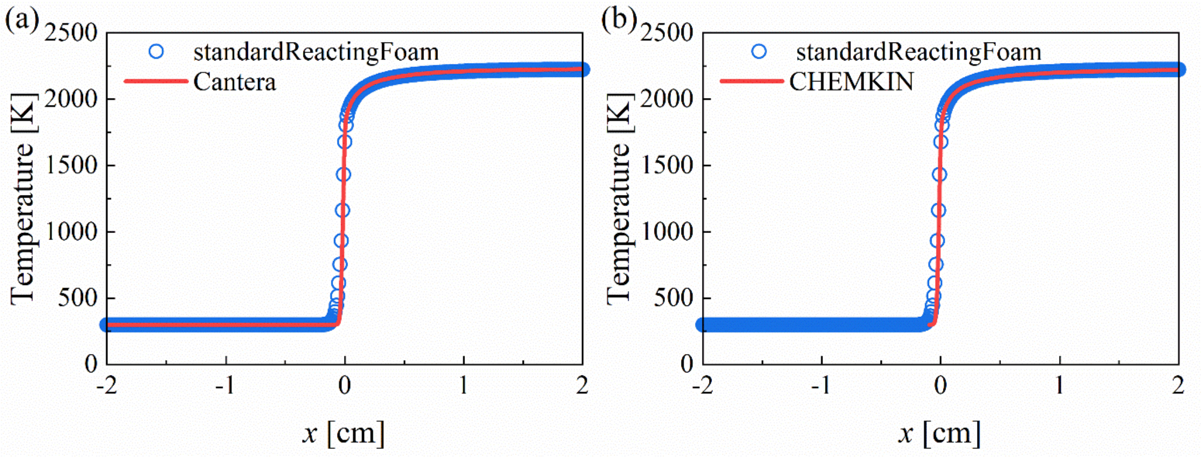

Figure 6.8 Comparison of temperature profile obtained from *standardReactingFoam*, Cantera and CHEMKIN of 1D steady state premixed flame [53].

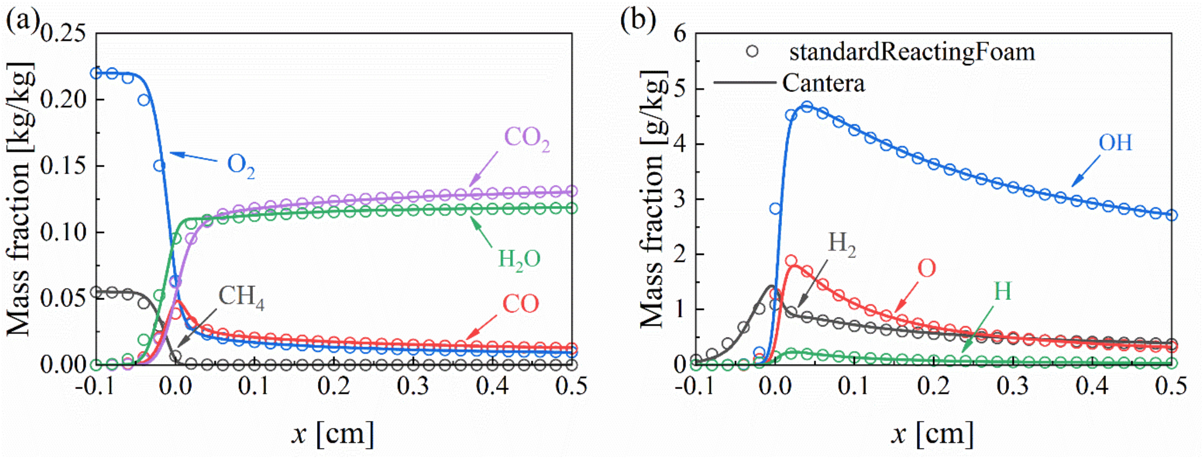

Figure 6.9 Comparison of species mass fraction profiles obtained from *standardReactingFoam* and Cantera of 1D steady state premixed flame [53].

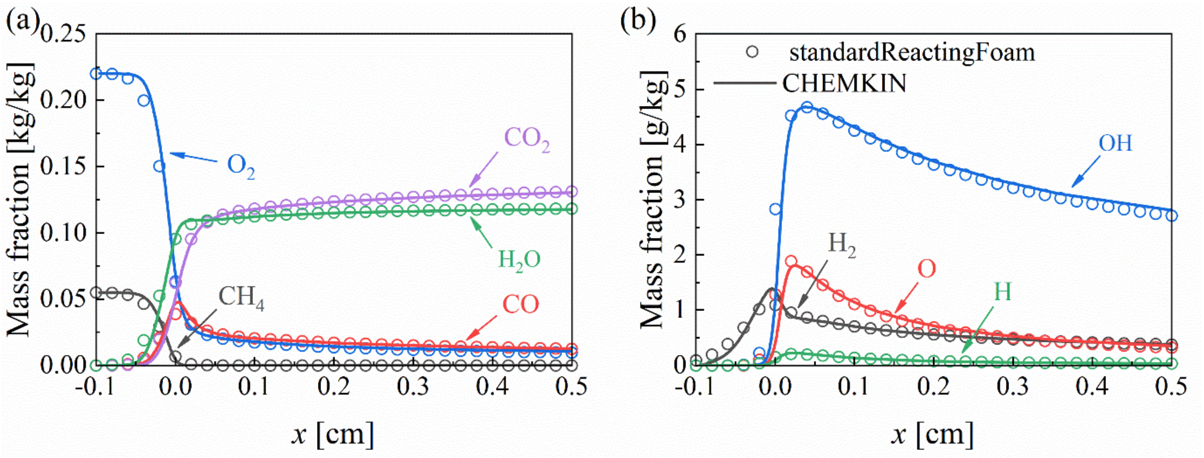

Figure 6.10 Comparison of species mass fraction profiles obtained from *standardReactingFoam* and CHEMKIN of 1D steady state premixed flame [53].

6.4.3 Two-dimensional non-premixed counterflow flame

A counterflow configuration is also simulated to examine the *standardReactingFoam* solver for a two-dimensional (2D) axisymmetric non-premixed laminar flame [81] by using a detailed chemical kinetics and transport model. This 2D case is widely used for understanding the basics of diffusion flames due to its relatively simple flow field, whose solution can be approximated by 1D simulations. Figure 6.11 shows the schematic diagram of the 2D non-premixed counterflow flame setup, where the inlets of fuel (i.e., CH_4) and air (i.e., 21% O_2 and

79% N_2 by volume) are on the left and right sides, respectively. The counterflow flame outlet is on the top while the bottom side is the axis of symmetry. The computational domain is a wedge of a cylinder, whose length and radius are 2 cm. Pure methane and regular air are injected into the computational domain from the left and right side, respectively, leading to a mixing process of methane and air. It should be noted that this case can be also used to examine the capability of the newly developed *standardReactingFoam* solver for pure species (i.e., methane) diffusion in addition to multi-species diffusion. The initial temperature and velocity of both inlets are set to be 293 K and 10 cm/s [71,81], while the pressure of the computational domain is fixed at 101325 Pa. The consistent computational conditions are used in Cantera and CHEMKIN simulations for the purpose of providing benchmark solutions, so the 2D numerical simulation results of the *standardReactingFoam* solver are validated against the 1D axial profiles obtained from the Cantera and CHEMKIN softwares.

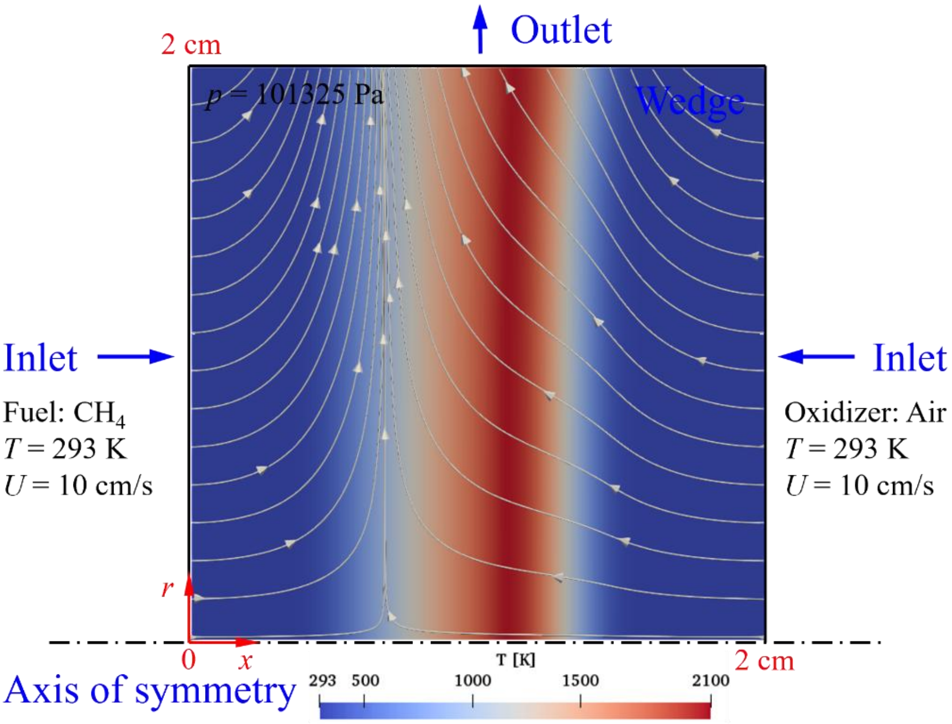

Figure 6.11 Schematic diagram of 2D non-premixed counterflow flame setup, temperature distributions and streamline profiles [53].

The grid independence is firstly validated by different grid resolutions. It is reported that the prediction of the heat release rate of this flame has a strong dependence on the grid resolution [81]. In the present study, the grid size along with the radial direction (i.e., r) is uniformly 200 μm, while the grid size along with the axial direction (i.e., x) is set to be uniformly 200 μm, 20 μm, 10 μm and 5 μm. Numerical simulation results show that two peaks of the heat release rate can be fully resolved and remain unchanged when the grid size is less than 10 μm, which demonstrates that the grid resolution is high enough to obtain convergent results. Figure 6.11 also shows the temperature distribution of the 2D axisymmetric non-premixed laminar flame at a grid size of 5 μm, where streamlines denoted by white solid lines with arrows are also presented, leading to a clear presentation of the flame and stagnation plane. As the global equivalence ratio is larger than unity, the flame stabilizes at the air side relative to the stagnation plane. The reason is that the flame front moves towards the air side to maintain stable combustion with a complete fuel-air reaction.

The comparisons of thermodynamic properties, transport properties and main species mass fractions obtained from the *standardReactingFoam* solver with Cantera and CHEMKIN are presented in Figures 6.12 and 6.13, respectively. It should be noted that the real distance instead of non-dimensional distance is used to reflect the actual physical scale of this type of flame setup. Excellent agreements of the heat release rate are observed between the *standardReactingFoam* solver and Cantera as well as CHEMKIN, in which two peaks of the heat release rate and heat absorption region are accurately captured by the *standardReactingFoam* solver. The numerical predictions of the variations of temperature, axial velocity, density, viscosity, thermal conductivity and specific heat capacity of the mixture along the center axis by using the *standardReactingFoam* solver are very consistent with those obtained from other two platforms. In addition, the resulting spatial mass fraction profiles of main species at the central axis of the new solver also show a consistent tendency and a very good agreement with their counterparts obtained from Cantera and CHEMKIN, which demonstrates the correct implementation of the algorithm in terms of coupling the detailed transport model with the new combustion solver. It should be noted that the slight deviations between the numerical results obtained from the *standardReactingFoam* solver and Cantera as well as CHEMKIN platform are mainly attributed to the different computational grids used in these platforms as discussed in Section 6.4.2 as well as solver settings including discretization schemes.

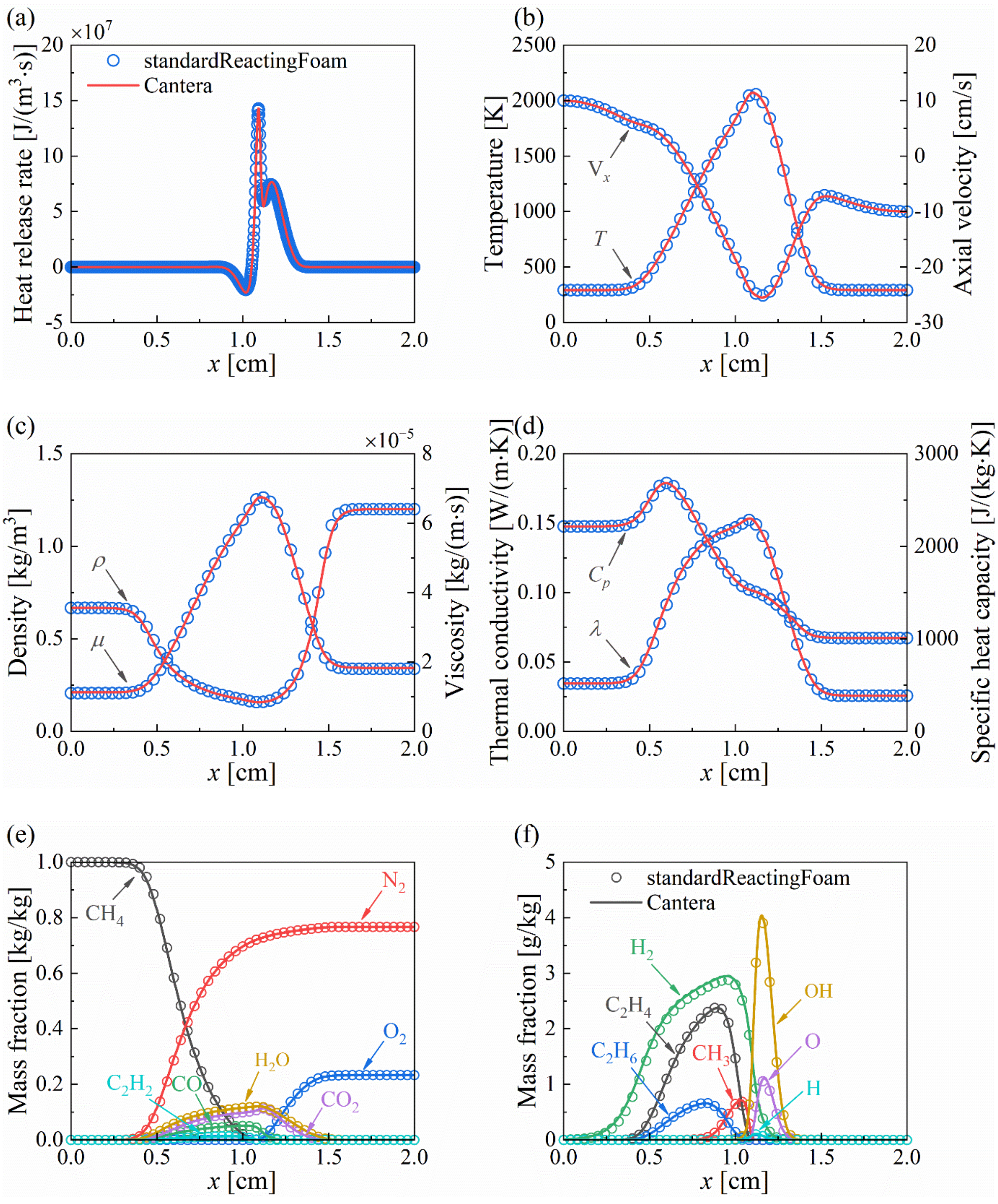

Figure 6.12 Comparison of thermodynamic property, transport property and species mass fraction profiles obtained from *standardReactingFoam* and Cantera of 2D steady state non-premixed counterflow flame [53].

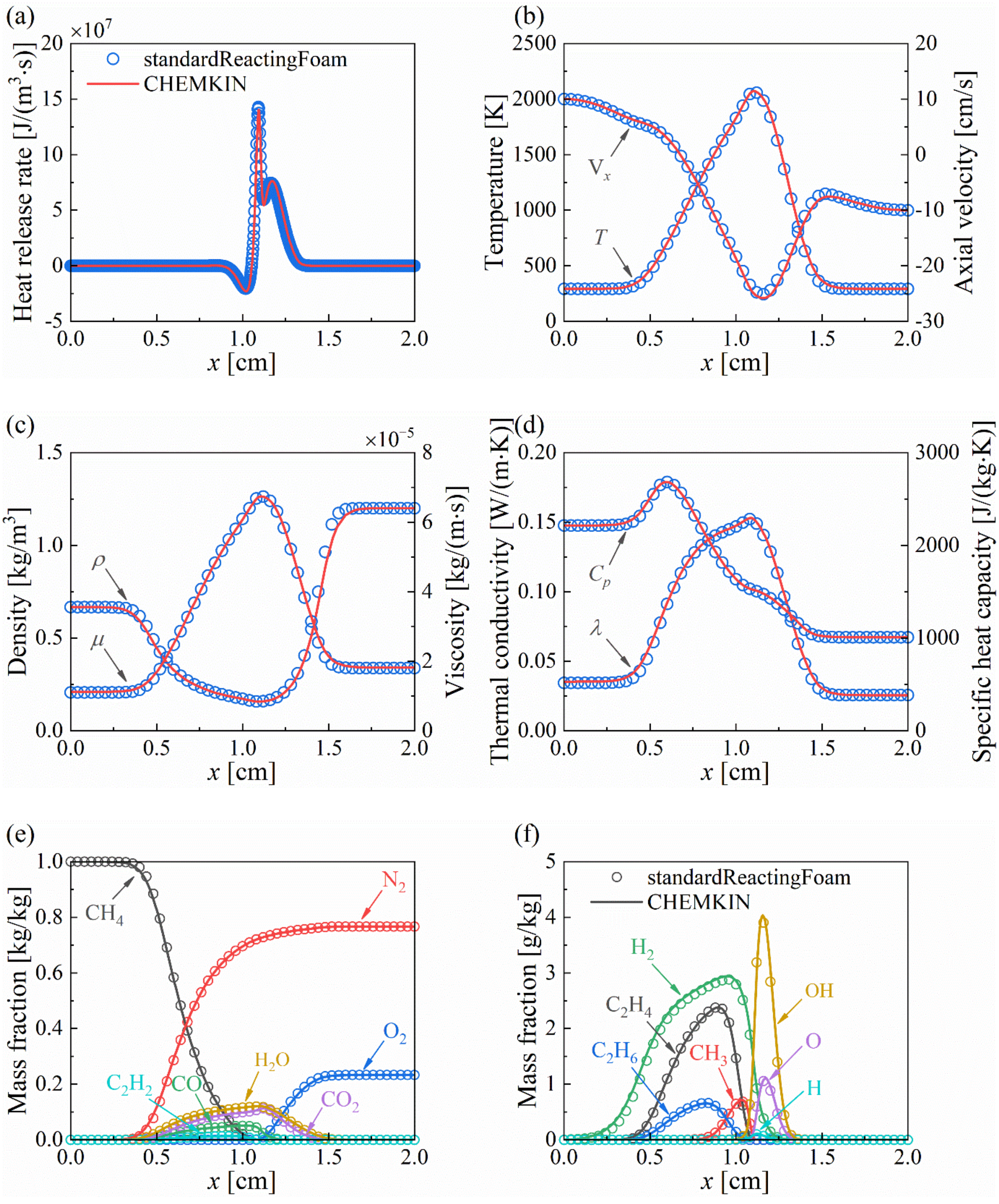

Figure 6.13 Comparison of thermodynamic property, transport property and species mass fraction profiles obtained from *standardReactingFoam* and CHEMKIN of 2D steady state non-premixed counterflow flame [53].

6.4.4 Two-dimensional partially premixed coflow flame

Except for premixed and diffusion flames, a partially premixed coflow laminar flame is considered in the present study to evaluate the computational performance of the newly developed algorithm, which couples a detailed transport model with a combustion solver for a realistic combustion simulation. The experimental setup of the partially premixed coflow flame used from Bennett et al. [228] consists of two concentric tubes and a cylindrical shield as shown in Figure 6.14. A mixture of methane and air is injected from the inner tube with a fully developed laminar profile while a regular air is supplied from the concentric annulus. Chemical compositions, initial temperature (i.e., ambient temperature) and pressure (i.e., standard atmospheric pressure) of both jets are shown in Figure 6.14. The inner and outer radii of the inner tube are 5.55 mm and 6.35 mm, while the inner and outer radii of the outer tube are 47.6 mm and 51 mm, respectively. The air volumetric flowrate of the concentric annulus is 44000 cm^3/min, while the volumetric flowrates of methane and air in the inner tube are 330 cm^3/min and 1050 cm^3/min, respectively. The length of the computational domain at the downstream of the inlets is 200 mm.

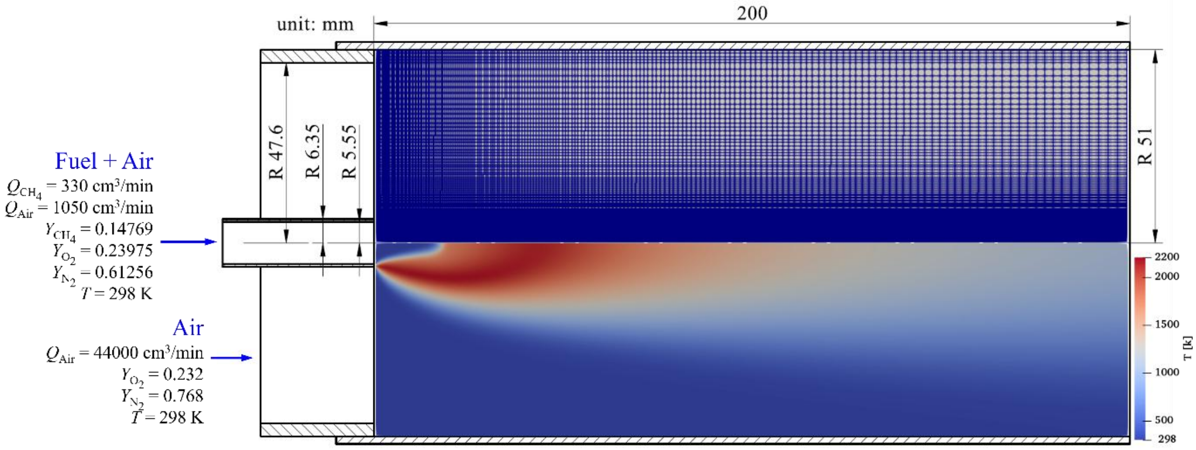

Figure 6.14 Schematic diagram of 2D partially premixed coflow flame setup, computational mesh and temperature distribution [53].

Figure 6.14 shows the 2D axisymmetric structured mesh of the flame setup including 18400 hexahedra cells for the numerical simulation, where local refinements are conducted near the inlets. Gird independence validation shows that further mesh refinements have no significant effect on the numerical solution. As it is found that there is a relative heat loss of about 15% [77,228], radiation heat transfer is considered in the numerical simulation, which is achieved by the radiative heat source term in the energy equation. The optically thin radiation model is adopted for this flame, in which H_2O, CO_2, CH_4 and CO are regarded as the significant radiative species and self-absorption is neglected [77,89,228,230]. The resulting temperature distribution at the central section of the computational domain numerically simulated by the newly developed *standardReactingFoam* solver is also shown in Figure 6.14.

A comparison of the CFD predictions with experimental measurements [228] along the centerline in the axial direction is presented in Figure 6.15, which includes temperature profile and mole fraction profiles of main species (i.e., CH_4, O_2, H_2O, CO_2 and OH). It should be noted that all the experiment data [228] were collected within the flame height (i.e., around 5 cm). Numerical simulation results show that the simulated magnitude and axial position of the maximum temperature at the centerline are almost the same as the experimental results [228], which demonstrates that the *standardReactingFoam* solver has the capacity to capture the temperature peak in terms of both position and magnitude. In addition, temperature profiles along the centerline in the axial direction obtained from the numerical simulation show a very similar tendency with that of the experiment. Simultaneously, mole fraction profiles of the main species along the centerline in the axial direction can be well predicted by the new solver especially for CO_2 and OH, and the simulated species mole fraction profiles vary consistently with the experimental data. With respect to CH_4 and O_2, the numerical predictions of mole fraction profiles of both species along the centerline in the axial direction agree very well with the experimental results except for the region near the exit of the inner jet. Obviously, the experimental data near the exit of the inner jet should not be of great difference from the boundary condition, which demonstrates the unreasonable experimental data near the exit of the inner jet. As reported by Bennett et al. [228], the same species calibration procedure was applied throughout the measurement domain, which introduced relatively large measurement error near the exit of the inner jet. As a result, it is appropriate not to compare the experimental data at this exit region of inner jet, and focus can be paid on other regions and the profile shape. It should be noted that the experimental mole fraction profile of H_2O along the centerline in the axial direction in Figure 6.15 was corrected by a scale factor [228] due to the difficulties in experimental calibration of low vapor pressure of H_2O at non-flame temperature, which makes it more appropriate to qualitatively compare the tendency of mole fraction of H_2O between numerical results and experimental data [73,89]. Considering the consistent tendency between numerical and experimental results including temperature and species mass fraction along the centerline in the axial direction, the overall agreement is quite satisfactory.

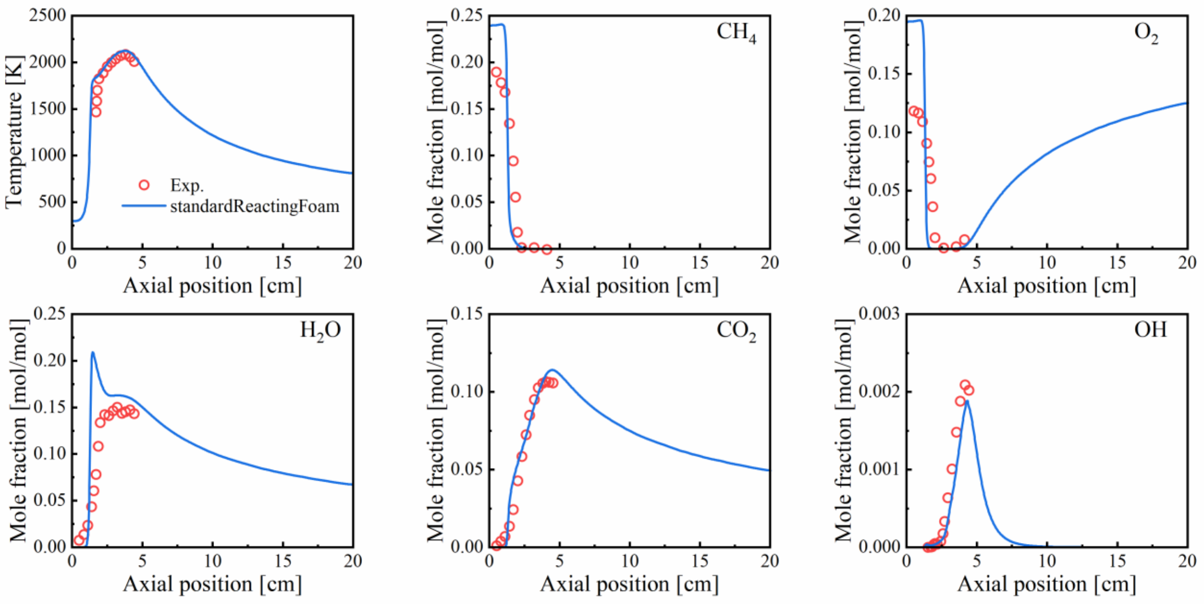

Figure 6.15 Comparison of temperature and species mole fraction profiles along the centerline in the axial direction obtained from *standardReactingFoam* with experimental results of 2D partially premixed coflow flame [53].

6.5 Summary

The free, open-source platform (i.e., OpenFOAM) has been widely used to solve various scientific problems in terms of fluid dynamics based on the finite volume method, in which libraries, solvers and pre- and post-processing utilities can be conveniently customized. As for reacting flows, however, the use of OpenFOAM is greatly limited by a highly simplified transport model, which makes assumptions of unity Schmidt number and Lewis number and uses Sutherland formula, leading to incorrect numerical calculation of the critical transport properties. Thus, it is essentially required to incorporate a detailed transport model into OpenFOAM to calculate transport properties for combustion modelling. Developing an interface between OpenFOAM and Cantera to achieve data exchange is the most used way to evaluate transport properties of a detailed transport model, but it is highly version-dependent, making it difficult to widely use and inconvenient for maintenance. Another way is to develop a separate package for obtaining transport properties, resulting in a very complicated operation when using.

In the present study, a detailed transport model is implemented completely under the code framework of OpenFOAM, making it very easy to read, use, maintain, enhance and extend. The detailed transport model uses a mixture-averaged formulation based on the standard kinetic theory of gases, which takes molecular properties of each species into account. Thus, a new pre-processing utility named *standardChemkinToFoam* is newly developed to input the critical molecular transport parameters of each species, which is provided by a chemical reaction mechanism file. The function of the *standardChemkinToFoam* utility is examined by a newly developed *standardChemFoam* solver, which can be used to verify chemical source terms in the governing equations. The inputted molecular transport parameters of each species are then used to calculate transport properties by a new customized library named *thermophysicalModels*. The newly developed library is finally coupled with a new low-Mach combustion solver named *standardReactingFoam* for validation purpose, in which species and energy equations are solved without simplification. It implies that the *standardReactingFoam* solver can be used for direct or quasi-direct numerical simulation of reacting flows. Compared with the original OpenFOAM, any additional operation is not required when using the newly developed utility, library and solvers.

With a detailed chemical kinetics, a zero-dimensional auto ignition is used to verify the chemical source term and a one-dimensional premixed flame is used for validating convection and diffusion terms in the governing equations, which are solved by *standardChemFoam* and *standardReactingFoam*, respectively. A two-dimensional non-premixed counterflow flame is also simulated to evaluate the computational performance of the *standardReactingFoam* solver. Numerical simulation results of all these flames are compared with those obtained from Cantera and CHEMKIN platforms. In addition, a realistic combustion simulation of a two-dimensional partially premixed coflow flame is also verified. Numerical simulation results of the newly developed solvers are in very good agreements with counterparts, which demonstrates the successful incorporation of a detailed transport model into a combustion solver for accurate reacting flow simulations.

Chapter 7 Development of Dimer-based Soot Model for Soot Aerosol Dynamics in Laminar Combustion Flow

7.1 Introduction

The objective of this chapter is to develop a dimer-based soot model coupling the H-abstraction-C_2H_2-addition (HACA) mechanism with homogeneous and heterogeneous nucleation and dimer condensation, in which dimers are regarded as the link from polycyclic aromatic hydrocarbons (PAHs) to soot. The masses of PAHs used for dimer formation are determined based on a weighted average of total PAH masses and their densities are estimated to be associated with their chemical compositions. Rather than roughly including all PAHs, the PAHs selected for dimer formation in the present study are made up of 50 or more carbon atoms due to their stable nature. As the physical realization of the laminar flamelet and frequently used for fundamental soot studies in CFD, counterflow diffusion flames are adopted to validate the newly developed dimer-based soot model implemented in the *standardReactingFoam* solver developed by Wang et al. [53]. Numerical results would be in comparison with available experimental dataset in a wide range of strain rates as well as oxygen mole fractions in the oxidize stream.

7.2 Numerical Modelling

Numerical simulations are conducted by using OpenFOAM-v2012 in the present study, where governing equations of reacting flows are solved by mixture-averaged transport model and transport equations of the developed dimer-based soot model are coupled into combustion models.

7.2.1 Gas phase model

Continuity, momentum, species and enthalpy governing equations could be expressed by [223,224]:

$$\frac{\partial \rho}{\partial t} + \nabla \cdot (\rho \mathbf{U}) = 0 \tag{7-1}$$

$$\frac{\partial(\rho \mathbf{U})}{\partial t} + \nabla \cdot (\rho \mathbf{U}\mathbf{U}) - \nabla \cdot \boldsymbol{\tau} = -\nabla p \tag{7-2}$$

$$\frac{\partial(\rho Y_i)}{\partial t} + \nabla \cdot (\rho Y_i \mathbf{U}) + \nabla \cdot (\rho Y_i \mathbf{V}_i) = \omega_i \tag{7-3}$$

$$\frac{\partial(\rho h_s)}{\partial t} + \nabla \cdot (\rho h_s \mathbf{U}) + \frac{\partial(\rho K)}{\partial t} + \nabla \cdot (\rho K \mathbf{U}) = \frac{\partial p}{\partial t} - \nabla \cdot \mathbf{q} + Q_r + \omega_T + \nabla \cdot (\boldsymbol{\tau} \cdot \mathbf{U}) \tag{7-4}$$

where t and ρ are time and density; p and $\mathbf{U}$ represents pressure and velocity; ω_i and Y_i represents reaction rate and mass fraction of ith species, respectively; h_s and K are mixture sensible enthalpy and kinematic energy, respectively; $\nabla\cdot(\boldsymbol{\tau}\cdot\mathbf{U})$ represents the contribution of viscous stress to heat source, which is negligible in low Mach number flows; $\boldsymbol{\tau}$ represents viscous stress tensor by using Stokes assumption [224]:

$$\boldsymbol{\tau} = -\frac{2}{3}\mu(\nabla \cdot \mathbf{U})\boldsymbol{I} + \mu[\nabla \mathbf{U} + (\nabla \mathbf{U})^T] \tag{7-5}$$

where $\boldsymbol{I}$ represents identity tensor; the mixture viscosity, μ is calculated based on the viscosities of each pure species as [223,226]:

$$\mu = \sum_{i=1}^{N} \frac{X_i \mu_i}{\sum_{j=1}^{N} X_j \Phi_{ij}} \tag{7-6}$$

where

$$\Phi_{ij} = \frac{1}{\sqrt{8}}\left(1 + \frac{W_i}{W_j}\right)^{-\frac{1}{2}}\left[1 + \left(\frac{\mu_i}{\mu_j}\right)^{\frac{1}{2}}\left(\frac{W_j}{W_i}\right)^{\frac{1}{4}}\right]^2 \tag{7-7}$$

where m_i and m_j are the viscosity, W_i and W_j are the molecular weight, and X_i and X_j are the ith and jth species mole fractions, respectively.

Diffusion velocity of ith species (i.e., $\mathbf{V}_i$) in Equation (7-3) is formulated based on mole fraction gradient by [223,224]:

$$\mathbf{V}_i = -\frac{D_{i,\mathrm{mix}}}{X_i}\nabla X_i \tag{7-8}$$

where $D_{i,\mathrm{mix}}$ is the diffusion coefficient of species i into the rest of the mixture, which is calculated in a mixture-averaged formulation as [223,226]:

$$D_{i,\mathrm{mix}} = \frac{1 - Y_i}{\sum_{j=1,j\neq i}^{N} X_j / D_{ji}} \tag{7-9}$$

where the binary diffusion coefficient (i.e., D_{ji}) as well as pure species properties including viscosity (μ_i) and thermal conductivity (λ_i) can be calculated via the standard kinetic theory of gas, which is described in detail by Kee et al. [223]. It should be noted that the diffusion velocity, $\mathbf{V}_i$ should be corrected by adding a spatially varying correction velocity, $\mathbf{V}_C$ [224] to ensure global mass conservation [224].

$$\mathbf{V}_C = -\sum_{i=1}^{N} Y_i \mathbf{V}_i \tag{7-10}$$

In Equation (7-4), the heat flux, $\mathbf{q}$ is calculated as [81,224]:

$$\mathbf{q} = -\lambda \nabla T + \rho \sum_{i=1}^{N} h_{s,i} Y_i \mathbf{V}_i \tag{7-11}$$

where T and N are temperature and the number of species; $h_{s,i}$ represents the specific enthalpy of ith species; λ represents mixture thermal conductivity, which is calculated using a combination averaging formula as [223,226]:

$$\lambda = \frac{1}{2}\left(\sum_{i=1}^{N} X_i \lambda_i + \frac{1}{\sum_{i=1}^{N} X_i / \lambda_i}\right) \tag{7-12}$$

where λ_i represents ith species thermal conductivity. Contributions to radiative heat source, Q_r [231] from significant radiative species including H_2O, CO_2, CO and CH_4) and soot are considered, which neglects self-absorption based on the optically thin radiation model [77].

$$Q_r = 4\sigma a_p (T^4 - T_{\mathrm{env}}^4) \tag{7-13}$$

where σ and T_{env} are the Stefan-Boltzmann constant and environment temperature, respectively; Planck mean absorption coefficient, a_p could be calculated as [231]:

$$a_p = \sum_{i=1}^{4} p_i a_i + k_p \tag{7-14}$$

where a_i and p_i are Planck mean absorption coefficient [232] and partial pressure of ith species, respectively; the soot absorption coefficient, k_p depends on soot volume fraction (SVF), f_v as well as temperature, which could be calculated by [231]:

$$k_p = 700 f_v T \tag{7-15}$$

The production rate of heat from combustion, ω_T could be calculated as [224]:

$$\omega_T = -\sum_{i=1}^{N} h_{f,i} \omega_i \tag{7-16}$$

where $h_{f,i}$ is the formation enthalpy of the ith species, and ω_i and ω_T include the contribution of soot particles.

Based on equation of state, total pressure of mixture with N perfect gases is formulated as [223,224]:

$$p = \sum_{i=1}^{N} \rho_i \frac{R_u}{W_i} T \tag{7-17}$$

where R_u is the universal gas constant, and ρ_i is the density of species i.

7.2.2 Soot model

Soot mass and number densities, i.e., M (kg/m^3) and N (#/m^3), are calculated as [125]:

$$M = \rho Y_s \tag{7-18}$$

$$N = N_A \rho N_s \tag{7-19}$$

where N_A is the Avogadro number. Taking thermophoresis and diffusion effects of soot into account, the resulting N_s and Y_s transport equations of soot number and mass densities could be formulated as [92,125,130]:

$$\begin{aligned} \frac{\partial}{\partial t}(\rho Y_s) + \nabla \cdot (\rho \mathbf{U} Y_s) + \nabla \cdot (\rho \mathbf{V}_T Y_s) - \nabla \cdot (\rho D_s \nabla Y_s) \\ = \left(S_{\mathrm{nuc}}^{Y} + S_{\mathrm{cond}}^{Y}\right) + S_{\mathrm{sg}}^{Y} + S_{\mathrm{O_2}}^{Y} + S_{\mathrm{OH}}^{Y} \end{aligned} \tag{7-20}$$

$$\frac{\partial}{\partial t}(\rho N_s) + \nabla \cdot (\rho \mathbf{U} N_s) + \nabla \cdot (\rho \mathbf{V}_T N_s) - \nabla \cdot (\rho D_s \nabla N_s) = \frac{1}{N_A}\left(S_{\mathrm{nuc}}^{N} + S_{\mathrm{coag}}^{N}\right) \tag{7-21}$$

where soot dynamics including nucleation (nuc), condensation (cond), surface growth (sg), O_2 and OH oxidation as well as coagulation (coag) are treated as sources terms in the present study, while breakage and fragmentation are not considered [150].

7.2.2.1 Soot morphology

Based on the soot mass fraction, SVF could be calculated as [136]:

$$f_v = \frac{M}{\rho_{\text{soot}}} \tag{7-22}$$

where ρ_{soot} is the soot density, which is 1850 kg/m^3 [233,234]. The particle diameter and particle surface area per volume are then determined as [130]:

$$d_p = \left(\frac{6M}{\pi\rho_{\text{soot}}N}\right)^{1/3} \tag{7-23}$$

$$A_S = \left(\frac{6M}{\rho_{\text{soot}}}\right)^{2/3} (\pi N)^{1/3} \tag{7-24}$$

The mass of an aggregate can be calculated via soot mass and number densities as [130]:

$$m_{\text{agg}} = \frac{M}{N} \tag{7-25}$$

Primary particle number in an aggregate could be calculated by [205]:

$$n_p = \frac{m_{\text{agg}}}{m_{\text{pri}}} \tag{7-26}$$

where m_{pri} is the mass of primary particles. Primary particles are formed from two PAH dimer collision, which means that the primary particle mass equals the sum of these two PAH dimers. The mobility diameter d_m and gyration diameter d_g is then expressed as [235,236]:

$$d_m = d_p n_p^{0.45} \tag{7-27}$$

$$d_g = \begin{cases} \dfrac{d_m}{n_p^{-0.2} + 0.4}, if\ n_p > 1.8 \\ \dfrac{d_m}{\sqrt{5/3}}, if\ n_p \le 1.8 \end{cases} \tag{7-28}$$

7.2.2.2 Thermophoresis

The thermophoretic velocity, $\mathbf{V}_T$ for soot is calculated from the gas kinetic theory as [49,237]:

$$\mathbf{V}_T = -\frac{3}{4\left(1 + \frac{\pi}{8}\alpha_m\right)} \frac{\mu}{\rho} \frac{\nabla T}{T} \tag{7-29}$$

where the accommodation factor, a_m is equal to unity [125].

7.2.2.3 Diffusion

The diffusion coefficient of soot, D_s is expressed as [202,238]:

$$D_s = \frac{k_B T}{3\pi\mu d_m} C_s \tag{7-30}$$

where k_B represents Boltzmann constant; the Cunningham slip correction factor of soot, C_s is expressed as [239,240]:

$$C_s = 1 + K_n \left[1.257 + 0.4 \exp\left(-\frac{1.1}{K_n}\right)\right] \tag{7-31}$$

where the Knudsen number, K_n is calculated as [202]:

$$K_n = \frac{2\lambda_l}{d_m} \tag{7-32}$$

where d_m is the mobility diameter of soot, and λ_l represents gas mean free path defined as mean air free path, which is calculated as [241]:

$$\lambda_l = \frac{\mu}{p}\sqrt{\frac{\pi R_u T}{2W}} = \frac{\mu}{\rho}\sqrt{\frac{\pi W}{2k_B N_A T}} \tag{7-33}$$

where W represents mixture molecular weight.

7.2.2.4 Dimerization

Nucleation or inception is a process in which soot particles with the smallest size are formed. Polycyclic aromatic hydrocarbon (PAH) molecule dimerization is regarded as the link from gas phase to soot. Collision frequency of PAH molecules are calculated as [147,148]:

$$\beta_{ij} = \sqrt{\frac{\pi k_B T}{2m_{ij}}}\left(d_i + d_j\right)^2 \tag{7-34}$$

where d_i is collision diameter of PAH molecule i; m_{ij} is reduced dimer mass based on the mass of PAH molecules i and j, which is calculated as [143,242]:

$$m_{ij} = \frac{m_i m_j}{m_i + m_j} \tag{7-35}$$

Therefore, the dimerization rate of PAH molecules *i* and *j* is then determined from the collision rate of these two molecules as [144,147,148]:

$$\omega_{ij} = \gamma_{ij}\beta_{ij}[\mathrm{PAH}_i][\mathrm{PAH}_j]N_A^2 \tag{7-36}$$

where γ_{ij} is the sticking coefficient between PAH species *i* and *j*, which is calculated as [143]:

$$\gamma_{ij} = \sqrt{\gamma_i\gamma_j} \tag{7-37}$$

It is assumed that the sticking coefficient of a PAH species scales with its mass to the fourth power, for example, the sticking coefficients of phenanthrene (A3) and pyrene (A4) are 0.015 and 0.025, respectively [143,147,148], and the combination of these two species is able to directly generate stable soot nuclei [144,149]. $[\mathrm{PAH}_i]$ and $[\mathrm{PAH}_j]$ are the molar concentrations of PAH species *i* and *j*, respectively. The diameter of different PAH molecules can be calculated based on the density of PAH species, which could be estimated by [242-244]:

$$\rho_{\mathrm{PAH}} = \frac{1}{0.260884 l^2 s}\,\frac{W_{\mathrm{C}}\frac{\mathrm{C}}{\mathrm{H}} + W_{\mathrm{H}}}{\frac{\mathrm{C}}{\mathrm{H}} + 1} \tag{7-38}$$

where *s* and *l* are interlayer spacing and graphite length unit cell of basal plane, respectively; w_{H} and w_{C} are hydrogen and carbon atom molecular weights, respectively; and C/H represents the ratio of carbon and hydrogen numbers in a PAH species [245].

The formation of dimers is modelled via heterogeneous collisions of PAH molecules based on detailed chemistry, so the dimer production rate due to the heterogeneous collision of PAH species is calculated as [144]:

$$\omega_{\mathrm{dimer,pro}} = \frac{1}{2}\sum_{i=1}^{n_{\mathrm{PAH}}}\sum_{j=1}^{n_{\mathrm{PAH}}}\omega_{ij} \tag{7-39}$$

where n_{PAH} represents total number of PAH species used for dimer formation. It should be noted that rather than calculating every possible dimer, only the total production rate of dimers would be evaluated [148]. The mass of each PAH species used for dimer formation can be determined based on a weighted average of total PAH masses involved in the dimerization process as [144]:

$$m_{\mathrm{PAH}} = \frac{\sum_{i=1}^{n_{\mathrm{PAH}}}\sum_{j=1}^{n_{\mathrm{PAH}}}(m_i + m_j)\omega_{ij}}{\sum_{i=1}^{n_{\mathrm{PAH}}}\sum_{j=1}^{n_{\mathrm{PAH}}}\omega_{ij}} \tag{7-40}$$

It is considered that the dimer number density is kept in a balance between the dimerization rate and consumption rate because of soot inception and growth of condensation, resulting in the realization of a steady state of the dimer number density due to the frequent collision with soot particles and other dimers. The dimer consumption rate is then determined as [144]:

$$\omega_{\text{dimer,con}} = \beta_N N_{\text{dimer}}^2 + \beta_C N_{\text{dimer}} \tag{7-41}$$

where N_{dimer} is the dimer number density; β_N and β_C are the nucleation and condensation collision rate with van der Walls enhancement factor (i.e., E_F=2.2), respectively.

7.2.2.5 Nucleation and condensation

Soot is nucleated by the collision of PAH dimers and grows via the condensation of these dimers in the present study. As the rate of dimer production equals that of dimer consumption because of nucleation and condensation, the mass increase rate of soot equals the net mass production rate of dimers while the soot number increase rate is the dimer collision rate. Therefore, source terms of transport equations of soot number and mass densities could be calculated:

$$S_{\text{nuc}}^Y + S_{\text{cond}}^Y = \frac{1}{2}\sum_{i=1}^{n_{\text{PAH}}}\sum_{j=1}^{n_{\text{PAH}}}(m_i + m_j)\omega_{ij} \tag{7-42}$$

$$S_{\text{nuc}}^N = \frac{1}{2}\beta_N N_{\text{dimer}}^2 \tag{7-43}$$

7.2.2.6 Coagulation

The coagulation source term is expressed as below [130]:

$$S_{\text{coag}}^N = -E_F\left(\frac{24k_BT}{\rho_{\text{soot}}}\right)^{1/2}\left(\frac{6M}{\pi\rho_{\text{soot}}}\right)^{1/6} N^{11/6} \tag{7-44}$$

7.2.2.7 Surface growth and oxidation

These dynamic events are described by HACA mechanism [59], which contains six reactions including two reversible reactions as listed in Table 7.1 with individual reaction rate constants (i.e., k). OH oxidation (i.e., S6) is modelled via collision theory of free molecular regime, in which collision efficiency γ_{OH} is 0.13. Other surface reactions (i.e., S1-S5) are regarded to take place on the soot surface activated sites, which is dehydrogenated ($C_{soot}\cdot$) or saturated (C_{soot}–H). The molar concentration of dehydrogenated sites [$C_{soot}\cdot$] on particle surface could be computed by [202]:

$$[\mathrm{C_{soot}}\,\cdot] = \frac{A_s}{N_A}\chi_{\mathrm{C_{soot}}\cdot} \tag{7-45}$$

where A_s represents primary particle surface area; $\chi_{\mathrm{C_{soot}}\cdot}$ represents dehydrogenated site number per unit surface area, which is calculated by [246]:

$$\chi_{\mathrm{C_{soot}}\cdot} = \frac{k_1[\mathrm{H}] + k_2[\mathrm{OH}]}{k_{-1}[\mathrm{H_2}] + k_{-2}[\mathrm{H_2O}] + k_3[\mathrm{H}] + k_4[\mathrm{C_2H_2}] + k_5[\mathrm{O_2}]}\chi_{\mathrm{C_{Soot}-H}} \tag{7-46}$$

where saturated site number of unit surface area, $\chi_{\mathrm{C_{soot}}\text{–H}}$ is 2.3×10^{19} m^{-2}. Surface activated site fraction for reactions, α is defined as [59]:

$$\alpha = \tanh\left(\frac{a}{\log \mu_1} + b\right) \tag{7-47}$$

where a and b are parameters associated with temperature, which is given by [59]:

$$a = 12.65 - 0.00563T \tag{7-48}$$

$$b = -1.38 + 0.00068T \tag{7-49}$$

μ_1 is calculated by [247]:

$$\mu_1 = \frac{\rho_{soot}\pi d_p^3}{6W_\mathrm{C}}N_A \tag{7-50}$$

where W_C is carbon atom molecular weight. The surface growth (sg) and O_2 oxidation reaction rates are then calculated as [246]:

$$\omega_{\mathrm{sg}} = \alpha k_4[\mathrm{C_2H_2}][\mathrm{C_{soot}}\,\cdot] \tag{7-51}$$

$$\omega_{\mathrm{O_2}} = \alpha k_5[\mathrm{O_2}][\mathrm{C_{soot}}\,\cdot] \tag{7-52}$$

The surface oxidation reaction rate originating from OH is calculated based on the collision theory, which is given as [202]:

$$\omega_{\mathrm{OH}} = k_6[\mathrm{OH}]\frac{N}{N_A} \tag{7-53}$$

Thus, source terms of surface growth and O_2 and OH oxidation are then expressed as follows:

$$S_{\mathrm{sg}}^{Y}=2W_{\mathrm{C}}\omega_{\mathrm{sg}} \tag{7-54}$$

$$S_{\mathrm{O_2}}^{Y}=-W_{\mathrm{C}}\omega_{\mathrm{O_2}} \tag{7-55}$$

$$S_{\mathrm{OH}}^{Y}=-W_{\mathrm{C}}\omega_{\mathrm{OH}} \tag{7-56}$$

Table 7.1 Soot surface growth and oxidation reactions [59,248], $k=AT^{n}\exp(-E/R_{u}T)$.

No.	Reaction	A (cm^{3}mol^{-1}s^{-1})	n	E (kcal/mol)
S1	$\mathrm{C_{soot}-H+H \leftrightarrow C_{soot}\cdot+H_2}$	4.2×10^{13}	0.0	13.0
		3.9×10^{12}	0.0	9.32
S2	$\mathrm{C_{soot}-H+OH \leftrightarrow C_{soot}\cdot+H_2O}$	1.0×10^{10}	0.734	1.43
		3.68×10^{8}	1.139	17.1
S3	$\mathrm{C_{soot}\cdot+H \rightarrow C_{soot}-H}$	2.0×10^{13}	0.0	0.0
S4	$\mathrm{C_{soot}\cdot+C_2H_2 \rightarrow C_{soot}-H+H}$	8.0×10^{7}	1.56	3.8
S5	$\mathrm{C_{soot}\cdot+O_2 \rightarrow 2CO+products}$	2.2×10^{12}	0.0	7.5
S6	$\mathrm{C_{soot}-H+OH \rightarrow CO+products}$	$\gamma_{\mathrm{OH}}=0.13$		

7.3 Results and Discussion

Governing equations including unsteady, convection, diffusion and source terms are solved based on the finite volume method. The pressure implicit with splitting of operator (PISO) algorithm [227] is adopted to achieve the pressure-velocity coupling. Different numerical schemes for different physically meaningful terms are readily available in OpenFOAM [249]. In the present study, unsteady terms are discretized by a first-order time-stepping while a second-order central differencing scheme is adopted to discretize the convection and diffusion terms. The chemical reaction mechanism used is the famous ABF mechanism [59] involving 544 reactions and 101 species, and an Euler implicit solver is used for chemistry. The maximum Courant number is set to be 0.2 for constraining the time step of integration. Transport properties are calculated by the mixture-averaged transport model, and the dimer-based soot model coupling with the combustion model is newly developed.

In the present study, the counterflow diffusion flame (CDF) configuration in Wang and Chung [250] is employed to validate the new dimer-based soot model. Two vertical nozzles with 10 mm inner diameters are opposed positioned from 8 mm, from which oxidizer and fuel are injected, respectively. The fuel is pure ethylene (X_F=1.0) while oxidizer is composed of nitrogen and oxygen. In the oxidizer, the oxygen mole fraction (X_O) ranges from 0.20 to 0.30, leading to different mixing processes of fuel and oxidizer, which is consistent with the boundary conditions provided in the related experiments. In the reference experiments, the lower sooting limit is the oxygen level of almost 0.20 for ethylene, which is effective for flame thermochemical structure validation. When the oxygen level is higher than the sooting limit (0.20), fuels have higher sooting tendencies, which can be used to validate the numerical framework developed for modelling soot formation and evolution in this study. The initial pressure is 1bar with temperature of 298K, respectively. The velocities at the nozzle exits are adjusted to manipulate the strain rate, which is normally employed to characterize the flow and flame defined as [251]:

$$K = \frac{2U_{\mathrm{O}}}{L}\left(1 + \frac{U_{\mathrm{F}}}{U_{\mathrm{O}}}\sqrt{\frac{\rho_{\mathrm{F}}}{\rho_{\mathrm{O}}}}\right) \tag{7-57}$$

where L represents the distance of two nozzle exits; U and ρ are axial velocity and density; subscripts “O” and “F” represents oxidizer and fuel.

7.3.1 Validation of grids and gas chemistry

As a necessary step, numerical simulation of a typical ethylene (C_2H_4) CDF should be conducted to verify the correctness of the developed program and validate the grid independence. The C_2H_4 CDF with X_O = 0.20 experimentally investigated by Jiang et al. [252] is considered, and oxidizer and fuel inlet velocities are 20cm/s. The grid independence is firstly validated by different grid resolutions in an axisymmetric cylindrical coordinate. The grid size along the radial direction (i.e., r) is uniformly 100 μm, while the grid size along the axial direction (i.e., x) is set to be uniformly 100 μm, 50 μm, 25 μm and 12.5 μm. Figure 7.1 presents the axial velocity profiles of the centerline at different grid sizes, which remain unchanged when the grid size is less than 50 μm, meaning that the grid size has no significant effect on the numerical results, which demonstrates that the grid resolution is high enough to obtain convergent results.

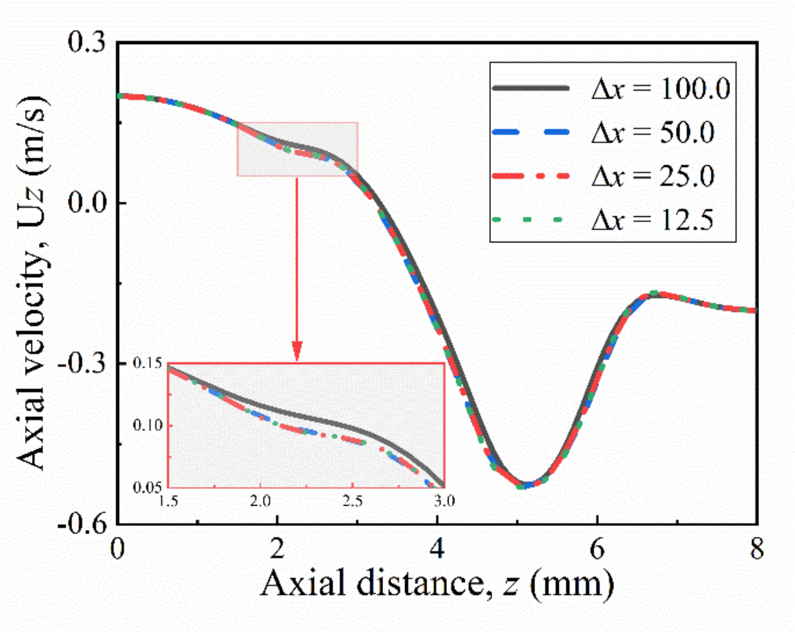

Figure 7.1 Comparison of axial velocities at different grid sizes along the flame centerline with X_F = 1.0 and X_O = 0.20.

It should be noted that the aerodynamic conditions in this case are almost the lower sooting limit [250,253], which would be effective for flame thermochemical structure validation. Figure 7.2 presents the CFD predictions of axial profiles of major species mole fractions and temperature compared with experimental dataset provided in Jiang et al. [252]. Numerical results show that the simulated magnitude and position of the temperature peak at the flame centerline are almost the same as the experimental results, which demonstrates the capacity of correctly capturing the temperature peak in terms of both position and magnitude. A consistent tendency of temperature profiles along the flame centerline between CFD predictions and experimental measurements is also shown. Predicted axial profiles of mole fractions of several species are also presented in Figure 7.2 together with experimental data of Jiang et al. [252]. Mole fraction profiles of the major species (i.e., C_2H_4, O_2, CO, H_2 and CO_2) along the flame centerline agree with experimental results very well, and the axial locations of the concentration peak of intermediate species (i.e., C_2H_2, C_4H_4 and $A1C_2H_3$) are well captured by the present simulation and in the same magnitude order as the experimental counterpart. More importantly, predictions on A1 and A2 concentrations are quite quantitatively satisfactory especially in the high temperature region, which are important for soot modelling as aromatic species are regarded as the origination of soot, therefore warranting the application in soot modelling [150].

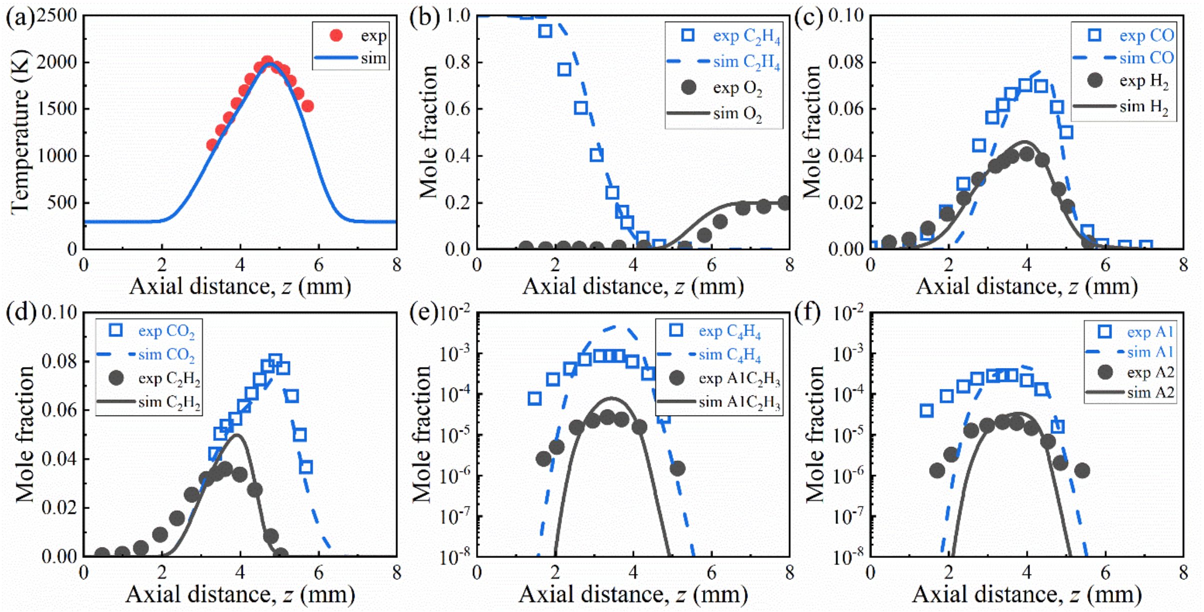

Figure 7.2 Comparisons between computed and experimental temperatures and species mole fractions along the flame centerline with X_F = 1.0 and X_O = 0.20.

7.3.2 Effect of oxygen mole fraction

It is reported that fuels generally have higher sooting tendencies [250,253] with oxygen mole fraction (i.e., X_O) of the oxidizer increasing for a CDF, especially when X_O is large than sooting limit (almost 0.2 for ethylene). The reason is that the variation of X_O leads to different flame temperatures while soot formation is sensitive to the flame temperature. The newly developed dimer-based soot model is validated at different X_O (0.25, 0.27 and 0.30) with both oxidizer and fuel inlet velocities of 20 cm/s in the present study, and the underlying mechanisms are discussed based on soot surface growth and oxidation and dimer production for soot inception and condensation.

Figure 7.3 presents effects of different X_O on SVF profiles along the flame centerline from the new dimer-based soot model in comparison with experimental dataset provided by Xu et al. [254]. As soot only exists at a specific region (i.e., 2 mm < z < 5 mm), only this region is presented for clear comparisons. Results show that the simulated SVF profiles along the flame centerline follow well with the experimental data at different X_O, especially both the magnitude and position of the SVF peak are well captured, which indicates that the new dimer-based soot mode is capable of correctly modelling soot formation and evolution in CDF. With axial distance (i.e., z) increasing, the SVF at different X_O increases firstly and then decreases sharply. It is worth noting that because soot could be generated on flame fuel-rich part, SVF profiles at different X_O are highly skewed towards the fuel stream, which are also well resolved by the numerical simulations. With the increase of X_O, this skewness to the fuel stream side becomes more markedly. Simultaneously, the SVF gradient become larger with the increase of X_O, and the shape of the SVF profiles becomes more asymmetrical. In addition, both flame temperature and mole fraction of C_2H_2 increase with X_O increasing as presented in Figure 7.4, resulting in the increase of surface growth and soot formation. This is consistent with previous research [253-255].

To explain these phenomena from the perspective of soot chemical kinetics, the changes in dimer number density as well as phenanthrene (A3) and pyrene (A4) mole fractions along the flame centerline at varying X_O are provided as shown in Figure 7.5, as dimers originating from A3 and A4 are responsible for soot formation in the present study. Results show that as X_O increases from 0.25 to 0.30, the maximum value of the dimer number density increases and its position moves towards the fuel stream gradually as shown in Figure 7.5(a). This reason is that the maximum concentrations of A3 and A4 also increase and the corresponding locations move towards the fuel stream with X_O increasing as presented in Figure 7.5(b). It should be noted that the profile shapes of A3, A4 and dimer concentrations are nearly symmetrical at different X_O, but the resulting SVF profiles as shown in Figure 7.3 are completely not symmetrical, which is originating from convection [254]. Specifically, soot particles generated in the oxidizing region are always transported away towards the fuel stream, leading to the skewness of the SVF profiles as shown in Figure 7.3.

Soot is assumed to be formed due to dimer collision and grows via dimer condensation, while a dimer is the heterogeneous collision result of PAH species (i.e., A3 and A4) in the present study. It is obvious that higher concentrations of A3 and A4 lead to higher dimer production rate as presented in Figure 7.6(a). HACA surface growth rates at different X_O would be presented in Figure 7.6(b). With X_O increasing, the HACA surface growth rate increases because of the increasing flame temperature and C_2H_2 as shown in Figure 7.4, which demonstrates that increasing X_O greatly enhances HACA surface growth rate as well as dimer production rate. The oxidation rate by O_2 increases but the OH oxidation rate decreases with X_O increasing as presented in Figure 7.6(c) and 7.6(d), but influence of OH oxidation rate is very small in comparison with O_2 at varying X_O. Compared with HACA surface growth rate, the oxidation rates due to O2 and OH are much smaller at different X_O, which implies that surface growth always plays a main role in HACA mechanisms for soot evolution. As a result, the collective effects of higher dimer production rate and dominant HACA surface growth rate result in larger mass growth rate of soot, therefore leading to higher SVF in the flame as shown in Figure 7.3. The soot number change rates due to nucleation and coagulation along the flame centerline are presented in Figure 7.7. As soot particles are nucleated via the collision of dimers, higher dimer number density leads to more frequently collision of dimers to generate new soot particles. As a result, the soot number nucleation rate increases to its peak and then drops, which shows a consistent tendency with dimer number density in Figure 7.5(a). The same tendency is also shown at different X_O, and the peak number nucleation rate increases with the increase of X_O. It should be noted that the soot number change rate due to coagulation is associated with the soot number density, which means that higher soot number density as shown in Figure 7.8(a) leads to higher coagulation frequency and higher coagulation rate. In addition, the number nucleation and coagulation rates increase with X_O increasing. It is of great interest to observe that with the increase of axial distance along the flame centerline, the soot number density increases quickly, then increase slower to its peak magnitude and then decreases sharply as shown in Figure 7.8(a). The reason is that coagulation starts to take effect at around z = 2.7 mm as presented in Figure 7.7(b), resulting in the slower increase in soot number density. Soot morphology is characterized by primary particles, mobility diameter and gyration diameter, which are shown in Figures 7.8(b) to 7.8(d), respectively. Simulation results present that the computed primary particle number in a soot aggregate, mobility diameter and gyration diameter increase to the maximum value and then drop along the centreline. With X_O increasing, peak primary particle number in a soot aggregate, mobility diameter and gyration diameter increase, and their peak positions are consistent with the SVF peak as presented in Figure 7.3.

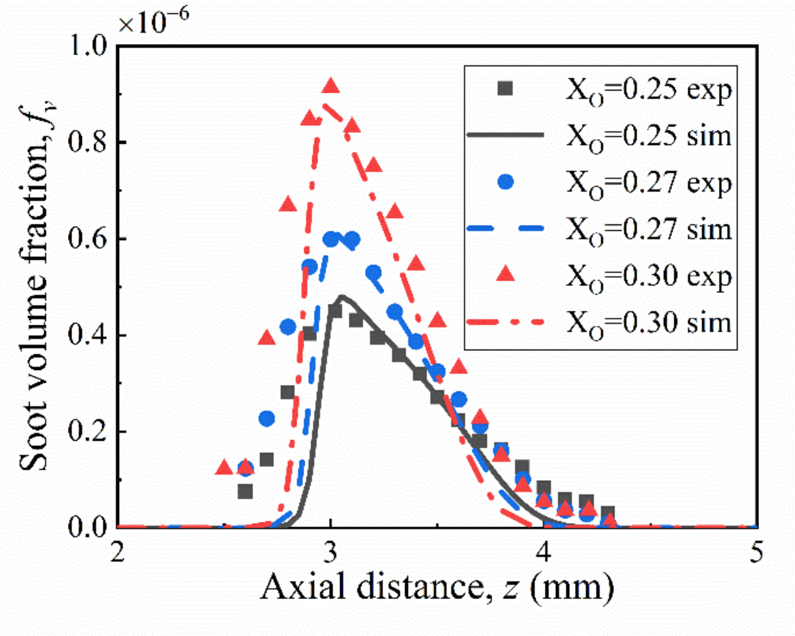

Figure 7.3 Comparisons between computed and experimental soot volume fractions along the flame centerline at different X_O ($X_F = 1.0$).

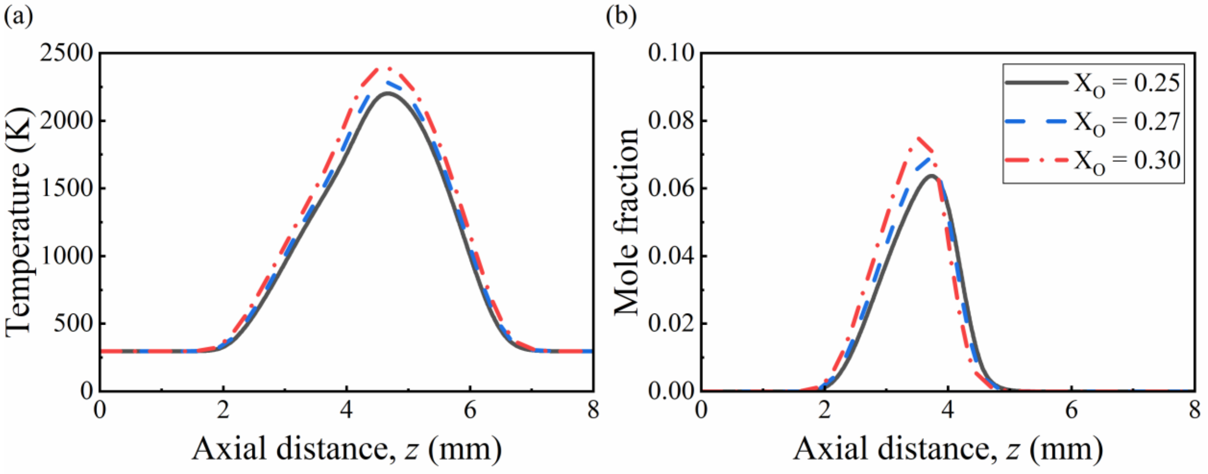

Figure 7.4 Temperature and C_2H_2 mole fraction profiles along the flame centerline at different X_O ($X_F = 1.0$).

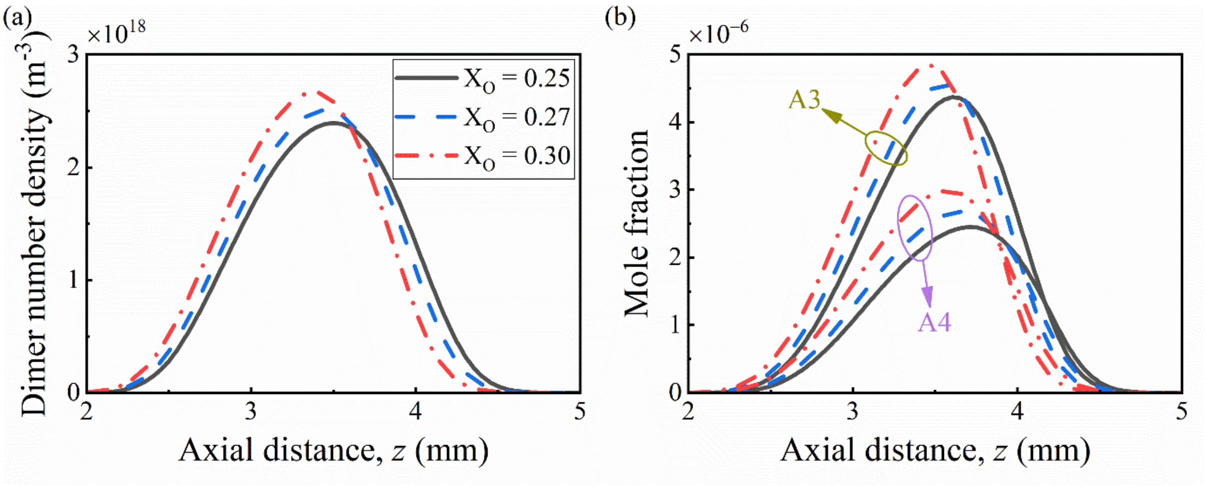

Figure 7.5 Dimer number density and mole fraction profiles of A3 and A4 along the flame centerline at different X_O (X_F = 1.0).

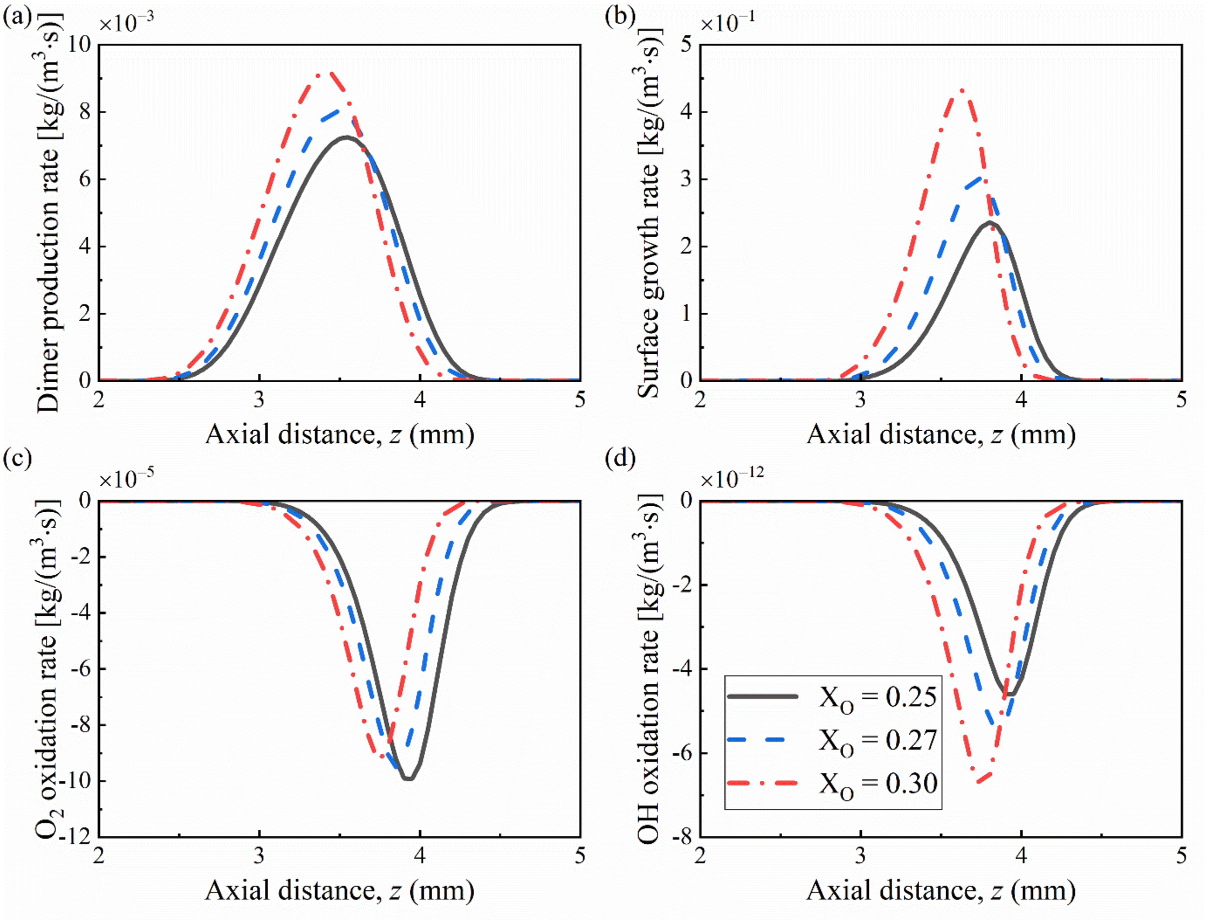

Figure 7.6 Dimer production rate, HACA surface growth rate, O2 oxidation rate and OH oxidation rate along the flame centerline at different X_O (X_F = 1.0).

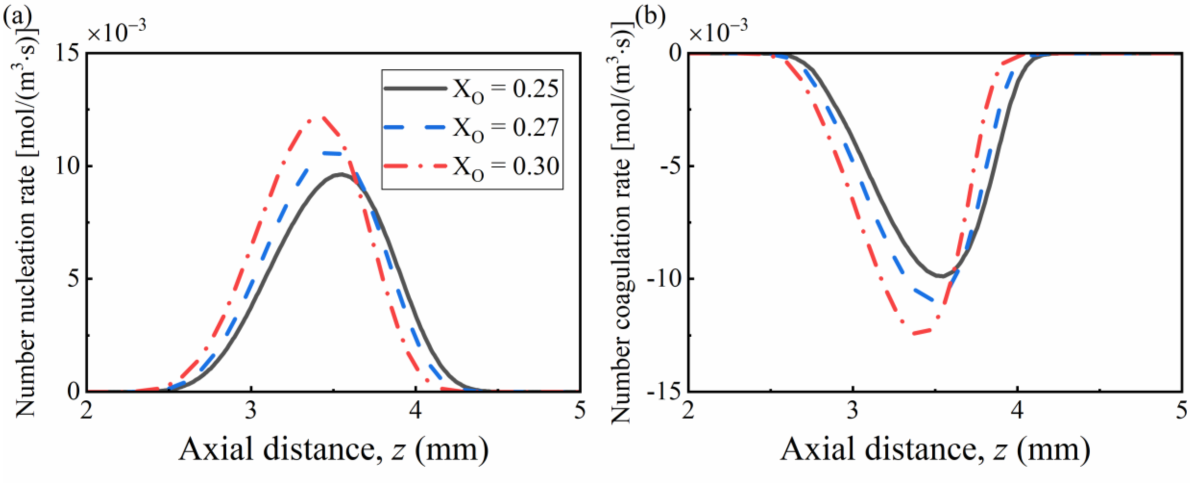

Figure 7.7 Numerical soot number change rate due to nucleation and coagulation along the flame centerline at different X_O ($X_F = 1.0$).

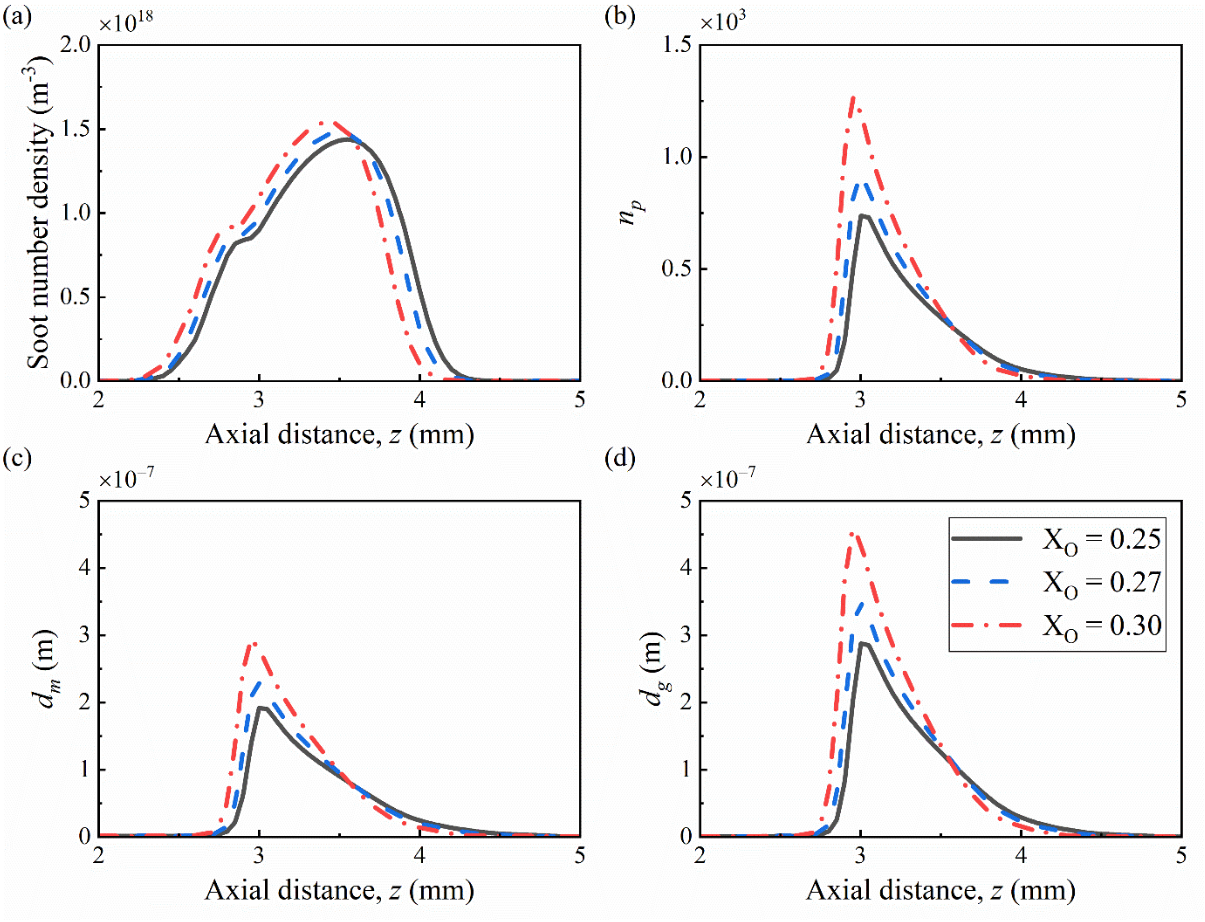

Figure 7.8 Numerical soot number density, number of primary particles in a soot aggregate, mobility diameter and gyration diameter along the flame centerline at different X_O ($X_F = 1.0$).

7.3.3 Effect of strain rate

The aerodynamic strain rate is an important factor in affecting soot formation, which could be determined by changing the oxidizer and fuel inlet velocities. The effect of adjusting strain rates with a wide range from 99 s^{-1} to 173 s^{-1} on SVF is numerically investigated by the new dimer-based soot model at $X_F = 1.0$ and $X_O = 0.25$. In this regard, simulations are conducted at varying oxidizer and fuel inlet velocities, whose experimental measurements are available in Zhou et al. [256].

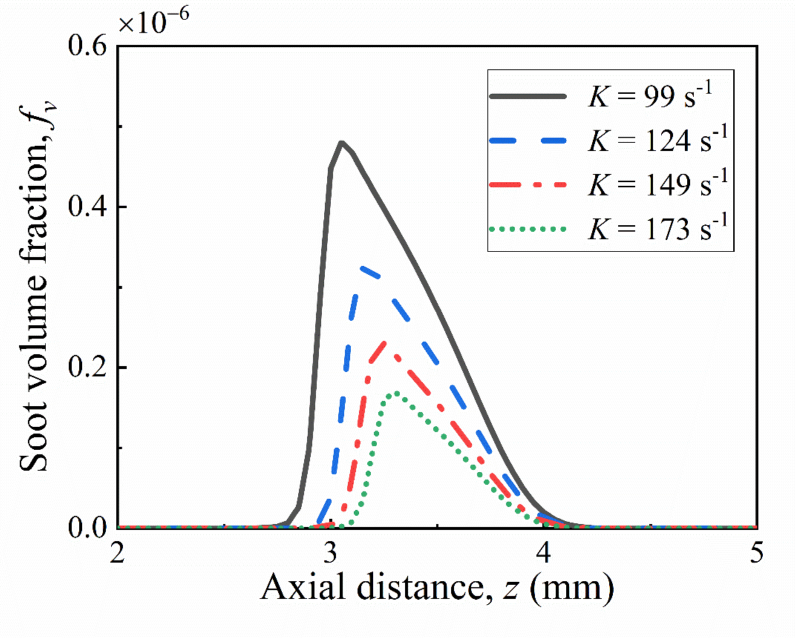

Figure 7.9 Computed soot volume fraction profiles along the flame centerline at different strain rates ($X_F = 1.0$ and $X_O = 0.25$).

The change of SVF profiles along the flame centerline with strain rates obtained from the dimer-based soot model is presented in Figure 7.9. Numerical results show that the SVF profile is more likely to skew towards the fuel stream with the reduction in strain rate, and the increasing strain rate leads to a gradually decrease of SVF due to the reducing residence time. The decreasing sooting tendency with strain rate increasing essentially stems from the evolution of dimers as well as A3 and A4. Specifically, with strain rate increasing, the concentrations of A3 and A4 decrease significantly, resulting in the reduction of dimer number density as shown in Figure 7.10. In addition, the resulting dimer production and HACA surface growth rates gradually decreases, while peak dimer production rate location gradually skews towards the oxidizer stream, leading to the skewness of the location of the peak dimer number density towards the oxidizer stream. Therefore, the resulting location of the peak SVF finally skews towards the oxidizer stream with the strain rate increasing. It should be noted that the SVF profiles in CDF show a unimodal function along the flame centerline, which makes it popular to use the maximum SVF in CDF for sooting comparisons. The computed peak SVF at varying strain rates are quantitatively compared with experimental dataset [256] as presented in Figure 7.11, and the peak SVF decreases monotonically with the strain rate increasing. Numerical results agree with experimental counterparts very well, among which slight discrepancies are shown at different strain rates from 99 s^{-1} to 173 s^{-1}. Their good agreements demonstrate that the dimer-based soot model is capable of reasonably predicting soot formation and evolution processes at a wide range of strain rates.

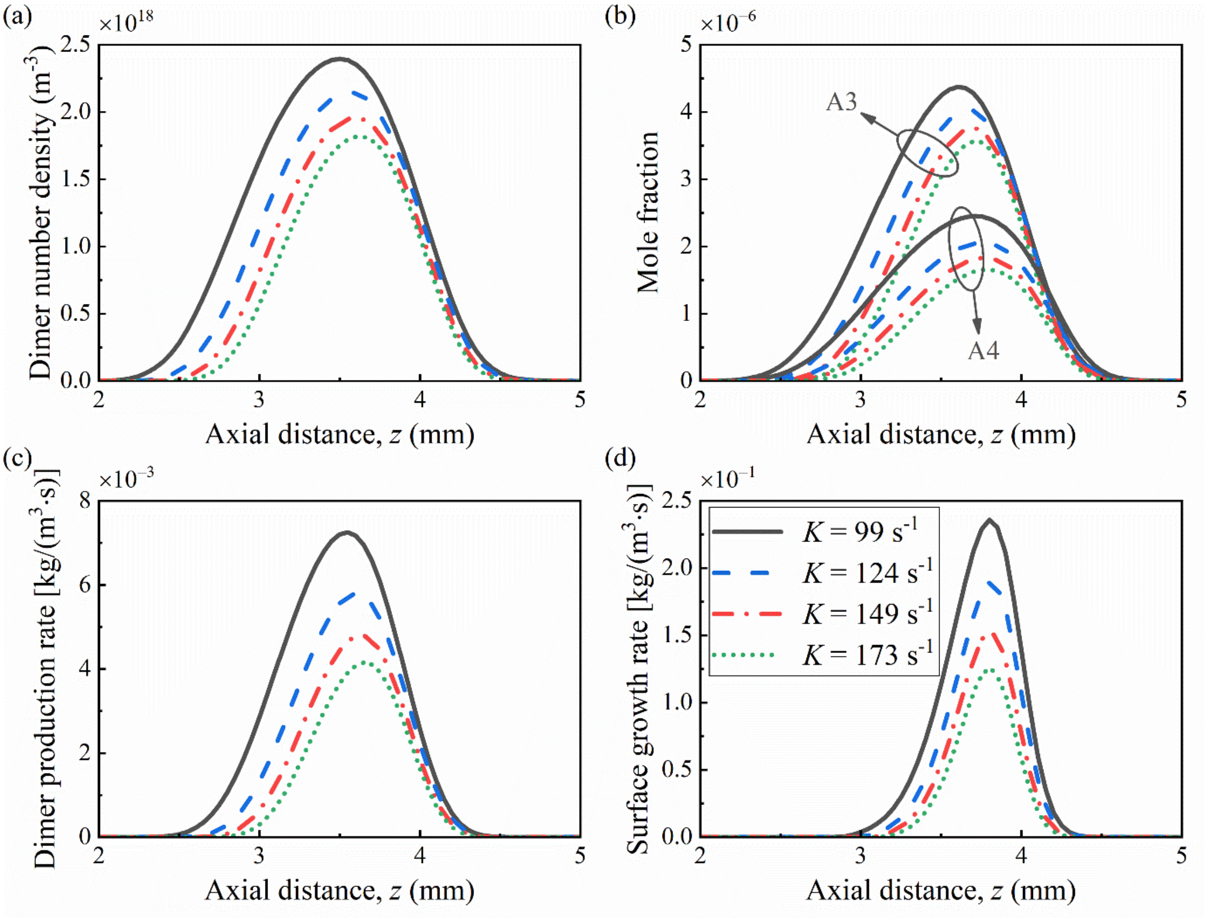

Figure 7.10 Dimer number density, mole fraction profiles of A3 and A4, dimer production rate and HACA surface growth rate along the flame centerline for varying strain rates ($X_F = 1.0$ and $X_O = 0.25$).

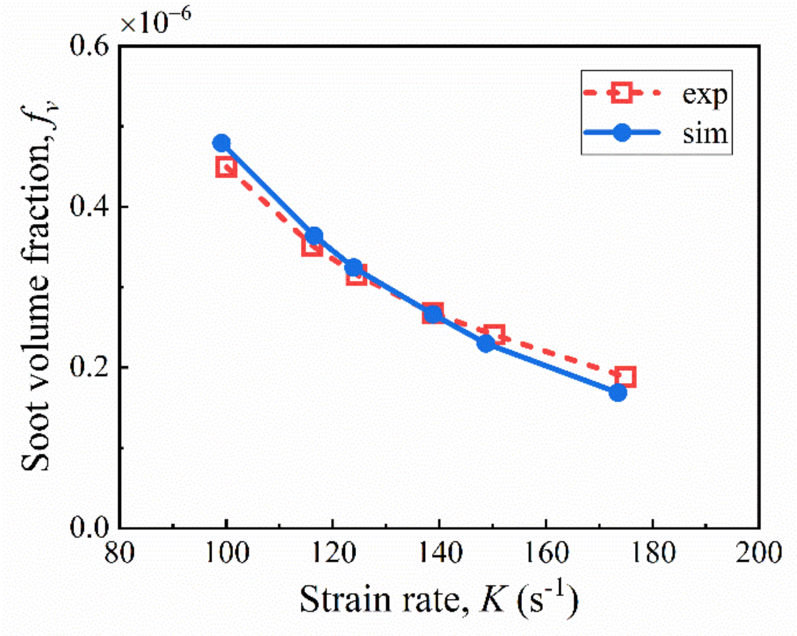

Figure 7.11 Comparisons between computed and experimental peak soot volume fractions at different strain rates (X_F = 1.0, X_O = 0.25).

7.4 Summary

In the present study, a new dimer-based soot model for laminar counterflow diffusion flames is proposed and developed to model soot formation. Transport equations of soot number and mass densities are formulated considering dimer formation and condensation, HACA surface growth and oxidation and coagulation. Soot would be formed because of dimer collision and grows via dimer condensation, while a dimer is the homogeneous and heterogeneous collision results of polycyclic aromatic hydrocarbon (PAH) species made up of 50 or more carbon atoms. In a steady state, the generation rate and consumption rate of dimers are kept in a balance. The masses of PAHs used for dimer formation are calculated based on a weighted average of total PAH masses and their densities are estimated to be associated with their chemical compositions. The dimer-based soot model is validated at different strain rates as well as varied oxygen mole fractions (X_O) of the oxidizer based on the OpenFOAM solver, which integrates the mixture-averaged transport model for reacting flows. Numerical results show that the simulated SVF profiles agree well with experimental counterparts, in which the magnitudes of the SVF peak are well captured. With the increase of X_O, HACA surface growth and dimer production (soot nucleation and surface growth via dimer condensation) are significantly enhanced, leading to an increase in the SVF. Compared with HACA surface growth, the impact of varying oxygen mole fractions on oxidation rates of O_2 and OH is slight, which implies that surface growth is a dominant factor in determining SVF. As the strain rate increases, the SVF gradually decreases as dimer production and HACA surface growth rates significantly decrease. With the increase in X_O or decrease in strain rate, the skewness of the SVF profile towards the fuel stream become more significant.

Chapter 8 Development of One-equation Turbulence Model

8.1 Introduction

Governing equations for turbulent flows are not closed by using Reynolds averaging due to the introduction of turbulent viscosity, which should be modelled. The present study is to derive the transport equations in the complete form and retain the third-order velocity gradient term without simply assuming equal coefficients of the diffusion terms in the process of transformation of the parent two-equation turbulence model to one-equation turbulence model. The newly proposed and developed one-equation turbulence model combines the best characteristics of the two-equation standard *k*-*ε* (SKE) [185] and Wilcox's *k*-*ω* (WKO) [257] turbulence models. The accuracy of the new one-equation turbulence model is compared with the results of the experimental dataset, the commonly used one- and two-equation turbulence models and the high-accuracy NASA codes (i.e., CFL3D and FUN3D) as well as the direct numerical simulation (DNS) for benchmark flow configurations. It should be noted that turbulent Schmidt and Prandtl numbers can be introduced for turbulent transport of scalar quantities based on the turbulent viscosity solved by the developed one-equation turbulence model.

8.2 Methodology

The development of a new one-equation turbulence model [54] based on two-equation SKE [185] and WKO [257] turbulence models is presented. The derived equations are written in boundary-layer coordinates for simplicity. *x* and *y* represent the streamwise coordinate and normal to the boundary layer, respectively, and *t* is time.

8.2.1 *k*-*ε* based one-equation turbulence model

The SKE two-equation in the boundary layer can be written as [54]:

$$\frac{Dk}{Dt} = G - \varepsilon + \frac{\partial}{\partial \mathrm{y}}\left[\left(\nu + \frac{\tilde{\nu}_t}{\sigma_k}\right)\frac{\partial k}{\partial y}\right] \tag{8-1}$$

$$\frac{D\varepsilon}{Dt} = C_{\varepsilon 1} G \frac{\varepsilon}{k} - C_{\varepsilon 2}\frac{\varepsilon^2}{k} + \frac{\partial}{\partial y}\left[\left(\nu + \frac{\tilde{\nu}_t}{\sigma_\varepsilon}\right)\frac{\partial \varepsilon}{\partial y}\right] \tag{8-2}$$

$$G = \frac{\tau_{ij}}{\rho}\frac{\partial u_i}{\partial y} \tag{8-3}$$

$$\tau_{ij} = \rho\tilde{v}_t\left(2S_{ij} - \frac{2}{3}\frac{\partial u_k}{\partial x_k}\delta_{ij}\right) - \frac{2}{3}\rho k\delta_{ij} \tag{8-4}$$

$$S_{ij} = \frac{1}{2}\left(\frac{\partial u_i}{\partial y} + \frac{\partial u_j}{\partial x}\right) \tag{8-5}$$

$$\widetilde{v}_t = C_\mu\frac{k^2}{\varepsilon} \tag{8-6}$$

where G is the production term and δ_{ij} is the Kronecker delta; S_{ij} and τ_{ij} are shear stress and strain rate tensors; v and $\widetilde{v}_t$ represent kinematic and eddy viscosities; k and ε represent turbulent kinetic energy and its dissipation rate.

Using the time derivatives of k and ε to express the time derivative of $\widetilde{v}_t$, a new transport equation for the turbulent viscosity is obtained as [54]:

$$\frac{D\widetilde{v}_t}{Dt} = C_\mu\left(2\frac{k}{\varepsilon}\frac{Dk}{Dt} - \frac{k^2}{\varepsilon^2}\frac{D\varepsilon}{Dt}\right) \tag{8-7}$$

The relationship between k and ε is confirmed by many experimental boundary layer data [96,101,258], which is expressed as:

$$\left|-\overline{u'v'}\right| = \widetilde{v}_t\left|\frac{\partial u}{\partial y}\right| = \sqrt{C_\mu}k \tag{8-8}$$

where $\left|-\overline{u'v'}\right|$ is the turbulent shear stress, and C_μ is a constant. Further, the invariant value, S, is widely used to replace the absolute value of streamwise velocity gradient along the normal direction, which is defined by [96]:

$$S = \sqrt{2S_{ij}S_{ij}} \tag{8-9}$$

Thus, a general form of the one-equation turbulence model transformed from SKE is obtained by straightforward substitution as [54]:

$$\frac{D\widetilde{v}_t}{Dt} = (C_{\varepsilon 2} - C_{\varepsilon 1})C_\mu^{\frac{1}{2}}\widetilde{v}_t S + 6\left(\frac{1}{\sigma_k} - \frac{1}{\sigma_\varepsilon}\right)\frac{\widetilde{v}_t}{S}\frac{\partial S}{\partial x_j}\frac{\partial\widetilde{v}_t}{\partial x_j} + 2\left(\frac{1}{\sigma_k} - \frac{1}{\sigma_\varepsilon}\right)\frac{\widetilde{v}_t^2}{S}\frac{\partial}{\partial x_j}\left(\frac{\partial S}{\partial x_j}\right) \tag{8-10}$$

$$-\frac{2}{\sigma_\varepsilon}\frac{\tilde{v}_t^2}{S^2}\frac{\partial S}{\partial x_j}\frac{\partial S}{\partial x_j}+\frac{\partial}{\partial x_j}\left\{\left[v+\left(\frac{2}{\sigma_k}-\frac{1}{\sigma_\varepsilon}\right)\tilde{v}_t\right]\frac{\partial \tilde{v}_t}{\partial x_j}\right\}$$

where $C_\mu = 0.09$, $C_{\varepsilon 1} = 1.44$, $C_{\varepsilon 2} = 1.92$, $\sigma_k = 1.0$ and $\sigma_\varepsilon = 1.3$.

It is worth noting that the third term on the right-hand side in Equation (8-10) involves the third-order velocity gradients, which is always neglected due to simplicity in many studies by assuming that the coefficients of the diffusion terms are equal [96]. It is reported that the third-order velocity gradients are essential to the combustion modelling due to their appearance in the thickened flame model, which are widely used [95,259]. Thus, a one-equation turbulence model preserving the completeness of the SKE is derived, and the transport equation for $\tilde{v}_t$ in the complete form is solved as [54]:

$$\frac{D\tilde{v}_t}{Dt}=\beta_\varepsilon\tilde{v}_t S+\gamma_\varepsilon\frac{\tilde{v}_t}{S}\frac{\partial S}{\partial x_j}\frac{\partial \tilde{v}_t}{\partial x_j}+C_1\frac{\tilde{v}_t^2}{S}\frac{\partial}{\partial x_j}\left(\frac{\partial S}{\partial x_j}\right)-C_2\frac{\tilde{v}_t^2}{S^2}\frac{\partial S}{\partial x_j}\frac{\partial S}{\partial x_j}+\frac{\partial}{\partial x_j}\left[(v+\alpha_\varepsilon\tilde{v}_t)\frac{\partial \tilde{v}_t}{\partial x_j}\right] \tag{8-11}$$

where the values of the coefficients are recalibrated and given by $\alpha_\varepsilon = 1.0$, $\beta_\varepsilon = 0.144$, $\gamma_\varepsilon = 0.2386$, $C_1 = 0.0795$ and $C_2 = 1.5385$.

The transport equation for $\tilde{v}_t$ based on SKE is still in the high-Reynolds-number form which does not have any damping function given.

8.2.2 *k-ω* based one-equation turbulence model

The WKO two-equation in the boundary layer can be written as [54]:

$$\frac{Dk}{Dt}=G-\beta^* k\omega+\frac{\partial}{\partial y}\left[(v+\alpha_k\tilde{v}_t)\frac{\partial k}{\partial y}\right] \tag{8-12}$$

$$\frac{D\omega}{Dt}=\gamma\frac{\omega}{k}G-\beta\omega^2+\frac{\partial}{\partial y}\left[(v+\alpha_\omega\tilde{v}_t)\frac{\partial \omega}{\partial y}\right] \tag{8-13}$$

where the eddy viscosity, $\tilde{v}_t = k/\omega$.

The substantial derivative of the eddy viscosity is expressed as [54]:

$$\frac{D\tilde{v}_t}{Dt}=\frac{1}{\omega}\frac{Dk}{Dt}-\frac{k}{\omega^2}\frac{D\omega}{Dt} \tag{8-14}$$

By a similar procedure with the above derivations (Equations (8-8) to (8-9)), the one-equation turbulence model transformed from WKO in a general form is expressed as [54]:

$$\frac{D\widetilde{\nu}_t}{Dt}=\left[(1-\gamma)C_\mu^{\frac{1}{2}}+\left(\beta-\beta^*\right)C_\mu^{-\frac{1}{2}}\right]\widetilde{\nu}_t S+(3\alpha_k-\alpha_\omega)\frac{\widetilde{\nu}_t}{S}\frac{\partial S}{\partial x_j}\frac{\partial\widetilde{\nu}_t}{\partial x_j}+\frac{\partial}{\partial x_j}\left[(\nu+\alpha_k\widetilde{\nu}_t)\frac{\partial\widetilde{\nu}_t}{\partial x_j}\right] \tag{8-15}$$

where $C_\mu = 0.09$, $\beta = 3/40$, $\beta^* = 0.09$, $\alpha_k = 0.5$, $\alpha_\omega = 0.0795$ and $\gamma = 1.5385$.

However, it is reported that the coefficient of the diffusion term is small, which leads to a large velocity gradient near the boundary layer edge [96] and a higher value is suggested [260]. The resulting one-equation based on WKO can be written as [54]:

$$\frac{D\widetilde{\nu}_t}{Dt}=\beta_\omega\widetilde{\nu}_t S+\gamma_\omega\frac{\widetilde{\nu}_t}{S}\frac{\partial S}{\partial x_j}\frac{\partial\widetilde{\nu}_t}{\partial x_j}+\frac{\partial}{\partial x_j}\left[(\nu+\alpha_\omega\widetilde{\nu}_t)\frac{\partial\widetilde{\nu}_t}{\partial x_j}\right] \tag{8-16}$$

where the recalibrated coefficients are $\alpha_\omega = 1.2$, $\beta_\omega = 0.084$ and $\gamma = 1.7$.

8.2.3 Development of a new one-equation turbulence model

Based on the two transport equations derived in Equations (8-11) and (8-16), Equation (8-11) is multiplied by (1-F_1) and Equation (8-16) is multiplied by F_1, a completely new equation is then obtained as [54]:

$$\frac{D\widetilde{\nu}_t}{Dt}=\beta_\nu\widetilde{\nu}_t S+\gamma_\nu\frac{\widetilde{\nu}_t}{S}\frac{\partial S}{\partial x_j}\frac{\partial\widetilde{\nu}_t}{\partial x_j}+C_1(1-F_1)\frac{\widetilde{\nu}_t^2}{L^2}-C_2(1-F_1)\frac{\widetilde{\nu}_t^2}{L_{\nu k}^2}+\frac{\partial}{\partial x_j}\left[(\nu+\alpha_\nu\widetilde{\nu}_t)\frac{\partial\widetilde{\nu}_t}{\partial x_j}\right] \tag{8-17}$$

where $L_{\nu k}$ and L represent von Kármán length scale and length scale, which are similar to the terms used in the k-kL equation [95] as:

$$\frac{1}{L^2}=\frac{1}{S}\frac{\partial}{\partial x_j}\left(\frac{\partial S}{\partial x_j}\right),\frac{1}{L_{\nu k}^2}=\frac{1}{S^2}\frac{\partial S}{\partial x_j}\frac{\partial S}{\partial x_j} \tag{8-18}$$

The coefficients in the Equation (8-17) are defined as [54]:

$$\alpha_\nu=\alpha_\omega F_1+\alpha_\varepsilon(1-F_1),\beta_\nu=\beta_\omega F_1+\beta_\varepsilon(1-F_1),\gamma_\nu=\gamma_\omega \mathrm{F}_1+\gamma_\varepsilon(1-F_1) \tag{8-19}$$

where F_1 is the blending function given by [54]:

$$F_1=\tanh\left(\arg 1^4\right) \tag{8-20}$$

The newly proposed and developed one-equation turbulence model [54] behaves like the SKE when $F_1 \rightarrow 0$, while it functions as the WKO when $F_1 \rightarrow 1$, which combines the best features of both two-equation turbulence models. More importantly, the blending function has the similar form with that of the SST k-ω turbulence model [261], so the new one-equation turbulence model can behave like the SST k-ω turbulence model [261].

$$\mathrm{arg1} = \max\left(\frac{C_\mu^{1/4}\tilde{\nu}_t^{1/2}}{\beta^* S^{1/2} d}, \frac{500 C_\mu^{1/2}\nu}{d^2 S}\right) \tag{8-21}$$

where d represents distance to nearest wall; ν_t represents turbulent eddy viscosity, which could be expressed as [54]:

$$\nu_t = f_\mu \tilde{\nu}_t \tag{8-22}$$

where the wall damping function, f_μ, is given by [54]:

$$f_\mu = \frac{\chi^3}{\chi^3 + C_w^3}, \chi = \frac{\tilde{\nu}_t}{\nu}, C_w = 9.1 \tag{8-23}$$

To prevent singularity when S goes to zero, it is necessary to bound S in the third term with a very small value while the fourth term of the right-hand side of Equation (8-17) can be given by [54]:

$$\frac{\tilde{\nu}_t^2}{L_{vk}^2} = C_3 E_{BB} \tanh\left(\frac{E_{\tilde{\nu}_t}}{C_3 E_{BB}}\right) \tag{8-24}$$

where

$$E_{\tilde{\nu}_t} = \frac{\tilde{\nu}_t^2}{S^2}\frac{\partial S}{\partial x_j}\frac{\partial S}{\partial x_j}, E_{BB} = \frac{\partial \tilde{\nu}_t}{\partial x_j}\frac{\partial \tilde{\nu}_t}{\partial x_j}, C_3 = 7.0 \tag{8-25}$$

The value of $\tilde{\nu}_t$ at smooth and viscous solid walls is prescribed to be zero while the value of $\tilde{\nu}_t$ for the freestream is set to be 3ν to 5ν.

8.3 Numerical Methods

The proposed new one-equation turbulence model is developed based on the open-source CFD toolbox, OpenFOAM [262], and is discretized using the Gaussian integration scheme based on the finite-volume method (FVM). The OpenFOAM solver used in the present study is the *simpleFoam*, which utilizes the Semi-Implicit Method for Pressure Linked Equations (SIMPLE) algorithm for pressure-velocity coupling. The central difference scheme (i.e., Gauss linear) is used for all gradient terms while a second-order upwind difference scheme (i.e., Gauss linearUpwind) is used to discretize the convection terms in all equations. The central difference interpolation scheme (i.e., linear) is used while the Gauss linear corrected is used for the Laplacian term. An explicit non-orthogonal correction method (i.e., corrected) is used for surface-normal gradients.

8.4 Results and Discussion

Several typical benchmark flow cases are used based on an open source CFD software OpenFOAM to evaluate the performance of the newly proposed and developed one-equation turbulence model based on the two-equation SKE [185] and WKO turbulence models [257]. Meshes in all typical benchmark flow cases are obtained from the website of the Langley Research Center Turbulence Modeling Resource (TMR) [263]. Mesh independence study is also performed for all cases where the value of the maximum wall y^+ is less than 1. Except for the third-order velocity gradient term, the one-equation Wray-Agarwal turbulence model (WA) [101] and the two-equation SST k-ω turbulence model (SST k-ω) [261] are very similar with the newly developed one-equation turbulence model. Thus, the numerical results of the new one-equation turbulence model [54] are fully validated and compared with the WA and SST k-ω turbulence models [101,261], the high-accuracy NASA codes (i.e., CFL3D and FUN3D) [263] and the experimental results [264-266].

Pressure coefficient, C_p and wall skin friction coefficient, C_f are defined as [267]:

$$C_\mathrm{p} = \frac{P_\mathrm{w} - P_\mathrm{ref}}{\frac{1}{2}\rho U_\mathrm{ref}^2} \tag{8-26}$$

$$C_\mathrm{f} = \frac{\tau_w}{\frac{1}{2}\rho U_\mathrm{ref}^2} \tag{8-27}$$

where τ_w is the skin shear stress on a surface, P_w is the wall static pressure and $\frac{1}{2}\rho U_\mathrm{ref}^2$ is the local dynamic pressure.

8.4.1 Flow over a flat plate at zero pressure gradient

The classical case for a turbulence modelling testing and validation is the flat plate with zero pressure gradient provided by the NASA TMR [263]. The flow configuration is shown in Figure 8.1 with the initial boundary conditions [263]. Two meters long of solid wall and one-third meter of symmetry boundary conditions are prescribed to obtain a uniform inlet flow. A far field Riemann boundary condition (BC) is also prescribed. The static pressure at the outlet, P is equal to the reference pressure, P_ref, while the total pressure at the inlet, P_t is $1.02828P_\mathrm{ref}$. The Reynolds number, $\mathrm{Re}_x = \rho U_\mathrm{ref}\, x/\mu$, based on the distance, x from the leading edge of a flat plate where U_ref is the uniform inlet velocity, and ρ and μ are the fluid density and dynamic viscosity, respectively. The Mach, Ma and Reynolds, Re_x numbers at the inlet are 0.2 and 5×10^6

based on x = 1 m.

The numerical results of the wall skin friction coefficient, C_f is compared with the experimental results [264] as well as the selected one-equation WA and two-equation SST k-ω turbulence models, along the streamwise Re_x as shown in Figure 8.2. The results show that the one-equation WA turbulence model [101] has the best prediction of C_f at $Re_x < 1.0\times10^6$, but overpredicts C_f at the rest of Re_x region. However, the values of C_f of the new one-equation turbulence model [54] agree well with that of the experimental results [264]. The new one-equation turbulence model performs much better in predicting C_f along the flat plate than the two-equation SST k-ω turbulence model [261].

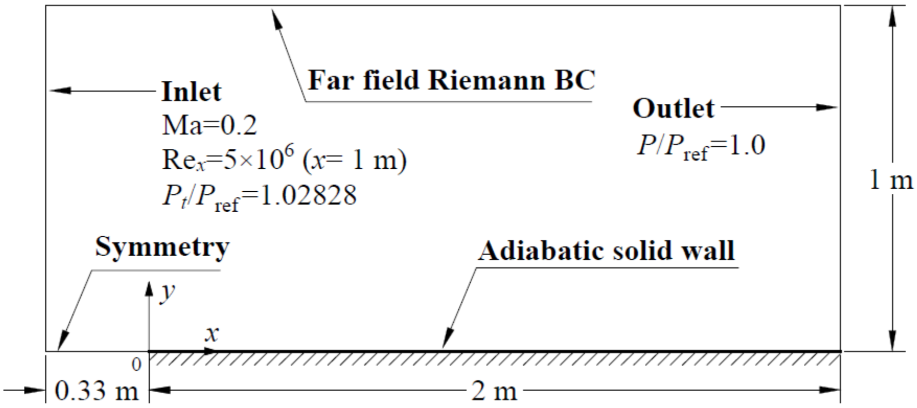

Figure 8.1 Configuration of the turbulent flow over a flat plate [54].

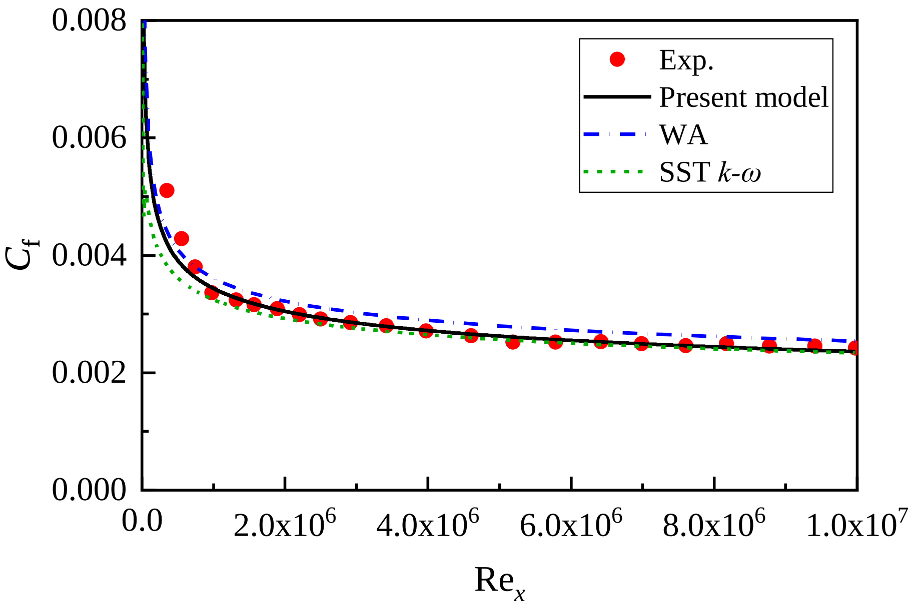

Figure 8.2 Wall skin friction coefficients for different Reynolds numbers [54].

8.4.2 Bump-in-channel flow

The main difference between the turbulent flat plate flow and bump-in-channel flow is that the latter involves pressure gradients due to the wall curvature. Figure 8.3 presents the flow configuration in terms of the bump in channel and the initial boundary conditions [263]. The solid wall including the bump extends from $x = 0$ to 1.5 m, and the symmetry boundary conditions with 25 m long are prescribed to the upstream and downstream of the solid bump wall. The Ma and Re_l based on the inlet velocity and length $l = 1$ m are 0.2 and 3×10^6, respectively. The static pressure at the outlet, P is equal to the reference pressure, P_{ref}, while the total pressure at the inlet, P_t is $1.02828P_{\mathrm{ref}}$.

Figure 8.4 shows the wall skin friction coefficient, C_{f} along the bump wall when compared with those numerical data obtained from CFL3D and FUN3D codes [263]. The SST k-ω turbulence model [261] has the best prediction of C_{f} at $x < 0.15$ m, but underpredicts the wall skin friction coefficient at $0.6 < x < 0.8$ m. Although the WA turbulence model [101] predicts C_{f} well at $0.6 < x < 0.8$ m, it overpredicts the values at the rest of x region. The new one-equation turbulence model [54] performs better in predicting C_{f} than the WA turbulence model at $x < 0.15$ m and has the better prediction of C_{f} than other turbulence models at $x > 0.15$ m. The pressure coefficients, C_{p} along the bump wall simulated by all these turbulence models have an excellent agreement with the results of CFL3D and FUN3D codes [263] as shown in Figure 8.5.

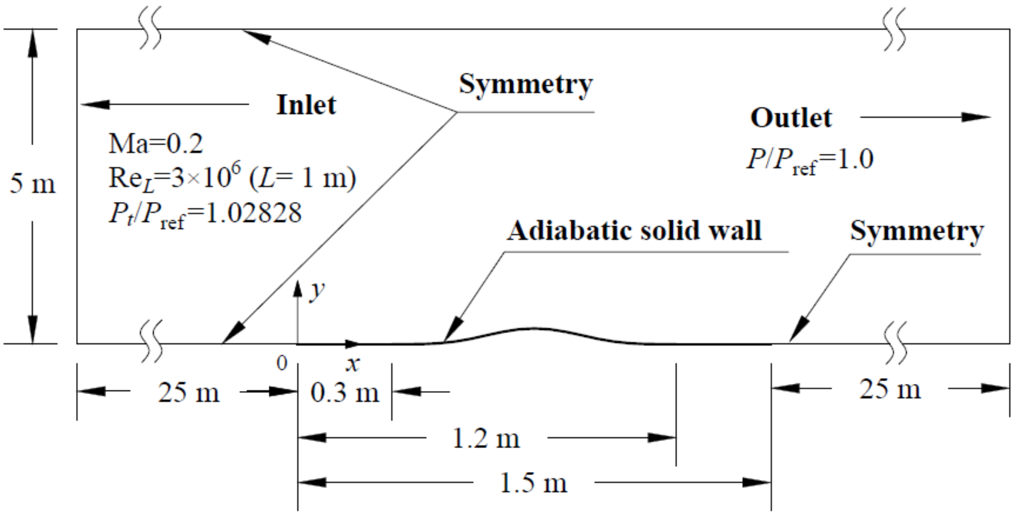

Figure 8.3 Bump-in-channel flow configuration.

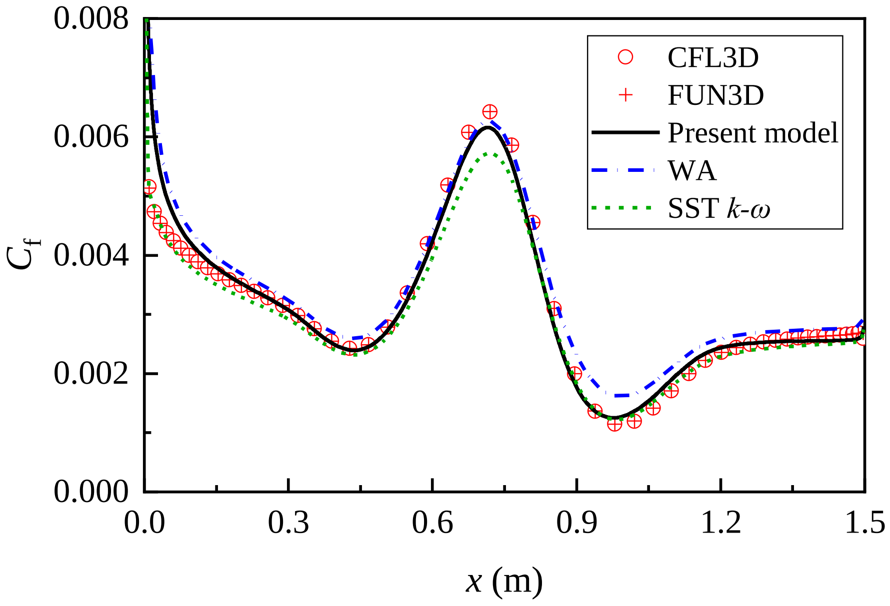

Figure 8.4 Wall skin friction coefficient along the bump wall [54].

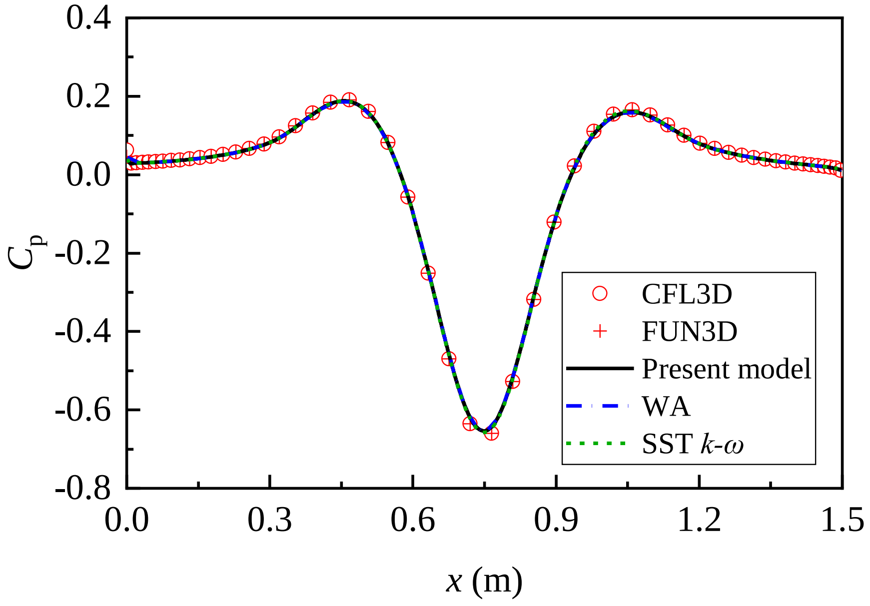

Figure 8.5 Pressure coefficient along the bump wall [54].

8.4.3 Backward facing step flow

The backward facing step flow is used as the benchmark validation, which is widely used for evaluating the turbulence models, due to its complicated flow mechanism but it is a simple geometric configuration. Figure 8.6 shows the backward facing step geometry and flow initial boundary conditions [265]. The step height, H is 12.7 mm, and the height of the inlet channel before the step is 8H. The inlet channel is 110H long before the step to ensure a fully developed turbulent flow condition in the numerical simulation. The distance between the step and outlet is 50H which is far larger than the distance from the flow separation point to the reattachment point of the flow. The Ma and Re_H based on the inlet velocity and step height are 0.128 and 3.6×10^4, respectively.

Figure 8.7 shows the wall skin friction coefficient, C_f along the step wall when compared with experimental data [265]. The new one-equation turbulence model [54] has the better prediction of C_f before the step than other turbulence models. When the flow is separated, the new one-equation turbulence model and one-equation WA turbulence model [101] predict precisely the values of C_f while the two-equation SST k-ω turbulence model [261] substantially overpredicts the values of C_f. In the reattachment region, the two-equation SST k-ω turbulence model underestimates the values of C_f, and the experimental results best match the numerical results of the one-equation WA turbulence model. The numerical results of the new one-equation turbulence model have an acceptable agreement with the experimental data [265]. But it is worth noting that the new one-equation turbulence model provides better prediction of the wall skin friction coefficient recovery after the reattachment point, while the WA and the SST k-ω turbulence models slowly recover the wall skin friction coefficients after the flow separation. The main reason is that the effect of the third-order velocity gradients can increase the turbulent diffusion which is also found in the research study of Elkhoury [95]. The pressure coefficient, C_p along the step wall is shown in Figure 8.8. Compared with the experimental data [265], there are the overpredictions of C_p by all these turbulence models at $x/H < 3$, while they have a good agreement with the experimental results at $x/H > 3$. Of all these turbulence models, the new one-equation turbulence model [54] performs comparably with the two-equation SST k-ω turbulence model [261] and has better prediction of C_p than the one-equation WA turbulence model [101].

The comparison of the velocity profiles at various x/H locations with the experimental results [265] is shown in Figure 8.9. The velocity profiles obtained by all these turbulence models are very close and agree well with the experimental data including the new one-equation turbulence model [54]. It implies that the introduction of the third-order velocity derivative term in the new one-equation turbulence model has little effect on the velocity profile near the boundary layer, which is also found in the research study of Elkhoury [95].

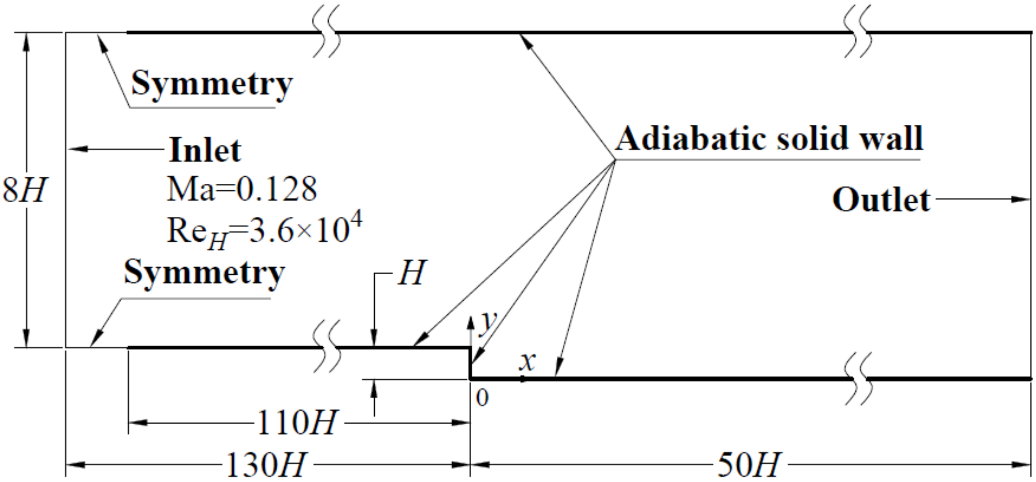

Figure 8.6 Backward facing step flow configuration.

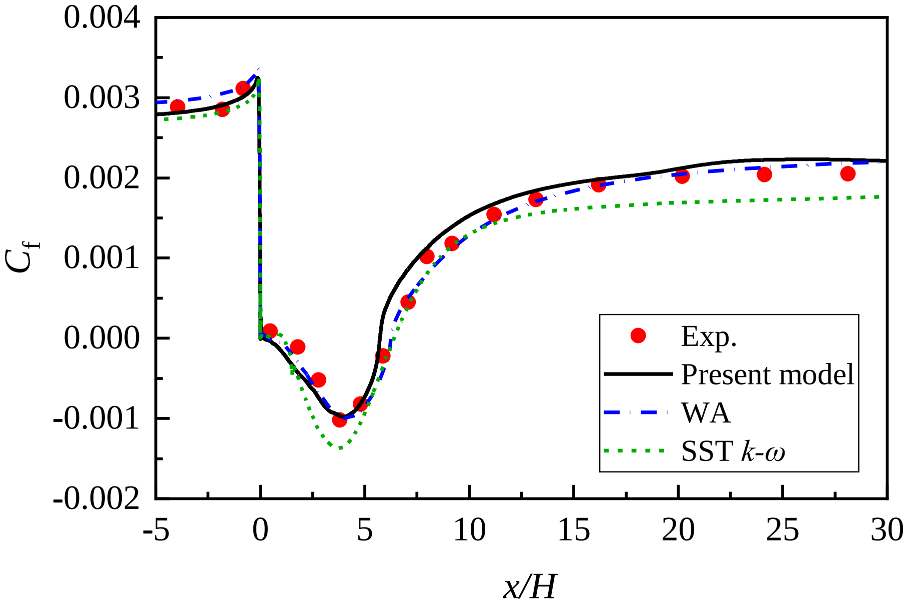

Figure 8.7 Wall skin friction coefficient along the step wall [54].

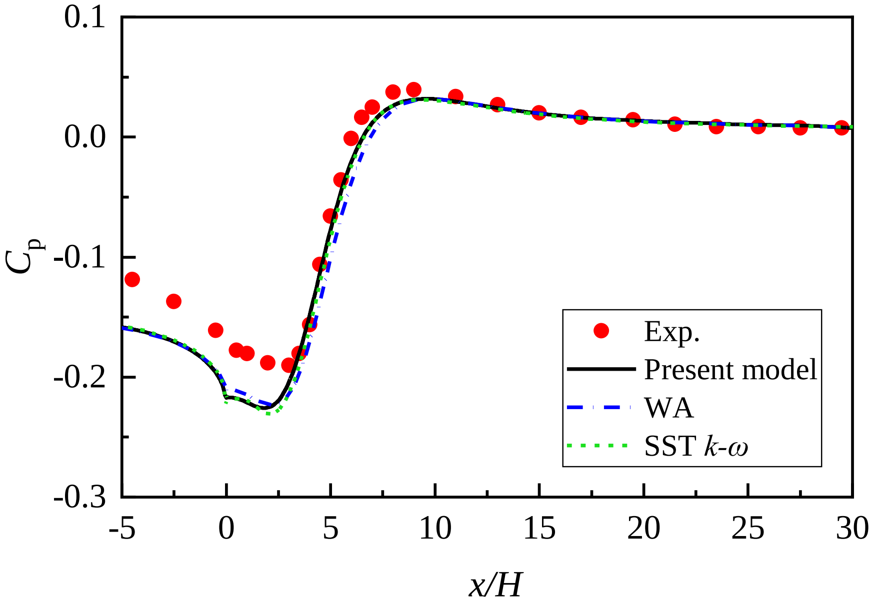

Figure 8.8 Pressure coefficient along the step wall [54].

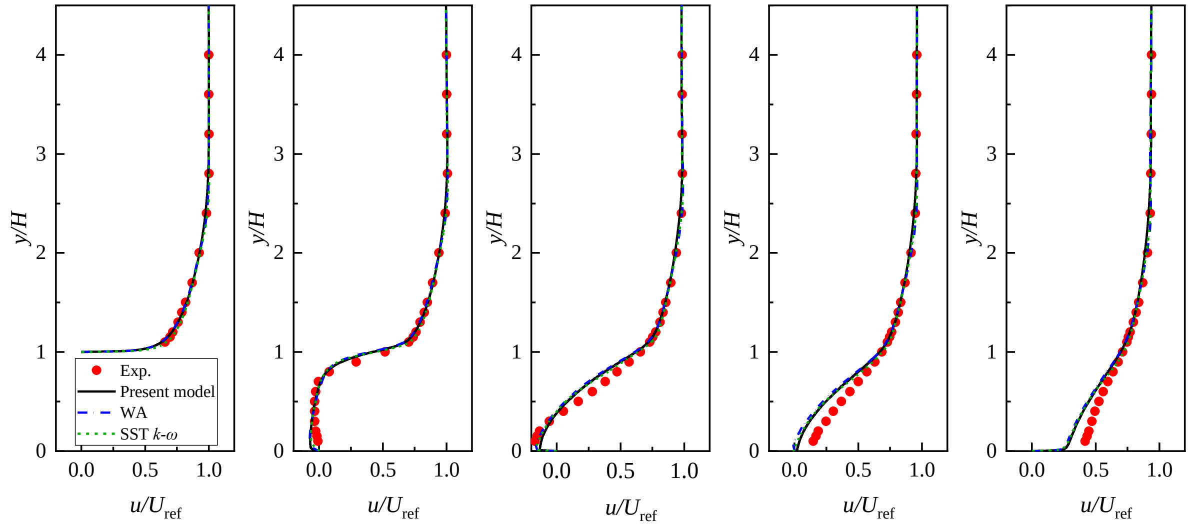

(a) x/H= −4 (b) x/H= 1 (c) x/H= 4 (d) x/H= 6 (e) x/H= 10

Figure 8.9 Velocity profiles of the backward facing step at x/H= −4, 1, 4, 6 and 10 [54].

8.4.4 NASA wall-mounted hump separated flow

The NASA wall-mounted hump separated flow configuration is also used as the benchmark validation. The accuracy of this benchmark test case is very challenging for many turbulence models. Figure 8.10 shows the configuration of wall-mounted hump separated flow

[268] and initial boundary conditions [266]. The hump chord length, c is 420 mm and the height of the inlet channel before the start of the hump is 2.17c. The inlet channel has a length of 15.2c before the start of the hump and the distance from the end of the hump to the outlet is 7.15c. The Ma and Re_c based on the inlet velocity and hump chord are 0.1 and 9.36×10^5, respectively. P_{ref} is the reference pressure, and the static pressure at the outlet, $P = 0.99962P_{\mathrm{ref}}$ while the total pressure at the inlet, P_t is $1.007P_{\mathrm{ref}}$.

Figure 8.11 shows the wall skin friction coefficient, C_{f} along the hump wall when compared with the experimental data [266]. Before the flow separation point, the values of C_{f} of the new one-equation turbulence model [54] along the hump wall agree well with that of the experimental results. The new one-equation turbulence model also provides better prediction of C_{f} than the one-equation WA turbulence model [101] in the flow separation region. Compared with the experimental data, the new one-equation turbulence model has a closer prediction of the reattachment point and the wall skin friction coefficient than that of other turbulence models after the reattachment point. The new one-equation turbulence model provides better prediction of the wall skin friction coefficient recovery after the reattachment point as shown in previous test case in Section 8.4.3. Figure 8.12 shows the pressure coefficient, C_{p} along the hump wall. In most regions, the new one-equation turbulence model predicts the pressure coefficients along the hump wall better than the WA turbulence model [101] when compared with the experimental data [266], and also predicts better in the recovery of C_{p} after the flow reattachment.

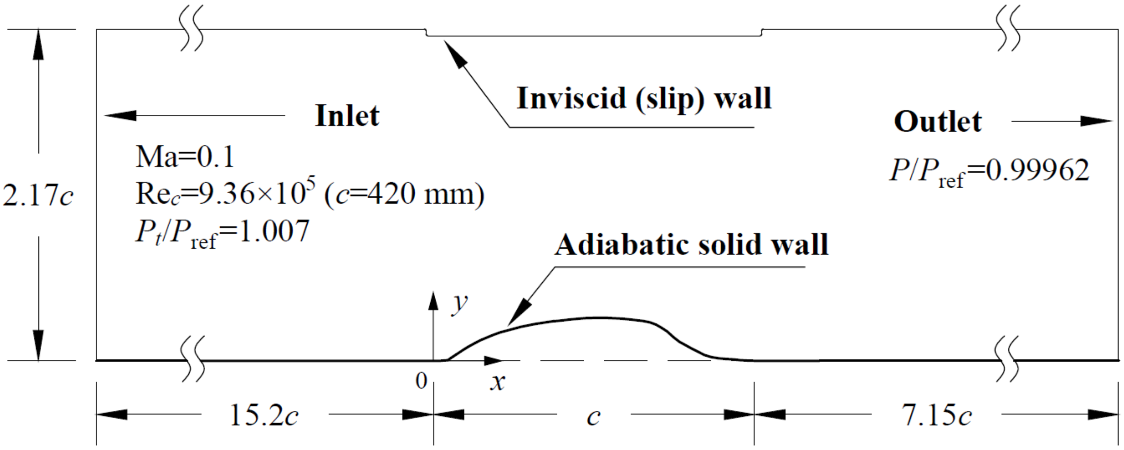

Figure 8.10 NASA wall-mounted hump separated flow configuration.

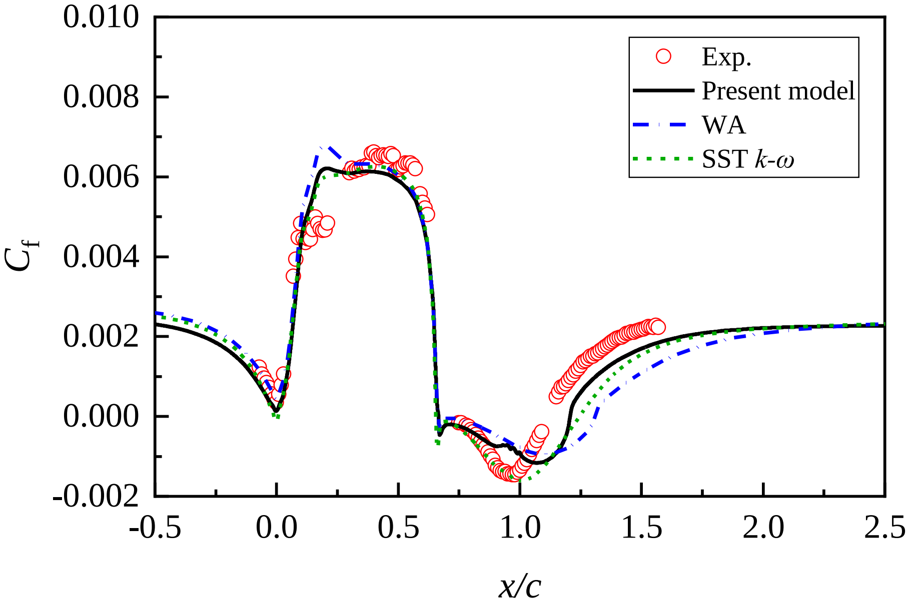

Figure 8.11 Wall skin friction coefficient along the hump wall [54].

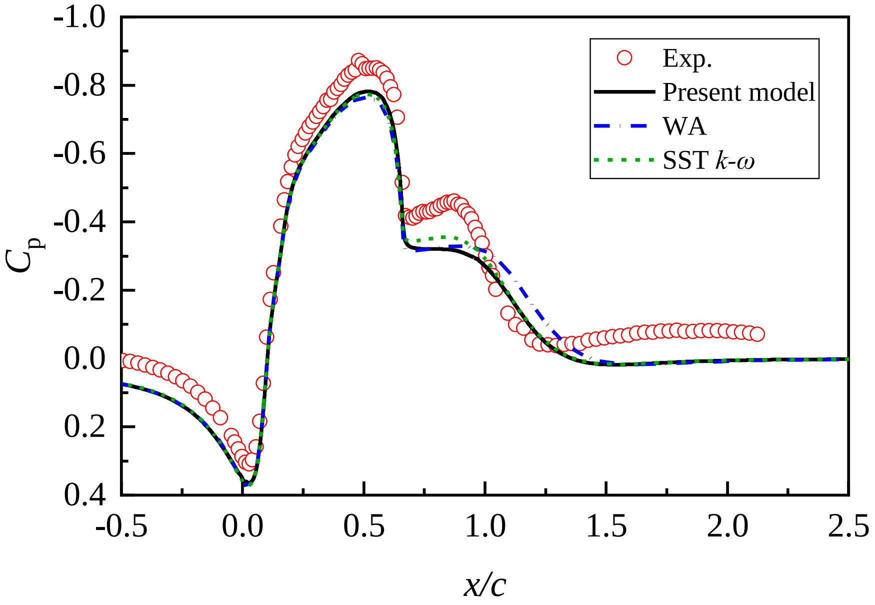

Figure 8.12 Pressure coefficient along the hump wall [54].

8.4.5 Channel flow

Another widely used benchmark for validating turbulence models is the fully developed turbulent channel flow. Figure 8.13 presents corresponding configuration with initial boundary conditions [269]. The axial length of the channel is $L_x = 8\pi\delta$, where δ is channel half-width.

The bulk and friction Reynolds numbers of this channel flow are 1.25×10^5 and 5.186×10^3, respectively.

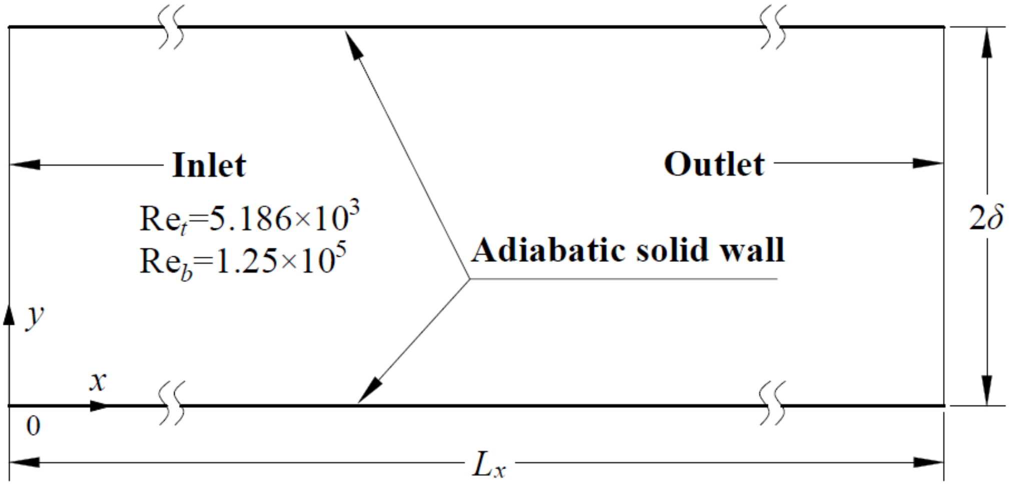

Figure 8.13 Channel flow configuration.

Velocity profiles of this fully developed turbulent channel flow obtained from the new one-equation turbulence model [54] and WA turbulence model [101] as depicted in Figure 8.14 agree excellently with the DNS results [269] when compared with the two equation SST k-ω turbulence model [261].

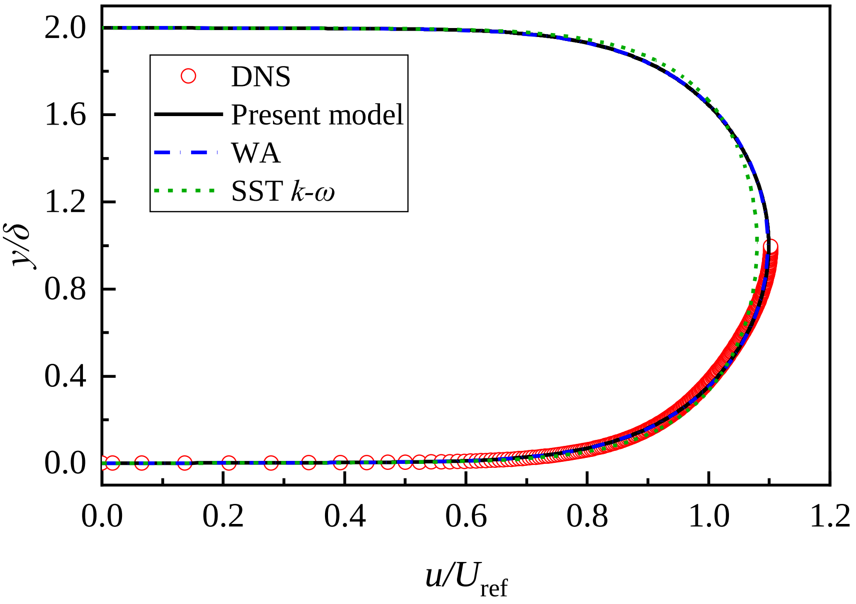

Figure 8.14 Velocity profiles of the channel flow.

8.5 Summary

A new one-equation turbulence model based on the two-equation standard *k*-*ε* and Wilcox's *k*-*ω* turbulence models is proposed and developed for validating the benchmark flow configurations including the flow over a flat plate at zero pressure gradient bump-in-channel flow, backward facing step flow, NASA wall-mounted hump separated flow and channel flow. The numerical results of the wall skin friction and pressure coefficients of the new one-equation turbulence model are fully validated and compared with the results of the experimental dataset, the one- and two-equation turbulence models and the high-accuracy NASA codes (i.e., CFL3D and FUN3D) as well as the direct numerical simulation (DNS). The new one-equation turbulence model makes better prediction on the turbulent flow over a flat plate than one-equation Wray-Agarwal (WA) and two-equation shear stress transport (SST) *k*-*ω* turbulence models. In addition, the new one-equation turbulence model almost always outperforms than the two-equation SST *k*-*ω* turbulence model for all benchmark test cases. It has also a better performance in simulating bump-in-channel flow and NASA wall-mounted hump separated flow than the one-equation WA turbulence model. The main feature of the new one-equation turbulence model has the improvement capacity in the prediction of the recovery of pressure and wall skin friction coefficients after reattachment point without affecting on the boundary-layer velocity profiles. It demonstrates that the present new one-equation turbulence model has a great potential to predict turbulent flow separation and reattachment.

Chapter 9 Numerical Investigation on Soot Particle Size Distribution in Turbulent Combustion Flows

9.1 Introduction

The objectives of this chapter are: (a) to develop a newly numerical framework coupling a finite-rate chemistry model with a soot sectional method based on detailed chemistry and differential diffusion; (b) to validate the feasibility and accuracy of the new numerical framework in real-time solving chemical species as well as soot in turbulent non-premixed flames; and (c) to obtain further insights into soot formation and evolution via the soot PSD. Specifically, a soot sectional method is firstly extended to solve soot aggregate and primary particle number densities for turbulent flows and is then fully coupled with a finite-rate chemistry model based on detailed chemistry, which are implemented into the modified OpenFOAM solver [53]. As a result, chemical species and soot can be solved simultaneously and accurately with considering differential diffusion as well as mass exchange between soot and chemical species. It should be noted that the newly developed CFD framework is not limited to the specific Partially Stirred Reactor (PaSR) combustion model, and coupling the soot sectional method with other finite-rate chemistry models [270,271] is also achievable. Considering the prohibitive computational cost of directly solving chemistry [88,272-274], a dynamic load balancing approach together with a reference mapping model [88] is incorporated into the numerical framework to deal with the load imbalance in parallel simulations based on high-performing computers. The numerical framework is validated by a well-characterized turbulent non-sooting bluff body flame for accurate estimation of gas-phase flow field and then adopted for simulating soot aerosol dynamics of turbulent sooting bluff body flames. The resulting flow, flame and soot characteristics are in comparison with available experimental dataset. The simulated soot PSDs at different locations are analyzed and the underlying competing mechanism of different dynamic processes is fully explored. It should be noted that turbulent bluff body flames involving jet and recirculating flows are commonly observed in different practical combustion systems since the generated recirculating flows close to the bluff body surface facilitate the effective fuel-oxidizer mixing, flame stabilization and ignition processes.

9.2 Mathematical Models

A numerical framework is newly developed in OpenFOAM for modelling soot aerosol dynamics in turbulent combustion. Specifically, governing equations in terms of turbulent chemically reacting flows could be solved by the equation of state and Reynolds-averaged Naver-Stokes method, in which a soot sectional model is formulated and coupled with the Partially Stirred Reactor (PaSR) combustion model [275] for simulating soot formation and evolution based on detailed chemistry. The optically thin radiation model and molecular diffusion of species and soot are also taken into consideration in the computational fluid dynamics (CFD) framework, in which a dynamic load balancing approach and a reference mapping model are utilized to accelerate the parallel CFD simulations of reacting flows.

9.2.1 Gas phase model

Turbulent chemically reacting flows for the gas phase are solved [115,276-279] with viscous heating in the enthalpy governing equation neglected for low-speed flows [106,280], which are implemented into OpenFOAM based on the *standardReactingFoam* solver developed by Wang et al. [53].

$$\frac{\partial \bar{\rho}}{\partial t}+\frac{\partial}{\partial x_i}(\bar{\rho}\tilde{u}_i)=0 \tag{9-1}$$

$$\frac{\partial(\bar{\rho}\tilde{u}_i)}{\partial t}+\frac{\partial}{\partial x_i}(\bar{\rho}\tilde{u}_i\tilde{u}_j)+\frac{\partial \bar{p}}{\partial x_j}=\frac{\partial}{\partial x_i}\left(\bar{\tau}_{ij}-\bar{\rho}\widetilde{u_i''u_j''}\right) \tag{9-2}$$

$$\frac{\partial(\bar{\rho}\tilde{Y}_k)}{\partial t}+\frac{\partial}{\partial x_i}(\bar{\rho}\tilde{u}_i\tilde{Y}_k)=\frac{\partial}{\partial x_i}\left[\left(\bar{\rho}D_{m,k}+\frac{\mu_t}{\mathrm{Sc}_t}\right)\frac{\partial \tilde{Y}_k}{\partial x_i}\right]+\bar{\omega}_k \tag{9-3}$$

$$\begin{aligned}\frac{\partial(\bar{\rho}\tilde{h}_s)}{\partial t}+\frac{\partial}{\partial x_i}(\bar{\rho}\tilde{u}_i\tilde{h}_s)-\overline{\frac{Dp}{Dt}}&\\ =\bar{\omega}_T+\frac{\partial}{\partial x_i}\left(\frac{\lambda}{C_p}+\frac{\mu_t}{\mathrm{Pr}_t}\right)\frac{\partial \tilde{h}_s}{\partial x_i}&\\ +\frac{\partial}{\partial x_i}\left[\frac{\lambda}{C_p}\sum_{k=1}^{N}\left(\frac{\rho C_p D_{m,k}}{\lambda}-1\right)\bar{h}_{s,k}\frac{\partial \tilde{Y}_k}{\partial x_i}\right]+Q_r&\end{aligned} \tag{9-4}$$

where t, ρ and p represent time, density and pressure; x_i and u_i are coordinate and velocity in i direction, respectively; $D_{m,k}$ represents the mixture-averaged molecular diffusion coefficient of kth species in the mixture [223] which takes differential diffusion into account; Y_k is kth species mass fraction; λ and C_p are the thermal conductivity and specific heat capacity at constant pressure, which are calculated via the standard gas kinetic theory as implemented by Wang et al. [53]; Q_r represents radiative heat loss from CH_4, H_2O, CO and CO_2 and as well as soot based on optically-thin approximation [231]; h_s is the sensible enthalpy and ω_T is the heat generation rate because of gas-phase species combustion and interaction with soot. The turbulence Prandtl (Pr_t) and Schmidt (Sc_t) numbers used are 0.7 [115]. The viscous tensor is given by the Newton law as [276]:

$$\bar{\tau}_{ij} = \mu\left(\frac{\partial \tilde{u}_i}{\partial x_j} + \frac{\partial \tilde{u}_j}{\partial x_i}\right) - \frac{2}{3}\mu\delta_{ij}\frac{\partial \tilde{u}_k}{\partial x_k} \tag{9-5}$$

whereδ_{ij} and μ represent Kronecker symbol and molecular viscosity. Reynolds stress tensor could be modeled based on the Boussinesq hypothesis as [115]:

$$\bar{\rho}\widetilde{u_i''u_j''} = -\mu_t\left(\frac{\partial \tilde{u}_i}{\partial x_j} + \frac{\partial \tilde{u}_j}{\partial x_i} - \frac{2}{3}\delta_{ij}\frac{\partial \tilde{u}_k}{\partial x_k}\right) + \frac{2}{3}\bar{\rho}k\delta_{ij} \tag{9-6}$$

By using turbulence dissipation rate (ε) and turbulence kinetic energy (k), the turbulence viscosity, μ_t is given as [279]:

$$\mu_t = \bar{\rho}C_\mu\frac{k^2}{\varepsilon} \tag{9-7}$$

The k-ε turbulence model used for turbulence closure is formulated as [279]:

$$\frac{\partial}{\partial t}(\bar{\rho}k) + \frac{\partial}{\partial x_i}(\bar{\rho}\tilde{u}_i k) = \frac{\partial}{\partial x_i}\left[\left(\mu + \frac{\mu_t}{\sigma_k}\right)\frac{\partial k}{\partial x_i}\right] + G - \bar{\rho}\varepsilon \tag{9-8}$$

$$\frac{\partial}{\partial t}(\bar{\rho}\varepsilon) + \frac{\partial}{\partial x_i}(\bar{\rho}\tilde{u}_i\varepsilon) = \frac{\partial}{\partial x_i}\left[\left(\mu + \frac{\mu_t}{\sigma_\varepsilon}\right)\frac{\partial \varepsilon}{\partial x_i}\right] + C_1\frac{\varepsilon}{k}G - C_2\bar{\rho}\frac{\varepsilon^2}{k} \tag{9-9}$$

where G is the production rate of k, which is defined as [115]:

$$G = -\bar{\rho}\widetilde{u_i''u_j''}\frac{\partial \tilde{u}_i}{\partial x_j} \tag{9-10}$$

where $C_\mu = 0.09$, $C_1 = 1.6$, $C_2 = 1.92$, $\sigma_k = 1.0$, $\sigma_\varepsilon = 1.3$. Dissipation coefficient (C_1) should be modified from 1.44 to 1.6 [281], because it is reported that the spreading and decaying rates for a round jet flow would be overpredicted in the standard k-ε turbulence model [282]. In Equation (9-3), ω_k is kth species source term because of gas-phase reaction as well as interaction with soot. Successful prediction of gas-phase species concentrations of a turbulent flow requires taking turbulence-chemistry interaction into consideration. The turbulence-chemistry interaction could be described by the PaSR combustion model [275], in which each computational cell would be split into non-reacting and reacting zones. The Perfectly Stirred Reactor is used to model the homogeneous reacting zone [275]. Mean reaction rate $\bar{\omega}_k$ of kth species could be calculated as:

$$\bar{\omega}_k = \kappa \omega_k^* \tag{9-11}$$

where ω_k^* represents kth species formation rate on the basis of mean species concentration in the cell based on kinetic mechanism, and κ is the reactive volume fraction which is calculated as [278]:

$$\kappa = \frac{\tau_c}{\tau_c + \tau_{\text{mix}}} \tag{9-12}$$

where τ_c is chemical time scale; τ_{mix} is the mixing time scale which is expressed as [280,283]:

$$\tau_{\text{mix}} = C_{\text{mix}} \sqrt{\frac{\mu_{\text{eff}}}{\bar{\rho}\varepsilon}} \tag{9-13}$$

where μ_{eff} is the effective dynamic viscosity based on turbulent and molecular viscosities, and the mixing constant C_{mix} used is 0.3.

9.2.2 Soot model

The soot sectional method is described via fixed pivot approach [284], in which soot aggregate mass range would be logarithmically discretized to several sections. Every section has a prescribed and fixed representative mass, and every soot aggregate according to its mass would be assigned to the corresponding section. It is assumed that soot aggregates within the same section are identical and every soot aggregate has the same sized spherical primary particles. Taking thermophoresis and diffusion effects of soot into account, transport equations of soot aggregate and (i.e., agg) primary particle (i.e., pri) number densities ($\widetilde{N}_{\text{agg},i}$ and $\widetilde{N}_{\text{pri},i}$) in section i are formulated and extended for turbulence flows. The introduced turbulent scalar fluxes are closed by the classical gradient transport assumptions generally used in turbulence models [277], in which the turbulence Schmidt number is used to estimate the turbulent diffusivity [283].

$$\frac{\partial}{\partial t}\left(\bar{\rho}\tilde{N}_{\mathrm{pri},i}\right)+\frac{\partial}{\partial x_i}\left(\bar{\rho}\tilde{u}_i\tilde{N}_{\mathrm{pri},i}\right)+\frac{\partial}{\partial x_i}\left(\bar{\rho}\tilde{V}_{T,i}\tilde{N}_{\mathrm{pri},i}\right) =\frac{\partial}{\partial x_i}\left[\left(\bar{\rho}D_i+\frac{\mu_t}{\mathrm{Sc}_t}\right)\frac{\partial\tilde{N}_{\mathrm{pri},i}}{\partial x_i}\right]+\bar{\rho}\bar{S}_{\mathrm{pri},i} \tag{9-14}$$

$$\frac{\partial}{\partial t}\left(\bar{\rho}\tilde{N}_{\mathrm{agg},i}\right)+\frac{\partial}{\partial x_i}\left(\bar{\rho}\tilde{u}_i\tilde{N}_{\mathrm{agg},i}\right)+\frac{\partial}{\partial x_i}\left(\bar{\rho}\tilde{V}_{T,i}\tilde{N}_{\mathrm{agg},i}\right) =\frac{\partial}{\partial x_i}\left[\left(\bar{\rho}D_i+\frac{\mu_t}{\mathrm{Sc}_t}\right)\frac{\partial\tilde{N}_{\mathrm{agg},i}}{\partial x_i}\right]+\bar{\rho}\bar{S}_{\mathrm{agg},i} \tag{9-15}$$

where $\bar{S}_{\mathrm{pri},i}$ and $\bar{S}_{\mathrm{agg},i}$ are the sum combining inception, coagulation, polycyclic aromatic hydrocarbon (PAH) condensation, H-abstraction-C_2H_2-addition (HACA) surface growth, O_2 and OH oxidation. Thermophoretic velocity, $\tilde{V}_{T,i}$ associated with temperature, T is defined as [92]:

$$\tilde{V}_{T,i}=-\frac{3}{4\left(1+\frac{\pi}{8}\right)}\frac{\mu}{\bar{\rho}\tilde{T}}\frac{\partial\tilde{T}}{\partial x_i} \tag{9-16}$$

The diffusion coefficient of soot, D_i is expressed as [202]:

$$D_i=\frac{k_B\tilde{T}}{3\pi\mu d_{\mathrm{m},i}}C_{s,i} \tag{9-17}$$

where k_B represents Boltzmann constant; Cunningham slip correction factor of soot, $C_{s,i}$ is expressed as [240]:

$$C_{s,i}=1+K_{n,i}\left[1.257+0.4\exp\left(-\frac{1.1}{K_{n,i}}\right)\right] \tag{9-18}$$

where the Knudsen number, K_n is calculated as [202]:

$$K_{n,i}=\frac{2\lambda_l}{d_{\mathrm{m},i}} \tag{9-19}$$

where $d_{\mathrm{m},i}$ is the mobility diameter of soot, and λ_l represents gas mean free path defined as mean air free path, which is calculated as [241]:

$$\lambda_l=\frac{\mu}{\bar{p}}\sqrt{\frac{\pi R_u\tilde{T}}{2W}}=\frac{\mu}{\rho}\sqrt{\frac{\pi W}{2k_BN_A\tilde{T}}} \tag{9-20}$$

where W represents mixture molecular weight; N_A and R_u are Avogadro number and the universal gas constant, respectively.

The mobility diameter $d_{\mathrm{m},i}$ and gyration diameter $d_{g,i}$ are expressed as [39,285]:

$$d_{\mathrm{m},i} = d_{\mathrm{p},i} n_{\mathrm{p},i}^{0.45} \tag{9-21}$$

$$d_{\mathrm{g},i} = \begin{cases} d_{\mathrm{m},i}\left(n_{\mathrm{p},i}^{-0.2} + 0.4\right)^{-1}, n_{\mathrm{p},i} > 1.8 \\ d_{\mathrm{m},i}\sqrt{3/5}, n_{\mathrm{p},i} \leq 1.8 \end{cases} \tag{9-22}$$

where $d_{\mathrm{p},i}$ and $n_{\mathrm{p},i}$ represent average diameter and primary particle number of a soot aggregate in ith section, respectively. The collision diameter of a soot aggregate is chosen as the large one between the mobility diameter and gyration diameter [39,235].

The source terms of soot transport equations of each section highly rely on the gas phase and soot characteristics [55]. It is reported that the impact of soot-turbulence interactions on soot prediction is less significant than the model parameters of aerosol dynamic processes [10,106], so interactions between turbulent and soot are neglected in many research studies [102,106,198]. The source terms of soot transport equations of each section could be calculated during run-time by using the local concentrations of related gas-phase species as well as thermochemical parameters in the present study. Inception or nucleation is modelled by the dimerization of PAH molecules, which links gas-phase species with incipient soot of the first section. Generally speaking, soot in a lower section moves to a higher section when coagulation, PAH condensation or HACA surface growth occurs, while soot in a higher section moves to a lower section by O_2 oxidation or OH oxidation. In the present study, an incipient soot could be formed by the dimerization of pyrene (A4) molecules and only contributes to the first soot section. Since all mass exchanges between soot and gas-phase species are given from exchanged number of carbon atoms, hydrogen atoms in gas-phase species are assigned to form H_2 to close the hydrogen balance [102], therefore achieving a complete gas-solid coupling. The nucleation or inception (i.e., inc) source terms (i.e., $S_{\mathrm{agg},1}^{\mathrm{inc}}$ and $S_{\mathrm{pri},1}^{\mathrm{inc}}$) are evaluated based on the gas kinetic theory as [147,148,246,286,287]:

$$S_{\mathrm{agg},1}^{\mathrm{inc}} = S_{\mathrm{pri},1}^{\mathrm{inc}} = \gamma E_F \left(\frac{4\pi k_B T}{m_{\mathrm{A4}}}\right)^{1/2} \left(\frac{6 m_{\mathrm{A4}}}{\pi \rho_{\mathrm{soot}}}\right)^{2/3} [\mathrm{A4}]^2 N_A^2 \tag{9-23}$$

where ρ_{soot}=1800kg/m^3 represents soot density [286,288]; [A4] and m_{A4} are the concentration and mass of A4, respectively; the parameter γ is 0.002 [287] and van der Waals enhancement factor E_F=2.2 [246,286]. Coagulation (i.e., coag) source terms (i.e., $S_{\mathrm{agg},i}^{\mathrm{coag}}$ and $S_{\mathrm{pri},i}^{\mathrm{coag}}$) are evaluated according to the Knudsen number of the collision soot aggregates as [203]:

$$S_{\mathrm{agg},i}^{\mathrm{coag}} = \sum_{m_{i-1} \le m_j + m_k \le m_{i+1}}^{k \le j \le i} \left(1 - \frac{\delta_{jk}}{2}\right) \eta_{ijk} \beta_{jk} N_{\mathrm{agg},j} N_{\mathrm{agg},k} - N_{\mathrm{agg},i} \sum_{m=1}^{N} \beta_{im} N_{\mathrm{agg},m} \tag{9-24}$$

$$S_{\mathrm{pri},i}^{\mathrm{coag}} = \sum_{m_{i-1} \le m_j + m_k \le m_{i+1}}^{k \le j \le i} \left(1 - \frac{\delta_{jk}}{2}\right) \eta_{\mathrm{p},ijk} \eta_{ijk} \beta_{jk} N_{\mathrm{agg},j} N_{\mathrm{agg},k} - N_{\mathrm{pri},i} \sum_{m=1}^{N} \beta_{im} N_{\mathrm{agg},m} \tag{9-25}$$

where N and m_i represent section number and soot aggregate mass in ith section, and δ_{jk} is delta function. In the present study, soot is represented by thirty-five sections [202-207] and a section spacing factor of two [204]. Parameter η_{ijk} could be evaluated by [203]:

$$\eta_{ijk} = \begin{cases} \dfrac{m_{i+1} - (m_j + m_k)}{m_{i+1} - m_i}, m_i \le m_j + m_k \le m_{i+1} \\ \dfrac{m_{i-1} - (m_j + m_k)}{m_{i-1} - m_i}, m_{i-1} \le m_j + m_k \le m_i \end{cases} \tag{9-26}$$

Parameter $\eta_{\mathrm{p},ijk}$ could be evaluated by [203]:

$$\eta_{\mathrm{p},ijk} = \frac{m_i}{m_j + m_k} \left(n_{\mathrm{p},j} + n_{\mathrm{p},k}\right) \tag{9-27}$$

The collision kernels of the free molecular, β_{ij}^{fm} (i.e., fm, $K_{n,i} > 10$) and continuum, $\beta_{ij}^{\mathrm{cont}}$ (i.e., cont, $K_{n,i} < 0.1$) regimes are calculated as [49,147,148]:

$$\beta_{ij}^{\mathrm{fm}} = E_F \sqrt{\frac{\pi k_B T}{2} \left(\frac{1}{m_i} + \frac{1}{m_j}\right)} \left(d_{c,i} + d_{c,j}\right)^2 \tag{9-28}$$

$$\beta_{ij}^{\mathrm{cont}} = \frac{2 k_B T}{3\mu} \left(\frac{C_{s,i}}{d_{c,i}} + \frac{C_{s,j}}{d_{c,i}}\right) \left(d_{c,i} + d_{c,j}\right) \tag{9-29}$$

where $d_{c,i}$ represents collision diameter of soot aggregates in ith section. Collision kernel in transition, $\beta_{ij}^{\mathrm{tran}}$ (i.e., tran, $0.1 \le K_{n,i} \le 10$) regime is calculated based on the harmonic mean technique as [147,148]:

$$\beta_{ij}^{\mathrm{tran}} = \frac{\beta_{ij}^{\mathrm{fm}}\beta_{ij}^{\mathrm{cont}}}{\beta_{ij}^{\mathrm{fm}} + \beta_{ij}^{\mathrm{cont}}} \tag{9-30}$$

PAH condensation consumes A4 and results in the mass growth of soot aggregates, which could be modelled as the collision of A4 molecules on soot aggregate surfaces based on the gas kinetic collision frequency with a collision efficiency of 0.5 [289-292]. The PAH condensation rate in section i, $I_{\mathrm{cond},i}$ is then calculated as [246]:

$$I_{\mathrm{cond},i} = 16W_C\beta_{\mathrm{A4},i}[\mathrm{A4}]N_{\mathrm{agg},i} \tag{9-31}$$

The soot aggregate mass also increases or decreases by the surface growth or oxidation, which can be modelled by the famous HACA mechanism [59]. Six reactions including two reversible reactions are listed in Table 9.1 with their individual reaction rate constants (i.e., k). OH oxidation (i.e., S6) is modelled via collision theory of free molecular regime, in which collision efficiency γ_{OH} is 0.13. Other surface reactions (i.e., S1-S5) are regarded to take place on the soot surface activated sites, which is dehydrogenated ($\mathrm{C_{soot}}\cdot$) or saturated ($\mathrm{C_{soot}}$–H). In each section, the molar concentration of dehydrogenated sites [$\mathrm{C_{soot}}\cdot$] on a soot aggregate surface can be calculated by [202]:

$$[\mathrm{C_{soot}}\cdot] = \frac{A_s}{N_A}\chi_{\mathrm{C_{soot}}\cdot} \tag{9-32}$$

where A_s represents primary particle surface area; $\chi_{\mathrm{Csoot}\cdot}$ represents dehydrogenated site number of unit surface area, which could be calculated by [246]:

$$\chi_{\mathrm{C_{soot}}\cdot} = \frac{k_1[\mathrm{H}] + k_2[\mathrm{OH}]}{k_{-1}[\mathrm{H_2}] + k_{-2}[\mathrm{H_2O}] + k_3[\mathrm{H}] + k_4[\mathrm{C_2H_2}] + k_5[\mathrm{O_2}]}\chi_{\mathrm{C_{soot}-H}} \tag{9-33}$$

where saturated site number of unit soot surface area, $\chi_{\mathrm{Csoot-H}}$ is 2.3×10^{19} m^{-2}; [H_2], [H_2O], [H], [C_2H_2], [O_2] and [OH] are molar concentrations of corresponding species. Surface activated site fraction for chemical reactions, α is defined by [59]:

$$\alpha = \tanh\left(\frac{a}{\log \mu_1} + b\right) \tag{9-34}$$

where a and b are parameters associated with temperature T, which is given as [59]:

$$a = 12.65 - 0.00563T \tag{9-35}$$

$$b = -1.38 + 0.00068T \tag{9-36}$$

μ_1 is calculated as [59]:

$$\mu_1 = \frac{\rho_{\text{soot}} \pi d_{\text{p}}^3}{6W_C} N_A \tag{9-37}$$

where W_C is carbon atom molecular weight. The surface growth and O_2 oxidation reaction rates (i.e., I_{HACA} and I_{O_2}) are then evaluated as [246]:

$$I_{\text{HACA}} = 2W_C \alpha k_4 [\text{C}_2\text{H}_2][\text{C}_{\text{soot}} \cdot] \tag{9-38}$$

$$I_{\text{O}_2} = -W_C \alpha k_5 [\text{O}_2][\text{C}_{\text{soot}} \cdot] \tag{9-39}$$

The surface oxidation reaction rate of the soot aggregate in the *i*th section originating from OH (i.e., $I_{\text{OH},i}$) is calculated based on the collision theory, which is evaluated as [202]:

$$I_{\text{OH},i} = -W_C k_6 [\text{OH}] \frac{N_{\text{agg},i}}{N_A} \tag{9-40}$$

Thus, the soot growth (i.e., sg) source terms (i.e., $S_{\text{agg},i}^{\text{sg}}$ and $S_{\text{pri},i}^{\text{sg}}$) of HACA surface growth and PAH condensation can be expressed as [202]:

$$S_{\text{agg},i}^{\text{sg}} = \begin{cases} -\dfrac{I_{\text{sg},1}}{m_2 - m_1}, i = 1 \\ \dfrac{I_{\text{sg},i-1}}{m_i - m_{i-1}} - \dfrac{I_{\text{sg},i}}{m_{i+1} - m_i}, i = 2, \dots, N-1 \\ \dfrac{I_{\text{sg},N-1}}{m_N - m_{N-1}}, i = N \end{cases} \tag{9-41}$$

$$S_{\text{pri},i}^{\text{sg}} = \begin{cases} -\dfrac{I_{\text{sg},1}}{m_2 - m_1}, i = 1 \\ \dfrac{I_{\text{sg},i-1} n_{\text{p},i-1}}{m_i - m_{i-1}} - \dfrac{I_{\text{sg},i} n_{\text{p},i}}{m_{i+1} - m_i}, i = 2, \dots, N-1 \\ \dfrac{I_{\text{sg},N-1} n_{\text{p},N-1}}{m_N - m_{N-1}}, i = N \end{cases} \tag{9-42}$$

The soot oxidation (i.e., ox) source terms (i.e., $S_{\text{agg},i}^{\text{ox}}$ and $S_{\text{pri},i}^{\text{ox}}$) of O_2 and OH can be calculated as [202]:

$$S_{\mathrm{agg},i}^{\mathrm{ox}} = \begin{cases} -\dfrac{I_{\mathrm{ox},2}}{m_2 - m_1} + \dfrac{I_{\mathrm{ox},1}}{m_1}, i = 1 \\ -\dfrac{I_{\mathrm{ox},i+1}}{m_{i+1} - m_i} + \dfrac{I_{\mathrm{ox},i}}{m_i - m_{i-1}}, i = 2, \dots, N-1 \\ \dfrac{I_{\mathrm{ox},N}}{m_N - m_{N-1}}, i = N \end{cases} \tag{9-43}$$

$$S_{\mathrm{pri},i}^{\mathrm{ox}} = \begin{cases} -\dfrac{I_{\mathrm{ox},2} n_{\mathrm{p},2}}{m_2 - m_1} + \dfrac{I_{\mathrm{ox},1}}{m_1}, i = 1 \\ -\dfrac{I_{\mathrm{ox},i+1} n_{\mathrm{p},i+1}}{m_{i+1} - m_i} + \dfrac{I_{\mathrm{ox},i} n_{\mathrm{p},i}}{m_i - m_{i-1}}, i = 2, \dots, N-1 \\ \dfrac{I_{\mathrm{ox},N} n_{\mathrm{p},N}}{m_N - m_{N-1}}, i = N \end{cases} \tag{9-44}$$

Table 9.1 Soot surface growth and oxidation reactions [59,201], $k = AT^n \exp(-E/R_uT)$.

No.	Reaction	A (cm^{3}mol^{-1}s^{-1})	n	E (kcal/mol)
S1	$\mathrm{C_{soot}-H + H \leftrightarrow C_{soot}\cdot + H_2}$	4.2×10^{13}	0.0	13.0
		3.9×10^{12}	0.0	11.0
S2	$\mathrm{C_{soot}-H + OH \leftrightarrow C_{soot}\cdot + H_2O}$	1.0×10^{10}	0.734	1.43
		3.68×10^{8}	1.139	17.1
S3	$\mathrm{C_{soot}\cdot + H \rightarrow C_{soot}-H}$	2.0×10^{13}	0.0	0.0
S4	$\mathrm{C_{soot}\cdot + C_2H_2 \rightarrow C_{soot}-H + H}$	8.0×10^{7}	1.56	3.8
S5	$\mathrm{C_{soot}\cdot + O_2 \rightarrow 2CO + products}$	2.2×10^{12}	0.0	7.5
S6	$\mathrm{C_{soot}-H + OH \rightarrow CO + products}$	$\gamma = 0.13$		

9.3 Results and Discussion

Governing equations including unsteady, convection, diffusion and source terms are solved by using the finite volume method in the present study. The pressure implicit with splitting of operator (PISO) algorithm [227] is used to achieve the pressure-velocity coupling. Different numerical schemes for different physically meaningful terms are readily available in OpenFOAM [54,249]. Unsteady terms are discretized by a first-order time-stepping while a second-order central differencing scheme is used to discretize the diffusion and convection terms [53]. The chemical reaction mechanism used is the famous ABF mechanism [59] involving 544 reactions and 101 species with the polycyclic aromatic hydrocarbon (PAH) species up to four aromatic rings (i.e., pyrene), and an Euler implicit solver is used for chemistry. Time step could be limited with Courant-Friedrichs-Lewy number, CFL=0.8 [293]. Transport and thermodynamic parameters are calculated by using the mixture-averaged transport model based on standard gas kinetic theory as incorporated into OpenFOAM by Wang et al. [53], while a dynamic load balancing approach and a reference mapping model [88] are utilized to accelerate the parallel computational fluid dynamics (CFD) simulations of reacting flows.

Turbulent bluff body flames are commonly observed in different practical combustion systems since the generated recirculating flows close to the bluff body surface facilitate the effective fuel-oxidizer mixing, flame stabilization and ignition processes [293,294]. However, bluff body flame configurations have not received enough attention and in-depth investigation [295] in comparison with the simple jet flame configurations which do not involve more complex fluid dynamics such as recirculating flows. Most previous investigations on bluff body flame configurations have mainly focused on the experimental and numerical flow and flame characteristics in non-sooting premixed and non-premixed flame configurations [293,294,296,297]. As the fuel mixtures may be rich at some specific conditions, soot could also be produced in the recirculation zone [294,295], which is undesirable for the design of many combustion systems. Research on soot formation and evolution of the bluff body flame configuration especially in the recirculation zone was then conducted because of its relatively simple but effective emulation of the recirculation component in many industrial combustion systems [298]. Soot prediction is highly challenging because of its strong reliance on flow and flame characteristics as well as soot properties, especially for turbulent flames [55]. A laboratory-scale bluff body sooting flame configuration was numerically and experimentally investigated firstly by Mueller et al. [299], and results show that large SVFs in the recirculation zone are the results of the entrainment effect of the circulation vortex and the dominant effect of the acetylene-based surface growth on soot particles. Deng et al. [300] numerically investigated a bluff body flame configuration and found that adding hydrogen to fuel dramatically reduces the maximum SVF in the recirculation zone because of both chemical and hydrodynamic effects. But it was reported that the computational model cannot correctly capture the soot evolution due to overprediction of soot oxidation [295]. Rowhani et al. [301,302] experimentally investigated bluff body flame configurations and showed that the bluff body radius substantially affects the SVF due to the different residence times in the recirculation zone. Colmán et al. [295] numerically studied the soot evolution of the bluff body flame configurations and qualitatively compared numerical results with experimental results, but the SVFs for all bluff body flame configurations were overpredicted. Rowhani et al. [303] investigated the soot formation and evolution of a bluff body flame configuration based on pure methane flames and found that soot nucleates early in the recirculation zone. It should be noted that numerical model uncertainties may be introduced in a methane-fueled flame [299] and the poorly understood nucleation dominates the soot formation mechanism in methane flames [303], which leads to further uncertainties in soot prediction. Accurately modelling of soot evolution necessitates a detailed description of the basic physicochemical soot kinetics for bluff body flames.

Schematic structure of the bluff body flame configuration, boundary conditions and computational domain are presented as Figure 9.1(a) based on the experimental set-up [294,301,302]. A central tube with 2.3 mm radius (R_j) is placed in the bluff body center, and the central tube is 385 mm length, which is far larger than the entrance length of a fully developed turbulent round pipe [304]. Different outer radii (i.e., R = 19 mm, 25 mm and 32 mm) of the bluff body are used, which are named as ENB-1, ENB-2 and ENB-3 [294,301,302]. The mixture with 4:1 by volume of ethylene/nitrogen of atmospheric pressure and ambient temperature is injected from the central tube with a bulk jet exit Reynolds number of 15000, while air is supplied as a coflow surrounding the burner with constant 20 m/s from a contraction having a radius of 95 mm (R_c). It should be noted that the addition of nitrogen to the fuel in the experiments is to help reduce the soot concentration so that reduce the interference from soot particles on the PIV measurements. The mixture fraction (Z) [305] is employed for describing turbulent mixing between the air co-flow and fuel jet. The stoichiometric mixture fraction (Z_{st}) for these flames is 0.078.

A two-dimensional axisymmetric model for the bluff body flame configuration is adopted as shown in Figure 9.1(a) of the present study, in which computational domain begins at fuel exit and extends axially to 10R with its radius of 120 mm [295]. The velocity profile of the fuel inlet is calculated in an analytical solution form [306] by the widely used 1/7th power law [106,283,307]. The corresponding turbulent intensity is set to be 5% [308]. The coflow inlet adopts a uniform velocity profile with a turbulence intensity of 2% [293]. Zero-gradient/total-pressure is applied for outlet while walls adopt no-slip and zero-gradient boundary conditions for velocity and other scalars [309], respectively. Grid independence validation is conducted on 8250, 10800, 13650 and 16800 cells, respectively. Grids are axially and radially stretched, where the inner and outer shear layers as well as the inlet zone are refined axially and radially as presented in Figure 9.1(b). The results of grid independence validation show that the second grid is fine enough and used, which includes 120×90 axial and radial cells.

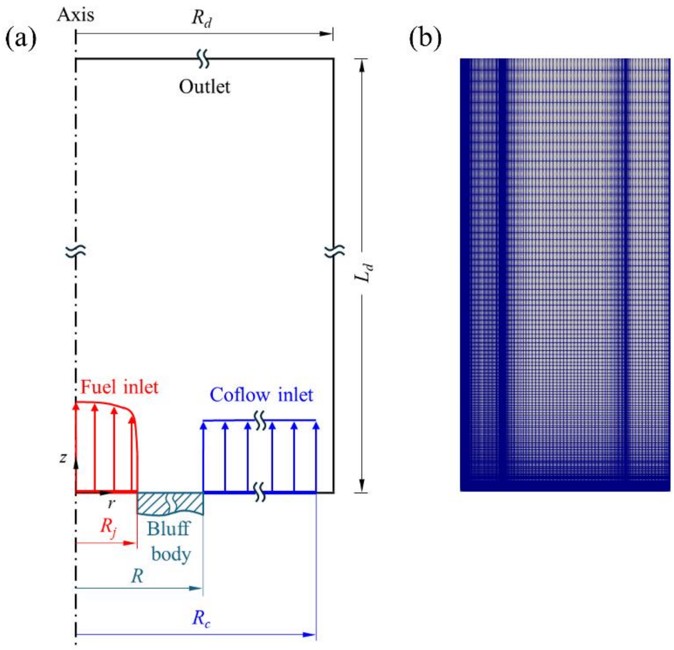

Figure 9.1 Schematic diagram of (a) bluff body flame configuration [294,301,302] and computational domain and (b) computational grid.

9.3.1 Validation of non-sooting turbulent flame

As an essential step to validate the newly developed numerical framework, simulated flame properties including axial and radial velocities, temperature, mixture fraction and species mass fractions should be validated against well-documented experimental dataset. Because of lacking corresponding experimental data of the present C_2H_4-fueled bluff body flame configurations, the experimental measurements of a similar designed burner, i.e., the famous Sydney & Sandia bluff body flame called HM1 [296,297] can serve as a comprehensive dataset for model validation purpose. Particularly, this non-sooting flame is well suited to validate species prediction of the newly developed CFD framework. The HM1 has a bluff body radius of 25 mm and is fueled by a mixture of methane/hydrogen (1:1 in volume) at 294 K, resulting in a non-sooting turbulent flame. The central tube of HM1 has a radius of 1.8 mm with bulk Reynolds number of 15800, while the mean velocity of air coflow equals 40 m/s.

Figure 9.2 presents comparison of numerical and experimental [296] results of mean axial and radial velocity radial profiles at five different axial locations (i.e., z/R = 0.52, 1.2, 1.8, 2.6 and 3.6) of HM1. The newly developed numerical framework reproduces excellently the mean axial velocity radial profiles. The first four axial locations are inside the recirculation zone (RZ) while the last location is situated at the downstream of the RZ. The mean radial velocity radial profiles at axial location near bluff body surface (i.e., z/R = 0.52) are also accurately predicted. For other axial locations, there are only slight underpredictions in the radial regions of $0.1 < r/R < 0.8$, and the reason is attributed to the high velocity gradient in the shear layers, leading to the change of the center of the RZ at any instance and an inaccuracy in the radial velocity. But the mean radial velocities of other radial regions are well predicted, which would facilitate the prediction of mixing process between the air coflow and fuel jet. Comparison of radial profiles of mean temperature between numerical and experimental results [296] is depicted as Figure 9.3. Results show that the simulated mean temperature distributions agree very well with the experimental measurements, especially within the RZ. More importantly, the spatial locations of chemical reaction zones can be well captured by the present numerical framework, as the radial regions of the largest temperature gradients for five axial locations are predicted at $0.8 < r/R < 1.0$, which are consistent with the experimental ones. The simulated mean mixture fractions at all axial locations also agree very well with the experimental counterparts [296,297] as presented in Figure 9.4. It implies that the turbulent mixing and chemical reaction processes in the flow field are successfully captured by the newly developed numerical framework, as the mixture fraction reflects the production of chemical species as well as the mixing degree and chemical reaction rate between the fuel and oxidizer. More specifically, the simulated mean mass fraction distributions of species including O_2, N_2, H_2, H_2O, CO and CO_2 at different axial locations have an overall excellent agreement with those experimental dataset [297] as presented in Figure 9.5. All these numerical results indicasste that the present new numerical framework can predict the flow and flame properties of the bluff body flame configuration, which forms a solid foundation for accurately and successful modelling soot formation and evolution as soot greatly depends on combustion flows.

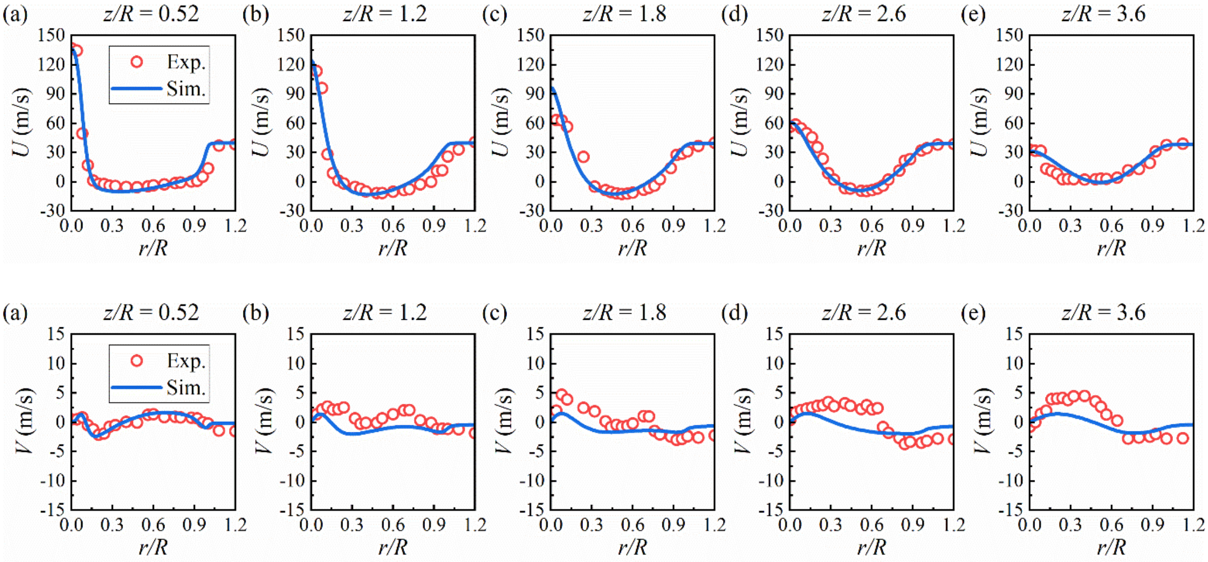

Figure 9.2 Comparison of experimental [296] and simulated radial profiles of axial velocity, U (upper row) and radial velocity, V (lower row) at different axial locations of HM1, z/R = 0.52, 1.2, 1.8, 2.6 and 3.6.

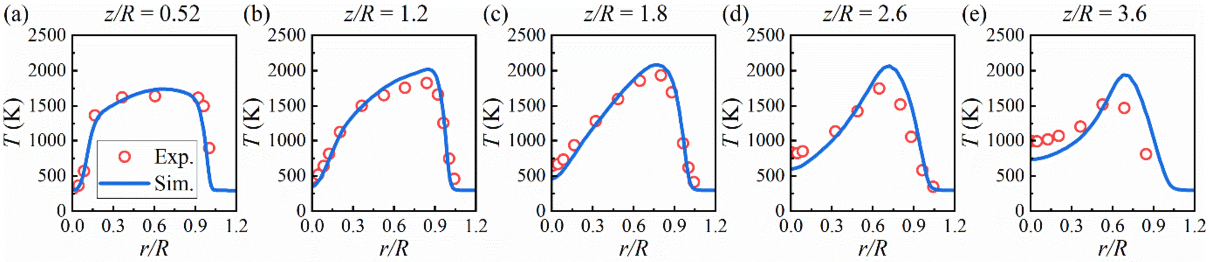

Figure 9.3 Comparison of experimental [296] and simulated radial profiles of temperature, T at different axial locations of HM1, z/R = 0.52, 1.2, 1.8, 2.6 and 3.6.

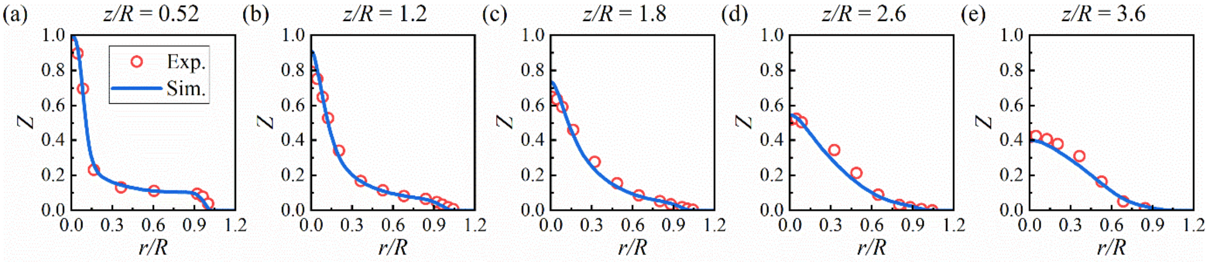

Figure 9.4 Comparison of experimental [296] and simulated radial profiles of mixture fraction, Z at different axial locations of HM1, z/R = 0.52, 1.2, 1.8, 2.6 and 3.6.

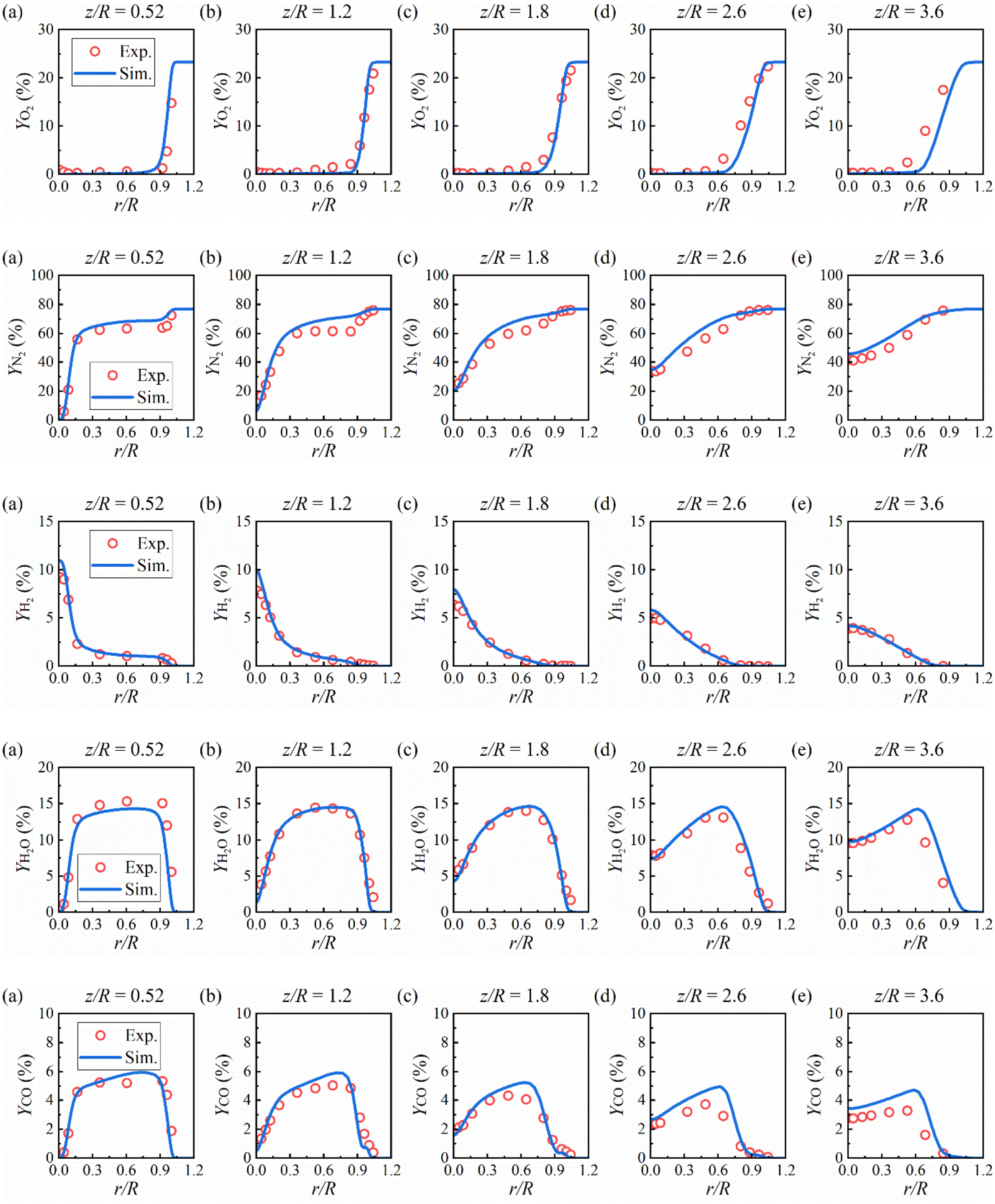
(a) z/R = 0.52
(b) z/R = 1.2
(c) z/R = 1.8
(d) z/R = 2.6
(e) z/R = 3.6
Y_{O_2} (%)
Y_{N_2} (%)
Y_{H_2} (%)
Y_{H_2O} (%)
Y_{CO} (%)
r/R
0.0 0.3 0.6 0.9 1.2
Exp.
Sim.

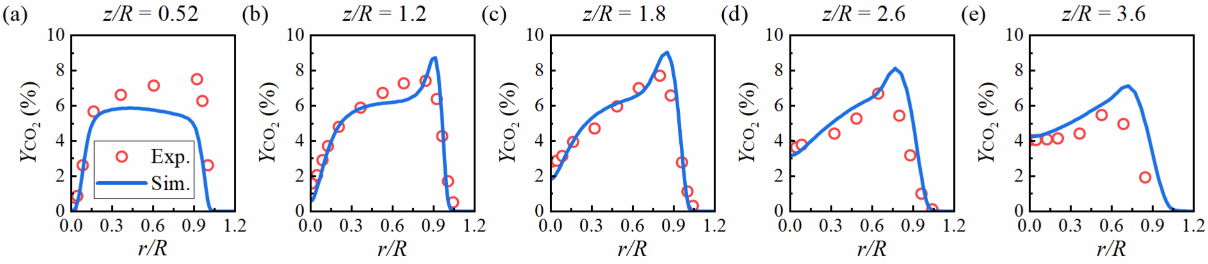

Figure 9.5 Comparison of experimental [297] and simulated radial profiles of mass fractions of O_2, N_2, H_2, H_2O, CO and CO_2 (from top row to bottom row) at different axial locations of HM1, *z/R* = 0.52, 1.2, 1.8, 2.6 and 3.6.

9.3.2 Simulation of sooting turbulent flames

Figures 9.6 to 9.8 show the numerical results of mean axial and radial velocity radial profiles in comparison to the experimental results [294] for ENB-1, ENB-2 and ENB-3 at four axial locations, where *z/R*=0.6, 1.2 and 1.8 are within the recirculation zone (RZ) and *z/R* = 4 is downstream of the RZ. Generally speaking, the overall distributions of axial and radial velocities estimated by the developed numerical framework agree very well with the experimental measurements. The minor discrepancy in the axial velocities and underprediction on the radial velocities at radial regions 0.6<*r/R*<0.9 are attributed to the high velocity gradient [294], but the numerical results for other radial regions (*r/R*<0.15 and 0.9<*r/R*<1.0) involving strong mixing process are well predicted, where an intermediate mixing layer (IML) is situated between the outer and inner shear layers (i.e., OSL and ISL) as shown in Figure 9.9. These two shear layers having high turbulent intensities are formed at both edges of the recirculation zone originating from the interactions of the air coflow and fuel jet with RZ, respectively. The simulated RZs for ENB-1, ENB-2 and ENB-3 in the flows would be also presented as Figure 9.9 by magenta dashed lines, which denote isolines of axial velocity equal to zero (i.e., *U* = 0). It should be noted that the magenta dashed lines of numerical simulations are irrespective of the black dotted lines representing ISL and OSL in the experimental results. Numerical results depict that the RZ size grows remarkably with bluff body radius increasing from 19 mm to 32 mm (i.e., ENB-1 to ENB-3). The most downstream locations of *U* = 0 measured by the experiments for three studied flames are also denoted by the horizontal magenta dashed lines, which describe the lengths of the RZ. The simulated and measured lengths of the RZ are quantitively compared in Figure 9.10, and the simulated results show consistent trends with the experimental results although there are slight underpredictions of the lengths of the RZ for these three studied flames. The larger discrepancy is observed at ENB-1, but the discrepancy gradually reduces with the bluff body radius increasing, which is also clearly reflected on the mean soot volume fraction (SVF) distributions. The simulated mean SVF distributions for three studied flames as depicted in Figure 9.9 have well agreement with experimental results, and qualitative and quantitative structure of the SVF distributions for three studied flames are well captured, where the highest SVF appears near the OSL between the RZ and the air coflow. For ENB-1, soot is incepted at the region of high mixture fraction, which is close to the ISL between the RZ and fuel jet, as well as bluff body surface. Incipient soot is transported radially towards the OSL and back towards the bluff body surface after entrained by the RZ, leading to the high SVF in the RZ. With the bluff body radius increasing from 19 mm to 32 mm (i.e., ENB-1 to ENB-3), more soot is formed near the ISL as well as near the bluff body surface. Since O_2 concentration in the air coflow would be high and OH is generated in high temperature zone near the OSL, their combined effect of rapid oxidation results in a relatively high gradient of SVF between the RZ and air coflow.

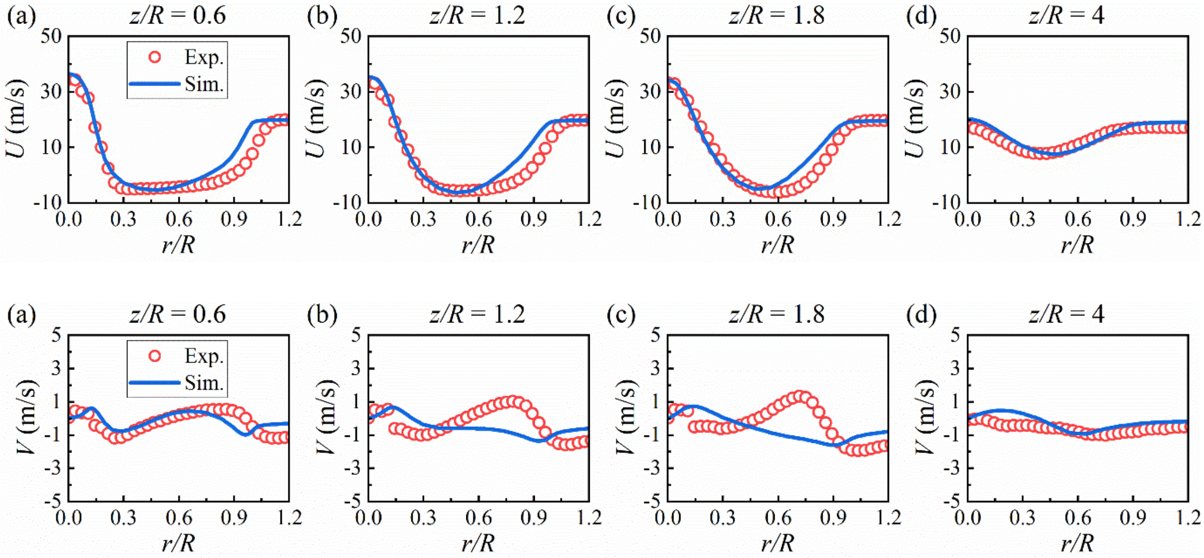

Figure 9.6 Comparison of experimental [294] and simulated radial profiles of axial velocity, U (upper row) and radial velocity, V (lower row) at different axial locations of ENB-1, z/R=0.6, 1.2, 1.8 and 4.

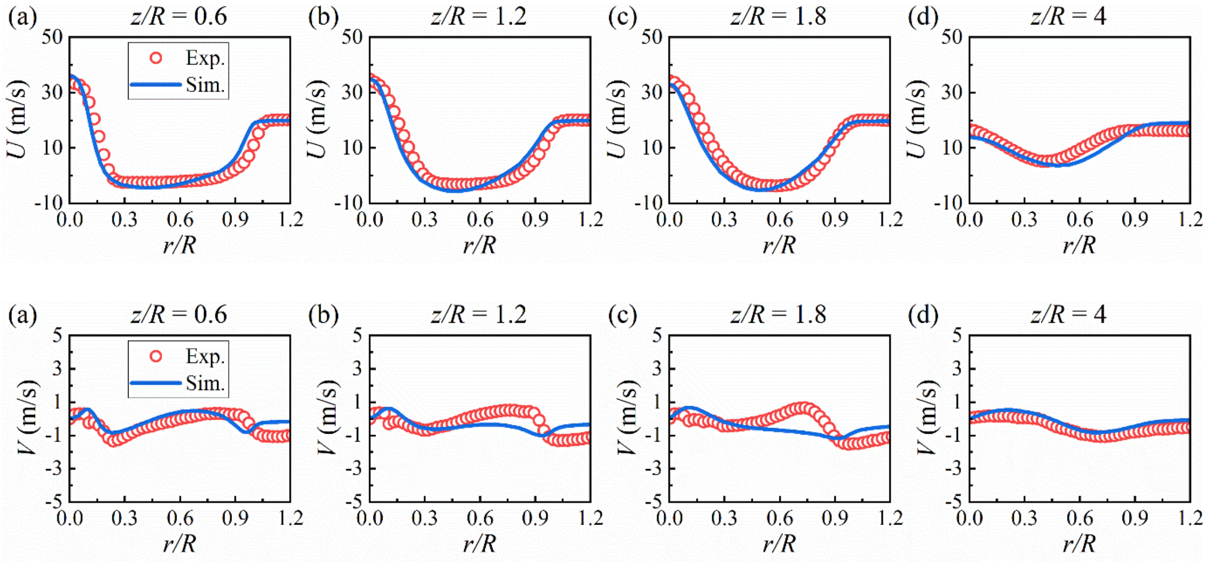

Figure 9.7 Comparison of experimental [294] and simulated radial profiles of axial velocity, *U* (upper row) and radial velocity, *V* (lower row) at different axial locations of ENB-2, *z*/*R*=0.6, 1.2, 1.8 and 4.

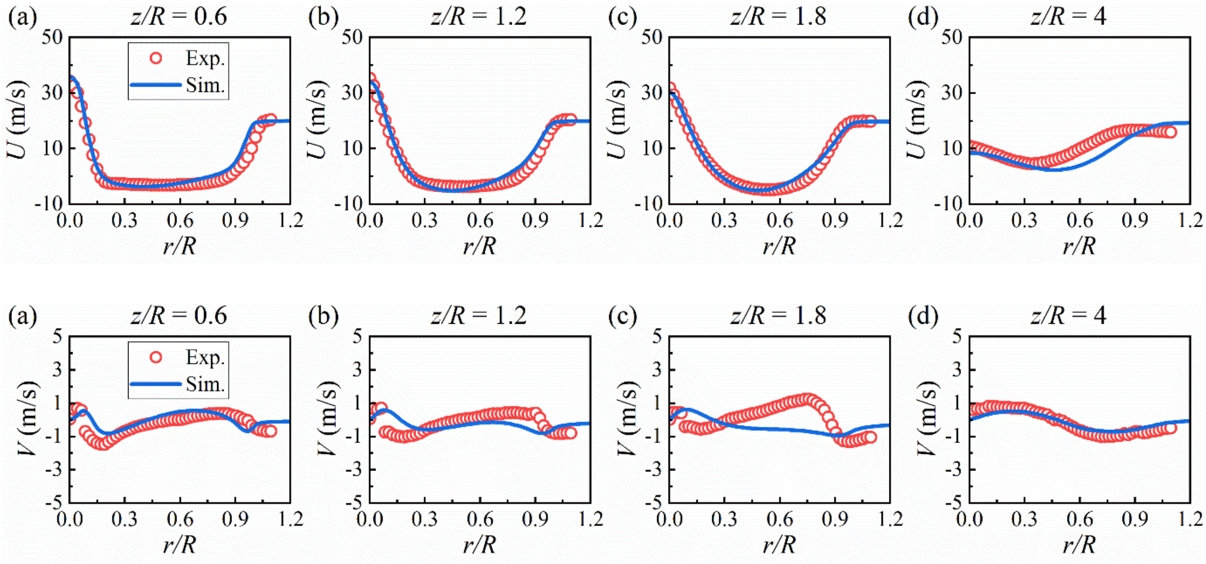

Figure 9.8 Comparison of experimental [294] and simulated radial profiles of axial velocity, *U* (upper row) and radial velocity, *V* (lower row) at different axial locations of ENB-3, *z*/*R*=0.6, 1.2, 1.8 and 4.

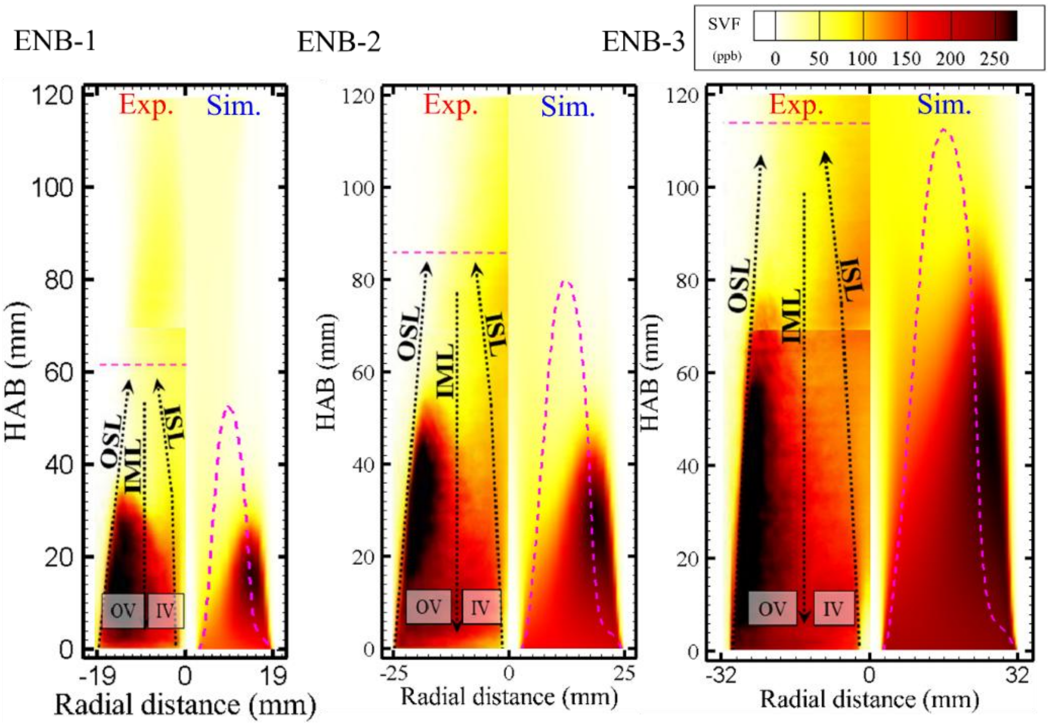

Figure 9.9 Comparison of experimental [301] and simulated mean soot volume fraction distributions for ENB-1, ENB-2 and ENB-3.

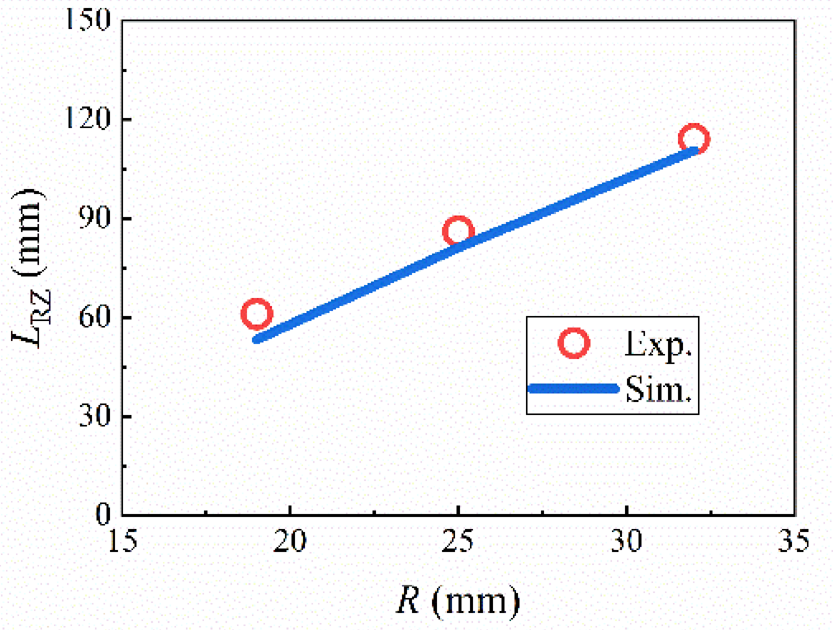

Figure 9.10 Comparison of experimental [301] and simulated lengths of recirculation zone, L_{RZ} for ENB-1, ENB-2 and ENB-3.

Figure 9.11 quantitatively compares the mean SVF profiles of three studied flames along the centerline between the experimental measurements and numerical simulations. Overall, the SVF changes along the centerline for three studied flames are well tracked, especially for ENB-2 and ENB-3, although there are some underpredictions at the axial locations of $z/R < 5$ for the ENB-1. The discrepancy may be caused by three reasons. Firstly, the soot inception mechanism is poorly understood. The present study assumes soot inception through pyrene (A4) dimerization, as A4 is the largest PAH in the chemical reaction mechanism which is commonly recognized as the soot precursor. Secondly, gas phase chemistry may be also a contributing factor. Since soot formation could be greatly influenced by the concentration of the soot precursor, gas chemistry for PAH prediction should be sufficiently reliable. Thirdly, the prediction of the flow pattern would be dictated by the interactions between the fuel jet and air coflow with the RZ, which reflects on the underprediction of the length of the RZ.

The simulated and measured mean SVF radial profiles for three studied flames at different axial locations (i.e., z/R = 1, 1.6, 4.9 and 10) are compared in Figure 9.12. Each flame has a RZ immediately downstream from the bluff body surface at $z/R < 3.2$, a neck zone at $3.2 < z/R < 4.4$ and a jet-like zone at $z/R > 4.4$ as the experimental measurements by Rowhani et al. [301]. Four axial locations are selected here for direct comparison, in which z/R = 1 and 1.6 are within the recirculation zone. It should be noted that z/R = 4.9 is just near the beginning of the jet-like zone and z/R = 10 is the location far from the recirculation zone. Numerical results show that the trends and structures of the mean SVF profiles for three studied flames along the radial direction are well reproduced. The slight underpredictions of the mean SVF for ENB-1 originate from the underprediction of the RZ, but the qualitative structure of the radial profile of the mean SVF is quite consistent with the experimental one, especially the non-uniform radial profile at axial location of z/R=1.6. Overall excellent agreements between the numerical and experimental results for three studied flames are shown especially for ENB-2 and ENB-3, in which the peaks of mean SVF are well captured at around the region of r/R = 1 within the recirculation zone. With the bluff body radius increasing from 19 mm to 32 mm, the residence time within the RZ extends which provides a longer time for soot and its precursor formation, therefore resulting in the increase of the SVF. This quantitative trend could be well reproduced by the numerical simulation, which demonstrates that the present new numerical framework could well capture the significant soot formation and evolution processes under different bluff body radii.

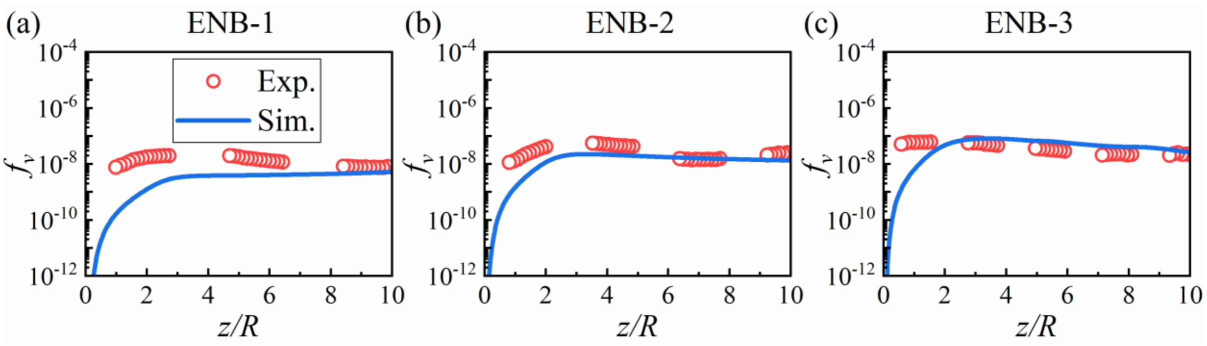

Figure 9.11 Comparison of experimental [302] and simulated mean soot volume fraction profiles for ENB-1, ENB-2 and ENB-3 (from left to right) along the centerline.

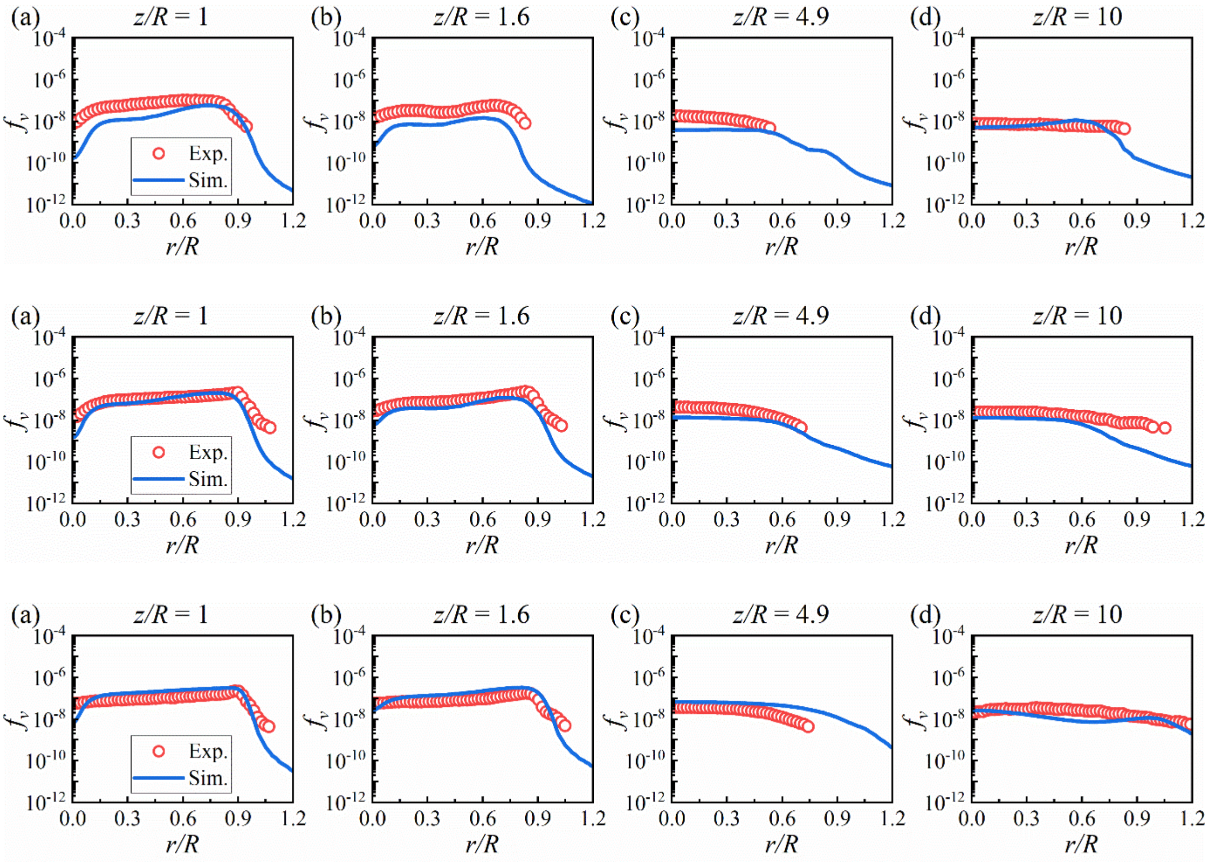

Figure 9.12 Comparison of experimental [302] and simulated radial profiles of mean soot volume fraction for ENB-1, ENB-2 and ENB-3 (from top row to bottom row) at different axial locations, *z/R* = 1, 1.6, 4.9 and 10.

Since the present numerical framework for soot modelling is newly developed on the basis of a soot sectional method, its significant advantage is that the full information about soot particle size distribution (PSD) evolution could be characterized directly, which can provide in-depth insights into soot formation and evolution at different regions for the turbulent flames with different bluff body radii. In the present study, Figures 9.13 to 9.15 firstly show the mean soot PSD profiles at four axial locations (i.e., *z/R*=0.5, 1, 2 and 4) of three radial regions (i.e., *r/R* = 0, 0.5 and 1) for further characterization of the sooting turbulent flames., which are not easily obtained from the experimental work.

At the centerline of *r/R* = 0 with high mixture fraction, soot is nucleated through the production of the soot precursor (A4). Bimodal PSD shapes are observed at axial location of *z/R*=0.5 for three studied flames as shown in Figure 9.13, which include four key features: (i) a mode of the inception peak representing incipient soot particles at small soot diameter, (ii) a trough, (iii) a mode of the coagulation peak at larger soot diameter by surface growth as well as coagulation, and (iv) the largest particle [49,188,310]. With the axial location of *z/R* increasing from 0.5 to 2, the soot aggregate number density increases significantly and the bimodal PSD shape remains almost unchanged for all these three studied flames, which demonstrates that the strong soot nucleation and growth processes take place in these regions. In addition, the bluff body radius increasing from 19 mm to 32 mm (i.e., ENB-1 to ENB-3) at axial location of *z/R*=0.5, inception peak gradually increases while the trough significantly drops, the coagulation peak gradually decreases and the number of large soot aggregates (i.e., d_m > 10 nm) considerably increases. It demonstrates that the PSD shifts gradually towards the larger soot aggregate side with bluff body radius increasing. This would be attributed to the growing axial distance from the fuel jet outlet, which facilitates the occurrence of soot nucleation and growth processes. The same trends are also observed at axial locations of *z/R*=1 and 2. Further increasing axial location of *z/R* to 4 which is larger than the length of the RZ, different PSD shapes are shown for different flames. For ENB-1, the PSD shape changes from bimodal to unimodal and the number density of soot aggregate further increases, especially those small soot aggregates. Obviously, the unimodal PSD shape in ENB-1 can be regarded as a bimodal PSD shape as a consequence of increasing the trough. By comparison, the number densities of soot aggregates for ENB-2 and ENB-3 also increase but remain bimodal PSD shapes. It is worth noting that the inception peak at axial location of *z/R*=4 gradually decreases with the increasing of bluff body radius while the trends of other three features are similar with those at axial locations of *z/R*=0.5, 1 and 2. In addition, the increasing magnitude of soot aggregate number density gradually decreases with the increasing of bluff body radius at axial location of *z/R*=4. This is due to that the distance to the largest length of the RZ for ENB-1 is larger than those for another two flames. As a result, less nucleated soot aggregates at the centerline are entrained into the recirculation zone and more soot aggregates are accumulated in the downstream. As the PAH is also accumulated in the downstream of the centerline, PAH-based soot growth process promotes.

The mean PSD profiles for different axial locations at radial region of *r/R*=0.5 are provided as Figure 9.14, in which axial locations of *z/R*=0.5, 1 and 2 are within the recirculation zone. At axial location of *z/R*=0.5, soot aggregate number density of *r/R* = 0.5 is significantly larger than that of the centerline for three studied flames, which implies that stronger soot nucleation and growth processes take place. The same trend is also seen at the axial locations of *z/R* = 1 and 2. At the RZ outside (i.e., *z/R* = 4), the number densities of soot aggregates at *r/R* = 0.5 for ENB-2 and ENB-3 are smaller than their corresponding counterparts at the centerline because of the oxidation effect of leaner mixture fraction. However, small soot aggregate number density at *r/R* = 0.5 for ENB-1 is larger than that of the centerline, but large soot aggregate number density at *r/R* = 0.5 is smaller than that of the centerline. The reason is that in addition to soot nucleation process, the soot growth process constantly takes effect at small soot aggregates but soot oxidation significantly occurs at large soot aggregates. For ENB-1, the soot aggregate number density decreases slightly with increasing the axial location of *z/R* from 0.5 to 1, which is also shown in another two studied flames. Further increasing the axial location of *z/R* to 2, the large soot aggregate number density reduces significantly because of the stronger oxidation, while the small soot aggregate number density increases because of nucleation as well as soot growth processes, leading to the transition of the PSD shape from bimodal to unimodal, which is also clearly observed in ENB-2. When the axial location of *z/R* increases to 4, the impacts of nucleation and soot growth on small soot aggregates become stronger in ENB-1 while the number density of soot aggregates further decreases in ENB-2 due to the stronger oxidation. By comparison, the bimodal PSD shape remains almost constant for ENB-3 with increasing the axial location of *z/R* from 0.5 to 4, and the soot aggregate number density in ENB-3 slightly decreases. Furthermore, large soot aggregate number density increases significantly at axial location of *z/R*=0.5 with bluff body radius increasing. This is because of the increasing soot aggregate residence time within RZ. The same trends are also seen at the axial locations of z/R = 1, 2 and 4, which illustrates a shift of the PSD towards the larger soot aggregate side due to the occurrence of soot growth processes.

Figure 9.15 shows the mean PSD profiles of three studied flames at different axial locations for the radial region of r/R = 1, which is just radially outside of the OSL. The lean mixture fraction inhibits soot precursor production and subsequently soot nucleation and growth processes, but the turbulent fluctuations can lead to the soot and soot precursor appearing outside the stoichiometric mixture fraction isoline. The number densities of soot aggregates for all three studied flames decrease gradually along with the increasing of axial location, z/R from 0.5 to 2 due to the constant oxidation, which is totally different from the trends at the centerline and r/R=0.5. At axial location of z/R=0.5, with bluff body radius increasing from 19 mm to 32 mm, the small soot aggregate number density decreases gradually but the large soot aggregate number density increases significantly. The similar trends are also observed at another three axial locations (i.e., z/R = 1, 2 and 4). As a consequence, the PSD shapes at different axial locations appear a unimodal distribution for ENB-1 and ENB-2, but the PSD shape of ENB-3 gradually changes from unimodal to bimodal distribution with the increasing of axial location, z/R from 0.5 to 4. A noticeable shift of the PSD towards the larger soot aggregate side with the increase in the bluff body radius is still observed.

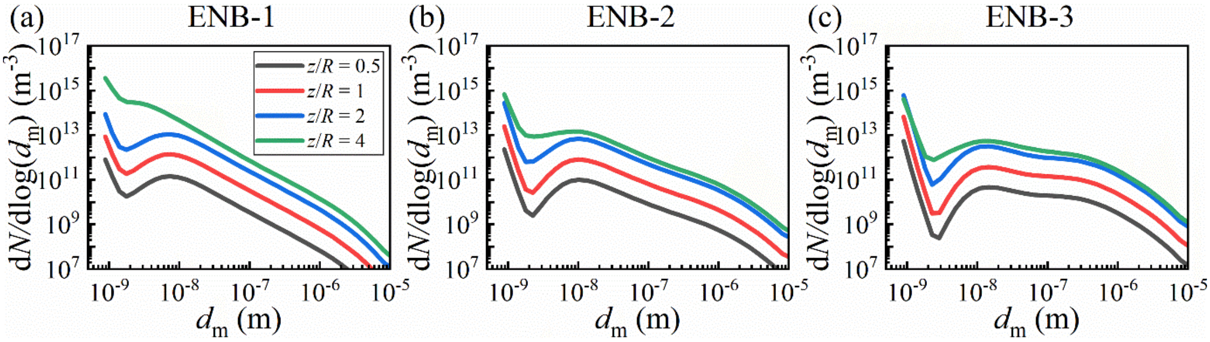

Figure 9.13 Mean soot particle size distribution profiles at different axial locations, z/R=0.5, 1, 2 and 4 along the centerline.

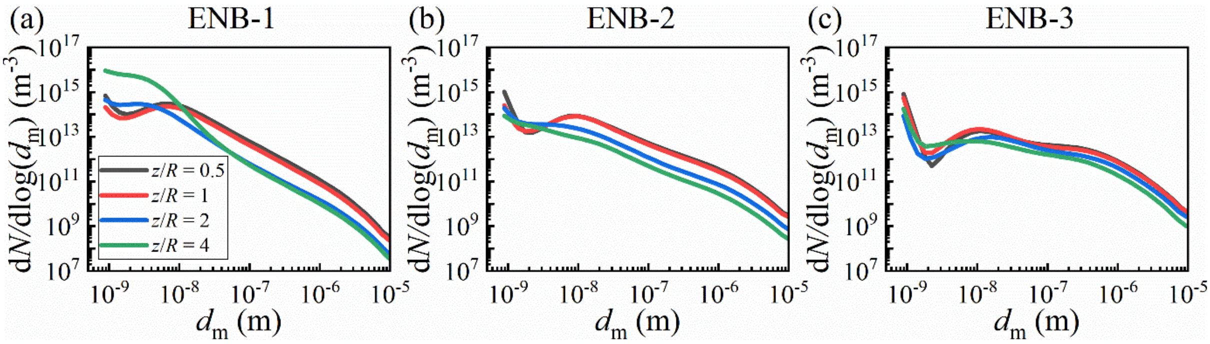

Figure 9.14 Mean soot particle size distribution profiles at different axial locations, z/R=0.5, 1, 2 and 4 of radial region, $r/R = 0.5$.

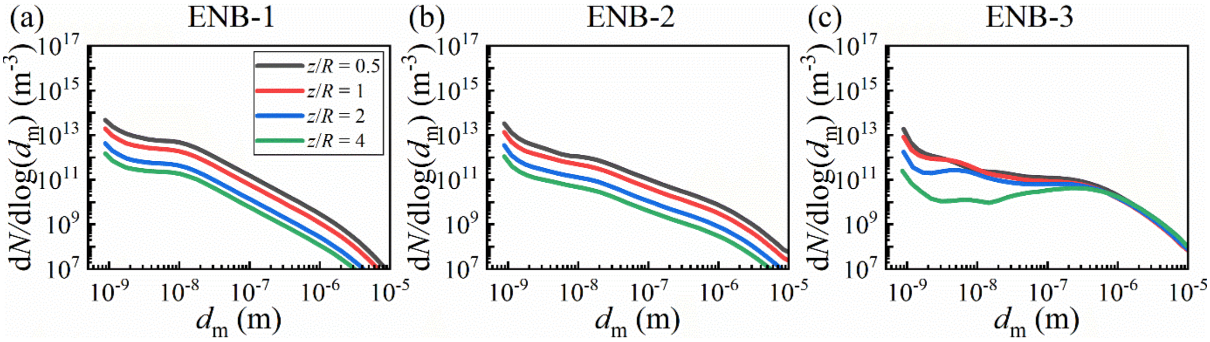

Figure 9.15 Mean soot particle size distribution profiles at different axial locations, z/R=0.5, 1, 2 and 4 of radial region, $r/R = 1$.

Figure 9.16 shows the mean soot aggregate sectional source terms in terms of PAH condensation and coagulation at different axial locations (i.e., z/R = 0.5, 1, 2 and 4) for the centerline (i.e., $r/R = 0$) to further elucidate the evolution of soot. The coagulation source terms here represent the consumption of soot aggregates, and the same treatments are also applied to the source terms of O_2 and OH oxidation. HACA surface growth, OH or O_2 oxidation occurs where concentrations of C_2H_2, OH or O_2 are high. At the centerline, the soot aggregate sectional source terms of O_2 and OH oxidation and HACA surface growth are extremely small due to their very low concentrations, therefore leading to the dominance of PAH condensation and coagulation. These two processes contribute to the production of large soot aggregates, which corresponds to the trends as shown in Figure 9.13. For ENB-1 at axial location of z/R=0.5, magnitudes of coagulation source terms are larger than those of PAH condensation at 2 nm < d_m < 7 nm, where corresponds to the region from the trough to the coagulation peak of the bimodal PSD shape as shown in Figure 9.13. It indicates the dominance of coagulation over PAH condensation in this region. At other soot aggregate diameters, the magnitudes of coagulation source terms are smaller than those of PAH condensation, which implies that the PAH condensation is dominant. In addition, with the increasing of bluff body radius, the magnitudes of coagulation source terms extend further towards the large soot aggregate side, which leads to the movement of the coagulation peak towards the large soot aggregate side. Similar trends are also observed at axial locations of z/R=1 and 2. However, when axial location of z/R is 4 which is larger than the length of the RZ, the PAH condensation always dominates over coagulation for ENB-1, which leads to the transition of the PSD shape from bimodal to unimodal distribution. By comparison, coagulation is dominant at small soot aggregates while PAH condensation dominates at large soot aggregates for ENB-2 and ENB-3. As a result, the PSD shapes of these two flames remain bimodal distribution. With the increase in the bluff body radius, the source terms of coagulation and PAH condensation decrease at small soot aggregates but increase at large soot aggregates. Overall, PAH condensation is comparable to coagulation at small soot aggregates but dominant at large soot aggregates along the centerline. Both coagulation and PAH condensation enhance significantly with the increase in the axial location.

The mean soot sectional source terms of PAH condensation, coagulation and HACA surface growth as well as O_2 and OH oxidation at different axial locations (i.e., z/R=0.5, 1, 2 and 4) for radial region of r/R=0.5 are shown in Figures 9.17 and 9.18. Obviously, stronger coagulation and PAH condensation occur at radial region of r/R=0.5 than at the centerline. It is observed that coagulation mainly occurs and dominates at small soot aggregates, while PAH condensation and HACA surface growth become dominant at large soot aggregates for ENB-1 at axial location of z/R=0.5. With bluff body radius increasing, the PAH condensation source terms decrease at small soot aggregates but gradually increase at large soot aggregates. It is also observed that the source terms of HACA surface growth as well as the magnitudes of OH and O_2 oxidation increase significantly, while the coagulation magnitudes decrease at small soot aggregates. The same trends are observed at axial locations of z/R=1 and 2. At axial location of z/R=4, PAH condensation dominates over coagulation for ENB-1, but the PAH condensation source terms are smaller than the magnitude of coagulation source terms at small soot aggregates but larger at large soot aggregates for ENB-2 and ENB-3. It should be noted that the effect of O_2 oxidation as well as OH oxidation on the soot evolution is small but gradually becomes significant for three studied flames with the increasing of axial location. Overall, coagulation dominates at small soot aggregates for ENB-1 and ENB-2, but HACA surface growth is dominant at large soot aggregates when the axial location of *z/R* is 0.5 and 1, which results in the bimodal PSD shape as shown in Figures 9.14(a) and 9.14(b). Further increasing the axial location of *z/R* to 4, HACA surface growth gradually dominates over coagulation, leading to the gradual change of the PSD shape from bimodal to unimodal distribution. The effect of PAH condensation on the soot evolution is also very significant, and O_2 oxidation as well as OH oxidation gradually enhances with the increase in the axial location. By comparison, coagulation is dominant at small soot aggregates for ENB-3 while PAH condensation dominates at large soot aggregates for different axial locations. Therefore, the bimodal PSD shape remains for varying axial locations as presented in Figure 9.14(c).

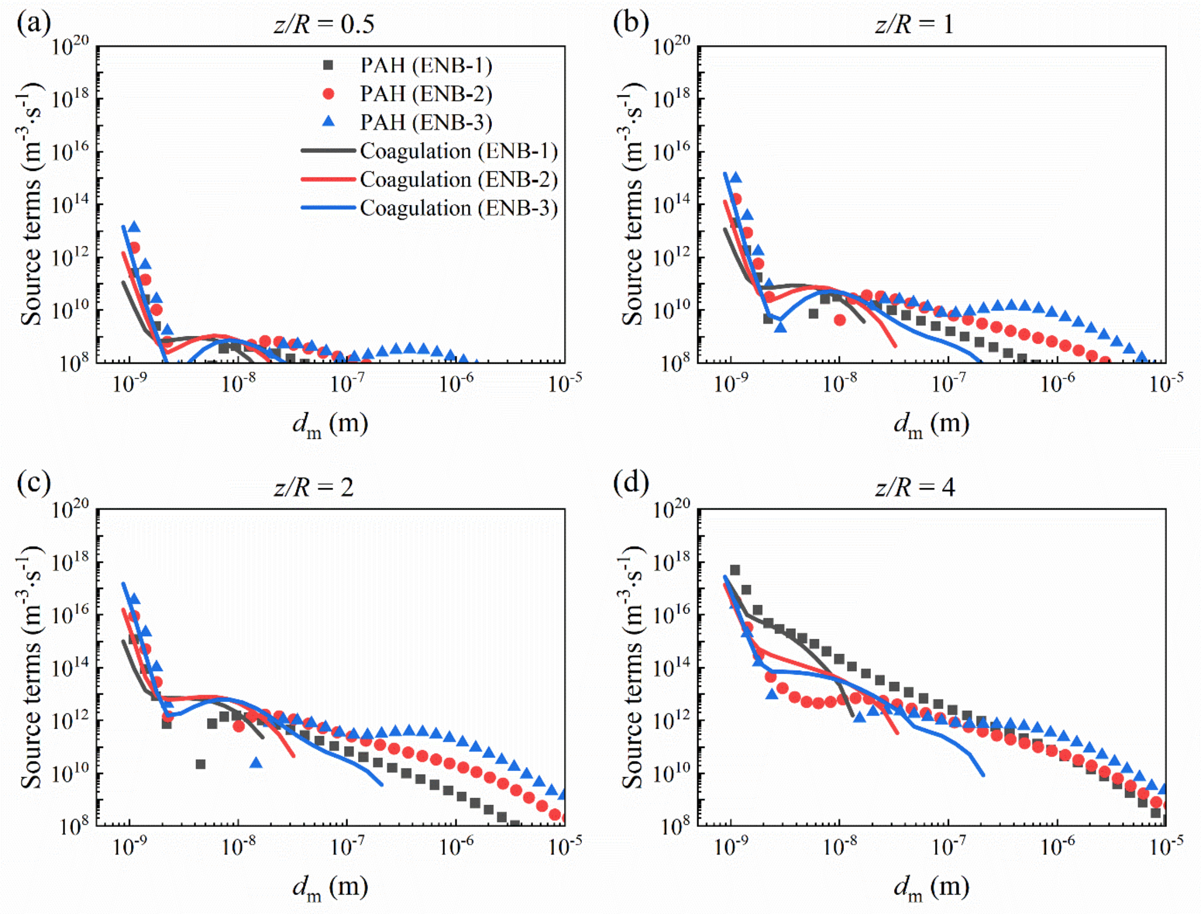

Figure 9.16 Mean soot sectional source terms of PAH condensation and coagulation at different axial locations, *z/R*=0.5, 1, 2 and 4 of radial region, *r/R*=0.

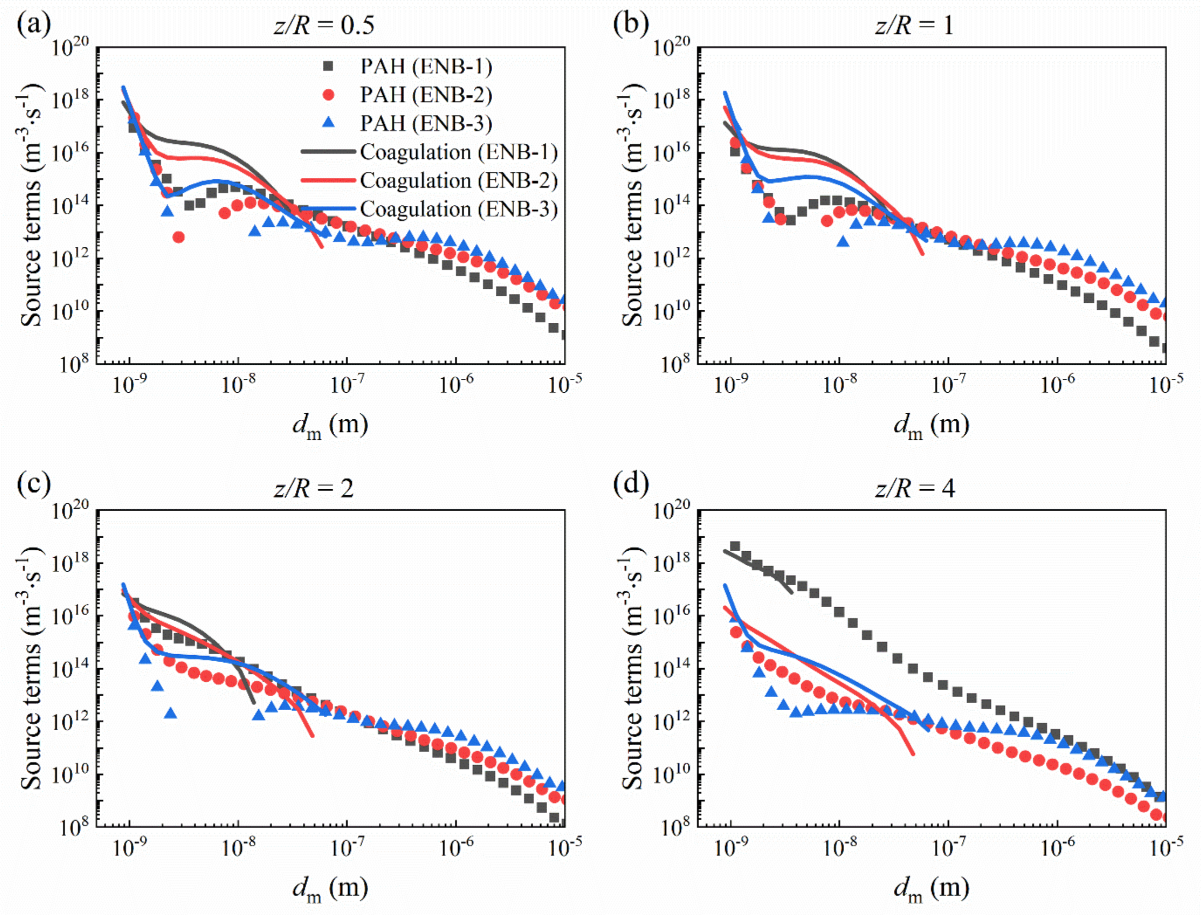

Figure 9.17 Mean soot sectional source terms of PAH condensation and coagulation at different axial locations, *z/R*=0.5, 1, 2 and 4 of radial region, *r/R* = 0.5.

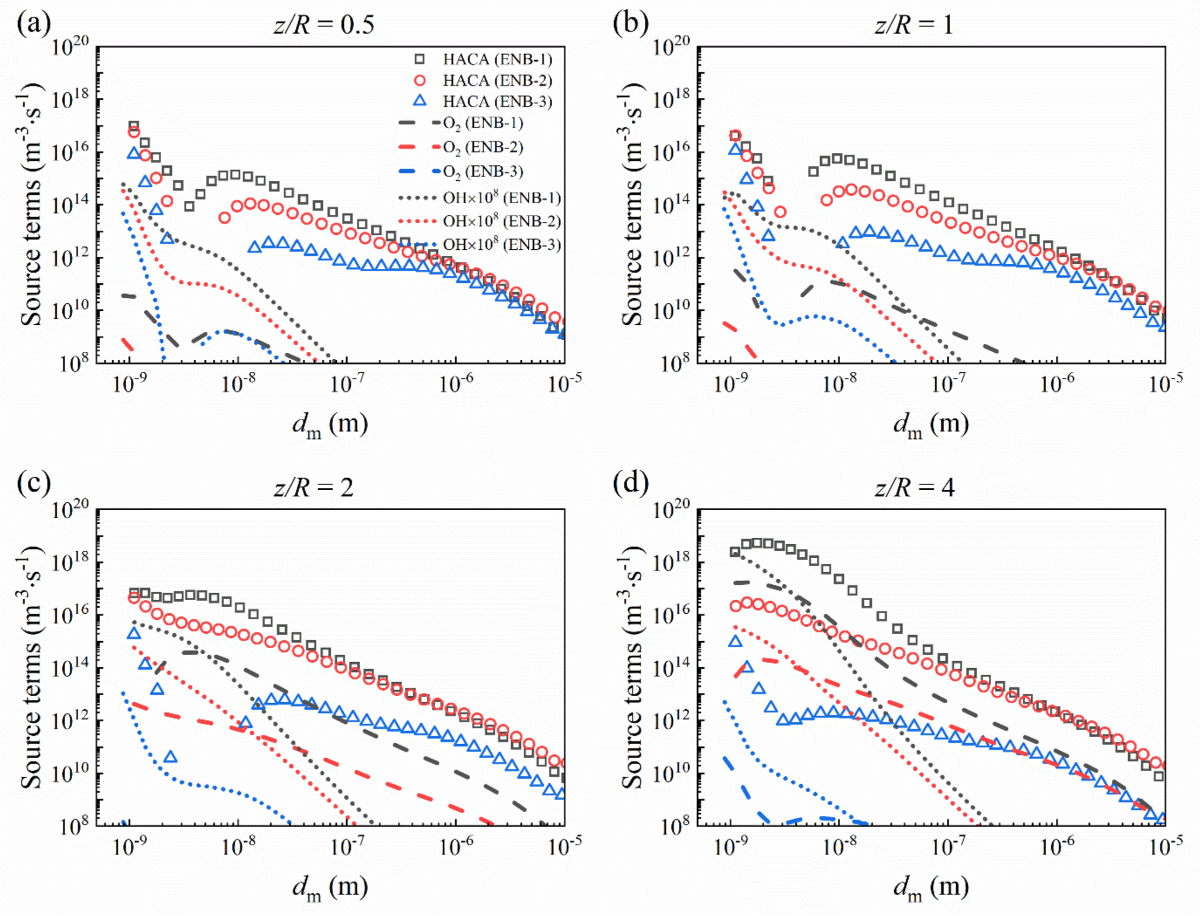

Figure 9.18 Mean soot sectional source terms of HACA surface growth, O_2 oxidation and OH oxidation at different axial locations, *z/R*=0.5, 1, 2 and 4 of radial region, *r/R* = 0.5.

Figures 9.19 and 9.20 show the mean soot sectional source terms of PAH condensation, coagulation and HACA surface growth as well aas O_2 and OH oxidation for different axial locations (i.e., *z/R* = 0.5, 1, 2 and 4) at radial region of *r/R*=1. It is obvious that O_2 oxidation at radial region of *r/R*=1 is stronger than that at the centerline as well as radial region of *r/R*=0.5 because of the high concentration of O_2. For ENB-1 at axial location of *z/R*=0.5, coagulation and PAH condensation effects are comparable at small soot aggregates, but the source terms of PAH condensation are larger than the magnitudes of coagulation source terms at large soot aggregates. With increasing the axial location of *z/R* to 4, the sources terms of coagulation and PAH condensation as well as HACA surface growth gradually decrease. By comparison, O_2 oxidation dominates at different axial locations due to the large concentration of O_2 in the air coflow, and HACA surface growth also significantly influences soot evolution while effects of OH oxidation are negligible due to the low concentration of OH. The same trends are observed in ENB-2 and ENB-3. The magnitudes of coagulation source terms for ENB-3 are larger than those for ENB-1 and ENB-2 at the axial locations of *z/R* = 2 and 4, which leads to the formation of the bimodal PSD shape of ENB-3 as shown in Figure 9.15. In addition, ENB-3 has stronger O_2 oxidation than the other two studied flames at axial location of *z/R*=1, while magnitudes of O_2 oxidation for ENB-3 become more significantly larger than those of ENB-1 and ENB-2 with increasing the axial location of *z/R* to 4.

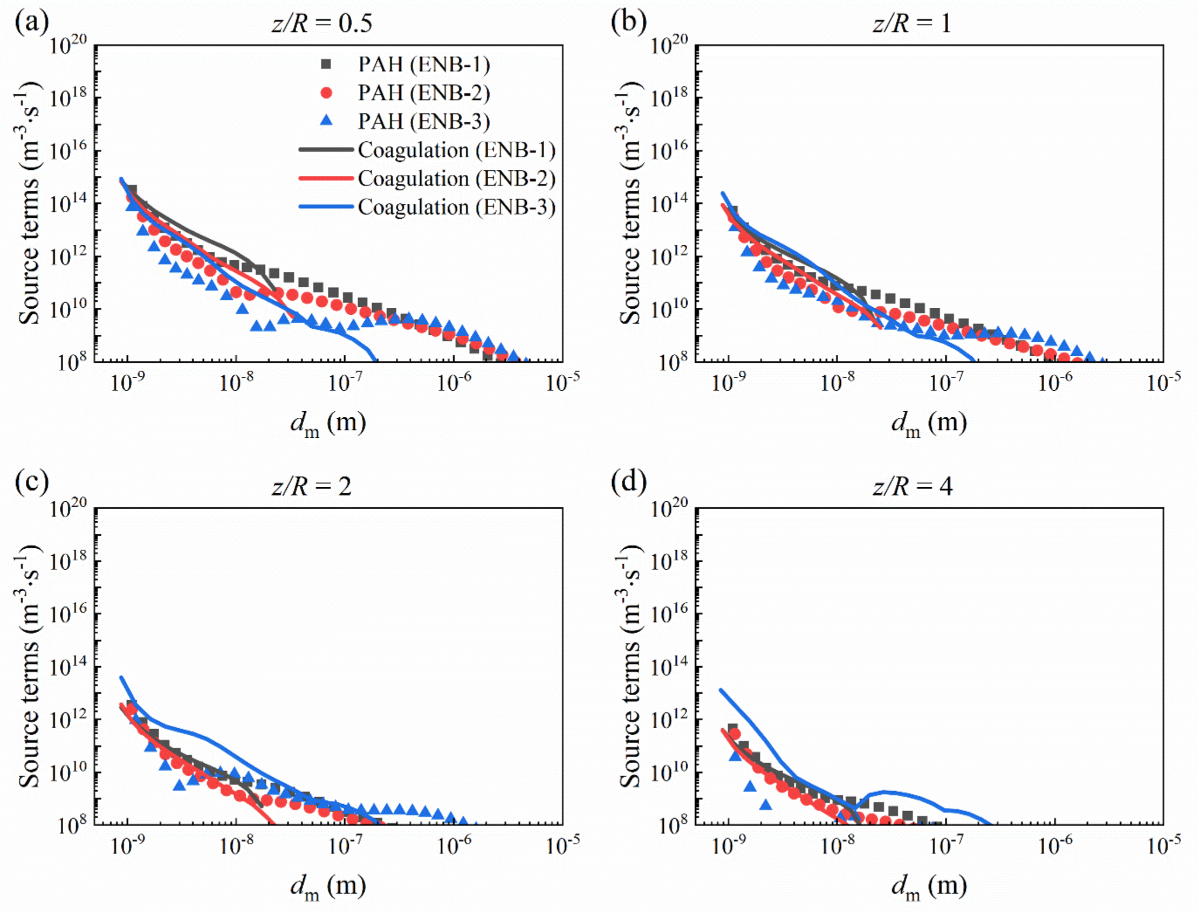

Figure 9.19 Mean soot sectional source terms of PAH condensation and coagulation at different axial locations, *z/R*=0.5, 1, 2 and 4 of radial region, *r/R* = 1.

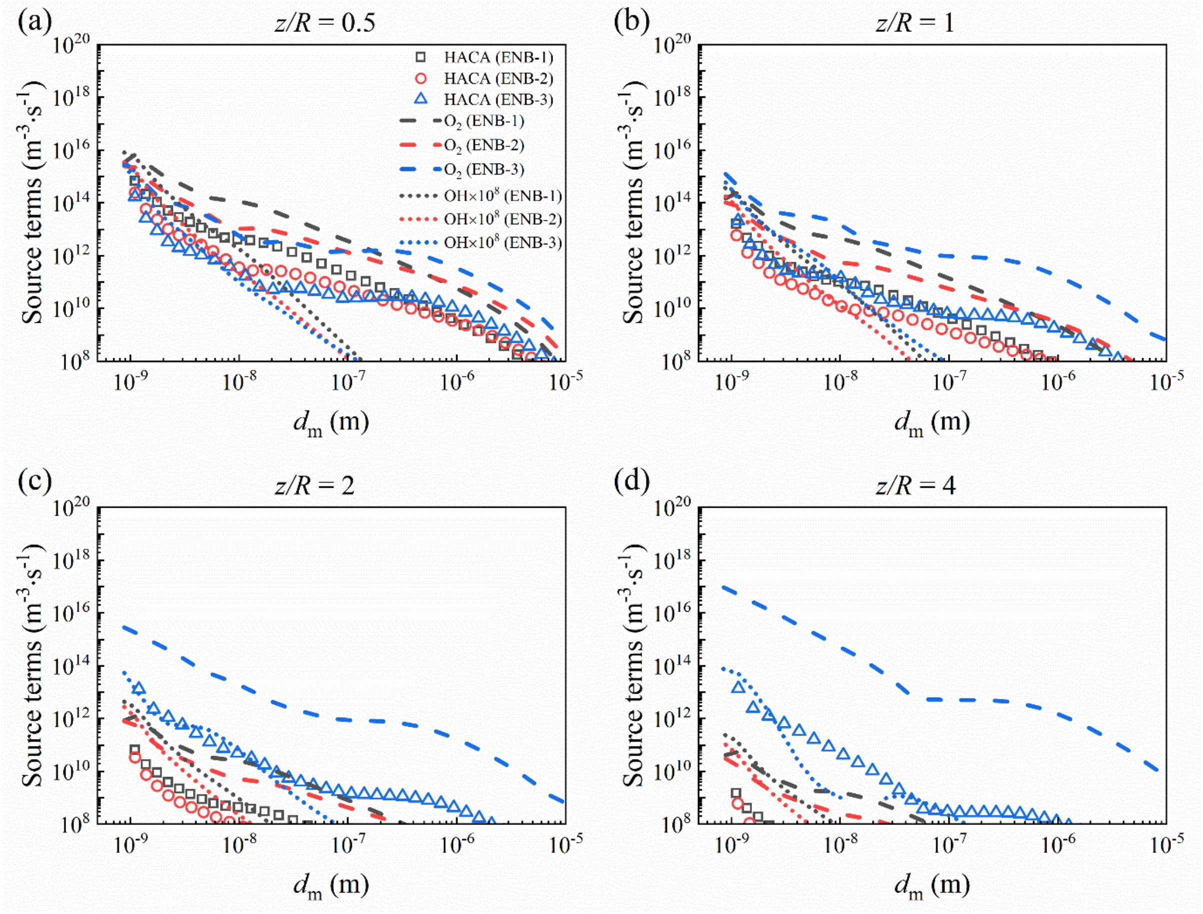

Figure 9.20 Mean soot sectional source terms of HACA surface growth, O_2 oxidation and OH oxidation at different axial locations, z/R=0.5, 1, 2 and 4 of radial region, r/R = 1.

9.4 Summary

In the present study, an OpenFOAM numerical framework coupling an extended soot sectional method with a finite-rate chemistry model based on detailed chemistry is newly developed for soot modelling in turbulent combustion. The soot sectional method is formulated to solve soot aggregate and primary particle number densities for every section. Soot aggregates and gas-phase species are solved simultaneously with considering differential diffusion and mass exchange between soot and chemical species. A dynamic load balancing approach together with a reference mapping model is incorporated into the new numerical framework to accelerate the parallel reacting flow simulations.

The newly developed numerical framework is validated by a well-characterized turbulent non-sooting bluff body flame and is then applied for simulating soot aerosol dynamics of turbulent sooting bluff body flames. Numerical results of gas-phase species and soot of flow, mixture, flame structure and SVF are fully compared with available experimental dataset. Excellent quantitative and qualitative agreements demonstrate that the new numerical framework can accurately predict the flow and flame properties and well capture the significant soot formation and evolution processes for different bluff body radii.

The soot PSDs as well as source terms of formulated soot transport equations at different axial and radial locations are numerically investigated. The soot aggregate number density gradually increases with the increasing axial location at the centerline because of the enhanced nucleation, coagulation and PAH condensation. The resulting soot PSD always remains a bimodal shape for the axial locations of $z/R < 4$. At the radial region of $r/R = 0.5$, coagulation dominates at small soot aggregates while PAH condensation and HACA surface growth take significant effect at large soot aggregates. Meanwhile, O_2 oxidation as well as OH oxidation gradually enhances with the increase in the axial location. These collectively lead to the gradual change of the PSD shape from bimodal to unimodal distribution. O_2 oxidation shows dominant at the radial region of $r/R = 1$ while the impacts of PAH condensation and HACA surface growth gradually drop with axial location increasing. This results in a gradual decrease in the soot aggregate number density. With bluff body radius increasing, the time of soot aggregates residing in the recirculation zone increases, leading to a significant shift of the soot PSD towards the larger soot aggregate side, and the PSD shape always remains bimodal distribution at the centerline and within the recirculation zone.

Chapter 10 Conclusions and Recommendations for Future Work

10.1 Review of the Present Research Study

The present research aimed at numerically modeling soot aerosol dynamics in both laminar and turbulent combustion flows, in which the population balance equation (PBE) of aerosol dynamics coupling with computational fluid dynamics (CFD) would be solved. The developed numerical framework can be used to model soot formation and evolution in practical combustion devices with different types of fuels, in which only the chemical reaction mechanism used should be changed. The research work in this thesis is mainly comprised of six parts.

In the first part of the present study, a new sorting algorithm-based merging weighted fraction Monte Carlo (SAMWFMC) method is proposed and developed to solve coagulation in aerosol dynamics in Chapter 4. In the new SAMWFMC method, the jump Markov process is constructed based on both adjustable and constant fraction functions, and a new merging scheme is proposed to ensure a constant-number and constant-volume scheme with the introduction of sorting algorithm. This new SAMWFMC method is fully validated by comparing with existing analytical solutions of six benchmark test cases. The numerical results obtained from the SAMWFMC method show excellent agreement with the analytical solutions, and lower stochastic errors are found in different order moments of the particle size distribution (PSD) at an only slightly higher computational cost when compared with other MC methods.

The second part of the present study focuses on developing a new sorting algorithm-based merging Monte Carlo method capable of solving all aerosol dynamic processes (nucleation, coagulation, breakage, deposition and condensation/evaporation) in Chapter 5. A neighbour merging method is proposed to maintain a constant-volume and constant-number scheme with minimal interference to the numerical particle population. Very comprehensive computational conditions are used to study their impacts on computational accuracy and efficiency by comparing the SAMMC method to previous Monte Carlo (MC) methods and analytical solutions. Numerical results show that the SAMMC method has excellent agreement with analytical solutions and very high computational accuracy for all specified cases of different aerosol dynamic processes. More importantly, the SAMMC method can deal with breakage-related processes and simultaneous coagulation and nucleation with very high computational accuracy and efficiency without introducing systematic errors.

The third part is to develop an Open-source Field Operation and Manipulation (OpenFOAM) solver incorporating a detailed transport model for reacting flow simulations as the use of the highly simplified molecular transport model in the CFD code greatly restricts the resolution of important physical scales for new insights into combustion phenomena, especially in laminar flows. A systematical validation in different flame configurations with detailed chemical kinetics are conducted to evaluate the computational performance of the new solver in Chapter 6. The successful development and implementation of the new accurate solver provide a new CFD tool and numerical framework for the combustion community.

The fourth part is to study the soot aerosol dynamics in laminar combustion flows by using the numerical framework coupled with a newly developed dimer-based soot model, which involves dimer formation and condensation as well as soot nucleation, coagulation, H-abstraction-C_2H_2-addition (HACA) surface growth, O_2 and OH oxidation. In Chapter 7, the formation of dimers is modelled via homogeneous and heterogeneous collisions of polycyclic aromatic hydrocarbon (PAH) molecules made up of 50 or more carbon atoms based on detailed chemistry while soot is nucleated by the collision of these dimers and grows via the condensation of these dimers. In a steady state, the generation rate and consumption rate of dimers are kept in a balance. Numerical results obtained from the new soot model agree well with the published experimental counterparts under different strain rates and oxygen mole fractions in the oxidizer for counterflow diffusion flames, and supplementary insights into soot formation and evolution are provided numerically.

The fifth part of the present study is aimed at turbulence modelling in CFD based on the developed numerical framework of OpenFOAM. In Chapter 8, a new one-equation turbulence model is developed by deriving the transport equations in the complete form without simply assuming equal coefficients of the diffusion terms, which combines the best characteristics of the two-equation standard k-ε and Wilcox's k-ω turbulence models. Five benchmark flow configurations with available results are used to validate the new one-equation turbulence model, which is compared with those widely adopted two- and one- equation turbulence models. Numerical results demonstrate that the present new one-equation turbulence model has a great potential to predict turbulent flow separation and reattachment.

The sixth part is to further extend the numerical framework coupling an extended soot sectional method with a finite-rate chemistry model based on detailed chemistry for simulating soot formation and particle size distribution (PSD) evolution in turbulent combustion. In Chapter 9, The soot sectional method is formulated to solve soot aggregate and primary particle number densities for every section. Soot aggregates and gas-phase species are solved simultaneously with considering differential diffusion and mass exchange between soot and chemical species. A dynamic load balancing approach together with a reference mapping model is incorporated into the new numerical framework to accelerate the parallel reacting flow simulations. The numerical framework is validated by a well-characterized turbulent non-sooting bluff body flame for accurate estimation of gas-phase flow field and then applied for simulating soot aerosol dynamics of turbulent sooting bluff body flames. The resulting flow, flame and soot characteristics are in comparison with available experimental dataset. The simulated soot PSDs at different locations are analyzed and the underlying competing mechanism of different dynamic processes is fully explored.

10.2 Main Conclusions of the Thesis

10.2.1 Conclusion of development of sorting algorithm-based merging weighted fraction Monte Carlo Method for coagulation

The new sorting algorithm-based merging weighted fraction Monte Carlo (SAMWFMC) method is fully validated by comparing with existing analytical solutions for six benchmark test cases. The numerical results obtained from the SAMWFMC method with both adjustable and constant fraction functions show excellent agreement with the analytical solutions and low stochastic errors. The SAMWFMC method has lower stochastic errors different order moments than the direct simulation Monte Carlo (DSMC) and multi-Monte Carlo (MMC) methods. Compared with the weighted fraction Monte Carlo (WFMC) method, the SAMWFMC method can significantly reduce the stochastic error in the total particle number concentration without increasing the stochastic errors in high-order moments of the particle size distribution (PSD) at only slightly higher computational cost. The new SAMWFMC method shows a significant advantage in dealing with weighted fraction coagulation process in aerosol dynamics, which demonstrates that the SAMWFMC method provides excellent potential to deal with various fraction functions with high computational accuracy and efficiency.

10.2.2 Conclusion of development of sorting algorithm-based merging Monte Carlo method for aerosol dynamics

Comprehensive computational conditions are used to study their impacts on computational accuracy and efficiency by comparing the sorting algorithm-based merging Monte Carlo (SAMMC) method to previous Monte Carlo (MC) methods and analytical solutions. Numerical results show that the SAMMC method has excellent agreement with analytical solutions for all specified cases of different aerosol dynamic processes and shows higher computational accuracy than equal-weight-based MC methods (i.e., the stepwise constant-volume method and mass- and number-based constant-number methods). In addition, the computational accuracy of the SAMMC method in the total particle number concentration is much higher than those of the weighted fraction Monte Carlo (WFMC) method and sorting algorithm-based merging weighted fraction Monte Carlo (SAMWFMC) method in non-homogeneous coagulation. The SAMMC method can also achieve the same computational precision as the multi-Monte Carlo (MMC) method at only slightly higher computational cost in homogeneous coagulation. More importantly, the SAMMC method can deal with breakage-related processes and simultaneous coagulation and nucleation with very high computational accuracy and efficiency, while the numerical results of the MMC method may significantly deviate from analytical solutions due to the introduction of systematic errors.

10.2.3 Conclusion of development of reacting flow solver incorporating detailed transport model for combustion simulations

A detailed transport model using a mixture-averaged formulation based on the standard kinetic theory of gases is newly incorporated into combustion solvers for dealing with reacting flow simulations in OpenFOAM. This is achieved by developing a new utility to input molecular transport parameters and a new library to calculate transport properties. All the codes are completely written under the code framework of OpenFOAM, making them very easy to read, use, maintain, enhance and extend. More importantly, the developed utility and library can be coupled with any reacting flow solver for accurately modelling a multi-species system without requiring any extra operation when using. In the present study, the function of the new utility is firstly examined and then a new solver (i.e., *standardReactingFoam*) is developed for solving reacting flows. A systematical validation and assessment in different flame configurations with detailed chemical kinetics is studied to evaluate the computational performance of these new solvers. A zero-dimensional auto ignition, one-dimensional premixed flame and two-dimensional non-premixed counterflow flame are selected to validate the solvers against Cantera and CHEMKIN, while a realistic combustion simulation of a two-dimensional partially premixed coflow flame is also verified. Numerical simulation results show that very good agreements with the benchmark data are obtained for all studied flames, which demonstrates the high computational accuracy of the developed combustion solvers incorporating a detailed transport model.

10.2.4 Conclusion of development of dimer-based soot model for soot aerosol dynamics in laminar combustion flows

A dimer-based soot model combining HACA surface growth and oxidation mechanism with homogeneous and heterogeneous nucleation and dimer condensation is proposed to investigate soot formation of counterflow diffusion flames. As intermediate species between soot and polycyclic aromatic hydrocarbons (PAHs), the formation of dimers is modelled by heterogeneous collision of PAHs, resulting in the direct generation of stable soot. The masses of PAHs used for dimer formation are calculated based on a weighted average of total PAH masses and their densities are estimated to be associated with their chemical compositions. Combined with the mixture-averaged transport model for combustion modelling, numerical validations of the dimer-based soot model would be conducted at varying strain rates as well as varying oxygen mole fractions of the oxidizer. Simulated soot volume fractions (SVF) show a satisfactory agreement with experimental dataset, and the peak SVF magnitudes are accurately captured. With oxygen mole fraction of the oxidizer increasing, surface growth via dimer condensation and HACA mechanism as well as soot nucleation are significantly enhanced, leading to an increase in the SVF. Compared with HACA surface growth, the impact of varying oxygen mole fractions on oxidation rates of O_2 and OH is slight, which implies that surface growth is a dominant factor in determining SVF. As the strain rate increases, the SVF gradually decreases as dimer production and HACA surface growth rates significantly decrease. Decreasing strain rate or increasing oxygen mole fractions leads to more significant skewness of the SVF profile towards the fuel stream.

10.2.5 Conclusion of development of one-equation turbulence model

The new one-equation turbulence model is used to simulate for different benchmark flow configurations including the flow over a flat plate at zero pressure gradient, bump-in-channel flow, backward facing step flow, NASA wall-mounted hump separated flow and channel flow. The numerical results are fully validated and compared with the results of the experimental dataset, the one- and two-equation turbulence models, and the high-accuracy NASA codes (i.e., CFL3D and FUN3D). The new one-equation turbulence model is proved to be more accurate when compared with the one-equation Wray-Agarwal and two-equation shear stress transport (SST) k-ω turbulence models for the benchmark flow configurations. It also demonstrates that the present new one-equation turbulence model has a great potential to predict turbulent flow separation and reattachment.

10.2.6 Conclusion of numerical investigation on soot particle size distribution in turbulent combustion flows.

The newly extended numerical framework is validated by a well-characterized turbulent non-sooting bluff body flame and is then applied for simulating soot aerosol dynamics of turbulent sooting bluff body flames. Numerical results of gas-phase species and soot of flow, mixture, flame structure and SVF are fully compared with available experimental dataset. Excellent quantitative and qualitative agreements demonstrate that the new numerical framework can accurately predict the flow and flame properties and well capture the significant soot formation and evolution processes for different bluff body radii. The soot PSDs as well as source terms of formulated soot transport equations at different axial and radial locations are numerically investigated. The soot aggregate number density gradually increases with the increasing axial location at the centerline because of the enhanced nucleation, coagulation and PAH condensation. The resulting soot PSD always remains a bimodal shape for the axial locations of $z/R < 4$. At the radial region of $r/R = 0.5$, coagulation dominates at small soot aggregates while PAH condensation and HACA surface growth take significant effect at large soot aggregates. Meanwhile, O_2 oxidation as well as OH oxidation gradually enhances with the increase in the axial location. These collectively lead to the gradual change of the PSD shape from bimodal to unimodal distribution. O_2 oxidation becomes dominant at the radial region of $r/R = 1$ while the impacts of PAH condensation and HACA surface growth gradually drop with axial location increasing. This results in a gradual decrease in the soot aggregate number density. With bluff body radius increasing, the time of soot aggregates residing in the recirculation zone increases, leading to a significant shift of the soot PSD towards the larger soot aggregate side, and the PSD shape always remains bimodal distribution at the centerline and within the recirculation zone.

10.3 Recommendations for Future Work

The transition of gas-phase hydrocarbon molecules to mature soot aerosols in combustion processes goes through various complex physical and chemical processes involving fluid dynamics, transport phenomena, chemical kinetics and aerosol dynamics and heat and mass transfer, which are required to be taken into account in soot modelling. This thesis aims at numerically modeling soot aerosol dynamics in both laminar and turbulent combustion flows, in which the population balance equation (PBE) of aerosol dynamics coupling with computational fluid dynamics (CFD) is solved.

However, recommendations with regard to further research work to overcome the limitations of the present research and further deepen the understanding of soot aerosol dynamics are still required.

1. More detailed chemistry that has a better prediction on species concentrations can be used to better capture soot aerosol dynamic processes as soot formation and evolution strongly depend on local thermodynamic conditions as well as chemical composition. In the present study, the popular ABF chemical reaction mechanism is used, which includes 544 reactions and 101 species. More detailed chemical reaction mechanisms can provide more intermediate reactions and species, which may include possible pathways leading to soot formation, therefore achieving a better prediction.

2. Chemical species contributed to the formation of precursors may require some modifications if different chemical reaction mechanisms are used. Normally, the largest PAH molecule of ABF mechanism would be employed as soot precursor. However, the heaviest PAH molecule may be up to coronene (A7) or more in some newly proposed chemical reaction mechanisms, which requires taking these species into account for a more general application to soot modelling.

3. More detailed chemistry normally involves many reactions and species, and direct resolution of the complete chemistry is very computationally expensive. As a result, actions should be taken to speed up the parallel reacting flow simulations as well as soot modelling based on high-performing computers.

4. More soot aerosol dynamics such as fragmentation and carbonization may be required to be considered, which are neglected in the present study. Fragmentation may influence the morphology and soot PSD, as the soot aggregate structures could be weakened by oxidation,

which may result in the formation of smaller aggregates fragmented from larger aggregates. Carbonization is a process that converts soot precursor particles into mature soot particles with an ordered graphitic shell, which dehydrogenates PAHs in soot primary particles, resulting in a slight decrease of soot masses.

References

[1] J.G. Speight, Handbook of industrial hydrocarbon processes, Gulf Professional Publishing, 2019.

[2] H. Maldonado Colmán, A. Cuoci, N. Darabiha, B. Fiorina, A virtual chemistry model for soot prediction in flames including radiative heat transfer, Combust. Flame 238 (2022) 111879.

[3] S. Veronesi, M. Commodo, L. Basta, G. De Falco, P. Minutolo, N. Kateris, H. Wang, A. D'Anna, S. Heun, Morphology and electronic properties of incipient soot by scanning tunneling microscopy and spectroscopy, Combust. Flame 243 (2022) 111980.

[4] J.W. Martin, M. Salamanca, M. Kraft, Soot inception: Carbonaceous nanoparticle formation in flames, Prog. Energy Combust. Sci. 88 (2022) 100956.

[5] I. Agranovski, Aerosols - Science and Technology, Wiley-VCH Verlag, Weinheim, 2010.

[6] F.J. Bauer, P.A.B. Braeuer, S. Aßmann, M.A. Thiele, F.J.T. Huber, S. Will, Characterisation of the transition type in optical band gap analysis of in-flame soot, Combust. Flame 243 (2022) 111986.

[7] M. Commodo, A.E. Karataş, G. De Falco, P. Minutolo, A. D’Anna, Ö.L. Gülder, On the effect of pressure on soot nanostructure: A Raman spectroscopy investigation, Combust. Flame 219 (2020) 13-19.

[8] H.A. Michelsen, M.B. Colket, P.-E. Bengtsson, A. D’Anna, P. Desgroux, B.S. Haynes, J.H. Miller, G.J. Nathan, H. Pitsch, H. Wang, A review of terminology used to describe soot formation and evolution under combustion and pyrolytic conditions, ACS Nano 14 (2020) 12470-12490.

[9] S.K. Friedlander, Smoke, Dust, and Haze: Fundamentals of Aerosol Dynamics, second ed., Oxford University Press, New York, 2000.

[10] S. Rigopoulos, Modelling of soot aerosol dynamics in turbulent flow, Flow Turbul. Combust. 103 (2019) 565-604.

[11] S.E. Pratsinis, Flame aerosol synthesis of ceramic powders, Prog. Energy Combust. Sci. 24 (1998) 197-219.

[12] V. Raman, R.O. Fox, Modeling of fine-particle formation in turbulent flames, Annu. Rev. Fluid Mech. 48 (2016) 159-190.

[13] H. Bockhorn, Soot formation in combustion : mechanisms and models, Springer-Verlag, Berlin, 1994.

[14] M. Frenklach, Reaction mechanism of soot formation in flames, Phys. Chem. Chem. Phys. 4 (2002) 2028-2037.

[15] V.B. Stephens, J. Bedwell, A.J. Josephson, K. Oldham, D.O. Lignell, SootLib: A soot model library for combustion simulation, SoftwareX 22 (2023) 101375.

[16] T.E. Ramabhadran, T.W. Peterson, J.H. Seinfeld, Dynamics of aerosol coagulation and condensation, AICHE J. 22 (1976) 840-851.

[17] F.E. Kruis, A. Maisels, H. Fissan, Direct simulation Monte Carlo method for particle coagulation and aggregation, AICHE J. 46 (2000) 1735-1742.

[18] H. Zhang, G. Sharma, S. Dhawan, D. Dhanraj, Z. Li, P. Biswas, Comparison of discrete, discrete-sectional, modal and moment models for aerosol dynamics simulations, Aerosol Sci. Technol. 54 (2020) 739-760.

[19] A. Kalinov, A.I. Osinsky, S.A. Matveev, W. Otieno, N.V. Brilliantov, Direct simulation Monte Carlo for new regimes in aggregation-fragmentation kinetics, J. Comput. Phys. 467 (2022) 111439.

[20] R. Dandekar, R. Rajesh, V. Subashri, O. Zaboronski, A Monte Carlo algorithm to measure probabilities of rare events in cluster-cluster aggregation, Comput. Phys. Commun. 288 (2023) 108727.

[21] D. Li, Z. Li, Z. Gao, Quadrature-based moment methods for the population balance equation: An algorithm review, Chin. J. Chem. Eng. 27 (2019) 483-500.

[22] T. Salminen, K.E.J. Lehtinen, J.P. Kaipio, V. Russell, A. Seppänen, Application of finite element method to general dynamic equation of aerosols – Comparison with classical numerical approximations, J. Aerosol. Sci. 160 (2022) 105902.

[23] S.E. Miller, S.C. Garrick, Nanoparticle coagulation in a planar jet, Aerosol Sci. Technol. 38 (2004) 79-89.

[24] M. Yu, J. Lin, J. Cao, M. Seipenbusch, An analytical solution for the population balance equation using a moment method, Particuology 18 (2015) 194-200.

[25] J. Shen, H. Jiang, M.Z. Yu, B. Kong, A bimodal population balance method for the dynamic process of engineered nanoparticles, Int. J. Heat Mass Transf. 188 (2022) 122605.

[26] J. Shen, M.Z. Yu, T.L. Chan, C. Tu, Y. Liu, Efficient method of moments for simulating atmospheric aerosol growth: Model description, verification, and application, J. Geophys.

Res.-Atmos. 125 (2020).

[27] K. Zhou, Z. He, M. Xiao, Z. Zhang, Parallel Monte Carlo simulation of aerosol dynamics, Adv. Mech. Eng. 6 (2014) 435936.

[28] A. Boje, M. Kraft, Stochastic population balance methods for detailed modelling of flame-made aerosol particles, J. Aerosol. Sci. 159 (2022) 105895.

[29] F.E. Kruis, J. Wei, T. van der Zwaag, S. Haep, Computational fluid dynamics based stochastic aerosol modeling: Combination of a cell-based weighted random walk method and a constant-number Monte-Carlo method for aerosol dynamics, Chem. Eng. Sci. 70 (2012) 109-120.

[30] J. Wei, F.E. Kruis, A GPU-based parallelized Monte-Carlo method for particle coagulation using an acceptance–rejection strategy, Chem. Eng. Sci. 104 (2013) 451-459.

[31] Z. Xu, H. Zhao, C. Zheng, Accelerating population balance-Monte Carlo simulation for coagulation dynamics from the Markov jump model, stochastic algorithm and GPU parallel computing, J. Comput. Phys. 281 (2015) 844-863.

[32] H. Zhao, F.E. Kruis, C. Zheng, Reducing statistical noise and extending the size spectrum by applying weighted simulation particles in Monte Carlo simulation of coagulation, Aerosol Sci. Technol. 43 (2009) 781-793.

[33] X. Jiang, T.L. Chan, A new weighted fraction Monte Carlo method for particle coagulation, Int. J. Numer. Methods Heat Fluid Flow 31 (2021) 3009-3029.

[34] Z. Xu, H. Zhao, C. Zheng, Fast Monte Carlo simulation for particle coagulation in population balance, J. Aerosol. Sci. 74 (2014) 11-25.

[35] F. Wang, T.L. Chan, A new sorting algorithm-based merging weighted fraction Monte Carlo method for solving the population balance equation for particle coagulation dynamics, Int. J. Numer. Methods Heat Fluid Flow 33 (2023) 881-911.

[36] A. Maisels, F. Einar Kruis, H. Fissan, Direct simulation Monte Carlo for simultaneous nucleation, coagulation, and surface growth in dispersed systems, Chem. Eng. Sci. 59 (2004) 2231-2239.

[37] Y. Lin, K. Lee, T. Matsoukas, Solution of the population balance equation using constant-number Monte Carlo, Chem. Eng. Sci. 57 (2002) 2241-2252.

[38] F. Wang, L. An, T.L. Chan, Event-driven sorting algorithm-based Monte Carlo method with neighbour merging method for solving aerosol dynamics, Appl. Math. Model. 120 (2023) 833-862.

[39] M.R. Kholghy, G.A. Kelesidis, Surface growth, coagulation and oxidation of soot by a monodisperse population balance model, Combust. Flame 227 (2021) 456-463.

[40] C.R. Kaplan, J.W. Gentry, Agglomeration of chain-like combustion aerosols due to Brownian motion, Aerosol Sci. Technol. 8 (1988) 11-28.

[41] P. Mitchell, M. Frenklach, Monte carlo simulation of soot aggregation with simultaneous surface growth-why primary particles appear spherical, Symp. (Int.) Combust. 27 (1998) 1507-1514.

[42] M. Balthasar, M. Kraft, A stochastic approach to calculate the particle size distribution function of soot particles in laminar premixed flames, Combust. Flame 133 (2003) 289-298.

[43] M. Balthasar, M. Frenklach, Detailed kinetic modeling of soot aggregate formation in laminar premixed flames, Combust. Flame 140 (2005) 130-145.

[44] R.I.A. Patterson, M. Kraft, Models for the aggregate structure of soot particles, Combust. Flame 151 (2007) 160-172.

[45] A. Raj, M. Celnik, R. Shirley, M. Sander, R. Patterson, R. West, M. Kraft, A statistical approach to develop a detailed soot growth model using PAH characteristics, Combust. Flame 156 (2009) 896-913.

[46] M. Lucchesi, A. Abdelgadir, A. Attili, F. Bisetti, Simulation and analysis of the soot particle size distribution in a turbulent nonpremixed flame, Combust. Flame 178 (2017) 35-45.

[47] N. Dellinger, N. Bertier, F. Dupoirieux, G. Legros, Hybrid Eulerian-Lagrangian method for soot modelling applied to ethylene-air premixed flames, Energy 194 (2020) 116858.

[48] L. Gallen, A. Felden, E. Riber, B. Cuenot, Lagrangian tracking of soot particles in LES of gas turbines, Proc. Combust. Inst. 37 (2019) 5429-5436.

[49] X. Jiang, T.L. Chan, Lagrangian particle tracking with new weighted fraction Monte Carlo method for studying the soot particle size distributions in premixed flames, Int. J. Numer. Methods Heat Fluid Flow 32 (2022) 1961-1998.

[50] J.C. Ong, K.M. Pang, J.H. Walther, J.-H. Ho, H.K. Ng, Evaluation of a Lagrangian soot tracking method for the prediction of primary soot particle size under engine-like conditions, J. Aerosol. Sci. 115 (2018) 70-95.

[51] H.G. Weller, G. Tabor, H. Jasak, C. Fureby, A tensorial approach to computational continuum mechanics using object-oriented techniques, Comput. Phys. 12 (1998) 620-631.

[52] OpenFOAM. OpenFOAM v6. https://openfoam.org/release/6/.

[53] F. Wang, L. An, T.L. Chan, An OpenFOAM solver incorporating detailed transport model for reacting flow simulations, Comput. Phys. Commun. 309 (2025) 109472.

[54] F. Wang, T.L. Chan, A new one-equation turbulence model based on the combined standard *k-ε* and *k-ω* turbulence models for benchmark flow configurations, in: Proceedings of the 7th World Congress on Momentum, Heat and Mass Transfer (MHMT'22), 2022, 1-8.

[55] P. Rodrigues, B. Franzelli, R. Vicquelin, O. Gicquel, N. Darabiha, Coupling an LES approach and a soot sectional model for the study of sooting turbulent non-premixed flames, Combust. Flame 190 (2018) 477-499.

[56] M. Thomson, T. Mitra, A radical approach to soot formation, Science 361 (2018) 978-979.

[57] C.S. McEnally, L.D. Pfefferle, B. Atakan, K. Kohse-Höinghaus, Studies of aromatic hydrocarbon formation mechanisms in flames: Progress towards closing the fuel gap, Prog. Energy Combust. Sci. 32 (2006) 247-294.

[58] M. Frenklach, H. Wang, Detailed modeling of soot particle nucleation and growth, Symp. (Int.) Combust. 23 (1991) 1559-1566.

[59] J. Appel, H. Bockhorn, M. Frenklach, Kinetic modeling of soot formation with detailed chemistry and physics: laminar premixed flames of C2 hydrocarbons, Combust. Flame 121 (2000) 122-136.

[60] M. Frenklach, H. Wang, Detailed mechanism and modeling of soot particle formation, in Soot Formation in Combustion, 1994.

[61] B. Sun, S. Rigopoulos, A. Liu, Modelling of soot coalescence and aggregation with a two-population balance equation model and a conservative finite volume method, Combust. Flame 229 (2021) 111382.

[62] Y. Cai, Z. Zhang, L. Zhou, Experimental study on correlation between PAHs and soot in laminar co-flow diffusion flames of n-heptane at elevated pressure, Fuel 309 (2022) 122107.

[63] D. Hou, L. Pascazio, J. Martin, Y. Zhou, M. Kraft, X. You, On the reactive coagulation of incipient soot nanoparticles, J. Aerosol. Sci. 159 (2022) 105866.

[64] A. Mansouri, L. Zimmer, S.B. Dworkin, N.A. Eaves, Impact of pressure-based HACA rates on soot formation in varying-pressure coflow laminar diffusion flames, Combust. Flame 218 (2020) 109-120.

[65] H. Chu, J. Qi, S. Feng, W. Dong, R. Hong, B. Qiu, W. Han, Soot formation in high-pressure combustion: Status and challenges, Fuel 345 (2023) 128236.

[66] N.J. Brown, K.L. Revzan, Comparative sensitivity analysis of transport properties and reaction rate coefficients, Int. J. Chem. Kinet. 37 (2005) 538-553.

[67] N.J. Brown, L.A.J. Bastien, P.N. Price, Transport properties for combustion modeling, Prog. Energy Combust. Sci. 37 (2011) 565-582.

[68] A. Dasgupta, E. Gonzalez-Juez, D.C. Haworth, Flame simulations with an open-source code, Comput. Phys. Commun. 237 (2019) 219-229.

[69] Q. Yang, P. Zhao, H. Ge, reactingFoam-SCI: An open source CFD platform for reacting flow simulation, Comput. Fluids 190 (2019) 114-127.

[70] D. Zhou, S. Yang, A robust reacting flow solver with detailed transport, chemistry, and steady-state preserving splitting schemes based on OpenFOAM and Cantera, in AIAA Scitech 2020 Forum, 2020.

[71] D. Zhou, H. Zhang, S. Yang, A robust reacting flow solver with computational diagnostics based on OpenFOAM and Cantera, Aerospace 9 (2022) 102.

[72] N. Burali, S. Lapointe, B. Bobbitt, G. Blanquart, Y. Xuan, Assessment of the constant non-unity Lewis number assumption in chemically-reacting flows, Combust. Theory Model. 20 (2016) 632-657.

[73] A. Cuoci, A. Frassoldati, T. Faravelli, E. Ranzi, Numerical modeling of laminar flames with detailed kinetics based on the operator-splitting method, Energy Fuels 27 (2013) 7730-7753.

[74] B. Naud, O. Córdoba, M. Arias-Zugasti, Accurate heat (Fourier) and mass (Fick and thermodiffusion) multicomponent transport at similar cost as mixture-averaged approximation, Combust. Flame 249 (2023) 112599.

[75] D.G. Goodwin, H.K. Moffat, I. Schoegl, R.L. Speth, B.W. Weber, Cantera: An object-oriented software toolkit for chemical kinetics, thermodynamics, and transport processes version, Zenodo, 2022. https://www.cantera.org.

[76] H. Bonart, Implementation and validation of a solver for direct numerical simulations of turbulent reacting flows in OpenFOAM, Bachelor's thesis, Karlsruhe Institute of Technology, 2012.

[77] D. Messig, F. Hunger, J. Keller, C. Hasse, Evaluation of radiation modeling approaches for non-premixed flamelets considering a laminar methane air flame, Combust. Flame 160

(2013) 251-264.

[78] F. Zhang, H. Bonart, T. Zirwes, P. Habisreuther, H. Bockhorn, N. Zarzalis, Direct numerical simulation of chemically reacting flows with the public domain code OpenFOAM, in: High Performance Computing in Science and Engineering ‘14, 2015, 221-236.

[79] T. Zirwes, M. Sontheimer, F. Zhang, A. Abdelsamie, F.E.H. Pérez, O.T. Stein, H.G. Im, A. Kronenburg, H. Bockhorn, Assessment of numerical accuracy and parallel performance of OpenFOAM and its reacting flow extension EBIdnsFoam, Flow Turbul. Combust. 111 (2023).

[80] S. Zhong, F. Zhang, Z. Peng, F. Bai, Q. Du, Roles of CO2 and H2O in premixed turbulent oxy-fuel combustion, Fuel 234 (2018) 1044-1054.

[81] T. Li, J. Pan, F. Kong, B. Xu, X. Wang, A quasi-direct numerical simulation solver for compressible reacting flows, Comput. Fluids 213 (2020) 104718.

[82] R. Mao, M. Lin, Y. Zhang, T. Zhang, Z.-Q.J. Xu, Z.X. Chen, DeepFlame: A deep learning empowered open-source platform for reacting flow simulations, Comput. Phys. Commun. 291 (2023) 108842.

[83] R.J. Kee, F.M. Rupley, J.A. Miller, Chemkin-II: A Fortran chemical kinetics package for the analysis of gas-phase chemical kinetics, Sandia National Laboratories, 1989.

[84] Q. Yang, P. Zhao, Minimum ignition energy and propagation dynamics of laminar premixed cool flames, Proc. Combust. Inst. 38 (2021) 2315-2322.

[85] Q. Yang, Z. Chen, A.J. Susa, R.K. Hanson, P. Zhao, Thermal-pyrolysis induced over-driven flame and its potential role in the negative-temperature dependence of iso-octane flame speed at elevated temperatures, Combust. Flame 223 (2021) 65-76.

[86] G. Xiao, H. Ge, P. Zhao, Initiation and propagation of one-dimensional planar flames in mixtures with variable reaction progress, Combust. Flame 236 (2022) 111765.

[87] J. Sun, Y. Wang, B. Tian, Z. Chen, detonationFoam: An open-source solver for simulation of gaseous detonation based on OpenFOAM, Comput. Phys. Commun. 292 (2023) 108859.

[88] B. Tekgül, P. Peltonen, H. Kahila, O. Kaario, V. Vuorinen, DLBFoam: An open-source dynamic load balancing model for fast reacting flow simulations in OpenFOAM, Comput. Phys. Commun. 267 (2021) 108073.

[89] A. Cuoci, A. Frassoldati, T. Faravelli, E. Ranzi, A computational tool for the detailed kinetic modeling of laminar flames: Application to C2H4/CH4 coflow flames, Combust.

Flame 160 (2013) 870-886.

[90] A. Cuoci, A. Frassoldati, T. Faravelli, E. Ranzi, OpenSMOKE++: An object-oriented framework for the numerical modeling of reactive systems with detailed kinetic mechanisms, Comput. Phys. Commun. 192 (2015) 237-264.

[91] S.Y. Liu, T.L. Chan, Z. He, Y.Y. Lu, X. Jiang, F.Z. Wei, Soot formation and evolution characteristics in premixed methane/ethylene-oxygen-argon burner-stabilized stagnation flames, Fuel 242 (2019) 871-882.

[92] S.Y. Liu, T.L. Chan, J.Z. Lin, M.Z. Yu, Numerical study on fractal-like soot aggregate dynamics of turbulent ethylene-oxygen flame, Fuel 256 (2019) 115857.

[93] M. Liao, S. Jia, Q. Wang, T.L. Chan, Y. Li, X. Xu, Z. He, Numerical simulation of methane combustion in two-layer porous media under oxy-fuel condition, Flow Turbul. Combust. 110 (2023) 649-670.

[94] D.N. Nguyen, K.S. Jung, J.W. Shim, C.S. Yoo, Real-fluid thermophysicalModels: An OpenFOAM-based library for reacting flow simulations at high pressure, Comput. Phys. Commun. 273 (2022) 108264.

[95] M. Elkhoury, Partially lagging one-equation turbulence model, AIAA J. 53 (2015) 3661-3673.

[96] F.R. Menter, Eddy viscosity transport equations and their relation to the k-ε model, J. Fluids Eng.-Trans. ASME 119 (1997) 876-884.

[97] B. Pinier, R. Lewandowski, E. Mémin, P. Chandramouli, Testing a one-closure equation turbulence model in neutral boundary layers, Comput. Meth. Appl. Mech. Eng. 376 (2021) 113662.

[98] S. Langer, G. Suarez, Loosely coupled and coupled solution methods for the RANS equations and a one-equation turbulence model, Comput. Fluids 232 (2022) 105186.

[99] K.L. Tang, Y. Ouyang, R.K. Agarwal, J.M. Chen, Y. Xiang, J.F. Chen, Computation of gas-liquid flow in a square bubble column with Wray-Agarwal one-equation turbulence model, Chem. Eng. Sci. 218 (2020) 115551.

[100] Y. Shao, R.K. Agarwal, X. Wang, B. Jin, Application of Wray-Agarwal turbulence model for numerical simulation of gas-solid flows in circulating fluidized bed risers, J. Energy Resour. Technol.-Trans. ASME 144 (2021).

[101] X. Han, M. Rahman, R.K. Agarwal, Development and application of wall-distance-free Wray-Agarwal turbulence model (WA2018), in 2018 AIAA Aerospace Sciences Meeting,

2018.

[102] D. Aubagnac-Karkar, J.-B. Michel, O. Colin, P.E. Vervisch-Kljakic, N. Darabiha, Sectional soot model coupled to tabulated chemistry for Diesel RANS simulations, Combust. Flame 162 (2015) 3081-3099.

[103] K. Li, P. Rahnama, R. Novella, B. Somers, Combining flamelet-generated manifold and machine learning models in simulation of a non-premixed diffusion flame, Energy AI 14 (2023) 100266.

[104] M. Song, X. Tang, J. Xing, K. Liu, K. Luo, J. Fan, Physics-informed neural networks coupled with flamelet/progress variable model for solving combustion physics considering detailed reaction mechanism, Phys. Fluids 36 (2024).

[105] F. Liu, J.-L. Consalvi, F. Nmira, The importance of accurately modelling soot and radiation coupling in laminar and laboratory-scale turbulent diffusion flames, Combust. Flame 258 (2023) 112573.

[106] A. Kalbhor, D. Mira, A. Both, J. van Oijen, LES investigation of soot formation in a turbulent non-premixed jet flame with sectional method and FGM chemistry, Combust. Flame 259 (2024) 113128.

[107] F. Nmira, A. Bouffard, J.-L. Consalvi, Y. Wang, Large-eddy simulation of lab-scale ethylene buoyant diffusion flames: Effects of subgrid turbulence/soot production interaction and radiation models, Proc. Combust. Inst. 39 (2023) 3959-3968.

[108] M.E. Mueller, H. Pitsch, LES model for sooting turbulent nonpremixed flames, Combust. Flame 159 (2012) 2166-2180.

[109] W. Zhang, S. Karaca, J. Wang, Z. Huang, J.v. Oijen, Large eddy simulation of the Cambridge/Sandia stratified flame with flamelet-generated manifolds: Effects of non-unity Lewis numbers and stretch, Combust. Flame 227 (2021) 106-119.

[110] H. Pitsch, Unsteady flamelet modeling of differential diffusion in turbulent jet diffusion flames, Combust. Flame 123 (2000) 358-374.

[111] R.S. Barlow, J.H. Frank, A.N. Karpetis, J.Y. Chen, Piloted methane/air jet flames: Transport effects and aspects of scalar structure, Combust. Flame 143 (2005) 433-449.

[112] N. Malik, T. Løvås, F. Mauss, The effect of preferential diffusion on the soot initiation process in ethylene diffusion flames, Flow Turbul. Combust. 87 (2011) 293-312.

[113] A. Attili, F. Bisetti, M.E. Mueller, H. Pitsch, Effects of non-unity Lewis number of gas-phase species in turbulent nonpremixed sooting flames, Combust. Flame 166 (2016) 192-

202.

[114] K. Netzell, H. Lehtiniemi, F. Mauss, Calculating the soot particle size distribution function in turbulent diffusion flames using a sectional method, Proc. Combust. Inst. 31 (2007) 667-674.

[115] D.A. Lysenko, I.S. Ertesvåg, K.E. Rian, Numerical simulation of non-premixed turbulent combustion using the eddy dissipation concept and comparing with the steady laminar flamelet model, Flow Turbul. Combust. 93 (2014) 577-605.

[116] S. Yang, J.K. Lew, M.E. Mueller, Large Eddy Simulation of soot evolution in turbulent reacting flows: Strain-Sensitive Transport Approach for Polycyclic Aromatic Hydrocarbons, Combust. Flame 220 (2020) 219-234.

[117] I.M. Kennedy, Models of soot formation and oxidation, Prog. Energy Combust. Sci. 23 (1997) 95-132.

[118] P.A. Tesner, T.D. Smegiriova, V.G. Knorre, Kinetics of dispersed carbon formation, Combust. Flame 17 (1971) 253-260.

[119] I.M. Kennedy, W. Kollmann, J.Y. Chen, A model for soot formation in a laminar diffusion flame, Combust. Flame 81 (1990) 73-85.

[120] J.B. Moss, C.D. Stewart, K.J. Syed, Flowfield modelling of soot formation at elevated pressure, Symp. (Int.) Combust. 22 (1989) 413-423.

[121] K.J. Syed, C.D. Stewart, J.B. Moss, Modelling soot formation and thermal radiation in buoyant turbulent diffusion flames, Symp. (Int.) Combust. 23 (1991) 1533-1541.

[122] M. Fairweather, W.P. Jones, R.P. Lindstedt, Predictions of radiative transfer from a turbulent reacting jet in a cross-wind, Combust. Flame 89 (1992) 45-63.

[123] S. Valencia, S. Ruiz, J. Manrique, C. Celis, L.F. Figueira da Silva, Soot modeling in turbulent diffusion flames: review and prospects, J. Braz. Soc. Mech. Sci. Eng. 43 (2021) 219.

[124] M.D. Smooke, C.S. McEnally, L.D. Pfefferle, R.J. Hall, M.B. Colket, Computational and experimental study of soot formation in a coflow, laminar diffusion flame, Combust. Flame 117 (1999) 117-139.

[125] H. Watanabe, R. Kurose, M. Hayashi, T. Kitano, S. Komori, Effects of ambient pressure and precursors on soot formation in spray flames, Adv. Powder Technol. 25 (2014) 1376-1387.

[126] P.R. Lindstedt, Simplified soot nucleation and surface growth steps for non-premixed

flames, in Soot formation in combustion: mechanisms and models, 1994.

[127] R.M. Woolley, M. Fairweather, Yunardi, Conditional moment closure modelling of soot formation in turbulent, non-premixed methane and propane flames, Fuel 88 (2009) 393-407.

[128] S.J. Harris, A.M. Weiner, Determination of the rate constant for soot surface growth, Combust. Sci. Technol. 32 (1983) 267-275.

[129] S.J. Harris, A.M. Weiner, Surface growth of soot particles in premixed ethylene/air flames, Combust. Sci. Technol. 31 (1983) 155-167.

[130] K.M. Leung, R.P. Lindstedt, W.P. Jones, A simplified reaction mechanism for soot formation in nonpremixed flames, Combust. Flame 87 (1991) 289-305.

[131] K.B. Lee, M.W. Thring, J.M. Beér, On the rate of combustion of soot in a laminar soot flame, Combust. Flame 6 (1962) 137-145.

[132] J. Nagle, R.F. Strickland-Constable, Oxidation of carbon between 1000–2000°C, in Proceedings of the Fifth Conference on Carbon, 1962.

[133] H. Guo, P.M. Anderson, P.B. Sunderland, Optimized rate expressions for soot oxidation by OH and O2, Fuel 172 (2016) 248-252.

[134] A.J. Josephson, N.D. Gaffin, S.T. Smith, T.H. Fletcher, D.O. Lignell, Modeling soot oxidation and gasification with Bayesian statistics, Energy Fuels 31 (2017) 11291-11303.

[135] F. Liu, H. Guo, G.J. Smallwood, ö.L. Gülder, Numerical modelling of soot formation and oxidation in laminar coflow non-smoking and smoking ethylene diffusion flames, Combust. Theory Model. 7 (2003) 301-315.

[136] M. Zhang, J.C. Ong, K.M. Pang, X.-S. Bai, J.H. Walther, An investigation on early evolution of soot in n-dodecane spray combustion using large eddy simulation, Fuel 293 (2021) 120072.

[137] K.M. Pang, M. Jangi, X.S. Bai, J. Schramm, Evaluation and optimisation of phenomenological multi-step soot model for spray combustion under diesel engine-like operating conditions, Combust. Theory Model. 19 (2015) 279-308.

[138] M. Zhang, J.C. Ong, K.M. Pang, X.-S. Bai, J.H. Walther, Effects of ambient CO_2 and H_2O on soot processes in n-dodecane spray combustion using large eddy simulation, Fuel 312 (2022) 122700.

[139] N. Slavinskaya, A. Mirzayeva, R. Whitside, J. Starke, M. Abbasi, M. Auyelkhankyzy, V. Chernov, A modelling study of acetylene oxidation and pyrolysis, Combust. Flame 210

(2019) 25-42.

[140] K. Narayanaswamy, G. Blanquart, H. Pitsch, A consistent chemical mechanism for oxidation of substituted aromatic species, Combust. Flame 157 (2010) 1879-1898.

[141] Y. Wang, A. Raj, S.H. Chung, A PAH growth mechanism and synergistic effect on PAH formation in counterflow diffusion flames, Combust. Flame 160 (2013) 1667-1676.

[142] H. Guo, F. Liu, G.J. Smallwood, Ö.L. Gülder, Numerical study on the influence of hydrogen addition on soot formation in a laminar ethylene–air diffusion flame, Combust. Flame 145 (2006) 324-338.

[143] A. Liu, C.E. Garcia, F. Sewerin, B.A.O. Williams, S. Rigopoulos, Population balance modelling and laser diagnostic validation of soot particle evolution in laminar ethylene diffusion flames, Combust. Flame 221 (2020) 384-400.

[144] E. Quadarella, J. Guo, H.G. Im, A consistent soot nucleation model for improved prediction of strain rate sensitivity in ethylene/air counterflow flames, Aerosol Sci. Technol. 56 (2022) 636-654.

[145] M.E. Mueller, G. Blanquart, H. Pitsch, A joint volume-surface model of soot aggregation with the method of moments, Proc. Combust. Inst. 32 (2009) 785-792.

[146] M.E. Mueller, G. Blanquart, H. Pitsch, Hybrid method of moments for modeling soot formation and growth, Combust. Flame 156 (2009) 1143-1155.

[147] G. Blanquart, H. Pitsch, Analyzing the effects of temperature on soot formation with a joint volume-surface-hydrogen model, Combust. Flame 156 (2009) 1614-1626.

[148] G. Blanquart, H. Pitsch, A joint volume-surface-hydrogen multi-variate model for soot formation, Combustion generated fine carbonaceous particles (2009) 437-463.

[149] J.D. Herdman, J.H. Miller, Intermolecular potential calculations for polynuclear aromatic hydrocarbon clusters, J. Phys. Chem. A 112 (2008) 6249-6256.

[150] Y. Wang, A. Raj, S.H. Chung, Soot modeling of counterflow diffusion flames of ethylene-based binary mixture fuels, Combust. Flame 162 (2015) 586-596.

[151] J.Y. Hwang, S.H. Chung, Growth of soot particles in counterflow diffusion flames of ethylene, Combust. Flame 125 (2001) 752-762.

[152] K. Zhou, X. Jiang, T.L. Chan, Error analysis in stochastic solutions of population balance equations, Appl. Math. Model. 80 (2020) 531-552.

[153] A.L. Garcia, C.V.D. Broeck, M. Aertsens, R. Serneels, A Monte Carlo simulation of coagulation, Physica A 143 (1987) 535-546.

[154] K. Liffman, A direct simulation Monte-Carlo method for cluster coagulation, J. Comput. Phys. 100 (1992) 116-127.

[155] M. Smith, T. Matsoukas, Constant-number Monte Carlo simulation of population balances, Chem. Eng. Sci. 53 (1998) 1777-1786.

[156] H. Zhao, C. Zheng, A new event-driven constant-volume method for solution of the time evolution of particle size distribution, J. Comput. Phys. 228 (2009) 1412-1428.

[157] H. Zhao, A. Maisels, T. Matsoukas, C. Zheng, Analysis of four Monte Carlo methods for the solution of population balances in dispersed systems, Powder Technol. 173 (2007) 38-50.

[158] A. Eibeck, W. Wagner, Stochastic particle approximations for Smoluchoski's coagualtion equation, Ann. Appl. Probab. 11 (2001) 1137-1165.

[159] R.I.A. Patterson, W. Wagner, M. Kraft, Stochastic weighted particle methods for population balance equations, J. Comput. Phys. 230 (2011) 7456-7472.

[160] A. Boje, J. Akroyd, M. Kraft, A hybrid particle-number and particle model for efficient solution of population balance equations, J. Comput. Phys. 389 (2019) 189-218.

[161] G. Kotalczyk, F.E. Kruis, A Monte Carlo method for the simulation of coagulation and nucleation based on weighted particles and the concepts of stochastic resolution and merging, J. Comput. Phys. 340 (2017) 276-296.

[162] Y. Chen, J. Ding, X. Xia, P. Weng, Reconstruction-based Monte Carlo method for accurate and efficient breakage simulation, Powder Technol. 401 (2022) 117318.

[163] P.K. Das, Monte Carlo simulation of drop breakage on the basis of drop volume, Comput. Chem. Eng. 20 (1996) 307-313.

[164] B.K. Mishra, Monte Carlo simulation of particle breakage process during grinding, Powder Technol. 110 (2000) 246-252.

[165] G. Kotalczyk, J. Devi, F.E. Kruis, A time-driven constant-number Monte Carlo method for the GPU-simulation of particle breakage based on weighted simulation particles, Powder Technol. 317 (2017) 417-429.

[166] R.E.L. DeVille, N. Riemer, M. West, Weighted Flow Algorithms (WFA) for stochastic particle coagulation, J. Comput. Phys. 230 (2011) 8427-8451.

[167] P.M. Bapat, L.L. Tavlarides, G.W. Smith, Monte carlo simulation of mass transfer in liquid-liquid dispersions, Chem. Eng. Sci. 38 (1983) 2003-2013.

[168] K. Rajamani, W.T. Pate, D.J. Kinneberg, Time-driven and event-driven Monte Carlo

simulations of liquid-liquid dispersions: a comparison, Ind. Eng. Chem. Fundamen. 25 (1986) 746-752.

[169] K. Lee, T. Matsoukas, Simultaneous coagulation and break-up using constant-*N* Monte Carlo, Powder Technol. 110 (2000) 82-89.

[170] M. Goodson, M. Kraft, Simulation of coalescence and breakage: an assessment of two stochastic methods suitable for simulating liquid–liquid extraction, Chem. Eng. Sci. 59 (2004) 3865-3881.

[171] K.F. Lee, R.I.A. Patterson, W. Wagner, M. Kraft, Stochastic weighted particle methods for population balance equations with coagulation, fragmentation and spatial inhomogeneity, J. Comput. Phys. 303 (2015) 1-18.

[172] H. Zhao, C. Zheng, M. Xu, Multi-Monte Carlo approach for general dynamic equation considering simultaneous particle coagulation and breakage, Powder Technol. 154 (2005) 164-178.

[173] E. Debry, B. Sportisse, B. Jourdain, A stochastic approach for the numerical simulation of the general dynamics equation for aerosols, J. Comput. Phys. 184 (2003) 649-669.

[174] M. Celnik, R. Patterson, M. Kraft, W. Wagner, Coupling a stochastic soot population balance to gas-phase chemistry using operator splitting, Combust. Flame 148 (2007) 158-176.

[175] S.Y. Liu, T.L. Chan, A coupled CFD-Monte Carlo method for simulating complex aerosol dynamics in turbulent flows, Aerosol Sci. Technol. 51 (2017) 269-281.

[176] S.Y. Liu, T.L. Chan, A stochastically weighted operator splitting Monte Carlo (SWOSMC) method for the numerical simulation of complex aerosol dynamic processes, Int. J. Numer. Methods Heat Fluid Flow 27 (2017) 263-278.

[177] H.M. Liu, T.L. Chan, Differentially weighted operator splitting Monte Carlo method for simulating complex aerosol dynamic processes, Particuology 36 (2018) 114-126.

[178] H.M. Liu, T.L. Chan, Two-component aerosol dynamic simulation using differentially weighted operator splitting Monte Carlo method, Appl. Math. Model. 62 (2018) 237-253.

[179] H.M. Liu, T.L. Chan, A coupled LES-Monte Carlo method for simulating aerosol dynamics in a turbulent planar jet, Int. J. Numer. Methods Heat Fluid Flow 30 (2020) 855-881.

[180] H.M. Liu, W. Jiang, W. Liu, X. Liu, S.Y. Liu, T.L. Chan, Monte Carlo simulation of polydisperse particle deposition and coagulation dynamics in enclosed chambers, Vacuum

184 (2021) 109952.

[181] H.M. Liu, J. Shao, W. Jiang, X. Liu, Numerical modeling of droplet aerosol coagulation, condensation/evaporation and deposition processes, Atmosphere 13 (2022) 326.

[182] J.H. Ferziger, Computational methods for fluid dynamics, 4th ed., Springer, Cham, Switzerland, 2020.

[183] H.K. Versteeg, W. Malalasekera, An introduction to computational fluid dynamics : the finite volume method, 2nd ed., Pearson Education Ltd., Harlow, England; New York, 2007.

[184] R.O. Fox, Computational models for turbulent reacting flows, Cambridge University Press, Cambridge; New York, 2003.

[185] B.E. Launder, D.B. Spalding, The numerical computation of turbulent flows, Comput. Meth. Appl. Mech. Eng. 3 (1974) 269-289.

[186] D.C. Wilcox, Turbulence modeling for CFD, DCW industries La Canada, CA, 1998.

[187] G.P. Smith, D.M. Golden, M. Frenklach, N.W. Moriarty, B. Eiteneer, M. Goldenberg, C.T. Bowman, R.K. Hanson, S. Song, W.C. Gardiner, J.V.V. Lissianski, Z. Qin. GRI-Mech 3.0. http://combustion.berkeley.edu/gri-mech/.

[188] E.K.Y. Yapp, D. Chen, J. Akroyd, S. Mosbach, M. Kraft, J. Camacho, H. Wang, Numerical simulation and parametric sensitivity study of particle size distributions in a burner-stabilised stagnation flame, Combust. Flame 162 (2015) 2569-2581.

[189] C. Chu, M.H. Zaher, M.J. Thomson, The temperature dependence of soot formation in laminar coflow aromatic flames, Combust. Flame 241 (2022) 112074.

[190] F. Mauss, T. Schäfer, H. Bockhorn, Inception and growth of soot particles in dependence on the surrounding gas phase, Combust. Flame 99 (1994) 697-705.

[191] C. Zhang, L. Chen, S. Ding, H. Xu, G. Li, J.-L. Consalvi, F. Liu, Effects of soot inception and condensation PAH species and fuel preheating on soot formation modeling in laminar coflow CH4/air diffusion flames doped with n-heptane/toluene mixtures, Fuel 253 (2019) 1371-1377.

[192] A. Kazakov, M. Frenklach, Dynamic modeling of soot particle coagulation and aggregation: Implementation with the Method of Moments and application to high-pressure laminar premixed flames, Combust. Flame 114 (1998) 484-501.

[193] H.M. Liu, T.L. Chan, A coupled LES-Monte Carlo method for simulating aerosol dynamics in a turbulent planar jet, Int. J. Numer. Methods Heat Fluid Flow 30 (2019) 855-881.

[194] S. Wu, D. Zhou, W. Yang, Implementation of an efficient method of moments for treatment of soot formation and oxidation processes in three-dimensional engine simulations, Appl. Energy 254 (2019) 113661.

[195] M. Frenklach, Method of moments with interpolative closure, Chem. Eng. Sci. 57 (2002) 2229-2239.

[196] D.L. Marchisio, R.O. Fox, Solution of population balance equations using the direct quadrature method of moments, J. Aerosol. Sci. 36 (2005) 43-73.

[197] A. Wick, T.-T. Nguyen, F. Laurent, R.O. Fox, H. Pitsch, Modeling soot oxidation with the extended quadrature method of moments, Proc. Combust. Inst. 36 (2017) 789-797.

[198] F. Ferraro, S. Gierth, S. Salenbauch, W. Han, C. Hasse, Soot particle size distribution reconstruction in a turbulent sooting flame with the split-based extended quadrature method of moments, Phys. Fluids 34 (2022).

[199] M.Z. Yu, J.Z. Lin, T.L. Chan, A new moment method for solving the coagulation equation for particles in Brownian motion, Aerosol Sci. Technol. 42 (2008) 705-713.

[200] S.Y. Liu, T.L. Chan, H.J. Liu, Numerical simulation of particle formation and evolution in a vehicle exhaust plume using the bimodal Taylor expansion method of moments, Particuology 43 (2019) 46-55.

[201] C.A. Hoerlle, F.M. Pereira, Effects of CO_2 addition on soot formation of ethylene non-premixed flames under oxygen enriched atmospheres, Combust. Flame 203 (2019) 407-423.

[202] N.A. Eaves, Q. Zhang, F. Liu, H. Guo, S.B. Dworkin, M.J. Thomson, CoFlame: A refined and validated numerical algorithm for modeling sooting laminar coflow diffusion flames, Comput. Phys. Commun. 207 (2016) 464-477.

[203] J.Z. Wen, M.J. Thomson, M.F. Lightstone, S.N. Rogak, Detailed kinetic modeling of carbonaceous nanoparticle inception and surface growth during the pyrolysis of C6H6 behind shock waves, Energy Fuels 20 (2006) 547-559.

[204] Q. Zhang, H. Guo, F. Liu, G.J. Smallwood, M.J. Thomson, Implementation of an advanced fixed sectional aerosol dynamics model with soot aggregate formation in a laminar methane/air coflow diffusion flame, Combust. Theory Model. 12 (2008) 621-641.

[205] Q. Zhang, H. Guo, F. Liu, G.J. Smallwood, M.J. Thomson, Modeling of soot aggregate formation and size distribution in a laminar ethylene/air coflow diffusion flame with detailed PAH chemistry and an advanced sectional aerosol dynamics model, Proc.

Combust. Inst. 32 (2009) 761-768.

[206] V. Chernov, Q. Zhang, M.J. Thomson, S.B. Dworkin, Numerical investigation of soot formation mechanisms in partially-premixed ethylene–air co-flow flames, Combust. Flame 159 (2012) 2789-2798.

[207] R. Demarco, A. Jerez, F. Liu, L. Chen, A. Fuentes, Modeling soot formation in laminar coflow ethylene inverse diffusion flames, Combust. Flame 232 (2021) 111513.

[208] D.T. Gillespie, An exact method for numerically simulating the stochastic coalescence process in a cloud, J. Atmos. Sci. 32 (1975) 1977-1989.

[209] R. Sedgewick, K. Wayne, Algorithms, fourth ed., Addison-Wesley, Upper Saddle River, NJ, 2011.

[210] S. Goel, R. Kumar, Brownian Motus and Clustered Binary insertion sort methods: An efficient progress over traditional methods, Future Generation Computer Systems 86 (2018) 266-280.

[211] E. Kapur, P. Kumar, S. Gupta, Proposal of a two way sorting algorithm and performance comparison with existing algorithms, International Journal of Computer Science, Engineering and Applications 2 (2012) 61-78.

[212] C.R. Cook, D.J. Kim, Best sorting algorithm for nearly sorted lists, Commun. ACM 23 (1980) 620-624.

[213] H. Zhao, C. Zheng, M. Xu, Multi-Monte Carlo method for coagulation and condensation/evaporation in dispersed systems, J. Colloid Interface Sci. 286 (2005) 195-208.

[214] H. Zhao, C. Zheng, Correcting the multi-Monte Carlo method for particle coagulation, Powder Technol. 193 (2009) 120-123.

[215] B.H. Shah, D. Ramkrishna, J.D. Borwanker, Simulation of particulate systems using the concept of the interval of quiescence, AICHE J. 23 (1977) 897-904.

[216] M. Sander, R.H. West, M.S. Celnik, M. Kraft, A detailed model for the sintering of polydispersed nanoparticle agglomerates, Aerosol Sci. Technol. 43 (2009) 978-989.

[217] C.S. Lindberg, M.Y. Manuputty, E.K.Y. Yapp, J. Akroyd, R. Xu, M. Kraft, A detailed particle model for polydisperse aggregate particles, J. Comput. Phys. 397 (2019) 108799.

[218] J.D. Landgrebe, S.E. Pratsinis, A discrete-sectional model for particulate production by gas-phase chemical reaction and aerosol coagulation in the free-molecular regime, J. Colloid Interface Sci. 139 (1990) 63-86.

[219] M. Kostoglou, A.J. Karabelas, An assessment of low-order methods for solving the breakage equation, Powder Technol. 127 (2002) 116-127.

[220] R.M. Ziff, E.D. McGrady, The kinetics of cluster fragmentation and depolymerisation, J. Phys. A-Math. Gen. 18 (1985) 3027-3037.

[221] G. Kaur, R. Singh, H. Briesen, Approximate solutions of aggregation and breakage population balance equations, J. Math. Anal. Appl. 512 (2022) 126166.

[222] D.P. Patil, J.R.G. Andrews, An analytical solution to continuous population balance model describing floc coalescence and breakage – A special case, Chem. Eng. Sci. 53 (1998) 599-601.

[223] R.J. Kee, M.E. Coltrin, P. Glarborg, Chemically reacting flow: theory and practice, Wiley-Interscience, New York, 2003.

[224] T. Poinsot, D. Veynante, Theoretical and numerical combustion, 3rd ed., RT Edwards, Inc., Philadelphia, 2012.

[225] B.J. McBride, Coefficients for calculating thermodynamic and transport properties of individual species, National Aeronautics and Space Administration, 1993.

[226] R.J. Kee, G. Dixon-Lewis, J. Warnatz, M.E. Coltrin, J.A. Miller, A Fortran computer code package for the evaluation of gas-phase, multicomponent transport properties, Sandia National Laboratories, 1986.

[227] R.I. Issa, Solution of the implicitly discretised fluid flow equations by operator-splitting, J. Comput. Phys. 62 (1986) 40-65.

[228] B.A.V. Bennett, C.S. McEnally, L.D. Pfefferle, M.D. Smooke, Computational and experimental study of axisymmetric coflow partially premixed methane/air flames, Combust. Flame 123 (2000) 522-546.

[229] T. Zirwes, F. Zhang, P. Habisreuther, M. Hansinger, H. Bockhorn, M. Pfitzner, D. Trimis, Quasi-DNS dataset of a piloted flame with inhomogeneous inlet conditions, Flow Turbul. Combust. 104 (2020) 997-1027.

[230] K. Claramunt, R. Cònsul, C.D. Pérez-Segarra, A. Oliva, Multidimensional mathematical modeling and numerical investigation of co-flow partially premixed methane/air laminar flames, Combust. Flame 137 (2004) 444-457.

[231] L. Xu, F. Yan, M. Zhou, Y. Wang, An experimental and modeling study on sooting characteristics of laminar counterflow diffusion flames with partial premixing, Energy 218 (2021) 119479.

[232] R.S. Barlow, A.N. Karpetis, J.H. Frank, J.Y. Chen, Scalar profiles and NO formation in laminar opposed-flow partially premixed methane/air flames, Combust. Flame 127 (2001) 2102-2118.

[233] F. Xu, P.B. Sunderland, G.M. Faeth, Soot formation in laminar premixed ethylene/air flames at atmospheric pressure, Combust. Flame 108 (1997) 471-493.

[234] P. Arora, P. Verma, A. Zare, F. Lodi, M. Jafari, S. Stevanovic, T.A. Bodisco, R.J. Brown, Z. Ristovski, Morphology and nanostructure of soot particles from diesel engine under transient and steady-state operating conditions with a microalgae fuel component, dioctyl phthalate biofuel, Sustain. Energy Technol. Assess. 60 (2023) 103504.

[235] A. Naseri, M.R. Kholghy, N.A. Juan, M.J. Thomson, Simulating yield and morphology of carbonaceous nanoparticles during fuel pyrolysis in laminar flow reactors enabled by reactive inception and aromatic adsorption, Combust. Flame 237 (2022) 111721.

[236] G.A. Kelesidis, E. Goudeli, S.E. Pratsinis, Morphology and mobility diameter of carbonaceous aerosols during agglomeration and surface growth, Carbon 121 (2017) 527-535.

[237] A. Gomez, D.E. Rosner, Thermophoretic effects on particles in counterflow laminar diffusion flames, Combust. Sci. Technol. 89 (1993) 335-362.

[238] W.L. Flower, Measurements of the diffusion coefficient for soot particles in flames, Phys. Rev. Lett. 51 (1983) 2287-2290.

[239] V.Y. Rudyak, S.N. Dubtsov, A.M. Baklanov, Measurements of the temperature dependent diffusion coefficient of nanoparticles in the range of 295–600K at atmospheric pressure, J. Aerosol. Sci. 40 (2009) 833-843.

[240] K. Gleason, F. Carbone, A. Gomez, Effect of temperature on soot inception in highly controlled counterflow ethylene diffusion flames, Combust. Flame 192 (2018) 283-294.

[241] U. Trivanovic, M. Pereira Martins, S. Benz, G.A. Kelesidis, S.E. Pratsinis, Dynamics of soot surface growth and agglomeration by enclosed spray combustion of jet fuel, Fuel 342 (2023) 127864.

[242] M.R. Kholghy, G.A. Kelesidis, S.E. Pratsinis, Reactive polycyclic aromatic hydrocarbon dimerization drives soot nucleation, Phys. Chem. Chem. Phys. 20 (2018) 10926-10938.

[243] K.O. Johansson, F. El Gabaly, P.E. Schrader, M.F. Campbell, H.A. Michelsen, Evolution of maturity levels of the particle surface and bulk during soot growth and

oxidation in a flame, Aerosol Sci. Technol. 51 (2017) 1333-1344.

[244] G.A. Kelesidis, S.E. Pratsinis, Estimating the internal and surface oxidation of soot agglomerates, Combust. Flame 209 (2019) 493-499.

[245] M.R. Kholghy, A. Veshkini, M.J. Thomson, The core–shell internal nanostructure of soot – A criterion to model soot maturity, Carbon 100 (2016) 508-536.

[246] M.J. Thomson, Modeling soot formation in flames and reactors: Recent progress and current challenges, Proc. Combust. Inst. 39 (2023) 805-823.

[247] W. Qian, X. Hui, B. Wang, A. Kronenburg, C.-J. Sung, Y. Lin, An investigation into oxidation-induced fragmentation of soot aggregates by Langevin dynamics simulations, Fuel 334 (2023) 126547.

[248] B. Yan, Y. Cheng, T. Li, Y. Cheng, Detailed kinetic modeling of acetylene decomposition/soot formation during quenching of coal pyrolysis in thermal plasma, Energy 121 (2017) 10-20.

[249] OpenCFD. OpenFOAM v2306. https://www.openfoam.com.

[250] Y. Wang, S.H. Chung, Effect of strain rate on sooting limits in counterflow diffusion flames of gaseous hydrocarbon fuels: Sooting temperature index and sooting sensitivity index, Combust. Flame 161 (2014) 1224-1234.

[251] H.K. Chelliah, C.K. Law, T. Ueda, M.D. Smooke, F.A. Williams, An experimental and theoretical investigation of the dilution, pressure and flow-field effects on the extinction condition of methane-air-nitrogen diffusion flames, Symp. (Int.) Combust. 23 (1991) 503-511.

[252] P. Jiang, L. Xu, Q. Wang, Z. Wang, S.H. Chung, Y. Wang, Experimental and kinetic study on aromatic formation in counterflow diffusion flames of methane and methane/ethylene mixtures, Fuel 354 (2023) 129304.

[253] P.H. Joo, Y. Wang, A. Raj, S.H. Chung, Sooting limit in counterflow diffusion flames of ethylene/propane fuels and implication to threshold soot index, Proc. Combust. Inst. 34 (2013) 1803-1809.

[254] L. Xu, F. Yan, M. Zhou, Y. Wang, S.H. Chung, Experimental and soot modeling studies of ethylene counterflow diffusion flames: Non-monotonic influence of the oxidizer composition on soot formation, Combust. Flame 197 (2018) 304-318.

[255] Y. Wang, S.H. Chung, Strain rate effect on sooting characteristics in laminar counterflow diffusion flames, Combust. Flame 165 (2016) 433-444.

[256] M. Zhou, L. Xu, F. Yan, S.H. Chung, Y. Wang, Effects of oxygen partial premixing on soot formation in ethylene counterflow flames with oscillating strain rates, Combust. Flame 258 (2023) 112442.

[257] D.C. Wilcox, Reassessment of the scale-determining equation for advanced turbulence models, AIAA J. 26 (1988) 1299-1310.

[258] B. Baldwin, T. Barth, A one-equation turbulence transport model for high Reynolds number wall-bounded flows, in 29th Aerospace Sciences Meeting, 1991.

[259] O. Colin, F. Ducros, D. Veynante, T. Poinsot, A thickened flame model for large eddy simulations of turbulent premixed combustion, Phys. Fluids 12 (2000) 1843-1863.

[260] E. Fares, W. Schröder, A general one-equation turbulence model for free shear and wall-bounded flows, Flow Turbul. Combust. 73 (2005) 187-215.

[261] F.R. Menter, M. Kuntz, R. Langtry, Ten years of industrial experience with the SST turbulence model, Turbulence, Heat and Mass Transfer 4 (2003) 625-632.

[262] OpenFOAM, OpenFOAM User Guide, OpenFOAM Foundation, 2014.

[263] C. Rumsey. NASA Langley Research Center Turbulence Modeling Resource. http://turbmodels.larc.nasa.gov.

[264] K. Wieghardt, W. Tillmann, On the turbulent friction layer for rising pressure, 1951.

[265] D.M. Driver, H.L. Seegmiller, Features of a reattaching turbulent shear layer in divergent channel flow, AIAA J. 23 (1985) 163-171.

[266] D. Greenblatt, K.B. Paschal, C.S. Yao, J. Harris, N.W. Schaeffler, A.E. Washburn, Experimental investigation of separation control part 1: baseline and steady suction, AIAA J. 44 (2006) 2820-2830.

[267] J.D. Anderson, Fundamentals of aerodynamics, Sixth ed., New York, NY: McGraw-Hill Education, New York, NY, 2017.

[268] A. Seifert, L.G. Pack, Active flow separation control on wall-mounted hump at high Reynolds humbers, AIAA J. 40 (2002) 1363-1372.

[269] M. Lee, R.D. Moser, Direct numerical simulation of turbulent channel flow up to $Re_\tau \approx 5200$, J. Fluid Mech. 774 (2015) 395-415.

[270] Z. Li, A. Cuoci, A. Parente, Large Eddy Simulation of MILD combustion using finite rate chemistry: Effect of combustion sub-grid closure, Proc. Combust. Inst. 37 (2019) 4519-4529.

[271] H. Liu, Z. Yin, W. Xie, B. Zhang, J. Le, H. Liu, Numerical and analytical assessment

of finite rate chemistry models for LES of turbulent premixed flames, Flow Turbul. Combust. 109 (2022) 435-458.

[272] I. Morev, B. Tekgül, M. Gadalla, A. Shahanaghi, J. Kannan, S. Karimkashi, O. Kaario, V. Vuorinen, Fast reactive flow simulations using analytical Jacobian and dynamic load balancing in OpenFOAM, Phys. Fluids 34 (2022) 021801.

[273] J.W. Gärtner, A. Shamooni, T. Zirwes, A. Kronenburg, A chemistry load balancing model for OpenFOAM, Comput. Phys. Commun. 305 (2024) 109322.

[274] Y. Yang, T. Hori, S. Sawada, F. Akamatsu, Accurate and rapid reactive flow simulations using dynamic load balancing and sparse analytical Jacobian approach, Phys. Fluids 36 (2024).

[275] J. Chomiak, A. Karlsson, Flame liftoff in diesel sprays, Symp. (Int.) Combust. 26 (1996) 2557-2564.

[276] D. Veynante, L. Vervisch, Turbulent combustion modeling, Prog. Energy Combust. Sci. 28 (2002) 193-266.

[277] T. Poinsot, D. Veynante, Theoretical and numerical combustion, 2nd ed., RT Edwards, Inc., 2005.

[278] Z. Li, M. Ferrarotti, A. Cuoci, A. Parente, Finite-rate chemistry modelling of non-conventional combustion regimes using a Partially-Stirred Reactor closure: Combustion model formulation and implementation details, Appl. Energy 225 (2018) 637-655.

[279] A. Azarinia, H. Mahdavy-Moghaddam, Comprehensive numerical study of molecular diffusion effects and Eddy Dissipation Concept model in MILD combustion, Int. J. Hydrog. Energy 46 (2021) 9252-9265.

[280] O.A. Marzouk, E.D. Huckaby, A comparative study of eight finite-rate chemistry kinetics for CO/H2 combustion, Eng. Appl. Comp. Fluid Mech. 4 (2010) 331-356.

[281] Z. Li, A. Cuoci, A. Sadiki, A. Parente, Comprehensive numerical study of the Adelaide Jet in Hot-Coflow burner by means of RANS and detailed chemistry, Energy 139 (2017) 555-570.

[282] M.T. Lewandowski, I.S. Ertesvåg, Analysis of the Eddy Dissipation Concept formulation for MILD combustion modelling, Fuel 224 (2018) 687-700.

[283] M.T. Lewandowski, P. Płuszka, J. Pozorski, Influence of inlet boundary conditions in computations of turbulent jet flames, Int. J. Numer. Methods Heat Fluid Flow 28 (2018) 1433-1456.

[284] S.H. Park, S.N. Rogak, A novel fixed-sectional model for the formation and growth of aerosol agglomerates, J. Aerosol. Sci. 35 (2004) 1385-1404.

[285] M.R. Kholghy, A. Schumann, A simple model for gas-phase synthesis of nickel nanoparticles, Energy Fuels 35 (2021) 5383-5391.

[286] T. Blacha, M. Di Domenico, P. Gerlinger, M. Aigner, Soot predictions in premixed and non-premixed laminar flames using a sectional approach for PAHs and soot, Combust. Flame 159 (2012) 181-193.

[287] M. Gu, F. Liu, J.-L. Consalvi, Ö.L. Gülder, Effects of pressure on soot formation in laminar coflow methane/air diffusion flames doped with n-heptane and toluene between 2 and 8 atm, Proc. Combust. Inst. 38 (2021) 1403-1412.

[288] H. Maldonado Colmán, M.E. Mueller, Large Eddy Simulation of the evolution of the soot size distribution in turbulent nonpremixed flames using the Bivariate Multi-Moment Sectional Method, Combust. Flame 265 (2024) 113496.

[289] D.F. Kronholm, J.B. Howard, Analysis of soot surface growth pathways using published plug-flow reactor data with new particle size distribution measurements and published premixed flame data, Proc. Combust. Inst. 28 (2000) 2555-2561.

[290] Q. Zhang, M.J. Thomson, H. Guo, F. Liu, G.J. Smallwood, A numerical study of soot aggregate formation in a laminar coflow diffusion flame, Combust. Flame 156 (2009) 697-705.

[291] M. Saffaripour, A. Veshkini, M. Kholghy, M.J. Thomson, Experimental investigation and detailed modeling of soot aggregate formation and size distribution in laminar coflow diffusion flames of Jet A-1, a synthetic kerosene, and n-decane, Combust. Flame 161 (2014) 848-863.

[292] G.A. Kelesidis, E. Goudeli, S.E. Pratsinis, Flame synthesis of functional nanostructured materials and devices: Surface growth and aggregation, Proc. Combust. Inst. 36 (2017) 29-50.

[293] J. Wei, Q. Xie, J. Zhang, Z. Ren, Flow, mixing, and flame stabilization in bluff-body burner with decreased central jet velocity, Phys. Fluids 33 (2021) 067122.

[294] A. Rowhani, Z.W. Sun, P.R. Medwell, Z.T. Alwahabi, G.J. Nathan, B.B. Dally, Effects of the bluff-body diameter on the flow-field characteristics of non-premixed turbulent highly-sooting flames, Combust. Sci. Technol. 194 (2022) 378-396.

[295] H.M. Colmán, P.P. Duvvuri, M.E. Mueller, Large eddy simulation of soot evolution in

turbulent nonpremixed bluff body flames, Proc. Combust. Inst. 39 (2023) 857-866.

[296] B.B. Dally, D.F. Fletcher, A.R. Masri, Flow and mixing fields of turbulent bluff-body jets and flames, Combust. Theory Model. 2 (1998) 193-219.

[297] B.B. Dally, A.R. Masri, R.S. Barlow, G.J. Fiechtner, Instantaneous and mean compositional structure of bluff-body stabilized nonpremixed flames, Combust. Flame 114 (1998) 119-148.

[298] A.J. Gee, Y. Yin, K.K. Foo, A. Chinnici, N. Smith, P.R. Medwell, Toluene addition to turbulent H2/natural gas flames in bluff-body burners, Int. J. Hydrog. Energy 47 (2022) 27733-27746.

[299] M.E. Mueller, Q.N. Chan, N.H. Qamar, B.B. Dally, H. Pitsch, Z.T. Alwahabi, G.J. Nathan, Experimental and computational study of soot evolution in a turbulent nonpremixed bluff body ethylene flame, Combust. Flame 160 (2013) 1298-1309.

[300] S. Deng, M.E. Mueller, Q.N. Chan, N.H. Qamar, B.B. Dally, Z.T. Alwahabi, G.J. Nathan, Hydrodynamic and chemical effects of hydrogen addition on soot evolution in turbulent nonpremixed bluff body ethylene flames, Proc. Combust. Inst. 36 (2017) 807-814.

[301] A. Rowhani, Z. Sun, P.R. Medwell, G.J. Nathan, B.B. Dally, Soot-flowfield interactions in turbulent non-premixed bluff-body flames of ethylene/nitrogen, Proc. Combust. Inst. 38 (2021) 1125-1132.

[302] A. Rowhani, Z. Sun, P.R. Medwell, G.J. Nathan, B.B. Dally, Relationships between soot and the local instantaneous strain rate in turbulent non-premixed bluff-body flames, Energy Fuels 36 (2022) 12181-12191.

[303] A. Rowhani, Z. Sun, A. Chinnici, P.R. Medwell, G.J. Nathan, B.B. Dally, Soot structure and flow characteristics in turbulent non-premixed methane flames stabilised on a bluff-body, Fuel 344 (2023) 128118.

[304] F. Anselmet, F. Ternat, M. Amielh, O. Boiron, P. Boyer, L. Pietri, Axial development of the mean flow in the entrance region of turbulent pipe and duct flows, C. R. Mec. 337 (2009) 573-584.

[305] R.W. Bilger, S.H. Stårner, R.J. Kee, On reduced mechanisms for methane air combustion in nonpremixed flames, Combust. Flame 80 (1990) 135-149.

[306] L.J. De Chant, The venerable 1/7th power law turbulent velocity profile: a classical nonlinear boundary value problem solution and its relationship to stochastic processes,

Appl. Math. Comput. 161 (2005) 463-474.

[307] L. Tian, R.P. Lindstedt, Impact of molecular mixing and scalar dissipation rate closures on turbulent bluff-body flames with increasing local extinction, Combust. Flame 206 (2019) 51-67.

[308] A. Alfazazi, A.M. Elbaz, J. Li, S. Abdelwahid, H.G. Im, B. Dally, Characteristics of ammonia-hydrogen nonpremixed bluff-body-stabilized flames, Combust. Flame 258 (2023) 113066.

[309] N.J. Curtis, K.E. Niemeyer, C.-J. Sung, Accelerating reactive-flow simulations using vectorized chemistry integration, Comput. Phys. Commun. 278 (2022) 108409.

[310] J. Singh, R.I.A. Patterson, M. Kraft, H. Wang, Numerical simulation and sensitivity analysis of detailed soot particle size distribution in laminar premixed ethylene flames, Combust. Flame 145 (2006) 117-127.